

Lead-free absorber materials for solar cell applications



A dissertation submitted to
The Faculty of Engineering,
University of Duisburg-Essen,
Institute of Materials Science
for the academic degree of
Doctor of Natural Sciences
Doctor rerum naturalium (Dr. rer. nat.)

by

Martina Pantaler, Mag. Ing. Chem.

(University of Zagreb, Faculty of Chemical Engineering and Technology, Croatia)

1st Examiner: Prof. Dr. Doru C. Lupascu

2nd Examiner: Prof. Dr. Giulia Grancini

Thesis submitted: February 2020, Essen

Thesis defense: June 10th, 2020, Essen

DuEPublico

Duisburg-Essen Publications online

UNIVERSITÄT
DUISBURG
ESSEN

Offen im Denken

ub | universitäts
bibliothek

Diese Dissertation wird über DuEPublico, dem Dokumenten- und Publikationsserver der Universität Duisburg-Essen, zur Verfügung gestellt und liegt auch als Print-Version vor.

DOI: 10.17185/duepublico/72147

URN: urn:nbn:de:hbz:464-20200729-085706-4

Alle Rechte vorbehalten.

*Za moje roditelje
Vericu i Zdravka Pantaler*

Declaration

I declare that the contents of this dissertation are original work prepared by myself, except when a particular reference is made to the work of others, including the electronic sources. This work has not been submitted entirely or partially for any other degree or qualification in this, or any other University. This dissertation is the outcome of my original work and the work done in collaboration has been duly acknowledged.

Martina Pantaler

Essen, January 2020.

Acknowledgements

This PhD Thesis could not be possible without the support, collaborations, help and encouragement of my professors, colleagues, friends and family, and therefore I would like to express my gratitude and acknowledgement for everything during this past 4 years.

First, I would like to thank, my supervisor, Professor Dr. Doru Constantin Lupascu, for giving me the opportunity to work in his group and to learn from him. Also, for giving me the possibility to improve my knowledge through research and scientific work. Thank you for all the support, help and encouragement. I am grateful for being a part of your group and being able to learn and accumulate experience for professional and personal life.

The second professor to whom I am very grateful and I admire is Professor Dr. Giulia Grancini, from the University of Pavia. I am grateful for the opportunity to be a part of your small EPFL (Ecole polytechnique fédérale de Lausanne) group in Switzerland for a total of 7 months for my PhD. I admire your work in scientific community and your passion for science. It was a wonderful time to work with you and with all members of GMF group. We had constructive discussions and I have learned a lot. Thanks to Professor Mohammad Khaja Nazeeruddin, for allowing me to be a part of his group as a visiting PhD student in Sion, Switzerland.

Furthermore, I would like to thank professors which I highly admire: professor Peter Chen from NCKU University Tainan, Taiwan for spending one month at your group, for the scholarship and great discussions, and also Dr. Selina Olthof from University of Cologne for all the help and support during the XPS/UPS/IPES measurements. Thank you that I could learn from you and for your encouragement. I admire your work and your enthusiasm for science.

I acknowledge the financial support from PEROBOOST project for my research in Germany and from DAAD for my stay at EPFL, Switzerland for 7 months. Therefore I would like to thank all PEROBOOST group members especially M.Sc. Svetlana Sirotinskaya from professor Roland Schmechel group for support in the solar cells fabrication and M.Sc. Alexander Schmitz, from professor Gerd Bacher group from Duisburg for the optical measurements. Great thanks goes to Dr. Kyung Taek Cho, Dr. Ines Garcia Benito and Valentin I. E. Queloz, from the EPFL group for great time during my stay and successful research, excellent work in the lab and all inspirational experiments. Thanks to all members of EPFL, GMF group (Group for Molecular Engineering of Functional Materials) and very joyful and educative period during

my stay in Switzerland, for the support and friendship, happy lunches and evenings. Thanks to the whole group of Professor Peter Chen especially Harvey (Po-Kai Kung) for being my supervisor and great support in Tainan. I would like to thank Dr. Olga Syzgantseva from the EPFL, Professor David Beljonne, Dr. Claudio Quarti and Dr. Valentin Diez Cabanes from Université de Mons (Belgium) for all theoretical calculations and nice and fruitful discussions.

Thanks to the whole UDEMAT group. Especially Dr. Hans-Joachim Keck for being great support and motivating me during my PhD writing process. I highly acknowledge the support in paperwork, which I got from Sabine Kriegel and Marianne Breitkopf. Thanks to former employee Patrick Dubray and Karl-Heinz Menze for technical support and thanks to all technicians. I would like to thank Dr. Vladimir Shvartsman and Dr. Vadala, Dr. Maryam Khazayee, Dr. Tommy Mielke, Dr. Escobar, Alfred Gäbel, Dr. Christian H., Dr. Kevin Voges, and great PhD students; Astita, Nicole, Daniil, Andrei, Jin, Domenic, Felix, Yusra, Gustav. Special gratitude I express to a former college Dr. Irina Anusca for support, encouragement, friendship, our fruitful discussions and café breaks.

Thanks to all my friends from Croatia, especially Vjeran, for all funny and encouraging moments, Natalija and Veronika, Sanja, Lidija, Kristina, and Martina for support and joy you gave me during my not so easy PhD period. My wonderful German friends Miri and Harald for being patient with me and always helpful, for sharing and being with me through all nice and less nicer times. Thanks to whole Totus Tuus friends for all the support, kindness, friendship and the joy you gave me.

Finally, most important gratitude goes to my whole family, my grandparents and especially my parents Verica and Zdravko and my brother Matija. Thank you for all the sacrifice and patience, for encouraging and supporting me in all my decisions. Thank you for setting a great example for hard work and devotion and showing me how to fight for the things you love and care.

Everybody of above mention people, made my life during PhD more beautiful.

PhD research and writing process was a very interesting adventure and I am deeply grateful for this experience.

Abstract

With the rise of industry and technology development based on the utilization of fossil fuels as a main energy source as well as environmental and air pollution greenhouse gases have drastically increased with the alert and demand to alter the sources of energy. One way to do so is to reduce the consumption of fossil fuels and replace it by other sources such as renewable energies. Most interesting and promising is solar energy. After the discovery of the photovoltaic effect and applying it for making solar cells, an effective way to convert solar energy into electric energy has become achievable. Throughout history three different solar cell generations can be observed mostly based on the evolution of solar cells by the decrease of the solar cell thickness and the lowering of the active layer thickness from μm to nm . Beyond the decrease in thickness of the solar cells, the price of solar cells has dropped over the years. Still, the silicon-based technology is complex and cost-intensive.

The third generation of solar cells are thin films with their most interesting and well-researched sub-group: perovskite solar cells. This new way of cheap and easy-to-fabricate solar cell has interested both, scientists and industry. A decade of lead-based perovskite solar cells in the scientific community has shown an increase in power conversion efficiency from 3.8 to 26 % and enormous interest of world scientists investigating the excellent photovoltaic properties of these lead-based perovskites (e.g. $\text{CH}_3\text{NH}_3\text{PbI}_3$) but also the possibility of large commercialization. Organic–inorganic lead halide perovskite absorbers have excellent photovoltaic properties, such as suitable bandgap, high optical absorption, and long carrier lifetime. Unfortunately, underlying issues are the presence of toxic lead and the cell instability under ambient atmosphere (e.g. O_2 and H_2O).

Bismuth-based lead-free double perovskites (e.g. $\text{Cs}_2\text{AgBiBr}_6$) have been considered as alternatives to the lead-based perovskites for solar cell applications. Trivalent cations, such as Bi^{3+} along with monovalent cations, Ag^+ , have been concurrently introduced to the B-sites of halide perovskites, leading to B cation double perovskites with the general chemical formula of $\text{A}_2\text{B}'\text{B}''\text{X}_6$. These Pb-free double perovskites have been reported to have promising photovoltaic properties, including long carrier recombination lifetime, good stability against air and moisture, and low carrier effective masses. Thus, they are a potential alternative to the toxic lead halide perovskites. Nevertheless, device development is still in its infancy, and its performance is affected by severe hysteresis.

In this work the realization of the synthesis and deposition of the double perovskite is presented via different deposition routes such as vacuum vapor and solution deposition. The double

perovskite thin films have been optimized and characterized using different surface and material characterization methods. Afterwards, hysteresis-free planar and mesoporous double perovskite solar cells with no s-shape in the device characteristics and increased device open circuit voltage have been realized for the first time. This has been achieved by fine-tuning the material deposition parameters and layer optimization using several modification routes such as different temperature annealings, the thicknesses of mesoporous and perovskite layer, ozone and TiCl₄ treatments leading to better infiltration of the double perovskite solution into mesoporous TiO₂-ending with a significant improvement in solar cell performance. Except of device and interface engineering, to improve the material properties, compositional engineering has been conducted using mixing elements such as organic cation methylammonium, inorganic cation antimony and halide anion iodine. Finally, dimensional engineering has been achieved by adding large organic cations to the double perovskite crystal structure resulting in the new white emissive 2D and quasi 2D lead-free double perovskite materials.

Keywords: lead-free perovskites, double perovskite solar cells, Cs₂AgBiBr₆, low-dimensional lead-free perovskites, hysteresis-free lead-free perovskites

Kurzfassung

Bleifreie Absorbermaterialien für Solarzellen-Anwendung

Die Zunahme von Industrie und Technikentwicklung, die hauptsächlich auf der Verwendung fossiler Brennstoffe als Hauptenergielieferant beruht, sowie die wachsende Umwelt- und Luftverschmutzung haben zu einem drastischen Anstieg von Treibhausgasen geführt, die mit der Mahnung und Forderung nach alternativen Energiequellen einhergeht. Eine Möglichkeit diese zu erschließen, ergibt sich aus einer Reduktion fossiler Brennstoffe zugunsten anderer Quellen wie erneuerbaren Energien. Am interessantesten und vielversprechendsten ist in diesem Kontext die Solarenergie. Durch die Entdeckung des photovoltaischen Effekts und seiner Erschließung für Solarzellen wurde eine effektive Möglichkeit verfügbar, Solarenergie in elektrische Energie umzuwandeln. Im Laufe der Zeit können drei verschiedene Generationen von Solarzellen identifiziert werden, die hauptsächlich auf dem Versuch beruhen, Solarzellen durch die Reduktion ihrer Dicke sowie die Verminderung der aktiven Schicht von μm zu nm weiterzuentwickeln. Abgesehen von der Verdünnung der Solarzellen ist ihr Preis in den letzten Jahren gesunken, dennoch ist die Silizium-basierte Technologie komplex und kostenintensiv.

Die dritte Generation der Solarzellen ist die Dünnschicht-Generation mit ihrer interessantesten und viel erforschten Untergruppe: Perowskit-Solarzellen. Diese neue Art günstiger und leicht herstellbarer Solarzellen hat sowohl das Interesse der Wissenschaft als auch das industrieller Firmen geweckt. Ein Jahrzehnt in der Wissenschaftsgemeinde von bleibasierten Perowskit-Solarzellen hat einen Anstieg der Effizienz der Energieumwandlung von 3,8 auf 26 % ergeben; dazu kommt, dass Wissenschaftler weltweit exzellente, photovoltaische Eigenschaften dieser bleibasierten Perowskite (z. B. $\text{CH}_3\text{NH}_3\text{PbI}_3$) bestätigen konnten, das mit der Möglichkeit lukrativer Vermarktung einhergeht. Organisch-anorganische blei-halogenide Perowskit-Absorber zeigen ausgezeichnete photovoltaische Eigenschaften wie eine passende Bandlücke, eine hohe optische Absorption und eine lange Ladungsträgerlebensdauer. Leider sind sie durch das zugrunde liegende toxische Blei und ihrer Instabilität angesichts des Umgebungsklimas als problematisch einzustufen (z. B. O_2 und H_2O).

Bismut-basierte, bleifreie Doppelperowskite (z. B. CsAgBiBr_6) wurden als Alternativen zu den Blei-basierten Perowskiten für Solarzellen in Betracht gezogen. Dreiwertige Kationen, wie Bi^{3+} ,

einhergehend mit einwertigen Kationen, Ag^+ , wurden dazu den B-Seiten der haliden Perowskite zugeführt, die zu B-Kationen-Doppel-Perowskiten mit der allgemeinen chemischen Formel $\text{A}_2\text{B}'\text{B}''\text{X}_6$ führen. Diese Blei-freien Doppel-Perowskite wurden mit vielversprechenden, photovoltaischen Eigenschaften beschrieben, wie z. B. einer langen Lebensdauer der Ladungsträger, einer guten Stabilität angesichts von Luft und Feuchtigkeit sowie einer niedrigen effektiven Masse des Ladungsträgers. Somit sind sie potenzielle Alternativen zu den toxischen Blei-Halogenid-Perowskiten. Dennoch steckt die Entwicklung dieser Zellen noch in den Kinderschuhen und ihre Leistung wird von starken Hysteresen beeinflusst.

In der vorliegenden Arbeit wird die Verwirklichung der Synthese und Beschichtung der Doppel-Perowskite durch verschiedene Arten der Beschichtung wie der Vakuum-Aufdampfung und Flüssig-Beschichtung dargestellt. Die dünn-schichtigen Doppel-Perowskite wurden optimiert und durch den Gebrauch verschiedener Oberflächen- und Materialcharakterisierungs Methoden untersucht. Im Anschluss wurden zum ersten Mal Hysterese-freie, planare und mesoporöse Perowskit-Solarzellen realisiert, die ohne die charakteristische S-Form und mit einer gesteigerten Leerlaufspannung auskamen. Dies wurde durch die Feinabstimmung der Parameter der Materialbeschichtung in Kombination mit verschiedenen Arten der Modifikation erreicht, wie z. B. verschiedenen Annealing-Temperaturen, der Veränderung der Dicke mesoporöser und perowskitischer Schichten sowie Ozon- und TiCl_4 -Behandlungen, die zu einer besseren Einsickerung der flüssigen Doppel-Perowskite in die mesoporöse TiO_2 -Schicht mit einer signifikanten Verbesserung der Leistung der Solarzelle führt. Außer der Zellen- und Grenzschichtbearbeitung wurden zur Verbesserung der Materialmerkmale verschiedene Variationen der Zusammensetzung durchgeführt, die verschiedene Elemente wie organisches Methylammonium- Kationen, Antimon-Kationen und Iod-Anionen verbanden. Abschließend wurde die dimensionelle Bearbeitung durch Hinzufügen großer organischer Kationen zu der kristallinen Struktur des Doppel-Perowskits vorgenommen, aus dem sich die neuen, weiß-emittierenden 2D und quasi 2D bleifreien Materialien der Doppel-Perowskite ergaben.

Schlagerwörter: Bleifreie Perowskite, Doppel-Perowskit Solarzellen, $\text{Cs}_2\text{AgBiBr}_6$, niedrigdimensionale bleifreie Perowskite, Hysterese-freie bleifreie Perowskite, Interfacetechnik, Solarzellentechnik

Table of Contents

Chapter 1. Introduction	1
1.1. General Introduction	2
1.2 Brief History of Photovoltaics and Solar Cells	3
1.3. Physics of Solar Cells	5
1.3.1 Physical Principles of Semiconductors	5
1.3.2 Solar Cell Principles	9
1.3.3. Solar Cell Characterization	10
1.4. Introduction of Perovskite	13
1.4.1. Perovskite Crystal Structure	13
1.4.2. Properties and Characterization of Lead-based Perovskite Solar Cells	14
1.4.3. Fabrication of Perovskite Solar Cells and Device Architecture	14
1.4.4. Issues and Challenges	15
1.5. Lead-Free Perovskites	16
1.5.1. Theoretical Calculations in Literature	16
1.5.2. Experimental Results in Literature	17
1.6. Motivation and Scope of this Work	18
Chapter 2. “State of the art” double perovskite $\text{Cs}_2\text{AgBiBr}_6$	21
2.1. History overview of Double Perovskites	22
2.2. Theoretical Calculations and Findings of the Lead Free Double Perovskites	24
2.3. Synthesis and Experimental Findings on $\text{Cs}_2\text{AgBiBr}_6$	32
2.4. Solar Cell Application and Thin Film Characterization of $\text{Cs}_2\text{AgBiBr}_6$	34
2.5. Other Applications and Remarks	38
Chapter 3. Synthesis and Deposition Routes of Double Perovskite $\text{Cs}_2\text{AgBiBr}_6$	42
3.1. Synthesis	43
3.1.1. Solution Synthesis	43
3.1.2. Solid-state Synthesis	45

3.1.3. Hydrothermal Synthesis	45
3.2. Deposition Routes - Thin Film Preparation	47
3.2.1. Thermal Evaporation	47
3.2.2. Spin Coating.....	49
3.3. Characterization Methods.....	51
3.3.1. X-ray Diffractometry (XRD)	51
3.3.2. Electron Microscopy	53
3.3.3. Optical Characterization.....	54
3.3.4. Atomic-Force Microscope (AFM)	55
3.3.5. Photoemission Spectroscopy (PES)	55
3.4. Results on Double Perovskite Layer.....	58
3.4.1. Vapor Deposition.....	58
3.4.2. Solution Deposition	62
3.4.3. Deposition of the Double Perovskite on Top of the Different Substrates and Characterization of Thin Film	63
Chapter 4. Cs ₂ AgBiBr ₆ Double Perovskite Solar Cells	70
4.1 Experimental Details and Fabrication of Solar Cells	71
4.1.1. Fabrication of Inverted Planar Solar Cells.....	71
4.1.2. Fabrication of Mesoscopic Solar Cell	72
4.1.3. Fabrication of Planar Solar Cells.....	73
4.2. Characterization Methods of Double Perovskite Solar Cells.....	74
4.2.1. Current Density - Voltage Measurements (J-V).....	74
4.2.2. External Quantum Efficiency Measurements (EQE).....	75
4.3.1 Planar and Inverted Planar Solar Cells.....	76
4.3.2. Mesoscopic Solar Cells – Results and Discussion	82
Chapter 5. Compositional Engineering of Double Perovskite Cs ₂ AgBiBr ₆	107
5.1. Cesium and Methyl-ammonium	108
5.1.1. Synthesis and Thin Film Preparation	108

5.1.2. Results and Discussion	109
5.2. Bromine and Iodine	110
5.2.1 Synthesis	110
5.3. Bismuth and Antimony	112
5.3.1. Band Gap Evolution in $\text{Cs}_2\text{AgBi}_{1-x}\text{Sb}_x\text{Br}_6$ Systems	113
5.3.2 Synthesis and Results	113
5.3.3 Bismuth-Antimony Mixed Double Perovskites $\text{Cs}_2\text{AgBi}_{1-x}\text{Sb}_x\text{Br}_6$ in Solar Cells	114
Chapter 6. Dimensional engineering of double perovskite $\text{Cs}_2\text{AgBiBr}_6$	125
6.1 Introduction to low dimensional perovskites	126
6.1.1 Low Dimensional Lead Free Perovskites: PeABr1 and PeABr2	127
6.1.2. BeABr1 and BeABr2.....	140
6.1.3. PeAI1 and BeAI1	145
7. Conclusions and Future Perspectives.....	149
7.1. Summary	151
7.1.1. Chapter 2 – “State of the art” $\text{Cs}_2\text{AgBiBr}_6$	151
7.1.2. Chapter 3 – $\text{Cs}_2\text{AgBiBr}_6$ double perovskite thin film characterization	152
7.1.3. Chapter 4 – $\text{Cs}_2\text{AgBiBr}_6$ solar cells and interface engineering	153
7.1.4. Chapter 5 – Compositional Engineering of Double Perovskites $\text{Cs}_2\text{AgBiBr}_6$	155
7.1.5 Chapter 6 – Dimensional engineering of double perovskite $\text{Cs}_2\text{AgBiBr}_6$	156
7.2. Future perspectives	157
List of Figures.....	159
List of Tables	169
References.....	171

List of symbols

A	Absorbance
Abs	Absorption
α	Absorption coefficient
d	Lattice spacing
D	Diffusion coefficient
e	Elementary charge
e-	Electron
h+	Hole
ε	Extinction coefficient
EB	Binding energy
E_g	Band gap energy
E_k	Kinetic energy
Φ	Photon flux density
ϕ	Work function
h	Planck's constant
J_{sc}	Short circuit current density
J_{mpp}	Current density at maximum power point
k	Crystal momentum
k_B	Boltzman constant
l	Optical pathway
$Le(h)$	Diffusion length for electrons (holes)
λ	Wavelength
P_{in}	Incident Power
P_{mpp}	Power at maximum power point
ν	Frequency
r_{eff}	Effective ionic radius
R	Reflected light
R_s	Serial resistance
R_{sh}	Paralell (shunt) resistance
T	Temperature
θ	Diffraction angle
t	Tolerance Factor

μ	Octahedral factor
V_{mpp}	Voltage at maximum power point
V_{oc}	Open circuit voltage

List of Abbreviations

Ag	Silver
Al	Aluminium
Au	Gold
AM	Air mass
AFM	Atomic force microscopy
BCP	Bathocuproine
Bi	Bismuth
c-TiO ₂	Compact titanium dioxide
CB(M)	Conduction band (maxima)
CdTe	Cadmium telluride
CIGS	Copper indium gallium selenide
Cs	Cesium
CZTS	Copper zinc tin sulfide
C60	Fullerene molecule consisting of 60 carbon atoms
C70	Fullerene molecule consisting of 70 carbon atoms
DMF	N,N-dimethylformamide
DMSO	Dimethylsulphoxide
DSSCs	Dye-sensitized solar cells
EDX	Energy-dispersive X-ray spectroscopy
ETM	Electron transport material
ETL	Electron transport layer
FF	Fill factor
FTO	Fluorine doped tin oxide
GaAs	Gallium arsenide
GBL	Gamma butyrolactone
HTL	Hole transport layer
HTM	Hole transport material
IE	Ionization energy
IPCE	Incident Photon to Current Efficiency
IPES	Inverse photoemission spectroscopy
ITO	Indium tin oxide
IQE	Internal Quantum Efficiency

LEDs	Light-emitting Diodes
LiTFSI	Bis(trifluoromethane)sulfonimide lithium salt
LUMO	Lowest unoccupied molecular orbital
MAI	Methylammonium iodide: $\text{CH}_3\text{NH}_3\text{I}$
MACl	Methylammonium chloride: MAPbCl_3
MABr	Methylammonium bromide: MAPbBr_3
MPP	Maximum power point
m-TiO ₂	Mesoporous-titanium dioxide
NREL	National Renewable Energy Laboratory
OSC	Organic solar cell
OPV	Organic photovoltaic
PCBM	Phenyl-C61-butyric acid methyl ester
PCE	Power conversion efficiency
PEDOT:PSS	Poly(3,4-ethylene-dioxy-thiophene):polystyrene
PES	Photoelectron Spectroscopy
PLQE	Photoluminescence quantum yield efficiency
PSC (PrSCEs)	Perovskite solar cell
P3HT	Poly(3-hexylthiophene)
PTAA	Poly(triaryl amine), Poly[bis(4-phenyl)(2,4,6-trimethylphenyl)amine]
PV	Photovoltaic
Rb	Rubidium
SEM	Scanning electron microscopy
Si	Silicon
Spiro-OMeTAD	N ₂ ,N ₂ ,N ₂ ',N ₂ ',N ₇ ,N ₇ ,N ₇ ',N ₇ '-octakis(4-methoxyphenyl)-9,9'-spirobi[9H-fluorene]-2,2',7,7'-tetramine
t-BP	4-tert-Butylpyridine
TCO	Transparent conductive oxide
TEM	Transmission electron microscopy
XPS	X-ray photoelectron spectroscopy
UHV	Ultra-high vacuum
UPS	Ultraviolet photoelectron spectroscopy
UV-Vis	Ultraviolet-visible
VB(M)	Valence band (maxima)

Chapter 1. Introduction

The sun is the source of the electromagnetic radiation which goes through the atmosphere and it is an inexhaustible source of renewable energy. It gives energy to maintain life, moves the atmosphere, and drives different motion systems forming weather and climate. The sun in just one second releases more energy than our whole civilization has used during its development. Researching the sun energy and its conversion into useful forms of energy offer a new dimension with huge possibility for solving the problem of economic and in particular ecologic crisis which is increasingly present in the world. One third of the total renewable energy is already provided by solar energy conversion.¹ After silicon based technologies have dominated the field of photovoltaics for half a century, thin film solar cells have become more and more interesting for research and economy. Among them, perovskite solar cells have experienced a tremendous rise in interest. Research has led to a remarkable increase in power conversion efficiency from 3.8 % in 2009 to 25.2 % today.^{2,3}

In this chapter the author will introduce photovoltaics and overview the different solar cell generations, the physics of solar cells, the introduction of the perovskites into photovoltaics, properties, issues, and challenges of lead-based perovskite solar cells and finally introduce lead-free perovskites.

1.1. General Introduction

There is a huge amount of energy received from sun radiation. Less than one hour of sunlight is sufficient to cover the overall need for energy for 6.5 billion people who are presently living on this planet. Figure 1 shows the annual solar radiation onto the surface of the earth in comparison to the annual consumption in the world, as well as stock (coal, oil, gas) and nuclear fuels (uranium). The big yellow box is 50 times larger than sum of all fossil and nuclear fuels together. The technical potential of solar energy is still bigger than the world energy consumption. (Figure 1, blue cube)

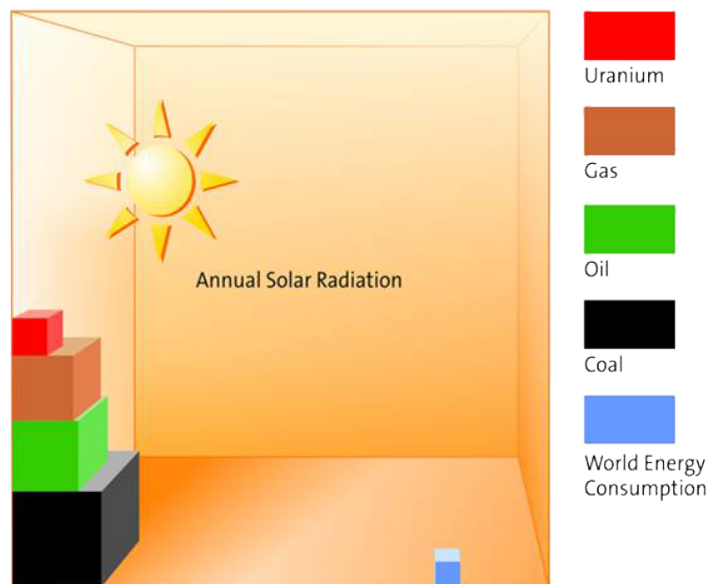


Figure 1 Annual solar radiation compared to stock of fossil fuels and nuclear fuels and the annual consumption of energy in the world. ⁴

All sources of renewable energy are actually different forms and conversion of solar energy. It is a fact that all fossil fuels (coal, oil, gas, nuclear fuels) are limited and exhausting and the energetic sector is more than less responsible for SO_2 , NO_2 and specially greenhouse gas CO_2 emission which contribute to global warming and climate changes. Therefore, it is important to ensure harmony of the modern way of life and the degree of technological progress, technocivilization of the 21st century with the nature and sustainable development for the wellbeing of present and future generations. Because of this reason, the energy must be received from new sources of energy such as solar, wind, geothermal, biomass and waste, hydro, tidal, sea currents and waves, and hydrogen. This is important for the economic and energetic system of every country. Solar energy, a pronouncedly acceptable renewable source of energy could become a

major carrier of environmentally sustainable energy development in the near future. Therefore, new methods and processes are intensively investigated for the solar energy conversion into electrical and thermal energy. The usage of the solar energy to effectively convert and produce electrical energy is called photovoltaic (PV) technology.

1.2 Brief History of Photovoltaics and Solar Cells

The Photovoltaic effect was discovered in 1839 by Alexandre Edmond Becquerel, described as producing electricity while platinum and gold plates are introduced in acidic, neutral and alkalic solutions and exposed to solar radiation. At that time, his discovery had not generated an interest. More than 40 years later, in 1883 Charles Fritts made a first solar cell by depositing a thin layer of gold on-top of the semiconductor selenium. Later on scientist Albert Einstein explained the photoelectric effect with an idea from quantum theory, where the light is made of packets of energy (photons) whose energy depends on frequency or color of the light. This energy of visible photons is enough to excite electrons in the material up to a higher energy level. In this level the electrons are freer to move and some built-in asymmetry feeds them to an external circuit. The first silicon solar cell was developed in 1941 by Russell Ohl with power conversion efficiency (PCE) less than 1%. The co-workers of Bell Laboratories (Pearson, Fuller and Chapin) in 1954 fabricated a silicon solar cell with PCE of around 6% and a first solar module called Bell solar battery. In the beginning, the price of the solar cells was very high and therefore primarily used in space for space exploration. After the oil-crisis at the end of the 70ies this price was reduced and become acceptable. In the last several years the production and the research on the solar cell technology drastically increased in order to increase the use of renewable energy and reduce environmental pollution.

The photovoltaic technology can be divided into two important subgroups. These are inorganic solar cells and organic solar cells. Through the solar cell generations a significant decrease in the thickness of the active material (absorber) can be observed from microns to nanometers, and, in general, the decrease in dimensions of the layers in the solar cell devices. The first generation (crystalline Si and GaAs) is also known as wafer-based technologies while the second (amorphous silicon, CdTe and CIGS) and the third generation (organic solar cells, OSC) are thin film-based technologies. The Si-based solar cells are the main representatives of the inorganic subgroup. Crystalline silicon as the main material, today yields power conversion efficiencies over 25%. The silicon based PV technology is known as very expensive due to the

fabrication process. Gallium Arsenide (GaAs) solar cell with a record near 30% efficiency are the best single junction solar cells. The second most used solar cell type, next to Si-solar cells, are cadmium telluride (CdTe) solar cells with PCE of 23% belongs also to the group of widely commercialized solar cells and Copper indium gallium selenide (CIGS) with PCEs of around 22%.³ The third generation of solar cells consists of DSSC (dye sensitized solar cells), organic (OPV) perovskite and quantum dot (QD) solar cells. The DSSC solar cell with a record PCE of 12%³ generates the power by electrochemistry and the absorber is not a normal solid semiconductor but a molecular organic dye. Following the DSSC idea, in the organic solar cell an active material is a conductive polymer with similar highest efficiency of 12.6%³. Inspired from DSSC as well, the perovskites have been introduced into the scientific community in 2009 by Miyasaka and co-workers by substituting the sensitizer in liquid dye-sensitized solar cells (DSSCs with efficiency of 3.8%) followed by first solid-state perovskite solar cells with an efficiency of 10.9% and 9.7% by Grätzel's and Snaith's co-workers, respectively.^{2,5} Nowadays the perovskite solar cells reach the record increase in only 5 years showing a PCE of 25.2%.³ The last type of solar cells are quantum dot solar cells (PdS or PdSe). Based on the previous knowledge and experience from other organic, DSSC and perovskite solar cells they are built to a very similar device architecture. In Figure 2 all solar cell generations and their development during the last 45 years are shown along with the record power conversion efficiencies of each type today.

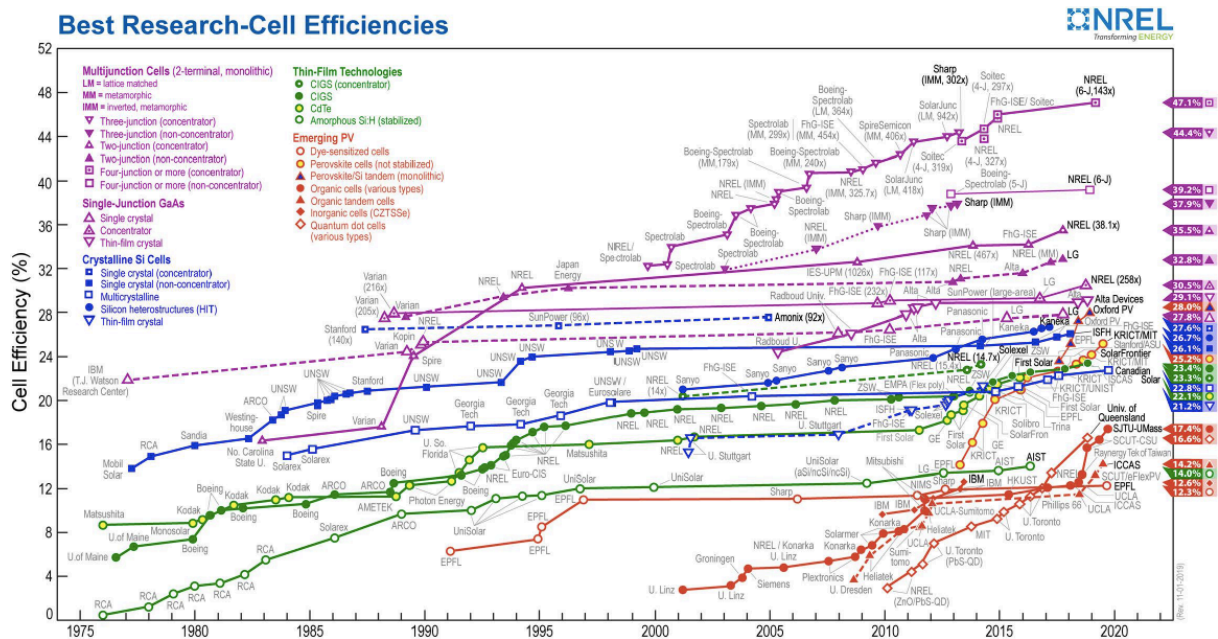


Figure 2 Best-research-cell chart showing the evolution of different PV technologies adopted from NREL online sources with update on 1st of November 2019.³

Within this chapter the physical principles of solar cells will be shown and described. Afterwards, the introduction of perovskites into photovoltaics will be explained and the properties and fabrication of the perovskite solar cells will be described. Finally, issues and challenges such as lead free absorber materials in perovskite solar cells will be discussed.

1.3. Physics of Solar Cells

1.3.1 Physical Principles of Semiconductors

In semiconductors, the energetically highest occupied band containing the valence electrons is called the valence band (VB) and the energetically lowest unoccupied band is called conduction band (CB). The energy gap in a semiconductor materials is given by the difference between the valence and conduction band edge and is called the bandgap. Depending on the bandgap we can distinguish three groups of materials. These are conductors (metals), semiconductors and insulators. The materials with bandgaps of around between 0.5 to 3 eV are called semiconductors. The bandgap in the semiconductors is important, because the electrons can be excited from the valence band to the conduction band upon photon absorption and therefore semiconductor materials are appropriate for photovoltaics. Due to the bandgap the electrons can stay in the higher energy levels the longer times, enough to be exploited. The large band gap of insulators does not allow to absorb visible light. The mechanism of carrier generation consists of absorbing the amount of energy equivalent to the band gap energy (E_g) shown in Figure 3. If the energy of photons is too low, the electron cannot be promoted to the excited state (Figure 3a). This minimum amount of energy is required to excite electrons from the valence band to the lowest unoccupied level in the conduction band (Figure 3b). Generation is the promotion of an electron from the VB to the CB and it creates an electron-hole pair called exciton. If the photon has more energy than the bandgap, the electron is elevated into a higher energetic state. From that state it relaxes down to the lowest energy state in the conduction band. This process is called thermalisation which typically occurs within femtoseconds (fs) shown in Figure 3c. Afterwards, since there are no states in the bandgap, the excited electron does not directly move back to the ground state but stays in the excited state for a long time on the order of μs to ms. The required energy for charge generation can be supplied by the vibrational energy of the lattice namely phonons, by light, which are photons, or the kinetic

energy of another carrier. The electron potential energy can be harvested by fabricating a solar cell out of the semiconductor.^{6,7}

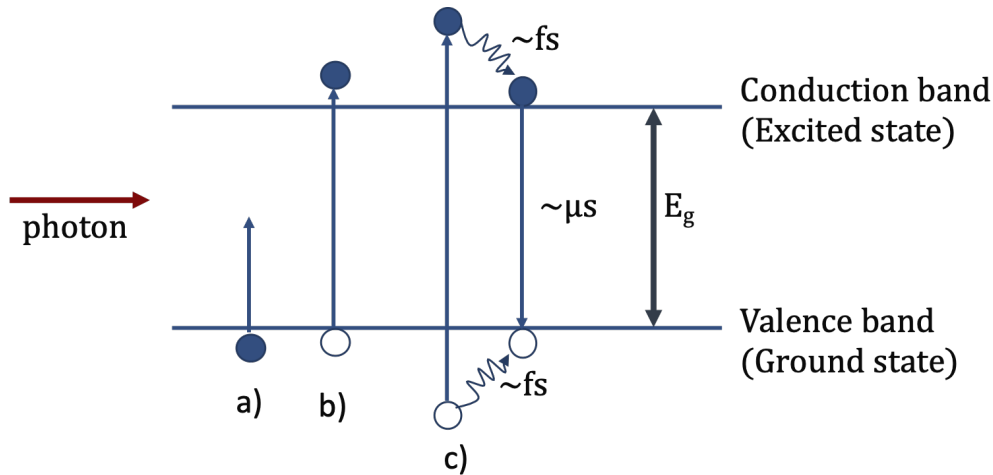


Figure 3 Promotion of an electron from the valence band to the conduction band. **a)** Photons with energy $E < E_g$ cannot promote an electron to the excited state. **b)** The incident photon with $E = E_g$ can promote an electron to the conduction band. For this reason it is the incident photon flux of sufficient energetic photons ($h\nu > E_g$) and not the photon energy density which determines photogeneration. Once excited, the electrons remain in the excited state for a relatively long time. **c)** Photons with $E \geq E_g$ can raise the electron but any excess energy is quickly lost when heat as the carriers relax to the band edges via thermalization and finally recombination.⁶

An incident photon with enough energy of E_g can promote an electron from the VB to the CB and create an electron-hole pair. An electron can also directly emit a photon decaying from the CB to the VB. The minimal energy state in the conduction band and the maximal-energy state in the valence band are each characterized by a certain electron momentum (k -vector) in the Brillouin zone. If the k -vectors are the same, it is called a direct gap. If they are different, it is called an indirect gap. In an indirect band gap semiconductor, the maximum energy of the VB occurs at a different value of k in respect to the minimum in the CB energy, as illustrated in Figure 4. In such a semiconductor, an incident photon with energy of E_g is not on its own sufficient to create an electron-hole pair simply by the absorption of a photon. Also a photon cannot be emitted by decaying an electron from the CB to the VB. However, the electron can be excited simultaneously with the absorption or emission of a phonon. In the first case, the ground state consists of an electron in the VB plus a phonon, while the final state consists of an electron in the conduction band and no phonon. If the band gap is called direct, an electron can directly emit a photon.^{6,7}

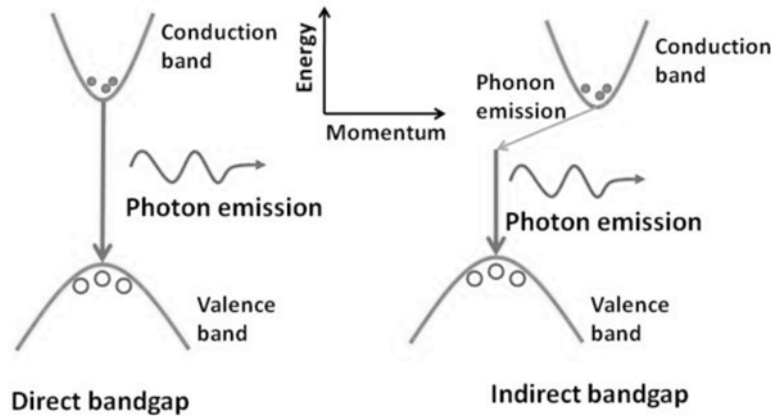


Figure 4 Direct and indirect bandgaps for electronic states.⁷

To determine the optical band gap in semiconductors the estimation method called Tauc plot is used. The author of this method is Jan Tauc and he showed on the example of amorphous germanium that the optical absorption spectrum looks like the spectrum of the indirect transitions in crystalline germanium and therefore he proposed an extrapolation to find the optical gap of the crystalline-like states.⁸ A Tauc plot shows the quantity $h\nu$ (the energy of the light) on the x-axis and the quantity $(\alpha h\nu)^r$ on the y-axis, where α is the absorption coefficient of the material. The value of the exponent r stands for the nature of the transition:⁹

$r = 1/2$ for direct allowed transitions

$r = 2$ for indirect allowed transitions

The resulting plot has a noticeable linear regime, which presents the onset of absorption. The extrapolation of this linear region to the x-axis yields the energy of the optical band gap of the inspected material.

If the excited states do not separate into free charges, they recombine and the mechanism is called carrier recombination. For every generation process there is an equivalent recombination process. Their recombination process is the loss of an electron or hole through the decay of an electron to a lower energy state. As shown in Figure 5, there are three different types of energy release via recombination that are radiative, non-radiative and Auger recombination. Among these, radiative recombination is the most relevant for photovoltaics. Radiative recombination is a spontaneous band-to-band recombination from the VB to the CB together with the emission of a photon with energy equal to E_g . The radiative recombination is slower in indirect band gap semiconductors than in the direct band gap semiconductors. Radiative and Auger recombination are categorized as unavoidable recombination, while non-radiative recombination is distinguished as avoidable recombination.^{6,7}

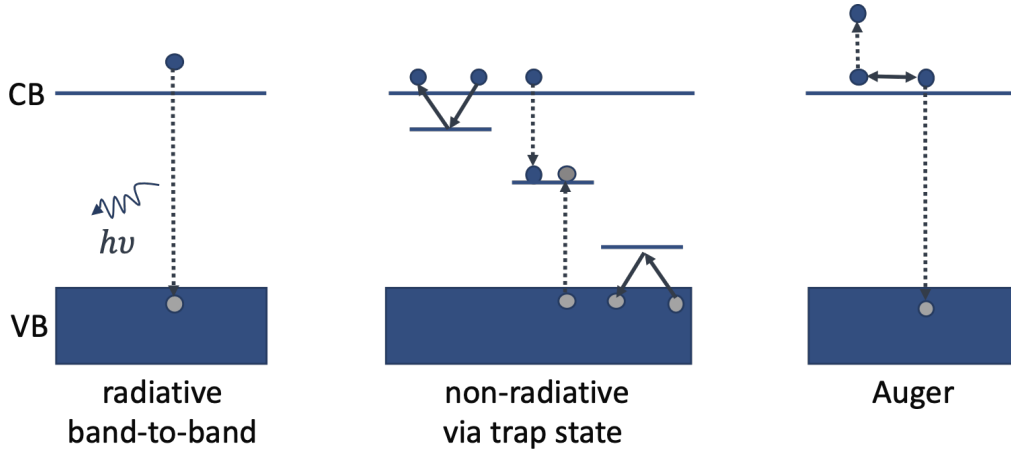


Figure 5 Mechanism of radiative, band-to-band recombination, non-radiative via trap state presenting electron trapping and detrapping, electron-hole recombination and hole trapping and detrapping, and finally Auger recombination.⁶

Non-radiative recombination is the recombination via trap states. Trap states are subband-gap levels close in energy to the CB and VB, presenting a recombination center when the energy of the state is deep in the bandgap. In this case, the electron recombination, takes place into the trap state and the released energy is in the form of heat through phonon emission. On top of recombination these localized states decrease the transport of carriers. Last is the Auger recombination, a non-radiative recombination where two similar carriers (e.g. electron) interact resulting in the decay of one electron across the band gap. The energy release through recombination yields an increase in the energy of the other carrier by an amount equal to the band gap putting it into a higher energy state, typically within the same band. Finally, the excited carrier relaxes within the conduction band down to its band edge and releases the extra energy as heat (phonons).⁶

For the carrier transport across the material the diffusion length must be defined.⁶ The diffusion length is a measure of the average distance, which a minority carrier will diffuse before recombining. In this case, the Einstein relation is used:

$$\mu = \frac{qD}{k_B T}$$

q is the elementary charge, D is the diffusion coefficient, k_B is the Boltzmann constant, T is the temperature (K), and μ is the mobility from which it derives the diffusion length for electrons and holes expressed as:

$$L_{e(h)} = \sqrt{\tau_{e(h)} D_{e(h)}}.$$

1.3.2 Solar Cell Principles

The solar cell is a light-in-current-out device, where the current can be driven against a certain potential and this is the power of incident photons partly converted into electric power.⁷ For determining the efficiency of semiconductors two main parameters should be considered: the bandgap, E_g and the incident photon spectrum. The power conversion efficiency of some photovoltaic device depends on several factors and these are absorption coefficient, separation of excited states and charge-carrier recombination. The maximum possible efficiency of a solar cell is referred to as the Shockley-Queisser limit, which is a bandgap-dependent maximum efficiency obtained with a solar cell fabricated by a single semiconductor as absorber (i.e. a p-n junction silicon device). The resulting maximum efficiency curve for illumination with AM 1.5G (air mass, 1.5 atmosphere thickness, i.e. the spectrum for light going through 1.5 atmospheres, which corresponds to a zenith angle of 48.2°) for a single-junction solar cell shows 30% and can be obtained for bandgap energies between 1 and 1.5 eV.^{6,7}

In a solar cell the light is absorbed, an electron-hole pair is generated, and the solar cell must be able to collect the free charges before their recombination. For the transport of the electrons and holes in the opposite directions and to an external circuit an internal electric field, defined as the built-in field is responsible. Figure 6 shows the equivalent circuit of a solar cell, which consists of a load and a diode as described by the Shockley model.^{6,7} The model contains a diode with current-voltage curve J_{dark} which follows the Shockly diode equation and a current source that generates a voltage-independent photocurrent J_{sc} . The solar cell is illuminated and the generated photocurrent, proportional to the light intensity, is split between the variable resistance of the diode and the load. The diode supplies the voltage to drive the photocurrent through the load. The J-V characteristics of a solar cell under dark and under illumination are shown in Figure 7.

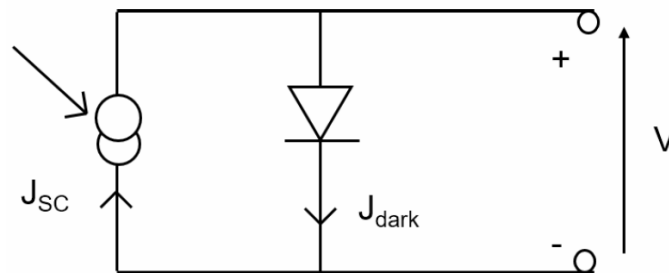


Figure 6 Equivalent circuit of an ideal solar cell adopted from “The physics of solar cells” by Jenny Nelson.⁶

1.3.3. Solar Cell Characterization

Measuring solar cell performance by performing a current – voltage (IV) sweep is done by applying a voltage across the solar cell and measuring the current response of the same. A solar simulator is typically used for precise measurements. The current through the solar cell is plotted against the applied voltage.

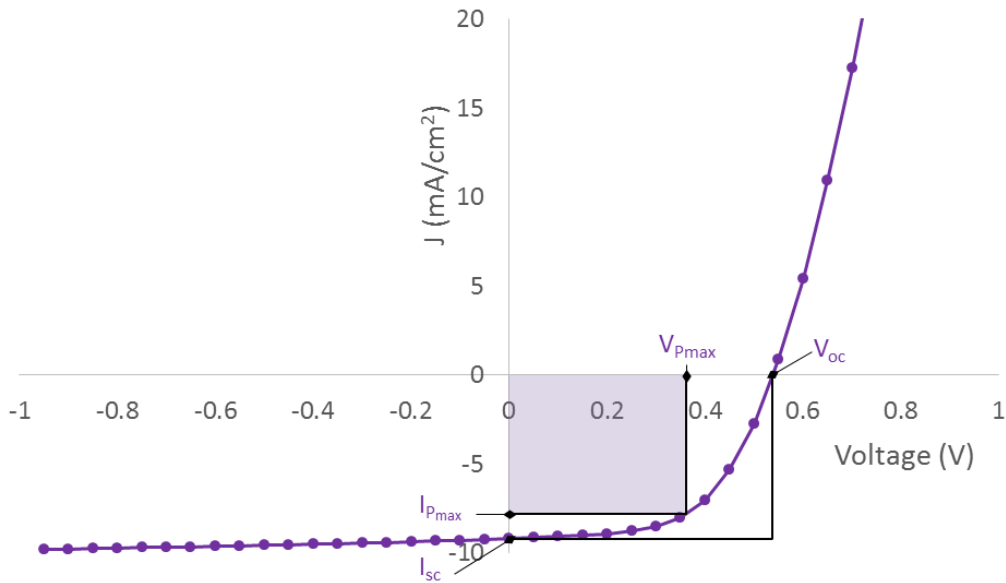


Figure 7 Example IV curve for a solar cell with an illustration of the square summing up the maximum power spanned by the V_{Pmax} and I_{Pmax} crosses and the open circuit voltage and short circuit current points.

Important parameters emerging from this measurement are:

- V_{OC} is the open circuit voltage. It is the maximum voltage that the solar cell will supply without any load applied.
- I_{SC} (J_{sc}) - short circuit current is the maximum current through the solar cell under condition of a zero resistance load; a free flow or zero volt potential drop across the cell, without any load applied.
- Fill factor (FF) is the ratio between the maximum power (represented by the colored rectangle in Figure 7) and the full rectangle spanned by the V_{OC} and I_{SC} values.

$$FF = \frac{I_{Pmax}V_{Pmax}}{I_{SC}V_{OC}}$$

- Power conversion efficiency (PCE) describes the general efficiency of the solar cell; that is the ratio of generated electric to incoming light power.

$$PCE = \frac{I_{sc}V_{oc}FF}{P_{light}}$$

For the characterization and evaluation of the spectrally resolved properties of the semiconductor devices, the quantum efficiency is used as a spectral response. The ratio of the number of charge carriers collected by the solar cell to the total number of photons incident on the solar cell with a particular wavelength is called quantum efficiency (QE) of the solar cell. It is expressed as a photon flux density of the incident light. The meaning of this is that if all photons of a specified wavelength are absorbed and the resulting minority charge carriers are collected (every absorbed photon creates one exciton) then at that particular wavelength the quantum efficiency is accomplished. This is measured as the externally measured optical short circuit current density (J_{sc}). The external quantum efficiency (EQE) is defined with respect to the wavelength of the light as:

$$EQE = \frac{J_{sc}(\lambda)}{e \cdot \phi(\lambda)}$$

where e is the elementary charge and Φ is the photon flux density of the incident light. The optical losses as the reflection of light from the solar cell are included. Different from the EQE, the Internal Quantum Efficiency (IQE) does not include the reflection loss. IQE is used to observe the losses within the solar cell free from the cell reflection and is defined as:

$$IQE(\lambda) = \frac{EQE(\lambda)}{1 - R(\lambda)}$$

where $R(\lambda)$ is the reflection from the solar cell and $1 - R(\lambda)$ gives the total absorption of the solar cell and can be calculated from the absorbance (A) of an absorbing material.^{7,10}

In the real solar cell, the power is reduced through the resistance of the contacts and by leakage currents along the device. These effects are electrically equivalent to two parasitic resistances in series (R_s) and in parallel (R_{sh}) with the solar cell. For the ideal solar cell the shunt resistance (R_{sh}) should be larger than the serial (R_s) resistance leading to maximal area of maximum power rectangle compared to $J_{sc} \times V_{oc}$ shown in Figure 7 ($R_{sh} = \infty$, $R_s = 0$).

For the explanation of the principle of solar cells, the p-n homojunction diode as the standard solar cell can be considered. A typical semiconductor Si is used. Each Si atom is covalently bound to four other Si atoms and all valence electrons are involved in the atomic bonds. If we take a phosphorus (P) atom with five valence electrons, the substitution of the bonds in the Si-crystal can be provided. Then the Si atom will be bound with four valence electrons of P. Phosphorus acts as a donor in the silicon lattice, because it donates the extra

electron to the conduction band. It is a n-dopant and silicon with n-dopants is n-type silicon. For p-type semiconductors we consider atoms of valency III, for example Boron (B) with three valence electrons. In that case the silicon (Si) will lack one electron, for bonding and will try to replace this missing electron. Effectively, the replacement of the missing bond by a neighboring electron yield finally the motion of the hole. A hole is moving freely in the valence band. Boron is a p-dopant and boron doped silicon becomes p-type. In both cases, the electric conductivity increases due to the increased number of free electrons and holes. When n-type and p-type semiconductors are attached to each other electrons and holes can move across the boundary by diffusion from high concentration to low concentration.⁷

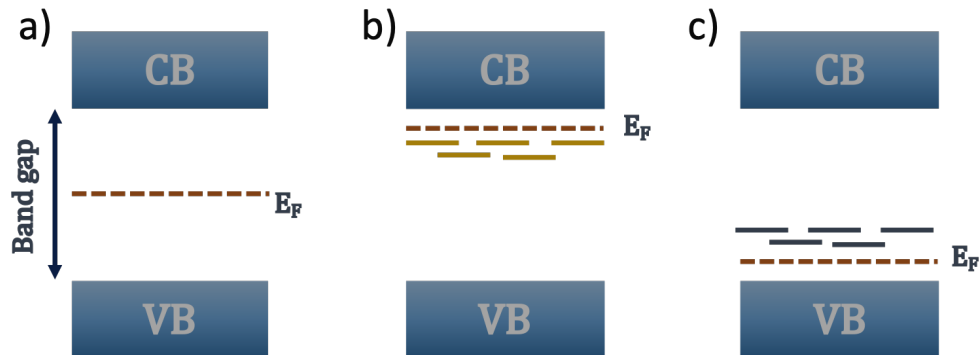


Figure 8 Schematic band diagrams of intrinsic and doped semiconductors **a)** intrinsic semiconductor, **b)** n-type semiconductor, **c)** p-type semiconductor.⁷

In Figure 8 the schematic band diagrams of intrinsic and doped semiconductors are shown. In the intrinsic (pure) semiconductor there are no electronic states in the band gap and the Fermi level (E_f is the energy required to add one electron to the otherwise unchanged system, or the energy that has a probability of $\frac{1}{2}$ of being occupied at thermodynamic equilibrium⁷) is located in the band gap center relatively far away from valence and conduction bands and thermal excitation is unlikely. In the case of n-doping (8b) there are additional occupied electron states introduced into the semiconductor by phosphorus (P). These states are located close to the conduction band. Thermal excitation is possible and the electrons which are transferred to the conduction band carry the electric current. For 8c, where p-doping is shown, empty electron states are introduced close to the valence band which can be thermally excited from the valence band. The holes remaining in the valence band can carry a current.⁷In the case of the perovskite solar cells (which will be explained in detail further below) we have another commonly used type called heterojunction *p-i-n* or *n-i-p* structure. This is accomplished by combining a material with a bandgap favorable for strong light absorption with a wide-bandgap material what serves

as an emitter. In these devices an intrinsic layer (i) is responsible for light absorption and exciton separation inserted between two strongly doped n-type (e.g. TiO₂) and p-type (e.g. spiro-OMeTAD) layer.

1.4. Introduction of Perovskite

1.4.1. Perovskite Crystal Structure

The crystal structure of the perovskite family stems from the mineral CaTiO₃, found by the Russian mineralogist Lev Perovski in 1839. Its formula unit is ABX₃, where A is a larger cation, B is a smaller cation and X is a large anion. It can be divided into oxide (O²⁻) and non-oxide based perovskites. Non-oxide based perovskites are chalcogenides (S²⁻, Se²⁻, Te²⁻) and halides (Cl, Br, I, F), while the additional anion group is formed from pseudo halide anions such as HCOO⁻, BF₄⁻, SCN⁻. (Figure 9)

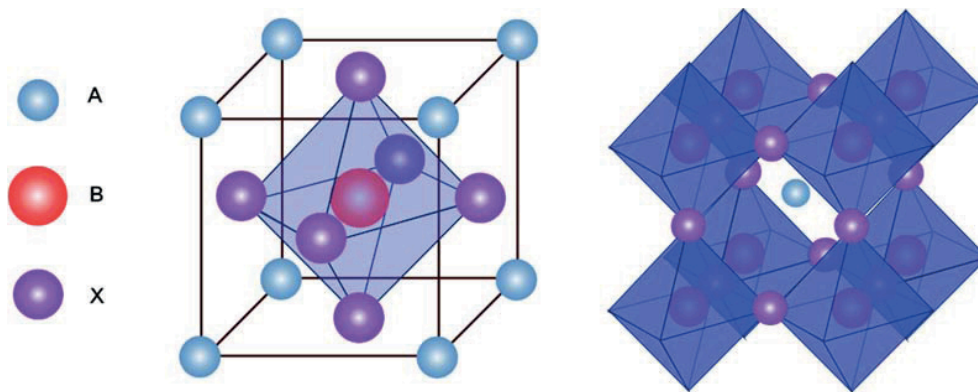


Figure 9 Scheme of the simplified perovskite structure for different section where the A is the cation centered and B cation is centered (X is the largest anion, A is intermediate and B is the *smallest*).

The ideal perovskite structure (ABX₃) is a cubic cell with a body centered B ion in 6-fold coordination surrounded by an octahedron of X anion and the A ion at the corners. For the crystal structure to be stable, the ion sizes are quite important. Calculating the Goldschmidt tolerance factor (t) is a good way to check the crystal structure stability and distortions. The equation for an ideal cubic perovskite is:

$$t = \frac{r_A + r_B}{\sqrt{2}(r_B + r_X)} = 1$$

where the r_A , r_B and r_X are the ionic radii.¹¹

The general formula of organic-inorganic perovskite absorber materials is given for monovalent ion at the A site: CH_3NH_3^+ , $\text{HC}(\text{NH}_2)_2^+$, Cs^+ , Rb^+ , and divalent ion at the B site Pb^{2+} or Sn^{2+} , and X site being occupied by the halide ion Cl, Br and I. When the tolerance factor shows a value larger than 1, the possible structures are hexagonal or tetragonal forming two dimensional (2D) layer structures, common for big A cations. In the hybrid perovskites, the tolerance factor well matches the value for the stable cubic crystal structure.

1.4.2. Properties and Characterization of Lead-based Perovskite Solar Cells

The prototype material of this low-cost alternative semiconductor is methylammonium lead iodide ($\text{CH}_3\text{NH}_3\text{PbI}_3$, MAPI). It possesses various beneficial properties: e.g. a direct (1.6 eV) band gap which is tunable by changing the constituents on the X-site¹², a high absorption coefficient (of 10^4cm^{-1} at 550 nm allowing saturated light absorption within 400–500 nm thickness)¹³, long carrier diffusion lengths and lifetimes¹⁴, high defect tolerance¹⁵, and high charge carrier mobility.¹⁶ Nevertheless, there are two major disadvantages: its instability in air and the presence of toxic lead in the structure.^{17,18}

1.4.3. Fabrication of Perovskite Solar Cells and Device Architecture

There are two types of configuration used for perovskite solar cells. Both are mesoporous and planar, and follow the n-i-p and p-i-n architectures, where n-type layer in n-i-p is represented by the TiO_2 electron transporting layer, i-type as perovskite layer and p-type material as hole transporting layer and p-i-n for the reverse layout. The mesoporous solar cells (n-i-p) were the first perovskite solar cells applying the methodology taken from DSSC. The each perovskite solar cell consists of a front electrode made of a transparent conductive oxide (ITO, FTO), an electron transporting layer (ETL), an active material (perovskite absorber), a hole transporting material (HTL), and a metal electrode. In a mesoporous solar cell the electron transporting layer is a mesoporous metal oxide (e.g. mostly TiO_2) usually deposited by spin coating on-top of a conductive substrate followed by annealing. The perovskite layer is then deposited onto the electron transporting layer from solution (DMF, DMSO, GBL) using different approaches such as one and two step solution deposition, or from powder using

vacuum vapor deposition. The hole transporting layer is mostly deposited using spin coating. The fabrication process ends by metal electrode evaporation, mostly gold (Au), but aluminum (Al), nickel (Ni) and silver (Ag) are used as well. The n-i-p solar cells can also be in planar configuration using a planar and compact electron transporting layer such as SnO₂. The p-i-n architecture of perovskite solar cells has the opposite layout of the ETL and HTL compare to n-i-p. The most common hole transporting layers are spiro-OMeTAD and PTAA. The main idea for commercialization of perovskite solar cells is to decrease the temperature during the fabrication process and exchange the glass substrate with a flexible substrate. In Figure 10, the evolution of the perovskite solar cells is shown showing the PCE for each configuration. The fabrication of solar cells will be explained in Chapter 3 in detail.

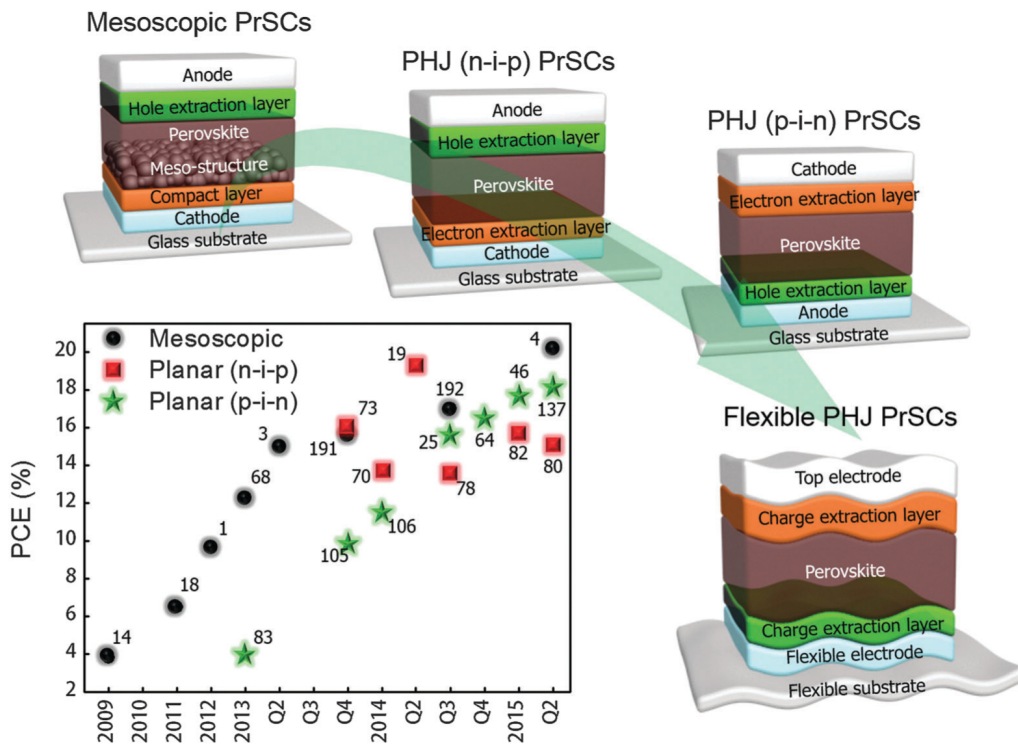


Figure 10 The green arrow represents improvement in the device architecture of perovskite solar cells. The graph shows progress in perovskite solar cells (PrSCEs) of mesoscopic perovskite solar cells and n-i-p (where n-type layer is represented by the TiO₂ electron transporting layer, i-type as perovskite layer and p-type material as hole transporting layer) and p-i-n perovskite solar cells (representing the hole transporting layer and electron transporting layer vice versa to n-i-p), where the PHJ stands for planar heterojunction. Adopted with permission.¹⁹

1.4.4. Issues and Challenges

After a decade of research on perovskites in photovoltaics the main issues regarding the instability and toxicity due to the constituents of organic compounds and lead remain. It has been shown that the perovskite material has a tendency to degrade upon exposure to moisture, heat, or prolonged illumination in ambient environment. The problem of instability has been considered to be solved with several approaches such as compositional engineering, dimensional engineering, lead substitution in perovskites, application of inorganic charge transport layers, and device encapsulation. These methods effectively prolong the lifetime of the device from a few days to a one year in certain aging scenarios. However, very few can really sustain under true working conditions for a long time. Furthermore, the problem of toxicity is occupying many scientific groups, who are on the way to replace the toxic lead in the solar cells with less toxic or non-toxic elements. This approach has been successful but still not with superior photovoltaic properties and power conversion efficiency like those, which have been reached with lead-based solar cells. This work investigates new possible materials and contribute to lead free perovskite solar cells.

1.5. Lead-Free Perovskites

1.5.1. Theoretical Calculations in Literature

Huge theoretical effort in screening “less toxic “materials is ongoing. In searching for new materials and good material properties, theoretical calculations are the first step to investigate and narrow down the range of desirable elements and properties. Properties for the materials for the photovoltaic applications, which have to be considered in the calculations are:

1. Suitable band gaps (electronic and optical properties): the solar cell application requires a high solar-energy absorption efficiency, with the suitable bandgap of 1.0–1.7 eV and strong absorption.
2. Small carrier effective masses in solar cell devices, because the photogenerated carriers should be mobile so that they can be efficiently collected at electrodes
3. Low exciton binding energies are important for the photogenerated electron–hole pairs (i.e., excitons) when they are effectively separated for collection before their recombination.

4. Good thermodynamic stability and crystallographic stability. First is the decomposition enthalpy, which is important for a stable structure. The more stable the material, the larger the magnitude of the decomposition enthalpy. Second is the crystallographic stability, with Goldschmidt factor and octahedral factor.
5. Defect tolerant behavior of the solar materials where this materials needs to be free of deep defect-derived states that are usually trapping centers for non-radiative recombination of the carriers.

Theoretical calculations showed many possibilities and for example the calculation for the double perovskite with composition $A_2B'B''X_6$ (will be in detail explained later on) a simple count indicates that 7 elements are found as A-site cations, 8 elements can occupy the B'-sites, 34 elements are found as B'' cations, and 5 elements can occupy the X sites which gives 9520 combinations thereof 10% possible to synthesize (900), presenting 600 which have never been synthesized and finally 350 different double perovskite (elpasolites) which could be synthesized and some of them have already been published.²⁰

1.5.2. Experimental Results in Literature

Many attempts have been made to improve the environmental stability of the perovskite solar cells e.g. by partial replacement of the methylammonium cation with cesium²¹ or the introduction of hydrophobic cations like phenylethylammonium.²² Isoelectronic ions like Sn²⁺ and Ge²⁺ were first considered as alternatives to Pb²⁺, but the high energies of their 4s and 5s orbitals lead to fast oxidation and degradation of the photovoltaic performance in ambient atmosphere.²³⁻²⁵ Tin (Sn) has first been used to replace the position of Pb²⁺ as $MA_{1-x}Sn_xPb_{1-x}I_3$, with a PCE now reaching 12%.²⁶ Lead free solar cells using Sn²⁺ have been reported to show an efficiency over 7%.^{27,28} Lead free solar cells using mixed Sn²⁺ and Ge²⁺ show a power conversion efficiency over 4.5% PCE²⁹ while solar cells using just Ge²⁺ show 0.2% PCE.³⁰ However, such samples are prone to oxidation (Sn²⁺ into Sn⁴⁺). On the other side, Sn has been incorporated into A_2SnX_6 structures (e.g., Cs_2SnI_6)^{31,32} which exhibit better stability because of the presence of Sn in its stable oxidation state, but also leading to rapid efficiency decay in ambient conditions.^{20,33,34} To solve this problem, “quasi-2D perovskites” in the form of $(PEA)_2(FA)_{n-1}Sn_nI_{3n+1}$ have been suggested as a possible solution to improve material stability.³⁵ They have been obtained by mixing the different organic cations in a sort of bulk heterojunction structure, where the PEA molecules infiltrate at the boundary of perovskite grains blocking the oxygen diffusion into the

perovskite lattice.³⁵ This resulted in a PCE of up to 6% with enhanced stability. Other quasi-2D perovskites in the form of $(\text{BA})_2(\text{MA})_{n-1}\text{SnI}_{3n+1}$ have also been developed that show promising PCE of around 2.5% for $n=4$ and are stable for more than 1 month.³⁶ However, despite the improvements, the presence of Sn does not eliminate all toxicity concerns.³⁷

Besides the group IV halide perovskites, other ns^2 (electron lone pair) ions like Sb^{3+} and Bi^{3+} have been used as lead replacements which results in low dimensional hybrid materials $(\text{A}_3\text{B}_2\text{X}_6)$ showing efficiencies $\leq 1.6\%$ ³⁸ for bismuth based and over 2% for antimony based solar cells.³⁹ The inferior performance of these absorber materials compared to MAPI can be explained by the larger band gap (2.1 eV) and the rather high charge carrier effective masses.^{40,41} Recently, another class of bismuth containing perovskite materials has been suggested for solar cell application: halide double perovskites. Instead of considering other divalent cations to eliminate the toxic Pb^{2+} , recent works have demonstrated the substitution of the two divalent Pb^{2+} ions by one monovalent ion B'^+ and one trivalent ion B''^{3+} keeping the total number of valence electrons unchanged at the halogen sites. The structure reads as $\text{A}_2\text{B}'\text{B}''\text{X}_6$, where $\text{A}'=\text{Rb}^+, \text{Cs}^+, \text{CH}_3\text{NH}_3^+$; $\text{M}^+=\text{Na}^+, \text{K}^+$; $\text{B}''^{3+}=\text{Bi}^{3+}$; and $\text{X}=\text{Cl}, \text{Br}$, which were first reported in the 1970s.⁴²⁻⁴⁶

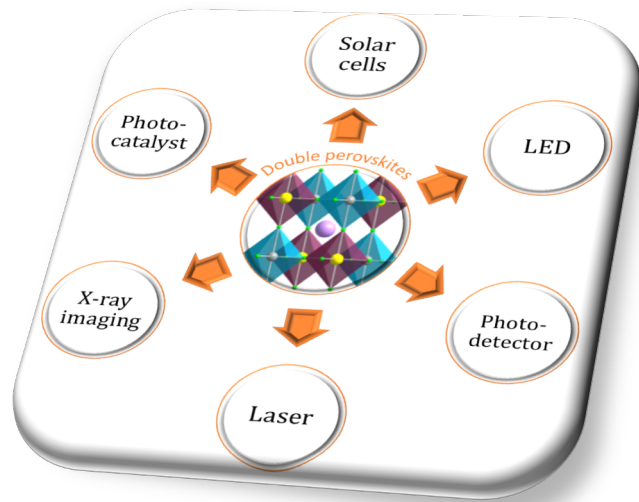
1.6. Motivation and Scope of this Work

Nowadays, lead based perovskite solar cells can be produced on the large scale manufacturing and can reach over 25% PCE. This success is the result of different efforts made in material optimization, optimization of devices and their architectures through interface engineering. The great optical and photophysical features of lead-perovskite are responsible for this remarkable enhancements. Limitation of commercial upraise of PSCs is in their instability to moisture, heat and long illumination, and toxic lead. Even though the stability has recently been improved using surface passivation through dimensional engineering, device encapsulation and improvement using inorganic charge transport layers, compositional engineering and tunability, showing stability over several months, the toxicity still remains. For lead substitution as previously brought up, hard work to find an alternative is still in progress. The presence of the lead in perovskite structure in total is not much but generally, its cause for the health and environment is meaningful. During the degradation, process of lead based perovskite the main product is PbI_2 , and the Pb^{2+} in water can cause harmful pollution by dissolution and therefore influence the environment contamination and pollution toward the human. Not just environmental harm, a lead also influences the nervous and reproductive

system in human where the woman and children are much more exposed and sensitive, where the lead remain over long time in the woman body especially on the ovaries and the children containing lead have learning disability, behaviors' difficulties, and in the worst case it can cause even death.⁴⁷

In this chapter, the author showed an overview starting from the solar cell generation and physics of devices, over thin film solar cells to the new generation of perovskite solar cells. We can see all superior properties and qualities of perovskite solar cells and also the whole material and device evolution but there is still much more space to work on. Because of the lead content of the perovskite solar cells, in the last 4 years, scientists have been working hard to develop stabilized, non-toxic, still cheap lead free perovskite solar cells. Starting to work on the PeroBOOST project financed by the European Union the main motivation was to work on this demanding task by synthesizing and investigating new or alternative materials. Working with other research groups and cooperating with industry companies, we received deeper insights, experience, and knowledge in the thin film perovskite solar cells and thus contribute to the scientific and industrial community.

In this work, the main idea is to investigate double perovskite materials and solar cells with of more stable and eco-friendly materials. One of the alternative materials is $\text{Cs}_2\text{AgBiBr}_6$, which will be mostly investigated in this work. The state of the art in $\text{Cs}_2\text{AgBiBr}_6$ research will be shown in **Chapter 2** with detailed literature analysis of theoretical and experimental findings. The experimental part of work will start with **Chapter 3** and therein with synthesis and deposition routes, different experiments approaches, followed by material characterization. In **Chapter 4**, the active layer of double perovskite $\text{Cs}_2\text{AgBiBr}_6$ will be introduced in solar cells using different device architectures and layer optimization, where the author will also investigate the stability and interface engineering. **Chapter 5** will show compositional engineering through element substitution on each site of perovskite structure. **Chapter 6** will show the investigation of dimensional engineering of the double perovskites and characterization of new double perovskite materials using different organic cations, which separate the inorganic part and implementing the bromine and iodine in metal octahedra, followed by optical and photophysical characterization. Finally, the author will summarize this work with **Chapter 7** showing all conclusions together received through this work, implementing some new ideas for future research.



Chapter 2. “State of the art” double perovskite

Cs₂AgBiBr₆

Regardless of the achievements in the stability of lead-based perovskite solar cells, the toxic lead must be replaced with environmentally acceptable elements. As mentioned previously, the best alternatives are the materials from the same IV group; tin and germanium. However, their instability and affinity to oxidize from the 2+ to the 4+ state due to their high energy 5s and 4s orbitals is not favorable in this case. To maintain the perovskite crystal structure, another solution to accomplish the active layer is to replace Pb²⁺ cation with two non-toxic cations of different valent cations, 1+ and 3+ to build the double perovskite compound with a typical formula of A₂B'(1+)B''(3+)X₆ sustaining charge neutrality. The pioneer in this group is the lead-free double perovskite Cs₂AgBiBr₆. The calculated spectroscopic limited maximum efficiency (SLME) reported by Savory et al.⁴⁸ is around 8%. Therefore, this compound can be considered as a candidate for use as the active layer in perovskite solar cells. In this chapter, the author will show the state of the art of the research on Cs₂AgBiBr₆.

An overview of the lead-free double perovskite group can be found in the review written with Prof. Peter Chen and his co-workers from NCKU, Taiwan.⁴⁹ In this chapter, the focus is mostly on Cs₂AgBiBr₆. Some parts of this chapter were adopted with permission by the publisher John Wiley & Sons and the Copyright Clearance Center.

2.1. History overview of Double Perovskites

The synthesis of double perovskites dates back to the middle of the 20th century. The transparent double perovskite K₂NaAlF₆ was first synthesized in 1948. It crystalizes in a face-centered cubic unit cell in the elpasolite structure, with a space group Fm-3m and a lattice cell constant $a=8.116 \text{ \AA}$.⁵⁰ The class of double perovskites can be expanded by replacing Al with other trivalent elements, such as Cr, Fe or Ga, resulting in K₂NaCrF₆, K₂NaFeF₆, K₂NaGaF₆. Single crystals of these have been synthesized before using the solid state route at high temperatures.⁵¹ K₂NaAlF₆ doped with Mn²⁺ has recently been used for the warm white emitting diode and backlights.⁵²

Reports on double perovskites continue with further replacements at the B' site in this case with Na. In 1970 Morss et al.⁴² published on the Cs₂NaMCl₆ chloro-complex showing their single crystal synthesis (evaporating to dryness a hot HCl aq. solution and from a melt) and the decrease of double perovskite solubility with the decrease of the ionic size of the actinides ions M(III) investigated on 22 M³⁺ metals where 20 of them were stable.

Furthermore, keeping the sodium (Na⁺) at the B' position of the Cs₂NaBiCl₆ crystal structure was reported with a unit cell of 10.839 Å and the choice of bismuth at the B'' site with an "active" non-bonded electron pair in Bi³⁺. It shows no significant structural distortion and fits well into the systematization of the double perovskite group.⁵³ Searching for applications of the above mentioned materials, Van der Steen et al.⁵⁴ reported on the crystal growth of Cs₂NaYCl₆ doped with Bi³⁺ and its luminescence properties. It is shown that the doped material has two absorption bands at room temperature while the undoped one only has one. This results in the emission at both low and high temperatures for the doped material. Except for the possible application as the luminescence material, some double perovskite activated with Ce³⁺ showed excellent scintillation properties: the capability to detect neutron and gamma rays and good light output for example Cs₂NaGdCl₆, Cs₂NaGdBr₆.⁵⁵ Otherwise, double perovskite oxides with formula A₂B'B''O₆ have been mostly used because of their interesting properties such as paramagnetism, ferromagnetism and magnetoresistance.⁵⁶ Nowadays, the research has shifted to halide based double perovskites for potential photovoltaic applications to overcome the issues of toxicity and instability of PSCs. In the beginning, the reports on double perovskites have mostly been focused on single crystals and single crystal synthesis techniques as well as investigations on crystal properties. As the thin film photovoltaic (PV) generation expanded with finding the CH₃NH₃PbI₃ perovskite as an excellent absorber material, few years later, one

of the possible alternatives was to try out a double perovskites. Up to now, the standard ABX₃ perovskite structure has been used for lead replacement. Additional reason was not so successful replacement with Ge³⁺ and Sn³⁺. The efficiency using tin-based perovskite materials has reached 9% and shows the highest power conversion efficiency for lead free materials. The standard perovskite structure compositions are moving to the cation transmutation principle, where the B sites occupy one trivalent and one monovalent cation keeping the stoichiometric neutrality and valence equilibrium. First reported halide double perovskites as absorber material and alternative to lead based perovskites for photovoltaic application have been Cs₂AgBiX₆, where X represents Cl, Br, or I. The incorporation of the non-toxic bismuth (Bi³⁺) and monovalent silver (Ag⁺) into the perovskite lattice results with a rock-salt ordering Ag⁺ and Bi³⁺ octahedra. Double perovskites show a superstructure observed in the bond lengths between Ag-Br and Bi-Br.⁵⁷⁻⁶⁰ Theoretical and experimental investigations and calculations have been conducted to get a deeper insight into the electronical and optical properties of this new class of materials.⁵⁷⁻⁶⁰ Antimony, Sb, has also been considered as non-toxic element, which can be implemented into the double perovskite structure. Other noble metals have also been considered to replace silver at the B' position.⁵⁹ The evolution of double perovskite absorbing materials consisted of combining and searching the best elements to fit into the double perovskite structure. This approach from the standard perovskite ABX₃ structure to the double perovskite structure and to the doped double perovskites is related to the previous development of other photovoltaic generations. For instance efforts in the simple binary system of ZnSe going to the ternary system CuGaSe₂ and finally to the more complex quaternary Cu₂ZnSnSe₄, show the development known as atomic transmutation.⁶¹

The evolution of double perovskites for PV application continues by introducing and probing more elements considered for the A, B' and B'' sites.⁶¹ According to their optical characteristics the most investigated double perovskite materials (i.e. Cs₂AgBiBr₆) possess an indirect band gap. The indirect band gap is caused by the mismatch of the angular momentum of Ag and Bi, which leads to wide indirect band gaps and large carrier effective masses. In the context of the solar cells, an indirect band gap reduces the photocurrent and photovoltage, leading to poor device performance. The search for new double perovskite materials has focused on appropriate elements which generate a direct transition.⁴⁸ In order to permit a direct band gap in a lead-free double perovskite, silver must be replaced by an atom with the valence states of the "lone pair" 5s and 6s, thereof indium (In⁺) and thallium (Tl⁺) also obtained in the

additional calculations.⁴⁸ Except In and Tl, Cu⁺ has been considered for the incorporation in the double perovskite structure, and it also shows a direct band gap.⁶²

Slavney et. al.⁶³ have reported on the improved photovoltaic properties when substituting Ag with Tl, which is also a system with a direct band gap. However, as thallium is even more toxic than lead, this approach is not compliant with the initial goal of the study.

2.2. Theoretical Calculations and Findings of the Lead Free Double Perovskites

Crystal structure

The standard perovskite crystal structure for MAPI (CH₃NH₃PbI₃) is a network of corner sharing octahedra with the cubo-octahedral cavity occupied by the A-site methylammonium cation and a six-fold coordination of the B-site lead ion with the halide ions. For a difference, in double perovskite crystal structure the B-sites are occupied by cations with I and III valences and the charge difference between two metal B-site cations induces a rock-salt-ordered crystal structure (Figure 11). Except for the most common rock-salt ordering of octahedra in double perovskite structure, there are layered orders where they alternate only in one direction and in rare cases columnar order with the two different B cations alternating in two directions.¹⁰

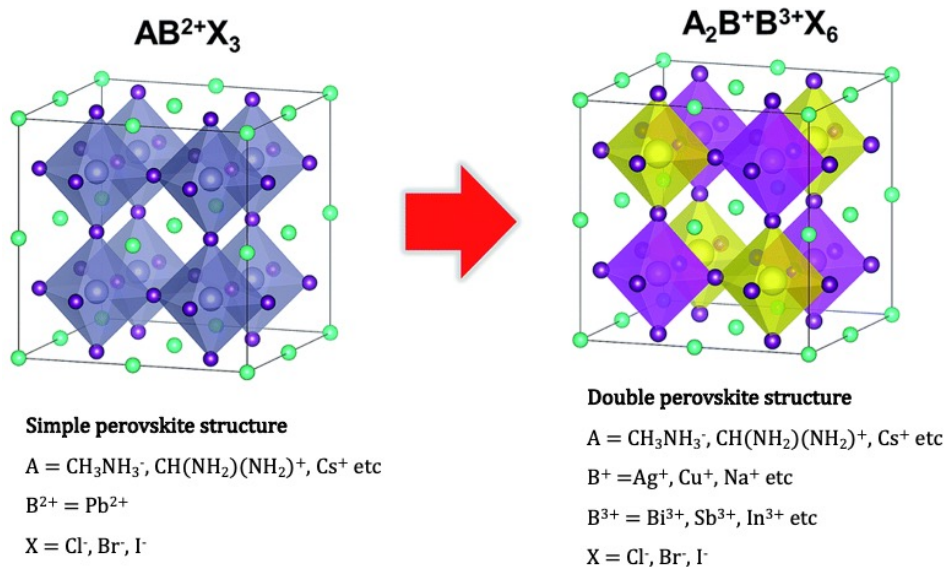


Figure 11 Schematic representation of the structures of simple and double perovskites showing the difference in the elemental composition on the B-site. The A, B⁺, B²⁺, B³⁺, and X ions are denoted by the cyan, grey, yellow, pink, and purple, respectively. Adopted with permission.⁶⁴

The Goldschmidt rule, introduced by Victor Moritz Goldschmidt, explains the stability and distortion of the crystal structure first observed on perovskite materials. In the case of the double perovskite, the silver ion in Cs₂AgBiBr₆ has a matching radius with bismuth, which supports the octahedral coordination of Br. The Cs₂AgBiBr₆ crystalizes in the cubic space group Fm-3m with a lattice constant of 11.25 Å. Although there are some bond length differences between metal and halide because of the different ionic radii (Ag–Br and Bi–Br) no crystallographic distortion of the lattice is noticed. Furthermore, the stability and formation of the double perovskite can be predicted using the tolerance (*t*) and octahedral (*μ*) factors. A stable perovskite structure is given if the calculated values for *t* and *μ* range from 0.81 to 1.11 and 0.44 to 0.90, respectively. For the double perovskites with the structure A₂B'B''X₆ these values are calculated using:⁶¹

$$t_{eff} = \frac{R_A + R_B}{\sqrt{\left(\left[\frac{R_{B'} + R_{B''}}{2}\right] + R_X\right)}}, \quad \text{and} \quad \mu_{eff} = \frac{(R_{B'} + R_{B''})}{2R_X},$$

where R represents the effective ionic radius. For Cs₂AgBiBr₆, R_A is the radius of caesium (167 pm), R_B of silver (115 pm), R_{B'} of bismuth (103 pm), and R_X of bromine (196 pm). The calculated values are *t*=0.84 and *μ* = 0.56.

Electronic band structure

The main strategy to predict the structural stability of new double perovskite materials is the use of first principles density functional theory (DFT) calculations. The combinatorial computational screening can help to design double perovskites with desirable photophysical properties. Pb²⁺ has the electronic configuration 6s²6p⁰ which significantly influences the band structure of MAPbI₃. In MAPbI₃ the valence band maximum is a combination of the hybrid electronic states of the filled 6s² state of the Pb²⁺ and the 5p⁶ state I, while the conduction band minimum has a contribution of the vacant 6p state of Pb²⁺, leading to the superior PV properties.⁶⁵ Only two options, thallium (Tl⁺) and bismuth (Bi³⁺), of which only the latter is not toxic, were suggested as an alternative for Pb²⁺ through electronic structure calculations, as they have the 6s²6p⁰ configuration. Although the toxicity is not excluded because of the presence of silver, the low solubility constant of silver (K_{sp} = 5x10⁻¹³) is still much smaller than that for Pb²⁺. Many elements, such as Cu⁺, K⁺, Tl⁺, In⁺ and Na⁺, have been considered as a substitution for silver. The main problem of Cs₂AgBiBr₆ is the indirect bandgap of 1.98 eV. The energy barrier for the

direct transition is 2.21 eV, which is lower than that of MAPbBr₃ (2.3 eV).⁵⁷ The chemical mismatch between the Ag and Bi is the main reason for the indirect bandgaps, and the presence of 4d states in the Ag atom is responsible for the reduced bandgap of Cs₂AgBiX₆ (X=Cl, Br, and I).⁵⁸ The first-principle calculations advise that the CBM of Cs₂AgBiX₆ is composed of the Bi-6p/ halogen-p antibonding states at the L point ($\pi/a, \pi/a, \pi/a$), whereas the VBM located at the X point ($2\pi/a, 0, 0$) resulted from the Ag-4d/halogen-p hybrid orbitals, leading to the formation of the indirect bandgap.⁶⁰ The values of the bandgaps are 1.8–2.2 and 2.2–2.8 eV for Cs₂AgBiBr₆ and Cs₂AgBiCl₆, respectively. A band gap of 2.52 eV was reported by Zhou et al. for Cs₂AgBiBr₆ nanocrystals (NCs). This is 0.57 eV higher than the bandgap of bulk Cs₂AgBiBr₆ (1.95 eV). This has been attributed to the quantum confinement effect in nanocrystals. The absorption spectrum of Cs₂AgBiBr₆ shows a sharp peak at 430 nm which is blue shifted from the band edge by more than 1 eV. This is attributed to the direct Bi s–p transition instead of the quantum-confined excitonic transition.⁶⁶ Furthermore, Li et al. reported that the width of the bandgap of Cs₂AgBiBr₆ could be adjusted by structural modulation under high pressure, showing a bandgap of 1.7 eV under 15 GPa.⁶⁷

Two commonly applied calculations for the estimation of the bandgaps of the materials are Perdew–Burke–Ernzerhof (PBE) and Heyd–Scuseria–Ernzerhof (HSE). Furthermore, the single-particle Green’s function and the screened Coulomb interaction (GW) approximation have effectively improved the limitation of DFT and hybrid functions used in the case of double perovskites.⁶⁸

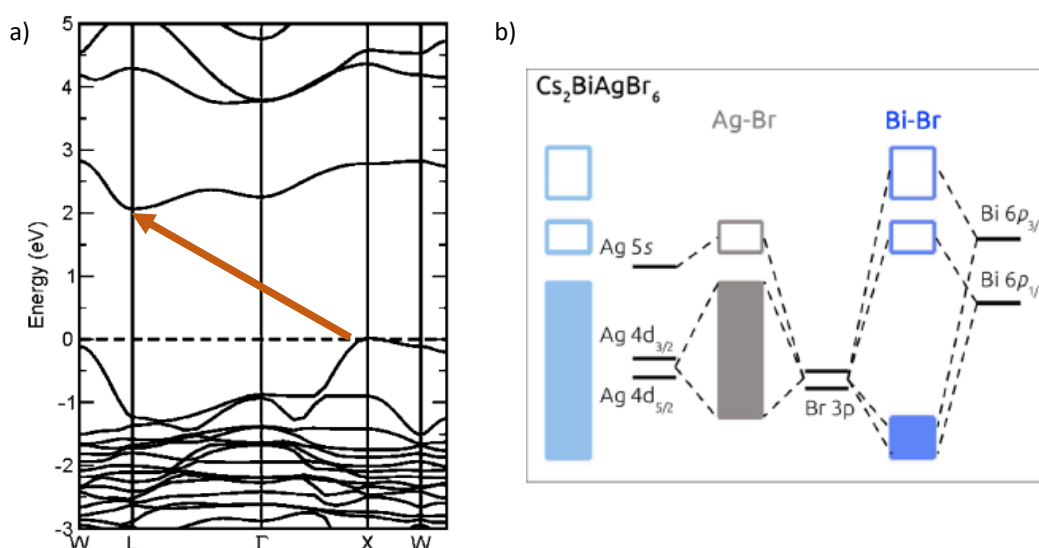


Figure 12 a) Electronic band structures of Cs₂AgBiBr₆, resulting from the DFT calculations. Reproduced with permission.⁵⁸ b) Molecular orbital diagrams in double perovskite Cs₂AgBiBr₆.⁶⁰ Copyright © 2016, American Chemical Society

Figure 12a shows the calculated electronic band structure of $Cs_2AgBiBr_6$ via DFT calculations and Figure 12b the molecular orbital diagram. The wide bandgap along with the indirect transition nature induced an inefficient optical extinction. The optical extinction is the sum of the scattering and absorption and it represents the total effect of the medium on the radiation passing through the medium. The valence band maximum increases when the X-site elements (e.g., halogen) shift downward in the periodic table, because the valence band is determined by the halogen-p states. The approximate calculation of the electron effective mass estimates 0.37 m_e along the L to W direction, while the hole effective mass is 0.14 m_e from along the X to Γ direction, which is comparable with the values for MAPbI₃. Elemental exchange and doping are effective methods for tuning the optoelectronic properties. Many attempts have been made to modify the electronic structure of the double perovskites.⁶³ Thallium was used as a dopant in $Cs_2AgBiBr_6$ to form the compound $Cs_2(Ag_{1-x}Bi_x)Tl_xBr_6$ ($x=a-b$) for bandgap modification. Calculation and experimental results demonstrate that the bandgap, as well as the transition nature, are strongly modified and influenced by the Tl dopant. The calculation results suggest a reduction of the bandgap by 0.1 eV with the low-level doping by the Tl⁺ cation and alteration of the indirect bandgap to a direct transition. In contrast, the bandgap of the experimentally prepared composition showed a reduction by 0.8 eV and turned the indirect nature into a direct one with Tl³⁺ doping on the Bi³⁺ site. Nevertheless, the toxicity of thallium is even more critical than for lead. To summarize, $Cs_2AgBiBr_6$ demonstrated flexibility in tuning the PV properties with different doping and element replacements. The calculations on $Cs_2AgBi_{1-x}In_xBr_6$ ($x=0, 0.25, 0.5, \text{ and } 0.75$) and $Cs_2AgBi_{1-x}Sb_xBr_6$ ($x=0, 0.125, \text{ and } 0.375$), reported by Mitzi and co-workers, show the important character of atomic substitution for photovoltaic properties with differing electronic structures.⁶⁹ The maximum substitution amount of In³⁺ was 75%, which increases the bandgap, while that of Sb₃₊ was 37.5%, on the B- site, resulting in a reduced bandgap and proven experimentally. Usually, the electronic configuration of a semiconductor is significantly influenced by the chemical composition.^{70,71} Controlling the ordering parameter at the mixed sublattice, the band structure of $Cs_2AgBiBr_6$ alters continuously from an indirect bandgap to a narrow pseudo-direct bandgap at Γ point because of the band hybridization and increased disorder of crystallization. The octahedral tilts and various steric sizes can be introduced to the A-site by doping or atomic substitution, such as methylammonium (MA) or formamidinium (FA), to further change the electronic configuration.⁷² The tuning of the bandgap can also be ascribed to the intrinsic disorder of atoms shown by simulations.⁶¹ Apart from the effect of bandgap tuning, the structural disorder allows the formation of point defects and deep trap

levels with low formation energy. Li et al. reported that one could control the effects of intrinsic defects on carrier trapping and Fermi-level pinning with the exploration of the phase diagram of double perovskites.⁷³ Experimental results show that an optimized heat treatment leads to an ordered crystal structure of $Cs_2AgBiBr_6$ with reduced defects and enhanced mobility.⁷⁴ Further investigation of the electronic interaction between B'(I)-, B''(III)-, and X-sites was realized by substituting Ag^+ (d states) with ions having valence s states, such as In (5s) and Tl (6s).⁷⁵ In the model of $Cs_2TlBiBr_6$, Tl ions possess s states, which are able to interact with the s states of bismuth. This interaction is the origin of the indirect bandgap of $Cs_2AgBiBr_6$, between Ag d and Bi s states, and is eliminated in the valence state when the Ag ion is absent.

Thermodynamic stability

To perform as promising active layer for photovoltaic applications, the semiconductors are expected to exhibit a high majority carrier density and low density of deep-level defects. Thermodynamic stability and defect chemistry of double perovskites has been reported as an important part for synthesis and material preparation to avoid not desirable extra phases and defects in the materials and in the same time prepare pure materials and improve photovoltaic properties. In double perovskite $Cs_2AgBiBr_6$ DFT calculation⁷⁶ found that the Ag vacancies easily form being shallow acceptors leading to p-type conductivity. Bi vacancies and Ag_{Bi} (Ag on Bi-site) are deep acceptors, dominant defects under Br-rich conditions. Therefore, the favourable condition to prepare and grow the double perovskite $Cs_2AgBiBr_6$ is a Br-poor and Bi-rich environment. The chemical potential range for pure $Cs_2AgBiBr_6$ formation is narrow. Therefore the chemical conditions should be carefully controlled also to suppress impurities such as $Cs_3Bi_2Br_9$, which crystallize in a lower-dimensional perovskite structure increasing the bandgap and the effective carrier masses.⁷⁶ Related to the stability of the double perovskite and decomposition pathways, decomposition energies have been calculated. While $Cs_2AgBiBr_6$ is not affected by spontaneous decomposition, because of its positive decomposition enthalpy, Cs_2AgBiI_6 , a material that would be more favourable because of its low bandgap of 0.89 eV, has a negative decomposition enthalpy and thus undergoes spontaneous decomposition. Because of this, the synthesis should only be considered under high pressure conditions (hydrothermal synthesis).

Introduction of organic cation

Ag⁺ and Bi³⁺ show a potential for replacing Pb²⁺ in double perovskites also incorporating an organic species (MA)₂AgBiI₆ shows an indirect bandgap of 1.96 eV and an effective electron mass higher than that of MAPbI₃. It also shows stability in the ambient as a crystal for up to 4 months.⁷⁷ The conduction band of (MA)₂AgBiI₆ (4.3 eV) is lower than that of the commonly used electron transporting layer (ETL; i.e., TiO₂), and therefore SnO₂ (4.5 eV) or C₆₀ (4.5 eV) are electronically more compatible with the CBM of (MA)₂AgBiI₆. Apart from introducing the MA cation into the Ag/Bi structure, the (MA)₂AgSbI₆ was synthesized by Li et al. with a bandgap value of 1.93 eV.⁷⁸ Even though Bi and Sb are in the same group, the evident difference in their electronic configuration was demonstrated to be due to the different ionic radii, 103 pm and 76 pm, respectively, and the spin-orbit coupling effect. Similar substitution has been made by replacing iodine with bromine in (MA)₂AgBiI₆, resulting in a bandgap of 2.02 eV which was 0.25 eV lower than that of Cs₂AgBiBr₆ due to the larger ionic radius of MA compared to Cs.⁷⁹ The indirect nature of the bandgap of (MA)₂AgBiBr₆ was confirmed by DFT calculations together with optical spectroscopy. The family of (MA)₂B'(I)B''(III)X₆ presents tunable bandgaps by changing the X-site halides and B'(I)-site cations. Particularly, the halide atoms with larger ionic radius would lead to a wider bandgap and the experimental results of Bi-based double perovskites indicate the possibility of applying double perovskites as active layers.^{31,80-85}

Interfacial carrier dynamics

Aside of the theoretical and experimental investigation on double perovskite photovoltaic properties such as the bandgap nature and effective masses, Feng et al. presented a comprehensive study of interfacial carrier dynamics between Cs₂MBiX₆ (M=Ag, Cu; X=Br, Cl) and the most common ETM such as TiO₂ to evaluate the carrier extraction efficiency.⁸⁶

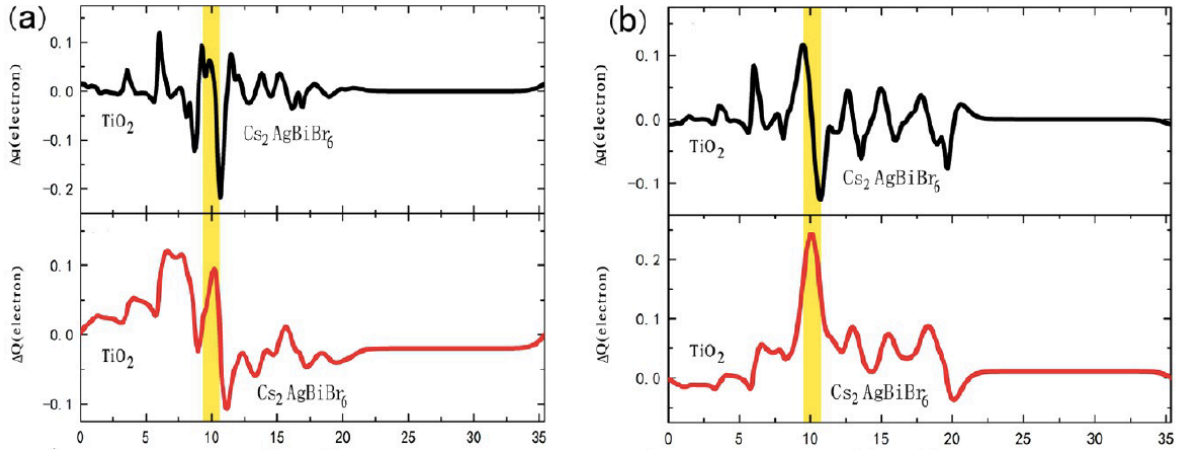


Figure 13 The plane-averaged charge difference and CDC of a) Ag₃Bi₂Br₇/TiO₂, b) Cs₂Br/TiO₂, c) Ag₃Bi₂Cl₇/TiO₂, and d) Cs₂Cl/TiO₂ heterojunctions in Cs₂AgBiX₆ (X = 1/4 Br and Cl)/TiO₂. The upper and lower scale bars represent the plane-averaged charge difference and the CDC, respectively. Reproduced with permission. Copyright 2017, American Chemical Society. *

The Cs₂Br₄/TiO₂-mediated interfaces were effective for charge extraction and separation due to the restrained trap states of TiO₂ when contacting with Cs₂Br₄. DFT calculations indicate a suitable band alignment, reduced bandgap of the double perovskites, and a smooth gradient distribution for the locally projected density of states in the direction, which is normal to the interfaces.⁸⁶ The results suggest that the interface between Cs₂AgBiBr₆ and TiO₂ is a good channel for charge transfer. Figure 13 shows the charge displacement curve (CDC) analysis of Ag-based double perovskites, which is an indicator of the efficient charge transfer at the interface.

Parity forbidden transitions

To alter the indirect bandgap of the Bi-based double perovskites, a promising idea is to substitute Bi with other trivalent ions, such as In. In³⁺ shows an electronic structure without lone-pair s electrons, resulting in a good matching with the Ag *d* orbital and forming a direct bandgap.⁸⁷ For example, the combinations of Ag–In and Cu–In were theoretically predicted to possess direct bandgaps.^{62,88} For Cu-based double perovskites, such as Cs₂CuInCl₆, exhibited a narrower direct bandgap compared with its corresponding Ag-based composition due to the antibonding hybridization, which is formed between the Cu *d*⁰ states and the halide *p* states.^{89,90} Though, the Cu-based double perovskites were pointed out to be more thermodynamically unstable by DFT calculations than the Ag-based double perovskites.⁶² The low decomposition enthalpy of Cu-based double perovskites was assigned to the higher energy level and the

smaller ionic radius of Cu⁺ (77 pm) than that of Ag⁺ (115 pm). Furthermore, Cs₂AgInCl₆ possesses a direct bandgap which is tunable when changing the halide such as Cs₂InAgCl_{6-x}Br_x, to realize maximum efficiency. However, this group of the compounds is shown to undergo from the parity-dependent weak optical transition. Meng et al. demonstrated that it is the inversion-symmetry-induced, parity-induced forbidden transitions that leads to such a difference.⁹¹ This observation explains why the powder shows white color with a measured bandgap of 3.3 eV, whereas the PL emission energy is 2.0 eV. The parity-induced forbidden transitions influence the optical absorption significantly and suppress applications in photovoltaics. As shown in Figure 14a, PBE calculated the band structure of Cs₂AgInCl₆ exhibiting VBM and CBM with the identical even parity, inducing the parity-induced forbidden transition at the Γ point. Figure 14c shows the calculated band structures that provide an indication of the strong transition parameter in Cs₂InBiCl₆. In Figure 14b a table with nine types of lead free double perovskites is proposed by Meng et al. Six of them show direct bandgaps and three of them exhibit inversion-symmetry-induced parity forbidden transitions which is not desirable for PV applications.⁹¹

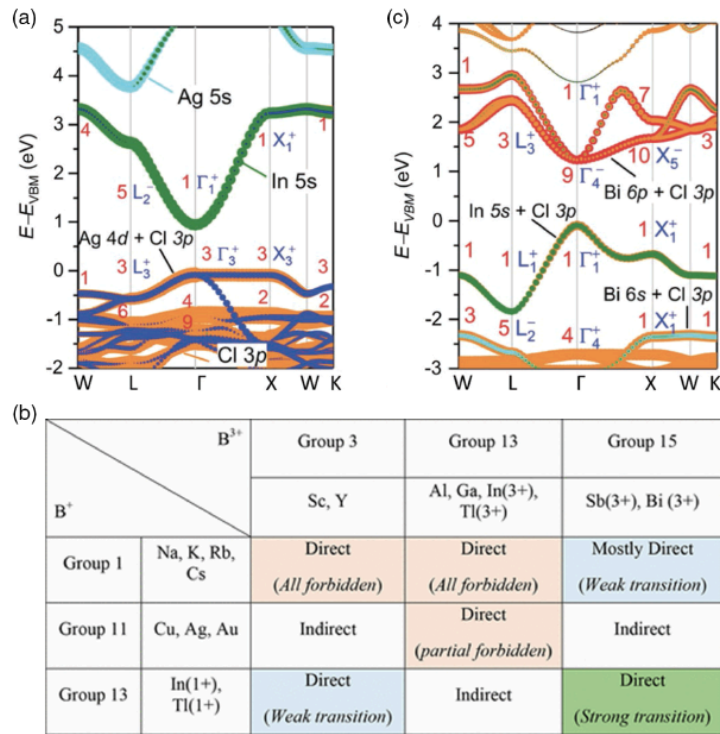


Figure 14 a) PBE calculated band structure provided an indication of the weak transition parameter in Cs₂AgInCl₆. b) PBE calculated band structures provided an indication of the strong transition parameter in Cs₂InBiCl₆. c) A table of probable combinations for A₂B'B''X₆ along with their parity dependent transitions. Reproduced with permission.⁹¹ Copyright © 2017 American Chemical Society.

Defect tolerance

Defect tolerance is a crucial property for PV applications. The calculated results and enable the optimization reveal that the growth conditions strongly modify the defect properties of defect property.^{92,93} Petrozza et al. showed that some properties such as the carrier dynamics including the mobility, diffusion length, and carrier lifetime of the non-radiative recombination of PSCs are significantly influenced by the defect properties.⁹⁴ In lead-based solar cells the performance sometimes shows a hysteresis of the IV curve and a degradation of the materials in the device. One reason for that is halide ion diffusion. Therefore, anion diffusion has been estimate to be significant in the double perovskite solar cells due to the lowest energy barrier for the X-site ion migration, which explains the huge hysteresis.⁹⁵ Apart from ionic diffusion, defect engineering of the grain boundaries in lead-free double perovskites can improve their optoelectronic performance.⁹³ Therefore in 2019, Xu et al. investigated the atomic structures and electronic properties of double perovskites by DFT calculations.⁹³ It was found that the grain boundary induces deep level defect states within the bandgap and thus hinders the PV application of double perovskites. On the other side, the formation of some intrinsic defects and defect complexes allows for the elimination of these deep levels. With the adjustment of the chemical potential, these defects or defect complexes were found to be incorporated into the grain boundary, avoiding the disadvantages of deep-level defects. Pan et al calculated the effective activation energy for ion migration along the (010) direction for the Cs₂AgBiBr₆ to be 348 meV which is much higher than for MAPbBr₃ showing 126 meV and 168 meV.⁹⁶ Furthermore, the differences in the bond lengths between Ag–Br and Bi–Br might be a reason for the lattice distortion which has an impact on defect formation, structural stability, and electronic properties. On the other side, getting a direct bandgap results in a parity-induced forbidden transition which is a hindrance in PV technology. Most recently, Karunadasa and co-workers reported on band gap tuning with Sn-doping showing interesting compositional engineering and a band gap reduced by 0.5 eV.⁹⁷

2.3. Synthesis and Experimental Findings on Cs₂AgBiBr₆

First double perovskite synthesis of Cs₂AgBiCl₆ and Cs₂AgBiBr₆ has been conducted using the solution route by dissolving all starting materials (AgBr/Cl, CsBr/Cl, BiBr₃/Cl₃) in hydrobromic acid and heated at 110 °C for 2 h. Crystals of double perovskites have been

obtained by controlled cooling rate with a lattice constant of 11.2499 Å and an indirect band gap (2.77 eV and 1.96 eV respectively) and show heat (up to 430 °C) and moisture stability. Double perovskites Cs₂AgBiX₆ show long room temperature photoluminescence resulting in non-radiative recombination, long carrier lifetime of 660 ns and high defect tolerance.⁵⁷ An indirect optical transition with valence band maximum at 6.04 eV is suited for application in tandem solar cells combined with a Si absorber.⁵⁷

A side of the solution synthesis route^{58,59} solid state synthesis has been carried out by grinding/mixing of the reactants and heating in a crucible at 210°C for 10h.

Dilute alloying substitution of Ag with Tl prepared by dissolving the starting materials of Cs₂AgBiBr₆ in TlBr/HBr solution held at 100°C for 3 h and black crystals were formed by controlled cooling.⁶³ Cs₂(Ag_{1-a}Bi_{1-b}) TlBr₆ shows a direct band gap and generally improved photovoltaic properties. The polycrystalline double perovskite Cs₂AgSbCl₆ (indirect band gap) and Cs₂AgInCl₆ (direct band gap) have been synthesized using solid state synthesis combining stoichiometric amounts of precursors (CsCl, AgCl, SbCl₃ /InCl₃) in evacuated quartz ampoules and heated at 210°C and 400°C, respectively, while single crystals have been grown by hydrothermal synthesis at 120°C and 160°C, by mixing polycrystalline samples with hydrochloric acid.⁹⁸ In Figure 15 the transition from the direct bandgap to the indirect bandgap using indium and antimony at the Bi-site, can be observed. Cs₂AgInCl₆ double perovskite was prepared by crystallization from acidic solution of hydrochloric acid yielding a direct band gap.^{87,90} The crystals were washed with ethanol and dried at 100°C overnight.

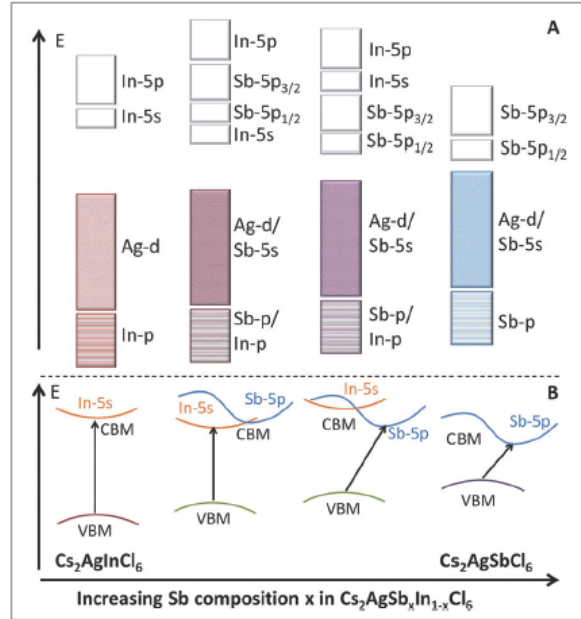


Figure 15 Schematic diagram showing the bonding and antibonding bands of $Cs_2AgSbIn_{1-x}Cl_6$. The lower shaded boxes represent the valence (occupied) bands while the top blank boxes represent the conduction (unoccupied) bands. The band gaps decrease with the transition from direct to indirect character * permission from Royal Society of Chemistry.

2.4. Solar Cell Application and Thin Film Characterization of $Cs_2AgBiBr_6$

After successfully synthesizing solutions, solid state powders and single crystals, the next step was to deposit double perovskites in thin film form for characterization and application in photovoltaics. Greul et al.⁷⁴ reported on the fabrication of double perovskite $Cs_2AgBiBr_6$ thin films by the one-step solution process and further integrated it into the solar cell. Their solution for deposition was prepared by dissolving $BiBr_3$, $AgBr$ and $CsBr$ in dimethyl sulfoxide (DMSO). The substrate was pre-heated at $75^\circ C$ together with the solution. After spin-coating deposition the substrate was annealed above $250^\circ C$ for 5 minutes to induce pure phase formation. The fabricated thin film was part of the standard n-i-p architecture solar cell composed of FTO/c- TiO_2 /mp- TiO_2 / $Cs_2AgBiBr_6$ /Spiro-OMeTAD/Au. The best solar cell showed a PCE of 2.43% with an open-circuit voltage (V_{oc}) of 0.98 V, short-circuit current density (J_{sc}) of 3.93 mA cm^{-2} , and a fill factor (FF) of 0.63 with a significant hysteresis explained by halide anion migration and trapping/de-trapping of charge carriers. The devices showed a stable power output for up to 300 min and stable PV performance under continuous illumination (AM1.5) for up to 100 min.

Low pressure-assisted deposition was reported to achieve uniform thin films with smooth morphology.⁸⁰ The importance of using high temperature annealing (more than 250°C) has been reported by several groups showing significant influence on solar cell performance. The reason is to finalize the reactions and convert all starting materials into double perovskites avoiding the formation of extra phases, especially Cs₃Bi₂Br₉, which is known from previous calculations and experiment to be as not desirable for photovoltaic application. A champion cell, reported by Wu et al. in planar heterojunction device architecture of ITO/SnO₂/Cs₂AgBiBr₆/P3HT/Au shows a PCE of 1.44% with a V_{oc} of 1.04 V, a J_{sc} of 1.78 mA/cm², and a high FF of 0.78. Nevertheless, the device with P3HT suffered from rapid degradation within a few hours while the device without P3HT was stable for over a month under ambient conditions without any encapsulation. Thin-film preparation of Cs₂AgBiBr₆ shifted from the solution process to vapor phase reaction.⁸³ In the first reported case of thin film-formation of the double perovskite Cs₂AgBiBr₆ through vapor deposition and the subsequent implementation into a solar cell device sequential vacuum-sublimation was applied.⁸⁰ It was reported that an excess of BiBr₃ effectively eliminated the impurities examined by XRD. The deposited film obtained diffusion lengths of 147 nm and 232 nm for electrons and holes, respectively, which are slightly longer than those of solution-processed Cs₂AgBiBr₆ (110 nm reported by Ning et al.⁸¹) In 2019 both solution process and vapor deposition were used by Igbari et al.⁹⁹ to investigate the dependence of the processes on the PV properties of Cs₂AgBiBr₆-based solar cells. It was observed that the vapor-processed film suffered a larger loss of Br and displayed a wide deviation from the expected atomic ratio, while the solution-processed film exhibited an accurate composition stoichiometry. Deficit of bromine can result in point defects, identified as deep electron traps. The solution-processed film had a higher crystallinity, lower bandgap, longer carrier lifetime, and higher carrier mobility than the vapor-processed film. The as-solution and as-vacuum processed Cs₂AgBiBr₆ thin films were respectively integrated into the n-i-p heterojunction devices composed of FTO/TiO₂/Cs₂AgBiBr₆/Spiro-OMeTAD/MoO₃/Ag. The champion device performed a PCE-value of 2.51%, a V_{oc} of 1.01 V, a J_{sc} of 3.82 mA/cm², and a FF of 0.65. Due to a well-controlled stoichiometric ratio and reduced hysteresis of solution-processed Cs₂AgBiBr₆ this is the best solar cell reported up to now in the literature. In contrast, the best performance of a vapor-processed device showed a PCE of 1.41%, a V_{oc} of 1.05 V, a J_{sc} of 2.06 mA/cm², and a FF 0.65. Both vacuum- and solution-processed solar cells demonstrated a good stability, with 90% of the initial PCE retained in ambient environment without encapsulation for 15 days. Another planar solar cell with an

architecture of FTO/c-TiO₂/Cs₂AgBiBr₆/P3HT/Au were fabricated with a PCE of 1.37% with a noteworthy V_{oc} of 1.12 V and a J_{sc} of 1.79 mA/cm² showing no hysteresis. A special property of these prepared devices was that they were stable for up to 10 h in an ambient environment in a temperature of 150°C and that they were able to maintain over 90% of the initial PCE value while in a dry box for at least 240 h.⁸³ Pantaler et al. reported an improvement of the mesoporous device architecture through interface engineering, which was previously proposed by theoretical calculation. No hysteresis has been found while having PCE value of 1.26% and an increased open circuit voltage. Screening with different polymeric HTMs have been performed, which is discussed in detail in Chapter 4.⁸² Furthermore, Gao et al.¹⁰⁰ used antisolvent treatment to improve the thin-film morphology in the first reported inverted solar cell. The films carrier trap state density was determined to be 9.1x10¹⁶ cm⁻³ by measuring space-charge-limited currents (SCLC). Such a value is comparable to Pb-based perovskites. The smooth film was integrated into solar cells composed of ITO/Cu-NiO/Cs₂AgBiBr₆/C60/BCP/Ag with a maximum PCE of 2.23% with the V_{oc} of 1.01 V, a J_{sc} of 3.19 mA/cm², and the FF of 0.69 with a minor hysteresis. The devices maintained stability for over 10 days, retaining 90% of their initial PCE. All reported data is summarized in Table 1.

Table 1 Device architecture and photovoltaic parameters of double perovskite-based solar cells.⁸⁹

Double Perovskites	Device Configuration	Perovskite Deposition Method	Voc (V)	Jsc (mA/cm ²)	FF	PCE (%)	Ref.
Cs ₂ AgBiBr ₆	ITO/SnO ₂ /Cs ₂ AgBiBr ₆ /P3HT/Au	one-step spin coating and low-pressure assisted method	1.04	1.78	0.78	1.44	⁸⁰
Cs ₂ AgBiBr ₆	ITO/SnO ₂ /Cs ₂ AgBiBr ₆ /Au	one-step spin coating & low-pressure assisted method	0.95	1.5	0.6	0.86	⁸⁰
Cs ₂ AgBiBr ₆	ITO/Cu-NiO/Cs ₂ AgBiBr ₆ /C60/BCP/Ag	one-step spin-coating with antisolvent	1.01	3.19	0.69	2.23	¹⁰⁰
Cs ₂ AgBiBr ₆	FTO/cl-TiO ₂ /mp-TiO ₂ /Cs ₂ AgBiBr ₆ /Spiro-OMeTAD/Au	one-step spin-coating	0.98	3.93	0.63	2.43	⁷⁴
Cs ₂ AgBiBr ₆	ITO/cl-TiO ₂ /Cs ₂ AgBiBr ₆ /Spiro-OMeTAD/Au	one-step spin-coating	1.06	1.55	0.74	1.22	⁸¹
Cs ₂ AgBiBr ₆	FTO/cl-TiO ₂ /mp-TiO ₂ /Cs ₂ AgBiBr ₆ /PTAA/Au	one-step spin-coating with antisolvent	1.02	1.84	0.67	1.26	⁸²
Cs ₂ AgBiBr ₆	FTO/cl-TiO ₂ /mp-TiO ₂ /Cs ₂ AgBiBr ₆ /Spiro-OMeTAD/Au	one-step spin-coating with antisolvent	0.64	2.45	0.57	0.9	⁸²
Cs ₂ AgBiBr ₆	FTO/cl-TiO ₂ /mp-TiO ₂ /Cs ₂ AgBiBr ₆ /PCPDTBT/Au	one-step spin-coating with antisolvent	0.71	1.67	0.57	0.68	⁸²
Cs ₂ AgBiBr ₆	FTO/cl-TiO ₂ /Cs ₂ AgBiBr ₆ /P3HT/Au	sequential-vapor-deposition	1.12	1.79	NA	1.37	⁸³

Cs₂NaBiI₆	FTO/cl-TiO ₂ /mp-TiO ₂ /Cs ₂ NaBiI ₆ /Spiro-OMeTAD/Au	one-step spin-coating	0.47	1.99	0.44	0.42	"
Cs₂AgBiBr₆	FTO/TiO ₂ /Cs ₂ AgBiBr ₆ /Spiro-OMeTAD/MoO ₃ /Ag	One-step spin-coating	1.01	3.82	0.65	2.51	"

In addition to moisture and heat stability, other properties have to be considered for PV and other optoelectronic applications. These include e.g. elastic properties and thermal expansion of single crystal materials.¹⁰¹ The double perovskite shows superior stiffness because of the strong Ag-Br and Bi-Br bonds. The small thermal expansion is due to stronger bonding characteristics and the absence of organic cations, resulting in improved moisture stability as a good property for PV application. All these properties are much better than those of the lead-bromide perovskite (MAPbBr₃).¹⁰² Next, the charge carrier dynamics have been characterized by excitation preformed on millimetre-sized Cs₂AgBiBr₆ double perovskite crystals using time-resolved microwave conductance (TRMC).¹⁰³ Using this measurement a low trap state density of around 10¹⁶/cm³ in the bulk of the crystal was determined which is a high concentration and means that the trap assisted recombination of charges is slow. This property might be promising for PV. All lifetime measurements indicate shallow electron and hole trap states in the bandgap. They also confirm that the recombination of charges at the surface is fast which is the dominant recombination pathway in thin film.

As mentioned above, the photovoltaic performance of double perovskite solar cells reported up to now is low and it has been shown that this might be because of fast carrier recombination at the film surface. The next step in optimization of the solar cells in general has to consider surface passivation to reduce surface traps and realize long carrier lifetimes.¹⁰³ To investigate carrier lifetime further, transient absorption spectroscopy was conducted on Cs₂AgBiBr₆ thin film to directly track the photo-carrier population in the material by measuring the ground state bleaching dynamics. Using this measurement, it is found that the fundamental lifetime of the Cs₂AgBiBr₆ thin film is 1.4 μ s and the carrier density of 2.2x10¹⁶ cm⁻³ under 1 sun (larger than for MAPI). The results also indicate that the transport properties in Cs₂AgBiBr₆ need a thicker active layer, which could lead to increased current densities and higher efficiencies through enhanced light absorption. Surface traps and insufficient light absorption are the next two important properties to be investigated. The authors further claim, that the exciton formation and dynamics, and the electron-phonon coupling affect the PV performance of Cs₂AgBiBr₆.¹⁰⁴ Femtoseconds UV-vis-NIR transient absorption experiments were performed to identify the presence of excitons. Strong electron phonon coupling via Fröhlich interactions

is observed. This kind of behaviour is also found for the vacancy-ordered perovskite Cs₃Bi₂Br₉ and the compound BiBr₃. It is known that this induces undesirable electron-hole recombination and prevents carrier transport. Additional strategies for improvement are efficient carrier extraction at the interfaces of the double perovskite with suitable electron and hole transport layer.

2.5. Other Applications and Remarks

In this section the author wants to elaborate on other optoelectronic applications of double perovskites as an eco-friendly material.

Fluoride double perovskites (Rb₂NaScF₆ and Rb₂NaYF₆) have been used as a host for visible-wavelength Ce³⁺-based *laser materials*.^{105,106} The fluoride host red shifts the 5d-to-4f emission of Ce³⁺. Cr³⁺, a 3d transition metal, was used for doping Cs₂NaAlF₆ and Cs₂NaGaF₆ to create new Cr³⁺-based laser materials.¹⁰⁶

Investigating *photocatalytic properties*, Zhou et al. synthesized double perovskite Cs₂AgBiBr₆ nanocrystals (NCs) using the hot-injection method with organic precursors and showed an impressive moisture, light, and temperature stability of the material. Due to the suitable conduction band of the material it can sustain the photochemical conversion of CO₂ into solar fuels. Additionally, after focusing on the synthesis method optimization, they applied this material to a photocatalytic CO₂ reduction reaction as well, reaching a total electron consumption of 105 μmolg⁻¹ under AM 1.5G illumination for 6 h.¹⁰⁷ Ning et al.¹⁰⁸ describe thermochromic lead-free double perovskite Cs₂AgBiBr₆ single crystals and films, demonstrating bandgap tuning by temperature variation under ambient condition. Using molecular dynamic simulation, the authors explained the *thermochromic effect* with the an-harmonic fluctuations of Ag-Br and Bi-Br bonds, strong electron-phonon coupling and strong spin-orbit coupling, therefore indicating the possibility for application of smart windows, temperature sensors and visual thermometers.

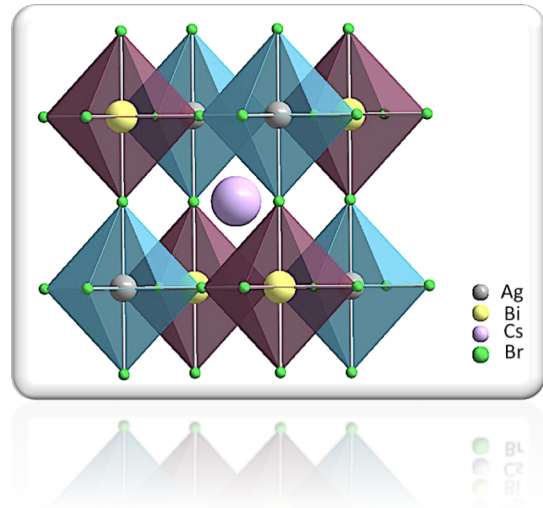
Application of double perovskites for *Light-Emitting Diodes (LEDs)* can be investigated by measuring PLQE (photoluminescence quantum yield) which is the yield defined as the number of photons emitted as a fraction of the number of photons absorbed in the material. Many double perovskite nanocrystals have been investigated for film purpose and their doping methods have been published. Some of the pure double perovskite nanocrystals (Cs₂AgInCl₆ and Cs₂AgBiCl₆) show a very low PLQE value of only around 1-2%.^{109,110} By employing Mn²⁺

doping in Cs₂AgInCl₆, the PLQE value improves up to 16% due to the shifted orange emission at 620 nm because of the ${}^4T_1 \rightarrow {}^6A_1$ transition of the dopant. In the case of Cs₂AgBiBr₆, doping with In³⁺ on the Bi-site results in not just the improvement of the PLQE value by up to >5 times but also in the transition from an indirect to a direct bandgap. The direct band-to-band transition causes violet emission with PLQE of 36% and an orange emission with PLQE of 2 % due to the parity-induced forbidden transition. On the other side, Bi-doping of Cs₂AgInCl₆ NCs results in a broad orange emission at 580 nm with 11.4% PLQE while Mn²⁺ doping of Cs₂NaBiCl₆ shows a broad emission at 590 nm with 15% of PLQE due to as well the spin-forbidden transition of the octahedral coordinated dopant. The best performance of double perovskite NCs was shown by Luo and co-workers¹¹¹ presenting the reduced electronic dimensionality by alloying Na-cations into Cs₂AgInCl₆ improving the PLQE by three times. Going a step further, they doped Cs₂Ag_{0.6}Na_{0.4}InCl₆ with Bi³⁺ and improved the crystal structure and PLQE up to 86% with emission at 550 nm so that the as-fabricated powder joined with commercial UV LED chips emitting warm white light.

Cs₂AgInCl₆ can be promising for *UV light detection* due to strong absorption of wavelengths lower than 400 nm. A stable UV detector based on the photoconductive planar structure showed a responsivity of $\approx 0.013 \text{ AW}^{-1}$, on/off photocurrent ratio of ≈ 500 , fast photo-response of $\approx 1 \text{ ms}$, and high detectivity of $\approx 10^{12}$ Jones.¹¹² A Cs₂AgBiBr₆ thin film as a light absorber in a *photo-detective planar structure* placed in the device structure ITO/SnO₂/Cs₂AgBiBr₆/Au showed not just high responsivity of 7.01 AW^{-1} , on/off photocurrent ratio of 2.16×10^4 , a fast response time of $\approx 1 \text{ ms}$, and a detectivity of 5.66×10^{11} Jones, but also remarkable ambient stability.^{113,114} Li et al. prepared not encapsulated photodetectors using solution-prepared Cs₂AgBiI₆ in the device architecture In/GaN/Cs₂AgBiI₆/Ag, presenting remarkable thermal and environmental stability.¹¹⁵ In this device the Cs₂AgBiI₆ double perovskite in contact with n-type GaN produces a built-in electrical field which effectively separates the photogenerated exciton and promotes electron extraction by GaN with champion photo-detection performances showing a high on/off photocurrent ratio of 4.16×10^4 , high photo-responsivity of 1.46 AW^{-1} , and a specific detectivity of 9.4×10^{13} Jones.

To finalize, the indirect bandgap of Cs₂AgBiBr₆ limits its application for solar cell and lighting applications. Anyway, its high X-ray absorption coefficient (due to the presence of the heavy element bismuth), high carrier lifetime and efficient charge extraction, high resistivity (10^9 – $10^{11} \text{ } \Omega \text{ cm}$ for Cs₂AgBiBr₆ single crystal), low ionization energy, and high X-ray detection (due to reduced field-driven ionic migration) make it a promising *X-ray detector*.⁴⁹ Tang et al⁶

first demonstrated solution-prepared Cs₂AgBiBr₆ single crystals and showed the high migration barrier of the crystal itself suppressing ion migration and allowing for a large external bias. This X-ray detector enabled an efficient charge collection without an increase in current and resulting in a high sensitivity of 105 $\mu\text{CGy}_{\text{air}}^{-1} \text{cm}^{-2}$ with a low detectable dose rate of 59.7 $\text{nGy}_{\text{air}} \text{s}^{-1}$ under a bias of 5 V. Preparing a composite film by mixing Cs₂AgBiBr₆ into a polymer PVA-poly(vinyl alcohol) matrix for X-ray detectors as an X-ray image sensing device, the device presents a sensitivity of 40 $\mu\text{CGy}_{\text{air}}^{-1} \text{cm}^{-2}$ at a bias of 400 V without degradation.¹¹⁶ Introducing an organic cation phenethylamine bromide (PeABr) to in situ modulate [BiX₆]³⁻ and [AgX₆]⁵⁻ octahedral disordering in a Cs₂AgBiBr₆ single crystal decreased the defect density and increased the carrier mobility with suppression of the self-trapped excitation formation. The X-ray detector was prepared in a device of Au/PEA-treated Cs₂AgBiBr₆/Au and achieved a high sensitivity of 288.8 $\mu\text{CGy}_{\text{air}}^{-1} \text{cm}^{-2}$ at 50 V bias voltage.¹¹⁷ Double perovskites using trivalent lanthanide, to replace bismuth site, i.e. Cs₂NaTbCl₆ and Cs₂NaEuCl₆, were synthesized using the hydrothermal synthesis route. The common f–f transition of the lanthanide cations by these double perovskites present strong green and weak red PL. Especially the high light yield of Cs₂NaTbCl₆ of 46 600 photons MeV⁻¹ under X-ray radiation supports its application in detecting high-energy radiation and medical imaging.¹¹⁸



Chapter 3. Synthesis and Deposition Routes of Double Perovskite Cs₂AgBiBr₆

In the introduction and Chapter 2 the author presented a detailed discussion about the double perovskites as an absorber materials and as an alternative to lead-based perovskites. In this chapter the author will show the synthesis routes and thin film preparation of double perovskite Cs₂AgBiBr₆. Up to now, the majority of investigations reported on this interesting material have been focused on polycrystalline powders and single crystals which will also be shown in this chapter. Here as well as in the following chapter, the author will present deposition methods like vapor deposition and solution-based approaches for the preparation of Cs₂AgBiBr₆ thin films. In this chapter all characterization methods will be defined and the results will be shown and discussed. Sequential vapor deposition processes starting from different source precursors will be shown and their weaknesses will be discussed. Additionally, the possibility of the preparation of planar Cs₂AgBiBr₆ thin films using a solution based process by spin coating in order to use it for solar cell fabrication will be presented.

This chapter is an extension of the publication: Pantaler et al.¹⁹ Deposition routes of Cs₂AgBiBr₆ double perovskites for photovoltaic applications, DOI: <https://doi.org/10.1557/adv.2018.151>, Volume 3, Issue 32 (Energy and Sustainability) 2018, pp. 1819-1823 Some parts are taken with permission and allowed according to MRS Advances copyright policy.

3.1. Synthesis

Bismuth based halide double perovskites have been suggested as an alternative to lead based perovskites for solar cells application. Slavney et al. first¹²⁰ synthesized the double perovskite Cs₂AgBiBr₆. Its band gap is around 1.95 eV and indirect. This material possesses advantageous photovoltaic properties like long room temperature photoluminescence lifetime (660 ns), high defect tolerance, low hole effective mass, and most importantly high heat and moisture stability, even more than MAPbI₃, up to 430°C and 55% relative humidity.^{58,59} In the following chapter the author will describe all synthesis and deposition methods used to prepare pure double perovskite crystals and double perovskite thin film Cs₂AgBiBr₆.

According to Mitzi et al.¹²¹ organic-inorganic hybrid perovskite materials mentioned in general are referred to as “self-assembling” since the atoms as well as the molecules accept a high degree of order because of the ionic or covalent interactions between the atoms. Still this term is unclear and it can be said that these systems involve scope of different types of interaction. One of the relevant interactions include the tendency of the organic cations to adjust to a “tail-to-tail” arrangement, with the ammonium parts hydrogen bonding to the halogens (X) in the inorganic layers, and the affinity of the metal (M) halides to side with the formation of extended corner-sharing arrangement of MX₆ octahedra.

In inorganic halide double perovskites the M⁺X₆ and M³⁺X₆ octahedra are surrounding the metal cation, A⁺. To maintain charge neutrality, the inorganic halide double perovskite may be “self-assembling”.

In the following the various methods for the formation of perovskite and double perovskite materials will be discussed which mostly includes crystallization from solutions at or near to room temperature.

3.1.1. Solution Synthesis

The solution synthesis method is a usual approach to synthesize organic and inorganic perovskites. Solution growth of these materials includes finding a suitable solvent for the metal halides. Some potential solvents include water, hydrochloric acid, hydrobromic acid, hydroiodic acid, methanol, ethanol, propanol, acetonitrile, acetone, DMF (dimethylformamide), DMSO (dimethyl sulfoxide). Commonly, stoichiometric quantities of

the organic and metal halides are dissolved in the suitable solvent. Finally, crystals are grown either through cooling of saturated solutions or through isothermal evaporation of the solution. In literature the methyl ammonium lead halides ($\text{CH}_3\text{NH}_3\text{PbX}_3$) were prepared by mixing PbX_2 and $\text{CH}_3\text{NH}_3\text{X}$ in 1:1 molar ratio in N,N-dimethylformamide (DMF) at 60°C for 12h. Crystals are collected and washed with diethyl ether.¹²² To prepare polycrystalline $\text{Cs}_2\text{AgBiBr}_6$, the author used CsBr (99.9 %), BiBr_3 (99.0 %), AgBr (99.5 %), and HBr (from Alfa Aesar) (Figure 16). Crystals of $\text{Cs}_2\text{AgBiBr}_6$ were prepared by precipitation from an acidic solution (HBr). A mixture of 1 mmol AgBr and 1 mmol of BiBr_3 were first dissolved in 15 mL of 9M HBr at 60°C . Afterwards, 2 mmol of CsBr were added and the solution was heated to 120°C . Metal bromides were dissolved in hydrobromic acid at 120°C for 2h, and slowly cooled down to room temperature ($5^\circ\text{C}/\text{h}$). Depending on the cooling rate different crystal sizes were achieved. The 5mm crystals can be obtained by $3^\circ\text{C}/\text{h}$ cooling rate. The orange crystals were washed with ethanol and dried overnight, (yield 60%).

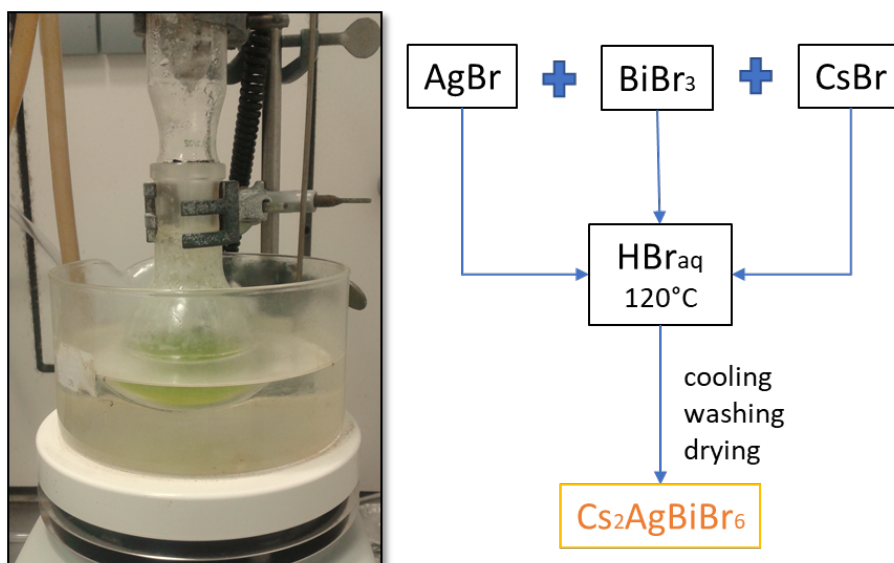


Figure 16 Solution synthesis experiment.

For some organic-inorganic perovskites it is not possible to use the melting process approach for preparing single crystals of polycrystalline material due to sample decomposition with increasing temperature. However, in this case using metal halide starting materials for double perovskite it is possible to use solid-state synthesis, because of the higher stability of the precursors.

3.1.2. Solid-state Synthesis

Solid state synthesis is usually used for the synthesis of materials which are not easily soluble or stable in the above mentioned solvents. To prepare polycrystalline samples via the solid-state route cesium, bismuth and silver halides salts are mixed in a molar ratio 2:1:1. AgBr, CsBr and BiBr₃ were ground in a mortar for around 30 minutes and placed in an alumina crucible and finally in an oven for 8h at 210°C. A similar solid-state approach is to use the solid-state reaction in a sealed fused silica ampoule. The starting materials (metal salts) are mixed in the same molar ratio and the mixture is loaded into a fused silica ampoule which is flame sealed under vacuum (10⁻² bar). The ampoule was heated to 500° C over 5 hours and held at 500°C for 4 hours. After cooling down to room temperature, orange polycrystalline Cs₂AgBiBr₆ was collected (Figure 17).



Figure 17 a) All starting materials grounded and inserted into a quartz ampoule before solid-state synthesis at 500°C, b) alumina crucible for solid state synthesis of double perovskite at 210 °C.

3.1.3. Hydrothermal Synthesis

Hydrothermal synthesis is a technique for crystallizing single crystals from high-temperature aqueous solutions at high vapor pressure. The crystal growth is achieved in a setup consisting of an autoclave (steel pressure vessel) with precursor solutions inside (Figure 18).

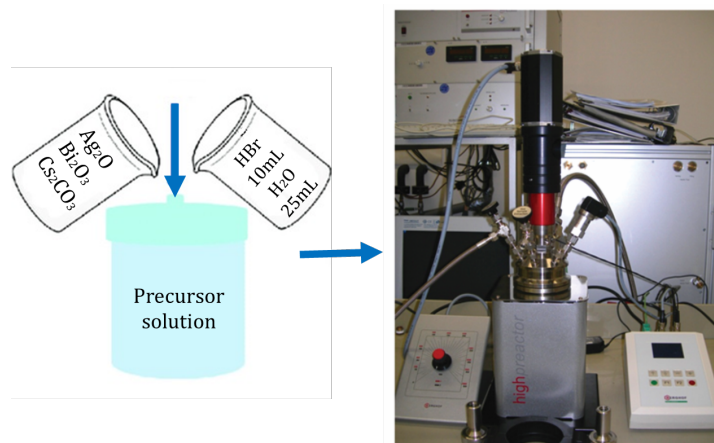
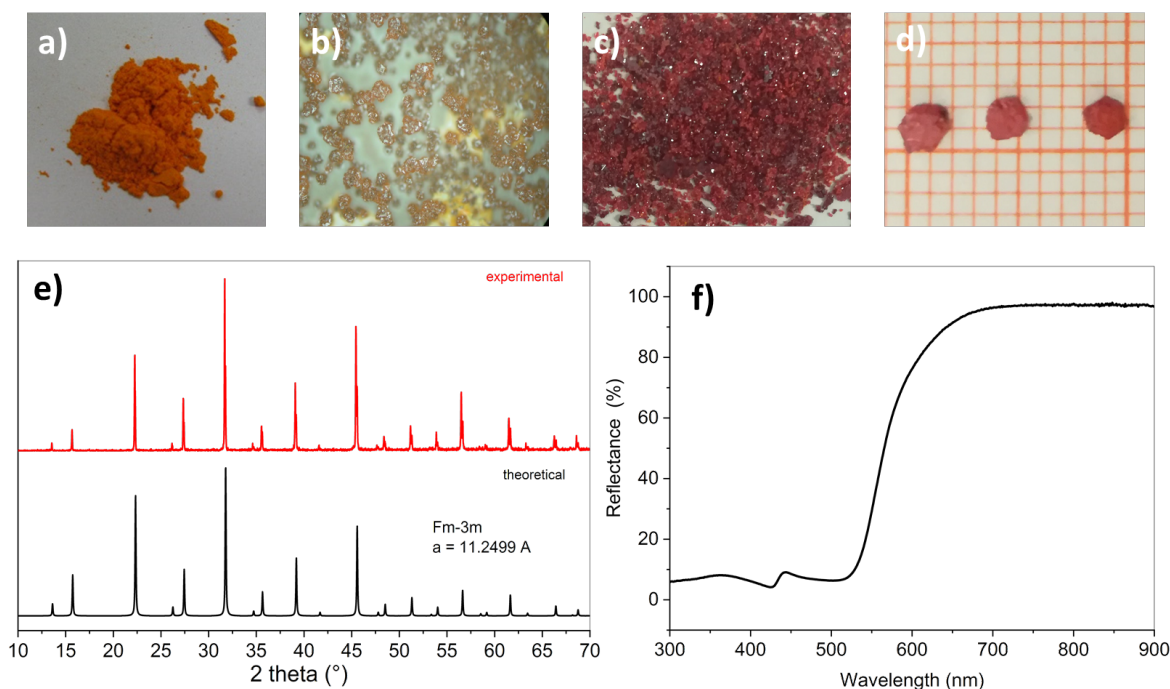


Figure 18 Hydrothermal synthesis setup.

A low concentrated mixture of starting materials in acidic aqueous solution was dissolved and introduced into the chamber of the autoclave. The chamber was closed with a cover and the parameters were set; the pressure which was used was 15 bar and the temperature was 200°C. The synthesis was conducted over 8h and small crystals around 0.8-1 mm were formed at the edge of the chamber.

A summary of all synthesis routes is present in Figure 19. Figure 19a shows powder of Cs₂AgBiBr₆ prepared by the solid-state synthesis in an alumina crucible, where Figure 19b shows millimeter size double perovskite crystals formed using the hydrothermal synthesis. Figure 19c shows crystals formed after solution synthesis with sizes of around 0.5 mm (5°C/h) while Figure 19d shows single crystals of 2 mm size after cooling the solution at the rate of 3°C/h. Figure 19e shows XRD experimental values of all prepared samples, which show excellent match with previously reported diffractogram.⁵⁷ Figure 19f shows reflectance values of all samples with a reflectance edge at 550 nm. More detailed characterization of these materials will be discussed in this chapter.

**Figure 19** Summary of all synthesis routes. **a)** Solid state synthesis, **b)** hydrothermal synthesis, **c)** solution synthesis, **d)** single crystal synthesis, **e)** XRD of all materials compared to theoretical, **f)** UV-Vis reflectance of Cs₂AgBiBr₆ powder samples.

3.2. Deposition Routes - Thin Film Preparation

While single crystals and powders of perovskites are most useful for analysis and investigating of the structural and physical properties, device applications requires the capability to develop materials in the form of thin films. There are many deposition methods used in thin film fabrication like spray pyrolysis, ultrasonic spray coating, atomic layer deposition, “roll-to-roll”, ink-jet printing, vapor deposition techniques and spin-dip coating. The author will consider spin coating and vapor deposition, which were used for thin film formation of double perovskite Cs₂AgBiBr₆ for applications in solar cells.

3.2.1. Thermal Evaporation

Thermal evaporation is a deposition method for thin-films where the starting materials are heated inside a high vacuum chamber using temperature to produce some vapor pressure. Inside the vacuum, even a relatively low vapor pressure is enough to raise a vapor cloud into the chamber. The evaporated material travels through the chamber and condensates on the substrate. The advantages of using thermal evaporation are the production of perovskite thin films without using any solvents, the ability to deposit perovskite thin films on large areas, better control of material incorporation, reproducible film characteristics, highly crystalline thin films, excellent composition with stoichiometry transferred from the powder material to the film, full surface coverage and well defined grain structure.^{123,124} There are different approaches to used material sources using a high vacuum environment. Except for the deposition of perovskite materials, the high vacuum techniques are primarily used for the deposition of metal contacts on-top of the solar cells. In this case, the thermal evaporation apparatus is divided into three different deposition sources, which are single, dual and triple source and even more sources for vapor deposition. It can be simultaneous and/or sequential. In this work, the investigations are focused on sequential deposition. (Figure 20)

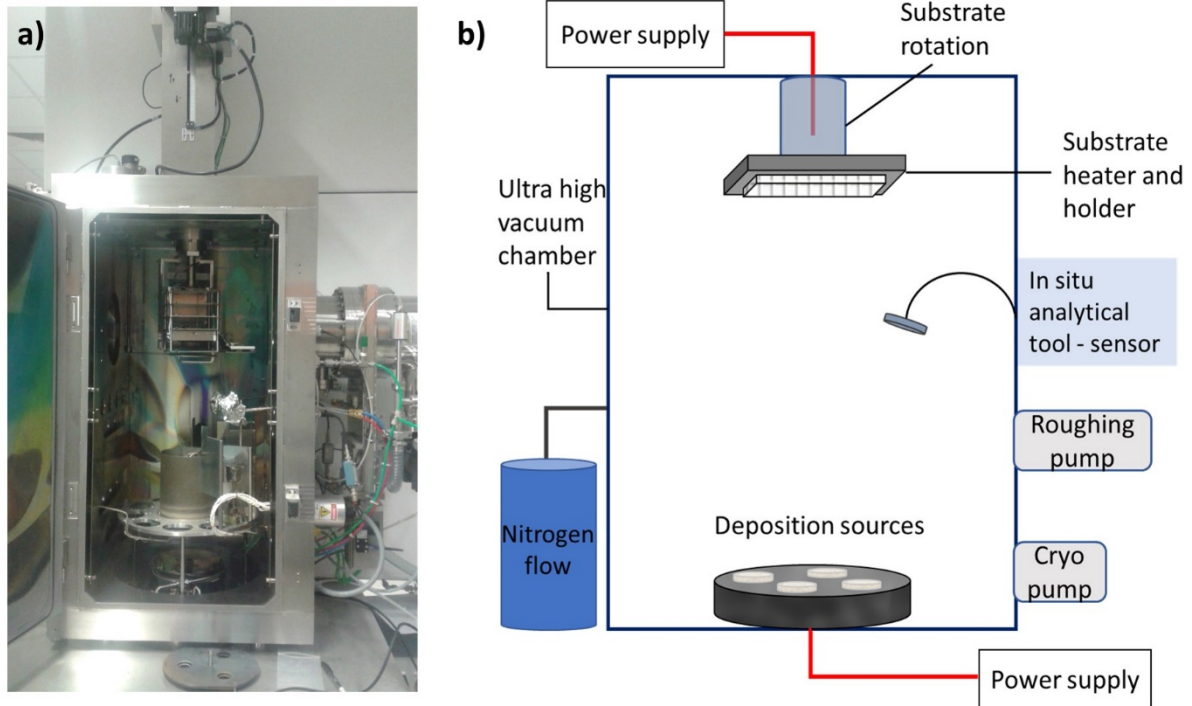


Figure 20 a) Spectros 150 system, Kurt J. Lesker - High vacuum deposition apparatus, b) working scheme of the thermal evaporation system.

The deposition process is controlled with a commercial software (Eva) where the deposition rate, power supply and control system are observed and operated. The Sigma software serves to detect and optimize the thickness.

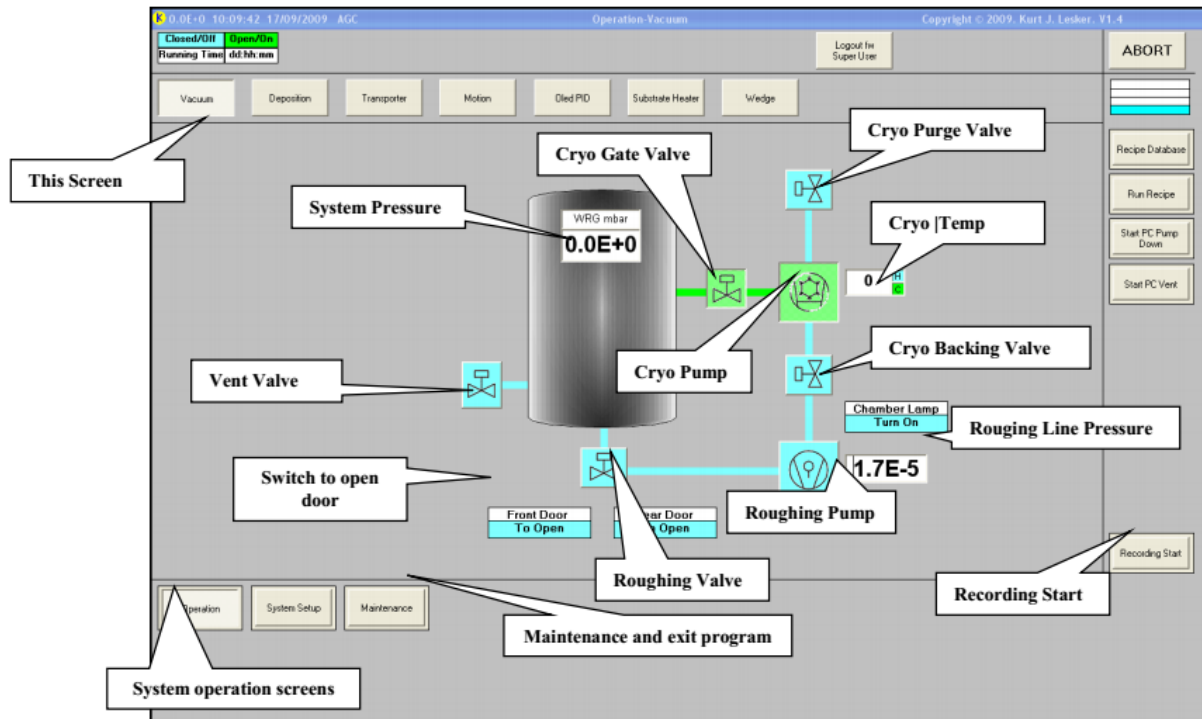


Figure 21 Vacuum display screen - Operation control program.

The working principle of the high vacuum deposition system is to first switch on the cryo pump to reach a chamber pressure of 10^{-3} mbar. After reaching this first pressure, the roughing pump (pump for high vacuum) is switched on to reach a pressure of 10^{-6} mbar. When the chamber pressure is stable the power supply of the deposition sources can be started. Once the heating process has started, the bottom shutter can be opened. The deposition rates were monitored with the quartz crystal sensor (Au) and were adjusted for each starting material using manual thermal evaporation through the Sigma software (SQS-242). When the constant and desirable rate is achieved, the substrate shutter is opened and the deposition starts until an optimized layer thickness is obtained. Finally, the all shutter will be closed and heating, deposition and vacuum will be stopped. Before opening, the chamber the system is purged using nitrogen to reach atmospheric pressure. (Figure 21)

3.2.2. Spin Coating

Spin coating is a simple deposition technique that provides thin film deposition of organic-inorganic perovskites on different substrates like glass, quartz, sapphire, silicon and even flexible substrates. The important parameters for the deposition are the selection of substrates and atmosphere used during spinning (inert or air atmosphere), the solvent, the concentration of perovskite solution and the spinning speed and acceleration steps. The author conducted all depositions in gloveboxes under inert atmosphere (Figure 22). Related to the different device architectures and characterizations the glass substrates ITO and FTO were used. To control the morphology and coverage of double perovskite thin films solvent engineering has been conducted.¹²⁵ It is known that using different solvents and in different volume fractions in the mixtures, the quality of films, the grain size, the film thickness, and the performance of solar cells change. This influence on perovskite thin film quality is due to the differences in density, vapor pressure, polarity and viscosity of the solvents. To investigate the solubility of double perovskites the author used several organic solvents. The starting materials of double perovskite and already synthesized double perovskite were dissolved in the following solvents and their mixtures and the results are shown in Table 2.

Table 2 Solvent engineering.

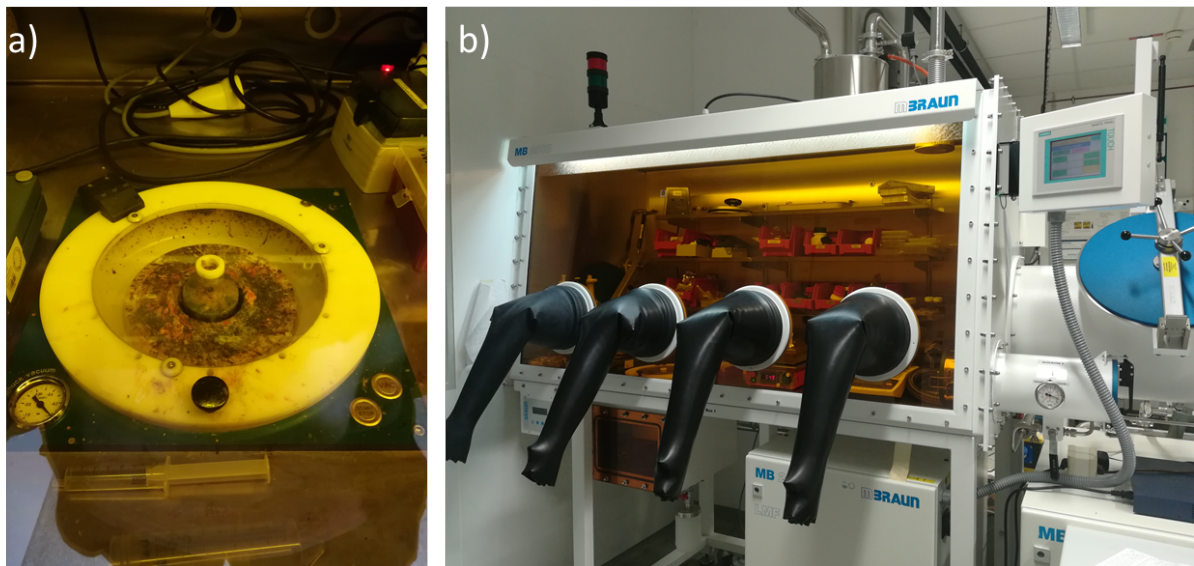
Solvent	Solubility mol/L
DMF	0.15
DMSO	0.52
GBL	Not dissolved
DMSO-GBL (1:1)	0.16
DMF-DMSO (1:1)	0.1

The film thickness can be adjusted not just by using different solvents and solution concentrations to change and control morphology and film quality, but also by using a different steps and coating speeds of by formula:

$$t \propto \frac{1}{\sqrt{\omega}},$$

where t is the thickness (nm), and ω is the spinning speed (RPM).

As the solubility was not so high compared to lead based hybrid perovskites (1.2 mol/L), vapor deposition was one alternative to obtain thicker and uniform thin film layers of the double perovskite. Another important parameter connected with spin coating is the annealing temperature after deposition. Once the pure powders and optimized thin films are achieved, the next step is to characterize them. In the following section, all characterization methods used for the analysis will be defined and the results will be shown and discussed.

**Figure 22** a) Spin coater and b) glovebox system.

3.3. Characterization Methods

Among the number of physical properties to be assessed the most demanding for fully evaluating the promise of perovskite and other materials for photovoltaic applications are:

- Structure and composition – crystallographic characteristics and purity of the material
- Electronic structure – related to energy diagram levels of the active material and in combination with used material in the contact
- Optoelectronic properties – nature of the bandgap and transition, absorption coefficient and photoluminescence
- Transport properties - carrier lifetime and mobility
- Solar cell properties – efficiency, performance and stability of the specific device architecture

In the following the author will explain the classic characterization techniques used to measure crystallographic structure (XRD), composition measurements (XPS/EDX), electronic structure (UPS/IPES), and calculations on perovskites through absorption (Tauc-plot) and photoluminescence measurements (carrier lifetime), relevant to perform a first screening of potential material for the photovoltaic application.

3.3.1. X-ray Diffractometry (XRD)

X-ray powder diffraction is an analytical method for determination of crystal structure and crystal characteristics. This analytic technique can be used for phase identification of single crystals and polycrystalline materials. The XRD analysis is based on constructive interference of monochromatic X-rays and a crystalline sample. As is shown in the Figure 23a, the XRD instrument consists of three basic parts: an X-ray tube, a sample holder and a detector, and two optical parts; primary optics (collimates and restricts X-ray beam before reaching the sample) and secondary optics (collimates and restricts diffracted X-ray beam). This diffraction method is based on the generation of X-rays in an X-ray tube. The X-rays are directed at the sample and the diffracted rays are collected. X-rays are generated in a cathode ray tube to produce high energy electrons and which are accelerated toward a target by using a voltage and bombarding a target sample with electrons. (Figure 23a) Conventional XRD instruments use monochromatic

X-ray radiation from Cu, Cr, Mo or Ag sources. In this case the author used Cu with K- α line to generate a wavelength of 0.15418 nm.

Qualitative X-ray analysis is based on Bragg's law

$$n\lambda = 2d_{hkl}\sin\theta,$$

where λ is the X-ray wavelength, n is the order of the respective reflection, d is the spacing between the planes of atoms (lattice spacing), θ is the diffraction angle and s is the diffraction vector, the vector that bisects the angle between the incident and diffracted beam plane normal $[hkl]$ is the normal vector for the plane of atoms for the corresponding Miller indices. The interplanar spacing d can be obtained by measuring the angle 2θ between the incident and diffracted directions of the radiation with wavelength λ in a material. (Figure 23b)

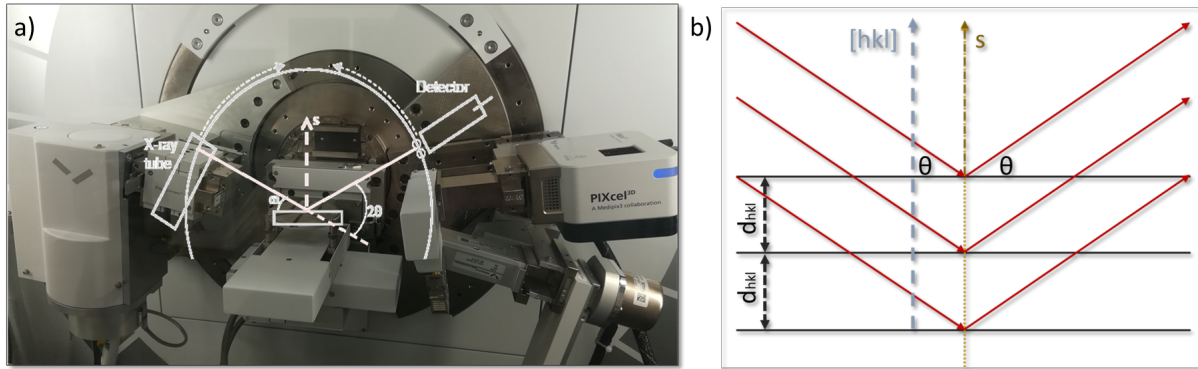


Figure 23 a) Scheme of the Bragg Brentano geometry of diffraction on the picture of the XRD instrument, b) Bragg's law shows the interplanar spacing d determined by measuring the angle 2θ between the incident and diffracted directions of the radiation with wavelength λ in a material respect to a normal line (s), where the (hkl) correspond to particular set of planes, in fact to a particular point in the reciprocal space.¹⁵

Many material properties (electric, magnetic, mechanic, optic, thermic, etc) depend on the spacing of the crystal lattice plane. The Miller indices are used to define the orientation of the planes of a crystal lattice. Miller indices (hkl) are reciprocal intersections of planes with axes reduced to small integers. The general index for a lattice plane is (hkl) , where the intercepts of the plane on the axes or unit cell vectors a , b , c , are a/h , b/k , c/l . The reciprocals of these fractions of the cell edge lengths and written as a whole numbers present the Miller index of the plane.

For instance, for a cubic lattice the relation is:

$$d_{hkl} = \frac{a_0}{\sqrt{h^2+k^2+l^2}},$$

a , is the lattice constant.

The XRD analysis method consist of the analysis of XRD diffractogram. Several parameters can be deduced: the diffraction peaks, the peak position, the peak areas, the angular width, and the shape of peak “tails”. Peak position and intensity results can be used to identify the phases present in the sample. Those parameters can be compared with the ICDD PDF database (International Center of Diffraction Data).

The X-ray diffraction patterns were measured on a Siemens D5000 diffractometer with Cu K α ($\lambda = 1.54 \text{ \AA}$) radiation from 2θ 5° to 70° with a step size of 0.02° 2θ and an acquisition time of 1s per step. For the data in Chapter 4 a Bruker D8 Advance diffractometer and in Chapter 5 a Panalytical Empirian diffractometer in Bragg Brentano configuration were used.

3.3.2. Electron Microscopy

Scanning Electron Microscopy (SEM) is a surface characterization method for the investigation and the observation of morphology and composition. It is producing high-resolution sample surface images. It is working on the principle that the electron beam is focused to sample surface in a vacuum chamber. The interaction results in different signals mostly the secondary electron (SE) signal as well as characteristic X-ray emission, and backscattered electrons (BSE). The devices and the film morphologies (Chapter 4) were investigated using a scanning electron microscope Teneo, Thermo Fischer Scientific (EPFL, Sion).

SEM/EDX measurements were carried out on the microscope Jeol JSM 7500F (Essen). The grain sizes were measured from SEM images, by simply extracting the grain size values and calculating an average grain size using the intercept method - Lince242e program (Chapter 3 and 5).

Transmission Electron Microscopy (TEM) is a technique, which uses high energy electrons to give morphologic and compositional information, as well as crystallographic data from a sample, for which the electrons go through the sample. Sample preparation is very demanding, because the sample should be thin enough for that purpose. The samples have been prepared using ion beam milling to prepare thin and smooth cross-sectional samples (Chapter 4).

3.3.3. Optical Characterization

3.3.3.1. Ultraviolet-Visible (UV-Vis) Spectroscopy and Photoluminescence

UV-Vis absorption spectroscopy is one of the most fundamental analysis techniques for the investigation of the light absorption of a sample in the range of 300-1200 nm. This is the range of frequencies for transferring energy of photons to atoms and molecules. In the absorption setup configuration usually two lamps are used as excitation sources (tungsten-visible and near IR and deuterium – UV excitation). While the light is passing through the sample, the transmitted intensity I_t is compared to the incident intensity I_0 , with A the wavelength-dependent absorbance.

$$A(\lambda) = -\log_{10} \left(\frac{I_t(\lambda)}{I_0(\lambda)} \right)$$

In this work, this measurement has been conducted on powder and film samples. To calculate the direct or indirect band gaps the author has used a linear fit of the Tauc-plot calculation using absorbance data.

Photoluminescence emission spectra are provided by exciting the sample at a fixed wavelength and scanning through different wavelengths using the emission monochromator.

Absorption measurements were conducted in a Shimadzu UV-2550 UV-VIS Spectrophotometer using an integrating sphere in transmittance geometry. Photoluminescence (PL) measurements were done using a custom setup where the sample was excited by a focused PicoQuant LDH-D-C-405 laser diode in continuous wave mode at 405 nm with a spot size of $\sim 10 \mu\text{m}$. PL spectra were recorded by a Horiba Spectrum-1 CCD coupled to a Horiba iHR550 grating monochromator, using a 150 g/mm grating. For the excitation power dependent measurements, neutral density filters adjusted the laser intensity. Optical spectra were measured using a Shimadzu UV-VIS 2600 spectrophotometer operating from 300 to 900 nm with a step size of 1 nm.⁸²

3.3.3.2 Time Resolved Photo-Luminescence (TRPL)

Time Resolved Photo-Luminescence (TRPL) is an experimental technique that shows the spectral and temporal change of the emission of a sample following its illumination by a short pulse of light. The short pulse of light generates electron-hole pairs that decay to lower

energy levels within the sample. They can subsequently recombine and emit light. The emitted light is composed of a set of wavelengths corresponding to transition energies of the electronic states and, as a result, the measurement of the optical spectrum as a function of time is a means to measure the electronic transition energies and their lifetimes. The decay times are on the order of picoseconds or nanoseconds.

Transient photoluminescence measurements in this chapter were performed in a Horiba Fluorolog-3 spectrofluorometer using the time correlated single photon counting method (TCSPC). The sample was excited by a pulsed Horiba DeltaDiode DD-375L laser diode at a wavelength of 374 nm with a maximum pulse width of 70 ps and a pulse intensity of ~ 1.5 nJ/cm². (Duisburg)

In chapter 4 the absorption spectra are acquired with a Perkins Elmer lambda 950s UV/Vis spectrophotometer using an integrating sphere to account for optical losses outside of the active layer. Steady state and time resolved photoluminescence measurements were carried out on a Horiba a Fluorolog-3, with a PMT (Photomultiplier-Tube) as detector. The excitation source for the TCSPC is a Horiba nanoLED-370 with an excitation wavelength of 369 nm and a pulse duration of 1.3 ns. (EPFL, Sion)

3.3.4. Atomic-Force Microscope (AFM)

Atomic force microscopy is a high resolution type of scanning probe microscopy to map the topography of a sample. The method works by the interaction between a mechanical probing tip (cantilever) and the sample surface when brought sufficient close to each other. The forces in between the sample and candilever lead to a deflection of the cantilever according to Hooke's law. The AFM measurement can be used for force measurement, imaging and manipulation. The author used AFM for topographic imaging of the deposited films using the contact mode of the tip motion.

3.3.5. Photoemission Spectroscopy (PES)

Photoemission spectroscopy is one of the most important methods to investigate the electronic structure of molecules, solids and surfaces. The basic principle of the photoemission process is shown in Figure 24. Monochromatic photons with energy $h\nu$ produced by an X-ray

anode (for XPS measurement) or a helium lamp (for UPS measurement) hit the sample surface. The kinetic energy (KE) of the photoelectrons can be measured by an electrostatic analyzer.

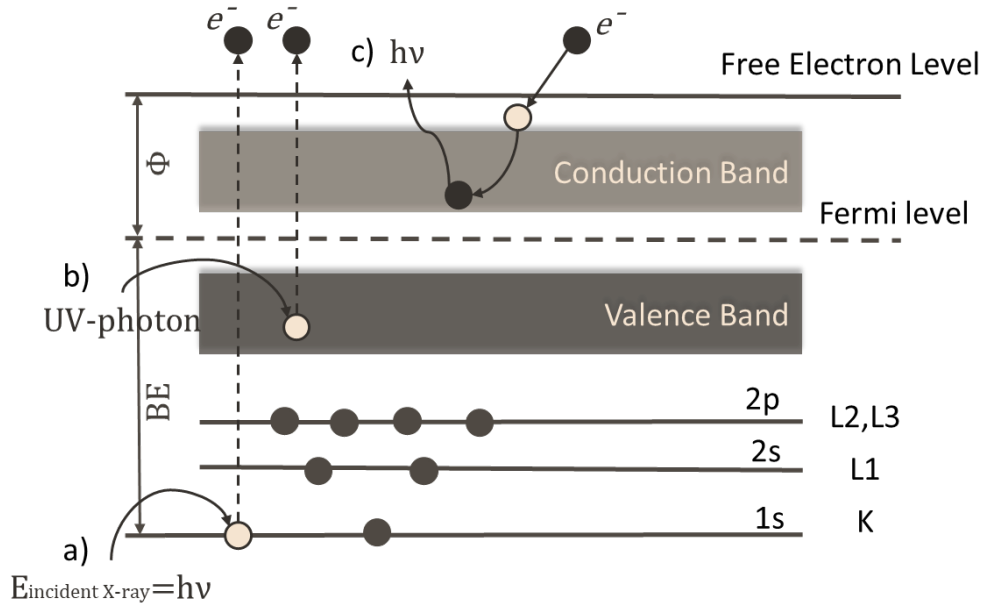


Figure 24 Photoelectron emission process, a) XPS, b) UPS, c) IPES.¹²⁶

$$KE = hv - BE - \phi_{spec}(\text{calibrated})$$

KE is the kinetic energy, h is Planck's constant, v is the frequency of the emitted/absorbed light, and ϕ is the work function of the spectrometer, BE is the binding energy.

In Figure 24a the basic principle of X-ray photoelectron spectroscopy is shown. After the X-ray hits the sample surface and the atom has adsorbed it, the photoelectron is the ejected electron from an electron shell of an atom. The binding energy is a specific value for every element and can be calculated from measuring the kinetic energy of the photoelectron. An elemental analysis of the material can be conducted.

For the analysis of the film stoichiometry, the integrated peak areas of characteristic core level excitations in the XPS spectra were evaluated. Here, first a Shirley background was subtracted and the peaks of Cs 3d_{5/2}, Ag 3d_{5/2}, Bi 4f_{7/2} and Br 3d_{5/2} were fitted by mixed Gaussian/Lorentzian peaks. The peak areas were corrected by the relative sensitivity factors (RSF) which were RSF(Cs 3d_{5/2}) = 40.3, RSF(Ag 3d_{5/2}) = 10.66, RSF(Bi 4f_{7/2}) = 19.1, and RSF(Br 3d_{5/2}) = 2.13.

In contrast to XPS, in ultraviolet photoelectron spectroscopy (UPS) the photoelectrons will be ejected from molecular orbitals by absorbing an ultraviolet photon (Figure 24b). By measuring

the kinetic energy of the photoelectrons, the valance band region of the material can be investigated.

Inverse photoemission spectroscopy (IPES) is the most surface sensitive technique compared to XPS and UPS. The method is used to investigate the unoccupied electronic structure of surfaces of thin film absorbing materials. Probing the electronic states above the Fermi level with a defined electron energy, these electrons couple to high-lying unoccupied electronic states and decay to low-lying unoccupied states. The photons emitted in the decay process are detected and an energy spectrum and the IPES can be used for determination of the conduction band region of the materials. (Figure 24c)

All photoemission spectroscopy measurements were performed at University of Cologne, under dr. Selina Olthof supervision, in a multi-chamber vacuum system at a pressure of 5×10^{-10} mbar using a hemispherical electron analyser (Phoibos 100, Specs). A Mg K α anode at $h\nu = 1252.6$ eV was used as the excitation source for XPS measurements while for UPS as monochromatic UV microwave source (VUV 5000, VG Scienta) at $h\nu = 21.22$ eV was employed.

3.4. Results on Double Perovskite Layer

3.4.1. Vapor Deposition

In this section, the results of powder and film sample characterization will be discussed. In the first part of this section the thermal evaporation deposition and results will be explained. For this purpose, Cs₃Bi₂Br₉ as one of starting materials for dual source thermal evaporation was synthesized without the addition of AgBr. Silver bromide was used as purchased starting material (Alfa Aesar). The thermal vapor deposition for each deposition route was performed at a chamber pressure of 10⁻⁷ mbar. The obtained films were annealed at 220°C for 24h in air to facilitate complete crystallization. For single source thermal deposition, the successful synthesis of Cs₂AgBiBr₆ via solution synthesis was confirmed by powder X-Ray diffraction measurements (XRD) representing the cubic structure (Fm-3m) with lattice constant of a=11.25 Å¹²⁰.(Figure 26)

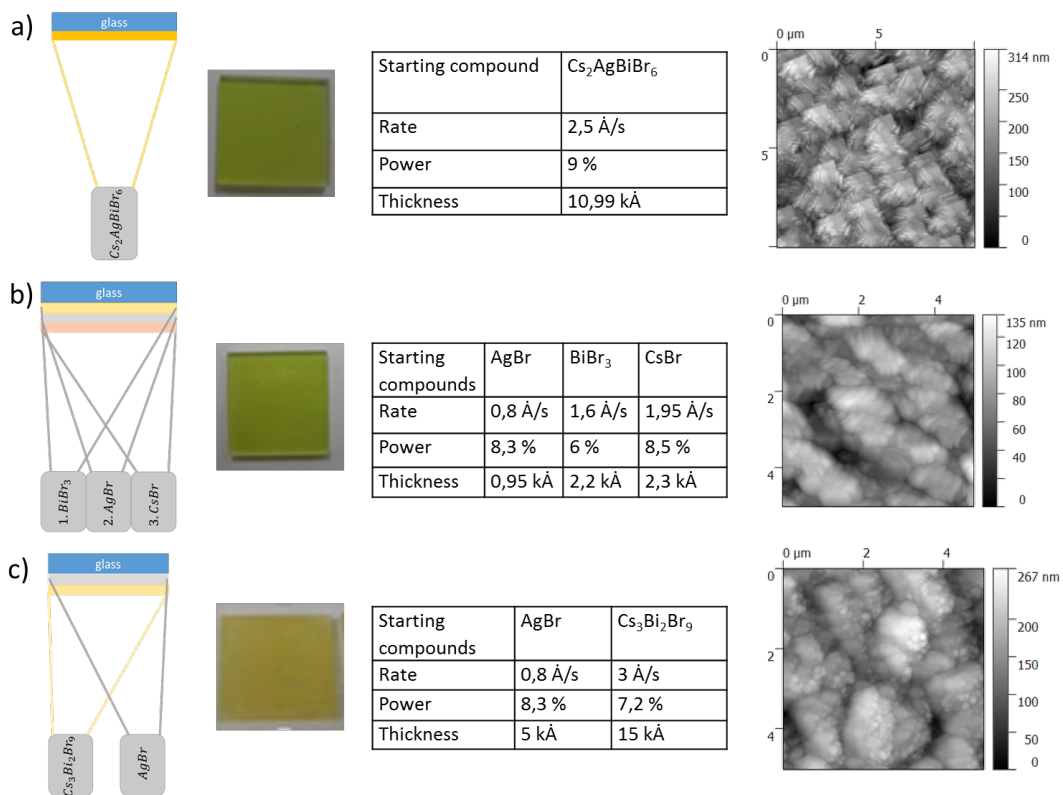


Figure 25 Schematic representation of the sequential vapor deposition processes, images, deposition parameters and AFM images of the resulting films; **a)** single source Cs₂AgBiBr₆, **b)** triple source BiBr₃-AgBr-CsBr, and **c)** dual source Cs₃Bi₂Br₉ and AgBr.

This route to prepare the thin films using vapor deposition under high vacuum offered good thickness control and the possibility of large area surface deposition. The evaporation and deposition of Cs₂AgBiBr₆ itself (Figure 25a) as a single source deposition, the sequential triple source deposition of CsBr, AgBr, and BiBr₃ (Figure 25b), and the sequential dual source deposition of Cs₃Bi₂Br₇ and AgBr were used (Figure 25c). All deposition routes have been used without substrate heating. For the single source deposition of Cs₂AgBiBr₆, a deposition rate of 2.5 Å/s was used on glass substrates at room temperature. The film coverage was complete and is bright yellow in colour. In the XRD diffractogram (Figure 26) the main reflection at 31.8° 2θ is attributed to the (400) reflection of Cs₂AgBiBr₆. The small XRD reflection at 15.8° 2θ can be assigned to the (200) peak of the double perovskite. One thus might assume an oriented crystal growth. The minor reflections can be attributed to BiOBr and AgBr. Apparently Cs₂AgBiBr₆ is not completely stable and formed under the conditions which were present in the evaporator. This led to partial decomposition into its binary metal bromides. Analysing the residue from the crucible, some decomposition of the material took place leading to dominated CsBr traces. During annealing, BiBr₃ reacted with oxygen from air and resulted in the BiOBr side phase and the annealing in the inert atmosphere was considered.

The sequential thermal deposition of the three binary metal bromides in 2:1:1 stoichiometry was conducted for purchased (Sigma Aldrich) starting materials of CsBr, BiBr₃ and AgBr, respectively. The main goal to achieve was a triple layer system which was supposed to react on the interface in the subsequent annealing step. The films are bright yellow, but the XRD diffractograms do not show Cs₂AgBiBr₆. Recently Wang et al.⁸³ reported on sequential vapour deposited Cs₂AgBiBr₆ using this approach in preparation of solar cells with thickness of 380 nm and power conversion efficiency of 1.37%. Six different deposition sequences of starting materials have been used by combining different rate (thicknesses) and “layer on layer” approaches. Changes in the order of the deposited layers and thickness did not lead to a successful formation of the pure or partial double perovskite (Figure 26b). The issues related to deposition are materials lost in to the vacuum chamber and not appropriate deposition rate for each compound. The results were not reliable. Therefore, the author focused on other deposition routes. The last attempt was to use sequential deposition of the ternary metal bromide, Cs₃Bi₂Br₇, followed by the deposition of AgBr as a first approach and the reverse procedure (first AgBr followed by Cs₃Bi₂Br₇) and annealing to facilitate inter-diffusion and reaction of the two layers. The deposition rate of AgBr layer was 0.8 Å/s and the deposition rate of Cs₃Bi₂Br₇ was 3 Å/s. The films appear darker in colour (Figure 25). Cs₃Bi₂Br₇ is supposed to be thermodynamically

more stable than Cs₂AgBiBr₆,⁷⁶ because of, according calculation, the stable chemical potential region of pure Cs₂AgBiBr₆ is narrow and the preparation should be careful in order to avoid impurity phases of Cs₂Bi₂Br₉. The author conducted several attempts using “layer on layer on layer” deposition. The presence of the main reflections of Cs₂AgBiBr₆ double perovskite (111, 200, 220, 311, 222, 400, 422, and 444) prove the successful formation of the double perovskite phase. Nevertheless, impurities of AgBr and BiOBr still remain, which should be contorted by adjusting stoichiometry, thickness as well annealing environment conditions (atmosphere or inert).

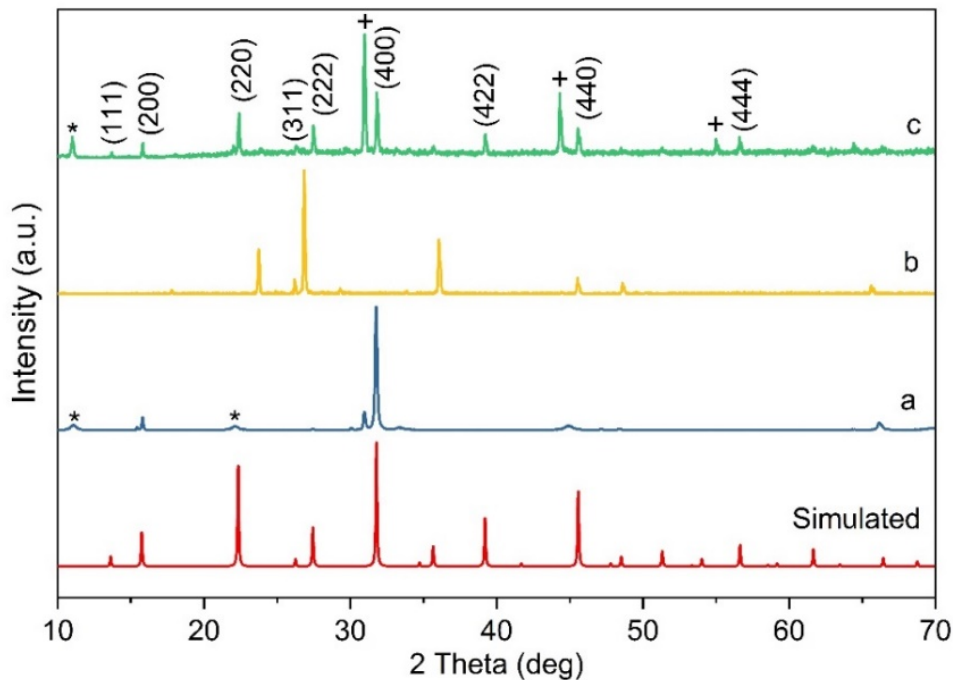


Figure 26 XRD pattern of the films using the full evaporation scheme **a)** Cs₂AgBiBr₆, **b)** BiBr₃-AgBr-CsBr, and **c)** Cs₂Bi₂Br₉ and AgBr.(+AgBr, *BiOBr)

After XRD analysis the author performed UV-Vis spectroscopy of the films measuring transmittance in the range from 300 nm to 800 nm. The curves on Figure 27 show the slight differences in transmittance slope from 440 nm, 430 nm and 460 nm for single source, triple and dual source deposition, respectively. The results correspond to the XRD analysis. Atomic force microscope was conducted to determine the thickness of the films using thermal evaporation. The results are shown in Figure 25 in the fourth column. The AFM image of single source deposition shows needle-like particles on top of ground grains. This is due to the decomposition of the films as well as of the starting materials in the crucible when the final step shows deposition of unwanted compounds and a thickness of around 300 nm. The triple source vapour deposition AFM images show particle sizes of around 130 nm and small round particles corresponding to the starting materials. For dual source deposition the AFM images show round

particles with some small grains showing formation of Cs₂AgBiBr₆ with some impurity residues and a thickness of around 260 nm.

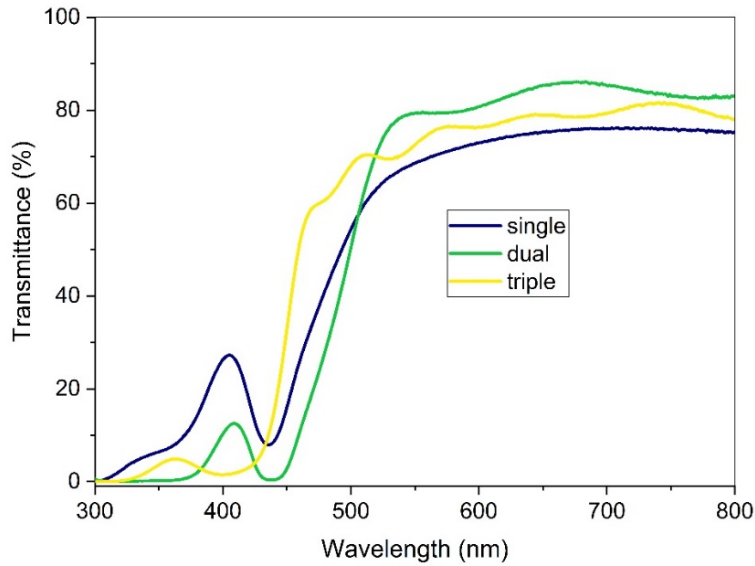


Figure 27 UV-Vis spectra for the three deposition approaches.

To sum up, preliminary attempts on vapor deposition for the preparation of Cs₂AgBiBr₆ thin films can be encouraging, but to improve formation of pure Cs₂AgBiBr₆ double perovskite phase, co-evaporation of starting materials, substrate heating during vapor deposition, and post-annealing conditions must be investigated. The lower thermodynamic stability of the double perovskite compared to some of the side phases (e.g. AgBr, Cs₃Bi₂Br₉) make a proper control of deposition parameters necessary by adjusting and diminishing deposition rate, pressure, and annealing temperature. Because of the thermal deposition system limitation, and the relevance of producing pure double perovskite active layer for solar cells application, the author considered another deposition approach and moved to solution deposition processing.

3.4.2. Solution Deposition

One of the alternative approaches for the deposition of Cs₂AgBiBr₆ thin films is the solution based spin coating process. The author conducted solubility tests and solvent engineering of Cs₂AgBiBr₆ in different organic solvents mentioned in Section 3.2.2, Table 2. The concentration should be as high as possible in order to achieve optimal film thickness and coverage. The highest solubility (0.52 mol/L) was achieved in dimethylsulfoxide (DMSO) at 70°C, which is slightly lower than the reported solubility concentration of 0.6 M.⁷⁴ Unlike reference⁷⁴ the pre-synthesized double perovskite Cs₂AgBiBr₆ powder dissolved in the solution has been used as precursor solution for the spin coating deposition. The superior solvent properties of DMSO can be understood considering its high relative permittivity of $\epsilon_r=46.6$.¹²⁷ Furthermore, a sequential dissolution process was observed which resulted in a colour change from orange to yellow to white prior to complete dissolution of the powder resulting in a yellow solution assumed due to the dissolution of the double perovskite Cs₂AgBiBr₆ on first AgBr and BiBr₃ followed by CsBr, respectively.

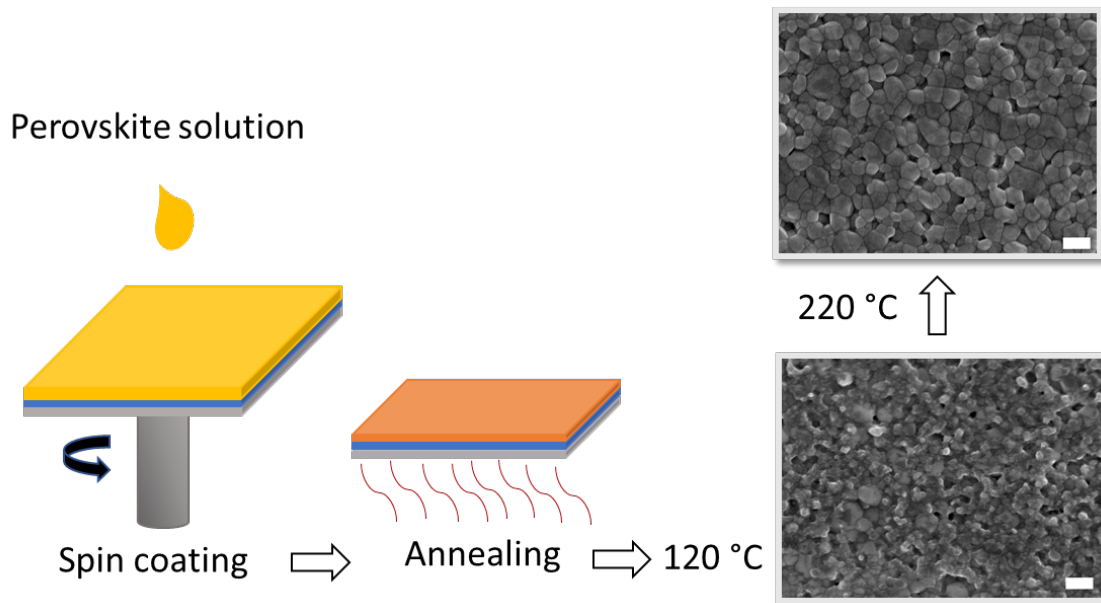


Figure 28 deposition process by spin coating and SEM images of Cs₂AgBiBr₆ thin film surfaces after annealing at 120°C and 220°C (scale bars: 200nm).

In order to optimize the thin film morphology with respect to its homogeneity, roughness, and thickness, the influence of the rotation speed and spin coating steps (2500 rpm - 5000 rpm, one and two step approaches), atmosphere (dry N₂ in the glovebox and ambient atmosphere), and annealing conditions after spin coating was investigated. Processing under ambient atmosphere leads to thin films appearing turbid very fast, whereas processing in dry nitrogen results in

nicely formed translucent films. After several attempts, the one-step spin coating process at 4000 rpm for 30 seconds was found to be the best as estimated from macro- and microscopic investigations. The most relevant step to form pure films of double perovskite and to induce crystal growth in the films is thermal treatment after spin coating. Here a subsequent annealing step under nitrogen is used. Starting with annealing at 120°C after deposition hardly shows any regular particles of around 50 nm in size (Figure 28) while annealing at 220°C is the optimal treatment for a gradual increase of the annealing temperature from 120°C to 220°C at 3 °C min⁻¹ which results in spherical particles with narrow size distribution (80 ± 5 nm), evaporation of the solvent and crystal phase formation. The thickness of the films is about 160-200 nm. The surface morphology of Cs₂AgBiBr₆ appears very homogenous (Figure 28).

3.4.3. Deposition of the Double Perovskite on Top of the Different Substrates and Characterization of Thin Film

After successful optimization of double perovskite deposition on glass via spin coating, the glass substrates were covered with a polymer layer of PEDOT:PSS (Heraeus Clevious polymer dispersion) via spin coating. The deposited double perovskite solution was deposited according to the above procedure and subsequent annealed. In order to investigate the interface surface behaviour and the incorporation of perovskite solution, the author considers compact and mesoporous inorganic layers of spin-coated titanium diisopropoxide bis(acetylacetonate) (0.15 M in 1-butanol; 20 s at 2800 rpm; annealing at 125°C for 5 min) and followed by spin-coating of TiO₂ paste (anatase 20 nm, Sigma Aldrich, 0.12 g/mL in 1-butanol; 20s at 2000 rpm; annealing at 125°C for 5 min), respectively. Final calcination at 550°C for 1 h leads to mesoporous titania covered substrates. The double perovskite thin films were prepared both on PEDOT:PSS and on mesoporous titania, because these are the commonly used hole and electron transporting layers in p-i-n and n-i-p solid state perovskite solar cells, respectively. In contrast to recent reports⁷⁴ the present approach uses a solution of Cs₂AgBiBr₆ as a precursor for the thin film deposition. In both cases the successful formation of the double perovskite could be confirmed according to XRD measurements (Figure 29).

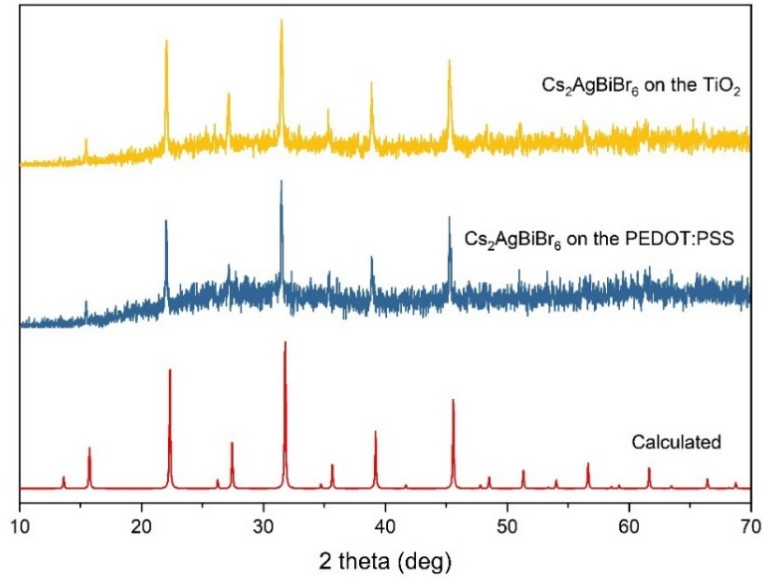


Figure 29 XRD of Cs₂AgBiBr₆ deposited on different sublayers.

The reflectance of films and powder samples of double perovskite Cs₂AgBiBr₆ was measured using UV-vis spectroscopy. The data are analysed according to Tauc-plot calculation equation. Comparing the Tauc-plots of both the thin film (2.42 eV) and the double perovskite powder (2.21 eV) we see a blue-shift of the absorption edge (Figure 30). This is probably caused by the low film thickness and particle size and/or remaining amorphous parts or side compounds of Cs₃Bi₂Br₇ in the thin film. The difference to the reported value of 2.21 eV for a thin film⁷⁴ can be explained by higher film thickness due to higher precursor concentration, and thicker mesoporous TiO₂ (as well higher dispersion concentration) and lower spin coating speed (2000 rpm for 30 s).

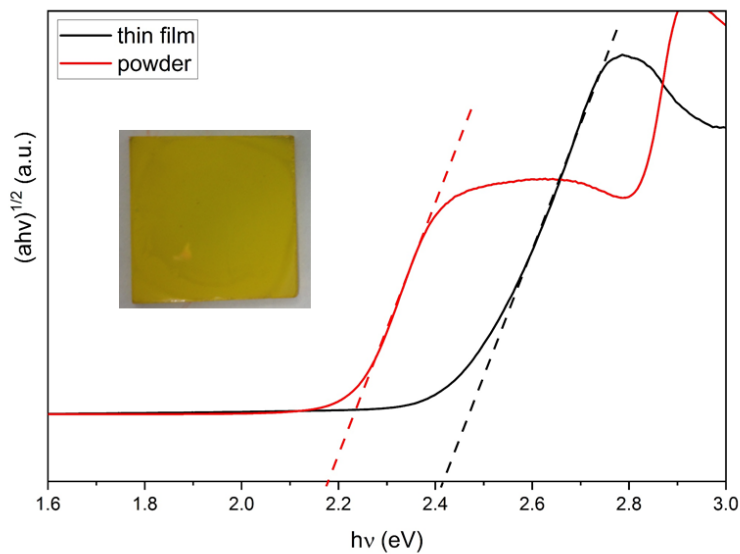


Figure 30 Tauc-plots of Cs₂AgBiBr₆ thin film and powder.

In this chapter the chemical composition, valence and conduction band, carrier lifetime and photoluminescence were analyzed using photoelectron spectroscopy, absorption and photoluminescence analysis, as well as time resolved photoluminescence.

In order to prove the chemical composition of the Cs₂AgBiBr₆ films, X-ray photoemission spectroscopy (XPS) was performed. Peaks centred at 724.2 eV (Cs 3d_{5/2}), 367.9 eV (Ag 3d_{5/2}), 159.3 eV (Bi 4f_{7/2}), and 68.8 eV (Br 3d_{5/2}) were found (Figure 31). The binding energy values correspond to the expected oxidation states of the elements. Thus, the presence of unwanted oxidation states like Ag⁰ it can be excluded. The examination of the peak areas allows to determine the film stoichiometry. A good agreement of the determined values measured by the surface sensitive XPS as well as the bulk sensitive EDX is found, namely Cs₂Ag_{1.23}Bi_{1.23}Br₅ and Cs₂Ag_{1.14}Bi_{0.90}Br_{5.8}. As there is a difference between XPS and EDX, the surface is assumed to be metal (Bi, Ag) terminated.

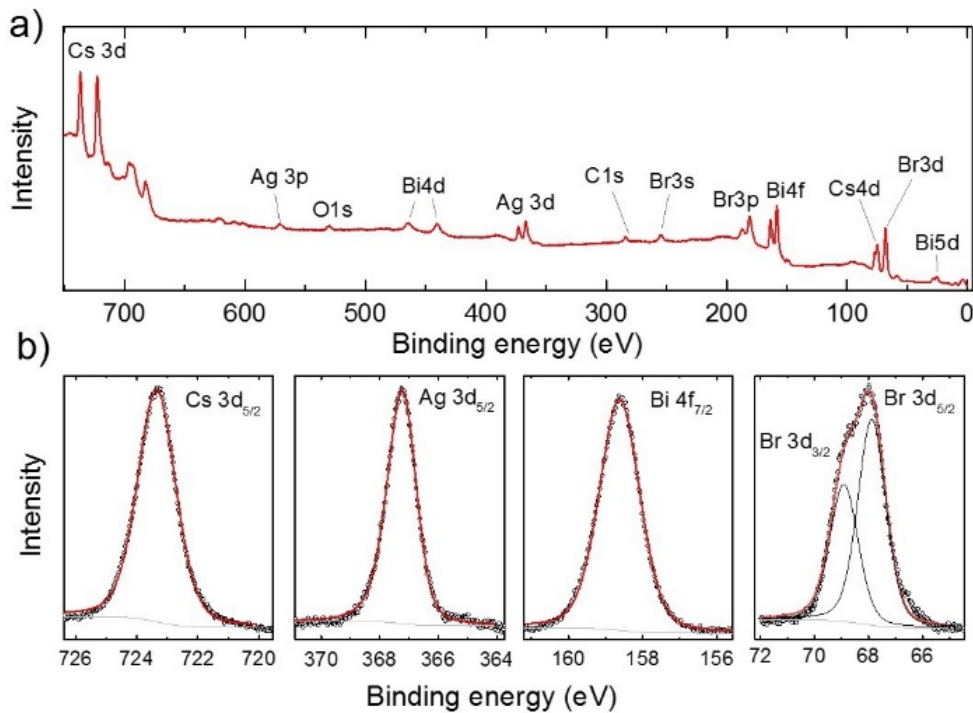


Figure 31 a) XPS survey spectrum of Cs₂AgBiBr₆ spin coated on glass/PEDOT:PSS and b) corresponding high resolution XPS-spectra of cesium, silver, bismuth, and bromine peaks.

To choose the appropriate charge extraction layers for the realization of an inverted solar cell, the ionization energy, IE, work functions, W_i , and electron affinity, EA, of the perovskite layers on PEDOT:PSS were determined using ultraviolet photoelectron spectroscopy (UPS) and

inverse photoelectron spectroscopy (IPES) (Figure 32). The same measurements were also performed on layers prepared on mesoporous TiO₂ in order to reveal the impact of different substrates on the band structure of the double perovskite. The resulting energy values (average of two measurements each) are listed below in Table 3. When Cs₂AgBiBr₆ is deposited on TiO₂, the secondary electron cut-off shows decrease in work function of about 0.5 eV compared with Cs₂AgBiBr₆ deposited on PEDOT:PSS. Concurrently, the UPS valence band and IPES conduction band features of Cs₂AgBiBr₆ on PEDOT:PSS shift by 0.7 eV compared with the sample deposited on TiO₂. The differences of shift in W_f and band onsets lead to some variation in the measured IE, however, the differences are within the experimental error of this measurement technique ($\sim\pm 0.1$ eV). A bandgap value of ~ 2.1 eV is formed independent of the substrate. The peak-shape in the valence band region differs significantly between TiO₂ and PEDOT:PSS covered substrates.

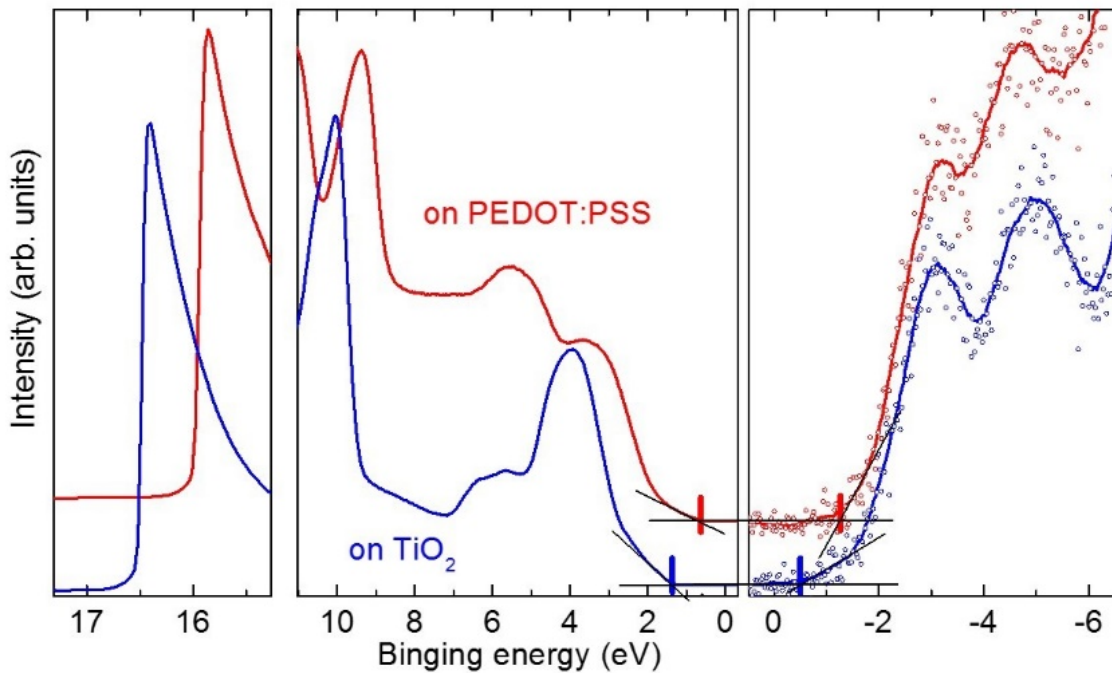


Figure 32 Combines He I UPS and IPES spectrum of Cs₂AgBiBr₆ on mesoporous TiO₂ (lower curve, blue) and PEDOT:PSS (upper curve, red).

The reason for that is currently unclear, but it might be explained by differences in crystallization on these surfaces. Similar variations in shape are commonly observed for MAPI films as well (see e.g. Emara et al.¹²⁸ and supporting information thereof). In the case of Cs₂AgBiBr₆ on PEDOT:PSS the Fermi level is situated about 0.67 eV above the valence band which means the material is slightly p-type whereas in the case of the TiO₂ substrate the Fermi

level is situated ca. 1.40 eV above the valence band which reveals the n-type character in this case. The fact that the substrate determines the Fermi level position in the material indicates a low intrinsic charge carrier density and therefore low defect density. Otherwise band bending would occur and mitigate any influence of the substrate.¹²⁹

Table 3 Calculated average values of work functions (W), ionization energies (IE), electron affinities (EA) and band gaps (E_g) of double perovskite thin films deposited on mesoporous TiO₂ and PEDOT:PSS.

	W _i (eV)	IE (eV)	EA (eV)	E _g (eV)
PEDOT:PSS	5.19	5.87	3.80	<u>2.07</u>
TiO₂	4.69	6.09	4.03	<u>2.06</u>

The optical absorption spectrum of a double perovskite thin film on glass reveals a sharp excitonic peak at 2.83 eV (438 nm) as shown in Figure 33a. This feature can be assigned to the vacancy ordered defect perovskite phase Cs₃Bi₂Br₉,^{130,131} that is known to originate either from the synthesis of the double perovskite where it appears as a side phase⁷⁴, or from degradation of the double perovskite layer⁶⁹. To extract the optical bandgap of the double perovskite from the absorption spectrum, a Tauc plot of the lower energy tail of the observed absorption feature is shown in the inset of Figure 33a assuming an indirect allowed transition, together with a photoluminescence (PL) spectrum of the sample.

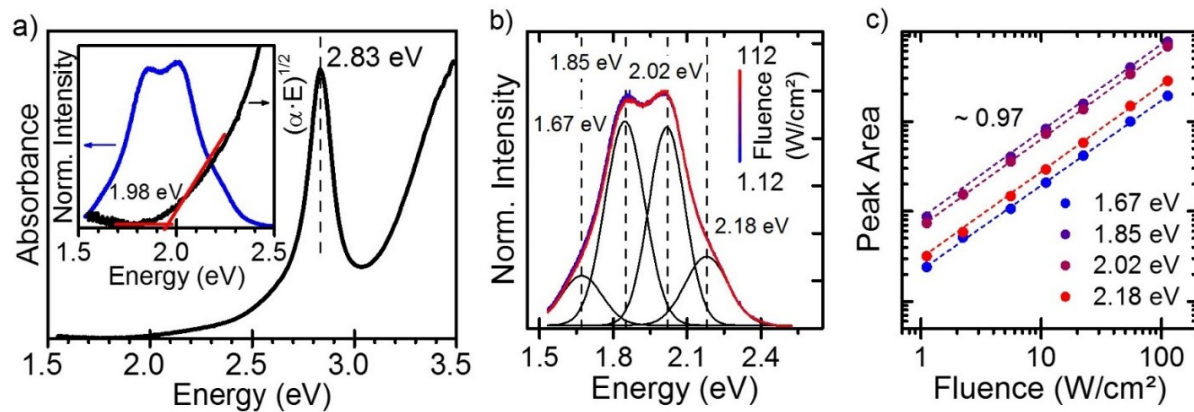


Figure 33 a) Absorption spectrum of a CsAgBiBr₆ thin film sample on glass (main panel). Normalized PL spectrum of the sample and Tauc-plot of the low energy tail of the absorption spectrum assuming an indirect allowed transition (inset). Excitation fluence dependent photoluminescence. b) Normalized PL spectra of a CsAgBiBr₆ thin film sample on glass for different excitation fluences (blue/red) and Gaussian fits (black). The peaks centers are indicated by the dotted lines, corresponding energy values are denoted. c) Dependence of the PL intensity of each emission feature on the excitation fluence extracted by cumulative fitting of the spectra shown in b) with Gaussian profiles.

From the Tauc-plot, an optical bandgap of ~ 2 eV can be estimated, which is in good agreement with the values extracted from photoemission spectroscopy above. The PL spectrum is centered around the onset of the absorption edge and shows broad emission of the double perovskite in the typical energy range from ~ 1.5 eV to ~ 2.5 eV as commonly observed.^{69,74,96,120} At least four different emission features can be clearly identified in the spectrum - in contrast to what is usually observed in literature. The dependence of the PL intensity on the excitation intensity can yield valuable information about the dominant recombination characteristics of semiconductors.¹³² The PL emission of the sample was examined at different excitation densities ranging from ~ 1 W/cm² to ~ 100 W/cm² ($\sim 2.28 \times 10^{18}$ photons/cm²s $\sim 2.30 \times 10^{20}$ Photons/cm²s). As shown in Figure 33b, the PL spectra do not change in shape across all applied fluences. To gain information about the luminescence intensity of each respective feature, the spectra were analyzed by applying a cumulative fit using four Gaussian-shaped functions as indicated in Figure 33b. The fitting shows good conformity with the measured spectra resulting in emission energies of 1.67 eV, 1.85 eV, 2.02 eV, and 2.18 eV, respectively. All four components exhibit similar linewidths of 190 ± 14 meV. The intensity of all four components rises nearly linear with a slope of ~ 0.97 , indicating predominant bimolecular recombination (Figure 33c). Thus suggest that the different emission features share similar recombination mechanisms.

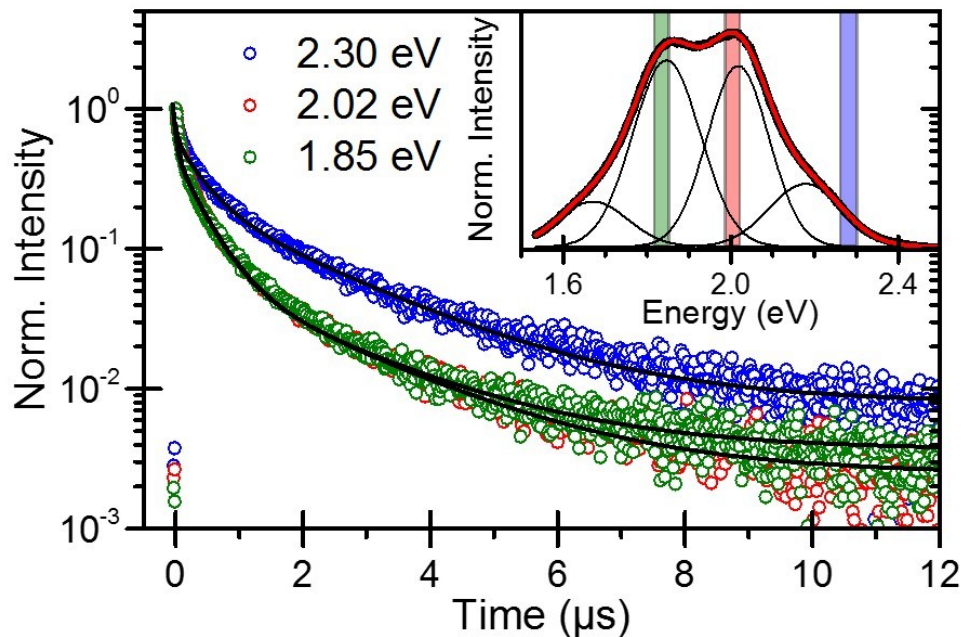
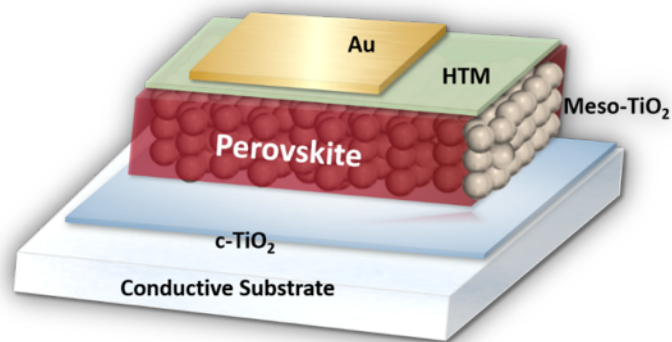


Figure 34 Time resolved photoluminescence traces of a Cs₂AgBiBr₆ thin film on glass measured at different emission energies (main panel) and triple exponential fits (black lines). Inset: Corresponding PL spectrum (black) and cumulative fit with four Gaussian functions (red). The spectral regions examined via TRPL are shadowed according to the colors in the main panel.

To further evaluate the origin of the different emission features, time resolved photoluminescence (TRPL) measurements using the time-correlated single photon counting (TSPCS) technique were carried out at different emission energies of the PL spectrum. The traces were recorded at 1.85 eV, 2.02 eV and 2.30 eV to ensure a major contribution of different emission features to the PL signal in each measurement as depicted in the main panel of Figure 33c. All emission features with a $\lambda_{\text{ex}}=375$ nm show long photoluminescence lifetimes that could be extracted using a triple exponential fit yielding lifetimes of $\tau_1 \approx 50$ ns, $\tau_2 = 400$ ns and $\tau_3 = 2$ μ s (Figure 34). The observed medium lifetime corresponds well with the commonly observed luminescence lifetime of several hundreds of nanoseconds^{74,120} of the double perovskite, while no short-lived component, as shown in other reports, in the order of a few ns was found.¹²⁰ Note, that the emission feature at 1.67 eV could not be measured due to overlap with a harmonic of the excitation laser. In combination with the shown intensity dependence of the different emissions, these findings underline the similarity of the underlying recombination mechanisms. As emissions can be found below as well as above the estimated optical band gap energy, phonon-assisted transition processes might contribute to the PL emission of the double perovskites to a great extent, as suggested recently.¹²⁰ It has been observed that corresponding phonon energies in the order of 100 meV are not commonly found in perovskite-related materials. The intermediate lifetime approximately corresponds to their 660 ns long-lived contribution.



Chapter 4. Cs₂AgBiBr₆ Double Perovskite Solar Cells

In this chapter the author will show the detailed investigation and preparation of solar cells in the two most investigated device architectures defined in Chapter 1, the planar solar cells, and the inverted planar and mesoscopic solar cells devices. Interface engineering by different charge selective layers and layer modifications were performed and optimized. This work establishes a defined and robust fabrication protocol and sets the basic guidelines for an optimized growth of Cs₂AgBiBr₆ perovskite active layers, resulting in a device behaviour free from hysteresis effects.

4.1 Experimental Details and Fabrication of Solar Cells

Processing and engineering of solar cells demands careful preparation. The first step is the cleaning of the glass substrate to avoid impurities, particles of dust and residues of grease. To minimize the risks of unexpected and unexplainable parameter changes further on in the preparation process, a standard procedure is established. Depending on the different solar cell architectures, conductive glass substrates are ITO mostly for inverted planar solar cells and FTO for mesoporous solar cells. ITO and FTO glass substrates are cleaned with an ultrasonic apparatus in diluted Mucosal detergent solution, in isopropanol and in ethanol (all purchased from Sigma-Aldrich) then undergoing ozone cleaning, with each step taking 15 minutes. The FTO and ITO substrates are then etched on the edges by Zn powder and 2M HCl. The cleaning setups can be seen in Figure 35.

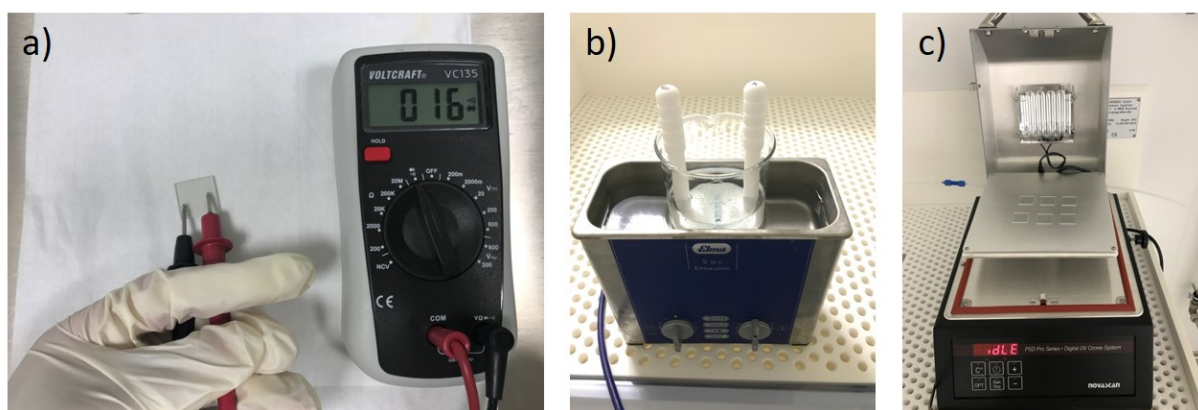


Figure 35 Glass substrate cleaning process **a)** measuring resistivity, **b)** cleaning in different solvents using ultrasonic, **c)** ozone cleaning.

4.1.1. Fabrication of Inverted Planar Solar Cells

Patterned indium tin oxide (ITO)-coated glass sheets with a resistivity of 15 Ω /sq were cleaned according to the procedure described above. Before applying the hole transport layer, remaining organic residues were removed by an oxygen plasma treatment for 10 min at 110°C. A PEDOT:PSS layer (Heraeus, Clevis Solar HTL) was deposited on the ITO substrates by spin-coating at 500 rpm for 5 s and at 3000 rpm for 40 s. The PEDOT:PSS layer was then annealed for 30 min at 130 °C. Afterwards, the substrates were transferred into a glovebox, where the perovskite layer was deposited using the method described in the previous chapter. For the electron transport and hole blocking layer, C₆₀ (20 nm) and BCP (8 nm) were

sequentially deposited by thermal evaporation under high vacuum (3×10^{-6} mbar). Finally, 150 nm of silver was thermally evaporated to create the top electrode (Figure 36). These devices have been prepared in the laboratory of the Institute of Technology for Nanostructures, Duisburg.

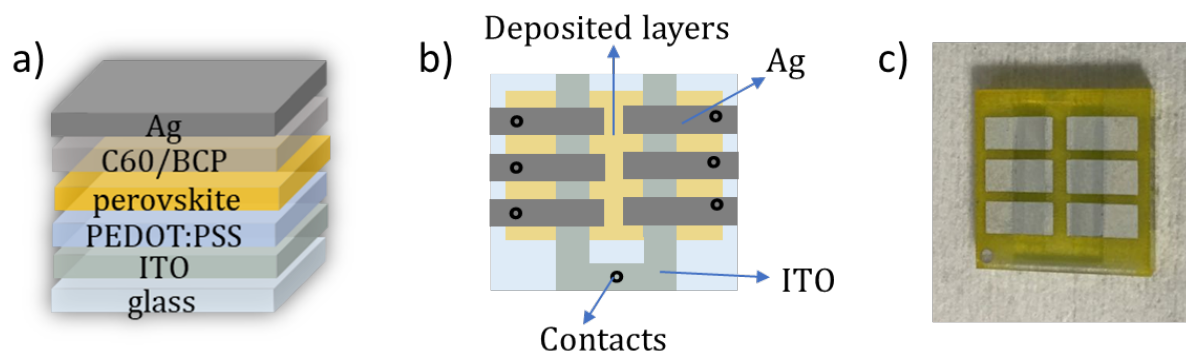


Figure 36 a) Inverted planar solar cell device, cross-sectional scheme, b) schematic illustration of the device architecture with ITO as transparent conductive anode and silver (Ag) as the metal cathode with 7 contact points, c) picture of prepared double perovskite solar cell.

4.1.2. Fabrication of Mesoscopic Solar Cell

The FTO glass substrates (Nippon sheet glass) are etched and sequentially cleaned using the same procedure as described in 4.1. Figure 37a shows the dimensions of the substrate and the areas designated for etching. The process is followed by spray pyrolysis deposition for a compact TiO₂ layer. The precursor for this layer is diluted titanium diisopropoxide (Sigma-Aldrich) solution in ethanol (0.6 ml: 10 ml). The compact TiO₂ layer was coated onto the cleaned FTO substrate heated at 450°C. After cooling, a mesoporous TiO₂ film was prepared by coating with a TiO₂ paste (Dyesol 30 NR-D) diluted in ethanol. The substrates were sintered on a hot plate at 500°C for 30 min. The mesoporous TiO₂ layer is electron transporting layer. Some of the cooled substrates were dipped into 40 mM TiCl₄ aqueous solution and kept at 70 °C for 10 min and sintered again at 500 °C for 30min. Finally, before spin coating them with the perovskite solution, the substrates were treated under UV-ozone for 15 min. The UV-O₃ cleaning technique is generally effective for removing organic contaminants. The double perovskite powder (Cs₂AgBiBr₆) was dissolved in DMSO (0.5 mol/L) at 70 °C, spin coated at 4000 rpm for 30 seconds, and annealed at 280 °C for 5 min. PCPDTBT (Poly[2,6-(4,4-bis-(2-ethylhexyl)-4H-cyclopenta [2,1-b;3,4-b']dithiophene)-alt-4,7(2,1,3-benzothiadiazole)]) as hole

transporting material was purchased from Sigma Aldrich. The solution was prepared by dissolving it in chlorobenzene (30 mg/mL), heating at 70°C and stirring overnight. The PCPDTBT solution was spin coated onto the double perovskite (or on the PTAA/spiro-OMeTAD) at 1000 rpm for 45 seconds.¹³³ PTAA (Poly (triaryl amine), Poly[bis(4-phenyl)(2,4,6-trimethylphenyl)amine]) hole transporting material was deposited on top of the double perovskite film at 3000 rpm for 30 seconds. The PTAA solution was prepared by dissolving 15 mg of PTAA in 1.5 mL toluene adding 15 μ L of 170 mg of Li-TFSI in 1 mL acetonitrile and 7.5 μ L TBP.¹³⁴ Spiro-OMeTAD (N₂,N₂,N₂',N₂',N₇,N₇,N₇',N₇'-octakis(4-methoxyphenyl)-9,9'-spirobi[9H-fluorene]-2,2',7,7'-tetramine) as hole transporting material solution was prepared by dissolving 80 mg of Spiro-OMeTAD powder in 933 mL of chlorobenzene with addition of 31.5 μ L TBP, 7.87 μ L of Co-Salt in acetonitrile and 18 μ L of Li-salt in acetonitrile. Finally, the 70 nm of gold electrode was thermally evaporated on top. In Figure 37b a cross sectional mesoporous device and all materials used are seen. Figure 37c shows an active area of one of the devices.

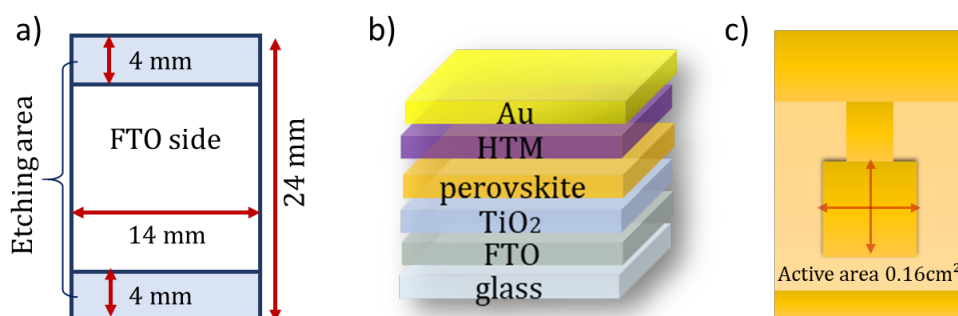


Figure 37 a) Etching approach on FTO substrates, b) scheme of mesoporous solar cells with layers used in this approach, c) final solar cell with an active area ready for measurement.

All devices were prepared in the Group for Molecular Engineering of Functional Materials, Ecole Polytechnique Federale de Lausanne, Sion, Switzerland.

4.1.3. Fabrication of Planar Solar Cells

For the planar solar cells, the author used the same procedure as described above. However, for the electron transporting layer SnO₂ is used. The SnO₂ layer was deposited using the colloid precursor SnO₂ using a 15% colloidal dispersion of SnO₂ in H₂O purchased from Alfa Aesar. Deposition of the ETL layer was conducted using spin coating of this solution with a

one-step deposition method, starting with 3000 rpm for 30 seconds, followed by annealing at 150°C for 30 min.

4.2. Characterization Methods of Double Perovskite Solar Cells

4.2.1. Current Density - Voltage Measurements (J-V)

The current density – voltage measurement is one of the most important characterization techniques for any solar cell device. In this measurement a Xe lamp is used as light source. To simulate AM 1.5G solar light the spectrum is modified with an appropriate filters. As shown in Figure 38a, the solar cell device is covered with a shadow mask to define the active area and light it up. A sourcemeter unit (Figure 38b) is used to apply a voltage between the top and the back contact of the solar device and to measure the strength of the electric current.

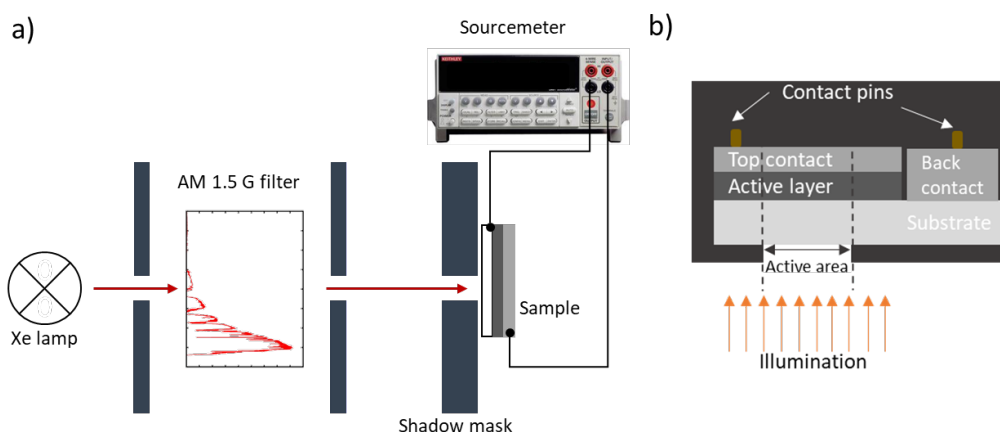


Figure 38 a) setup for measurements of current density – voltage curves under simulated solar light, and a voltage setup function is applied to the device while measuring the current response b) schematic of solar cell measurement holder where the device is illuminated through shadow mask and defined the active area (Scheme was remade from the book “Organic and hybrid solar cells”.)

Current density J is calculated by dividing the current strength I by the active area A :

$$J(\text{mA}/\text{cm}^2) = \frac{I(\text{mA})}{A(\text{cm}^2)}$$

Photocurrent-voltage measurements for inverted planar solar cells were performed using a Keithley model 238 sourcemeter unit controlled by a custom-made LabView program in the laboratory of the Institute of Technology for Nanostructures, Duisburg. The voltage was varied between -0.1 V and 1.1 V with a step size of 10 mV. The scan rate was 0.05 V/s. A solar

simulator (Wacom WXS-155s-10), equipped with a 1000 W Xenon lamp, was used as light source (AM 1.5 G). The light intensity was calibrated employing a pyranometer (CMP 11, Kipp & Zonen). The active area of all devices was 5 mm², as defined by a shadow mask. Photocurrent-voltage measurements for mesoporous solar cells have been conducted in the Group for Molecular Engineering of Functional Materials, EPFL, Sion, Switzerland. J-V curves were obtained using a commercial solar simulator (Oriel, 450 W, Xenon, AAA class) as light source. The light intensity was calibrated to match one sun (AM 1.5G or 100 mW cm⁻²) using a Si reference cell, equipped with an IR-cutoff filter (KG5, Newport). The calibration was repeated before each measurement. The voltage scan rate was 25 mV s⁻¹ for both forward and reverse scans. The cells were masked to limit the active area to 0.16 cm².

4.2.2. External Quantum Efficiency Measurements (EQE)

Another basic characterization method is the measurement of the external quantum efficiency. The conversion rate of incident photons to electrons is measured as a function of the wavelength λ , $EQE = EQE(\lambda)$. The EQE spectrum shows which spectral parts contribute to photocurrent generation.

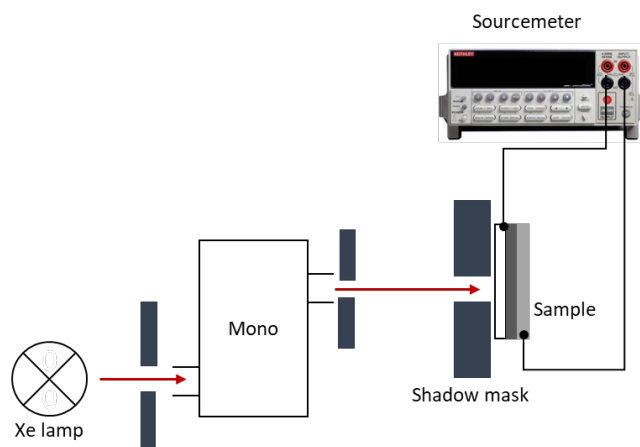


Figure 39 Experimental setup for external quantum efficiency measurements (Scheme was remade from the book “Organic and hybrid solar cells”.)

The principle of EQE measurements is shown in Figure 39. The monochromatic light source (combination of a Xenon lamp and a monochromator) is used to illuminate the active area of the sample through the mask. The solar cell was kept under short circuit conditions and the current through the solar cell was measured for each wavelength part of the monochromator using a source meter. Before measurement, the calibration with the reference solar cell has to

be conducted to obtain the number of the incident photons and established spectral response for each wavelength. Finally, the current data obtained from the device have to be normalized to the number of incident photons:

$$EQE = \frac{\text{number of photogenerated electrons}}{\text{number of incident photons}}$$

The EQE was measured using an IQE200B (Oriel) without a bias light in the range from 300 nm to 800 nm and using the calibration with the silicon solar cell as a reference.

4.3. Results and Discussion

In this section the author will show and discuss the results received from measurements mentioned above and compare the architectures of the planar, inverted planar and mesoporous solar cells. Each of these device architectures used in lead- based photovoltaics show advantages and disadvantages. Last, the introduction of lead-free materials will be discussed.

4.3.1 Planar and Inverted Planar Solar Cells

In this chapter, the photovoltaic performance of planar solar cells is investigated. The detailed description of the architecture can be found in Chapter 1.4.3.

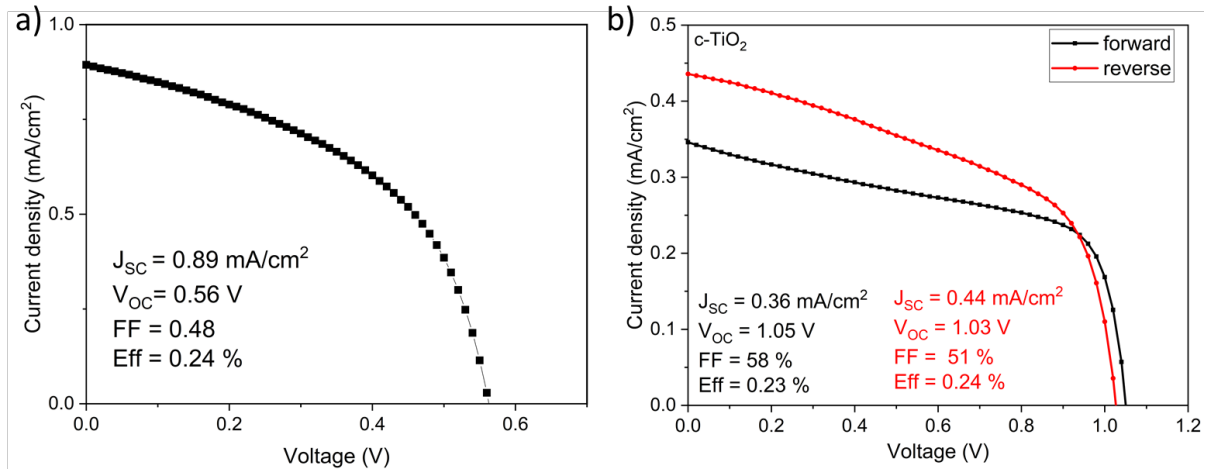


Figure 40 a) J-V curve of a planar solar cell using SnO₂ as electron transporting layer, b) J-V curve and hysteresis of the planar solar cell using c-TiO₂ as ETL.

The short circuit current is higher in SnO₂ devices than in c-TiO₂ devices, but the open circuit voltage is higher than in the SnO₂ devices (Figure 40). Power conversion efficiency shows the same results for different devices (Table 4). The Figure 40b shows significant hysteresis.

Table 4 Photovoltaic performance of planar solar cells using SnO₂ and c-TiO₂ as electron transporting layer and PTAA as hole transporting layer

Nr	Device	V _{oc} (V)	J _{sc} (mA/cm ²)	FF	PCE (%)
1	SnO ₂ /Cs ₂ AgBiBr ₆ /PTAA	0.56	0.89	48	0.24
2	c-TiO ₂ /Cs ₂ AgBiBr ₆ /PTAA	1.03	0.44	51	0.24

In the following, the author uses Cs₂AgBiBr₆ for the fabrication of inverted planar photovoltaic devices.

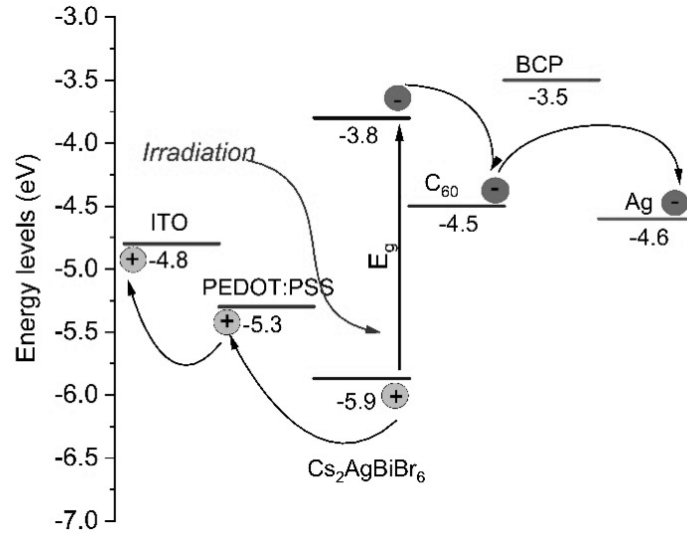


Figure 41 Energy level diagram of the inverted cell structure.

The relevant transport states of the chosen materials match well with the energetic band positions of the Cs₂AgBiBr₆ absorber (Figure 41).

The structure for the investigated solar cells is: anode (ITO on glass) / hole conductor (HTM, PEDOT:PSS about 50 nm) / Cs₂AgBiBr₆ (190 nm deposited via spin coating) / electron conductor (ETM, C60 20 nm / BCP 8 nm) / silver cathode (150 nm), which is illustrated in the cross sectional view in Figure 42c. The best solar cell exhibits an open circuit voltage of $V_{oc} = 0.68$ V, a short circuit current density of $J_{sc} = 1.4$ mA/cm², and a fill factor of $FF = 0.44$ with power conversion efficiency (PCE) of 0.42 % (Figure 42a).

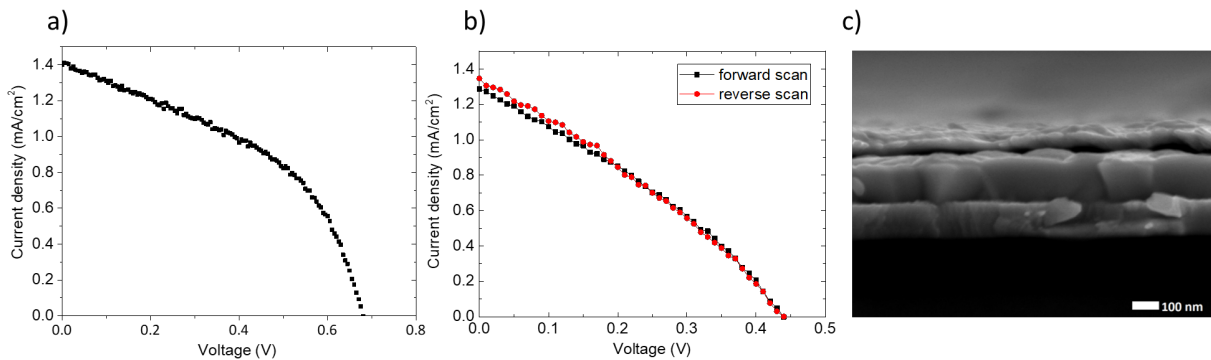


Figure 42 a) J-V curve for best performing device and b) 2 scan directions of J-V curve showing no hysteresis SEM image cross section of double perovskite solar cell.

The cells realized with the planar structure show virtually no hysteresis for a typical IV-characteristic (Figure 42b). This property is typically observed for inverted planar perovskite solar cell structures using other absorber materials such as MAPI (CH₃NH₃PbI₃).¹³⁵ To investigate the reproducibility of our devices, 17 solar cells, were produced on six different substrates and of two different days. The processing was done under inert nitrogen conditions, with the O₂ and

H₂O concentrations never exceeding 2 ppm. Figure 43a shows an average efficiency of about 0.25 % with a standard deviation of 0.08 % and a maximum value of 0.42 %. In Figure 43b the stabilized power output showing stability up to 120 s is shown.

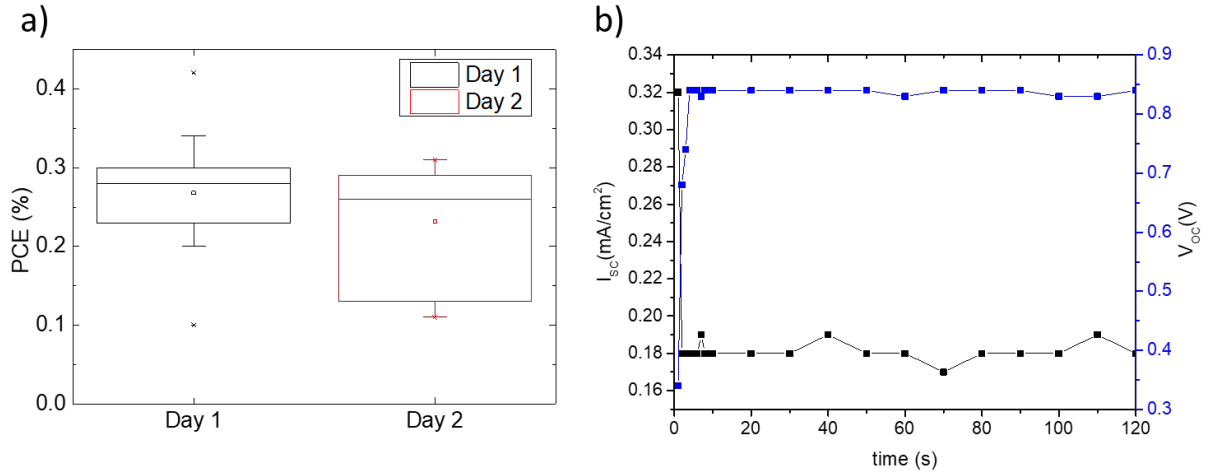


Figure 43 a) Boxplot of efficiencies of solar cells built on 2 different days, b) stabilized power output.

To investigate the origin of the variation in PCE, the V_{oc} , J_{sc} , R_s and R_{sh} (with the resistance values being estimated from the IV slope at V_{oc} and J_{sc}) of the individual solar cells are plotted over the respective PCE in Figure 44.

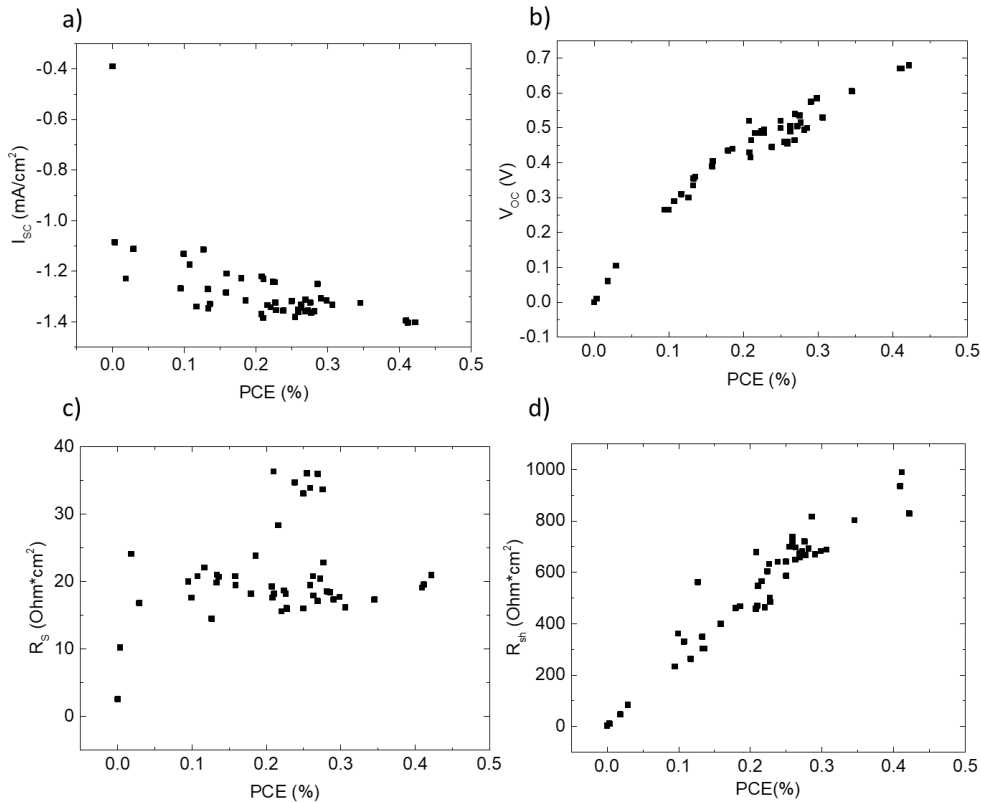


Figure 44 Dependence of different electrical parameters on the efficiency of the solar cells: a) short circuit current J_{sc} , b) open circuit voltage V_{oc} , c) serial resistance R_s and d) shunt resistance R_{sh} .

The author finds that the PCE only has a strong, almost linear dependency on the parameters V_{oc} and R_{sh} . The observed large parameter distribution is thus likely the result of charge carrier recombination or leakage currents through the device. With better blocking layers or further improved film formation, it can be expected to achieve significantly higher efficiency values. A recent publication by Greul et al.,⁷⁴ using the same perovskite material system, demonstrated solar cells with power conversion efficiency values of up to 2.4 %. The main difference to this work is that Greul et. al.⁷⁴ used a mesoporous TiO₂ scaffold. The use of this device architecture resulted in a strong hysteresis of the IV characteristic, which is also typically observed for other material systems using this type of device configuration. The benefits of a TiO₂ scaffold are an improved absorption due to a higher perovskite film thickness and light scattering due to the nanoparticle structure of the TiO₂. Greul et al. further observed a strong improvement in the electronic device characteristics upon annealing the perovskite thin film at 285 °C. To investigate the influence of this step on the solar cells properties, reference devices and devices with the perovskite thin film being annealed in 2 steps for 30 min at 120 °C and then for 10 min at 285 °C were fabricated. The first annealing step at 120 °C was necessary to produce a dense layer, while the actual crystallization of the perovskite occurred during the second step. The IV characteristic of a reference and a high temperature device are shown in Figure 45. It has been found that the J_{sc} and V_{oc} values are reduced by a factor of 2-3 for the high temperature device. The author suspects this to be the result of a damaged PEDOT:PSS layer. To validate this hypothesis, the author determined the conductivity of different PEDOT:PSS films on glass using the four-point-probe method after an annealing step at different temperatures.

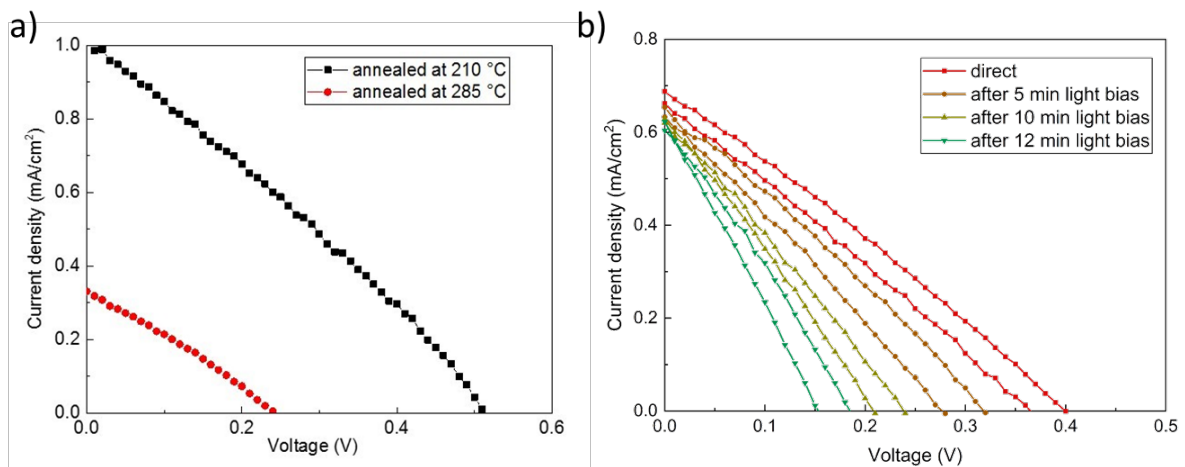


Figure 45 a) J-V characteristics of solar cells with a perovskite layer annealed at 210°C and 285°C, b) The I_{sc} doesn't change, but the FF and V_{oc} decrease meaning that there is more recombination with a time.

Due to the annealing step at 285 °C for 10 min., the conductivity is reduced by a factor of ~15 (2.3 S/m) from 35.7 S/m for PEDOT:PSS annealed at T = 210 °C for 30 min. Though this reduction in conductivity is too small to explain the observed degradation in the IV-characteristic, it is, however, an indication for the suspected damage of the PEDOT:PSS layer. If the interface between the PEDOT:PSS and the perovskite is damaged during this process, enhanced recombination losses at this interface could be the consequence and explain the observed strong degradation in solar cell performance. In Figure 45b applying light for extended time the J_{sc} values remain, and V_{oc} and the final solar cell performance dropped drastically. The R_{sc} also decreases and R_s increases, which can be a sign of the presence of pinholes and recombination centers. The comparison of several stability tests, which were conducted by applying higher temperatures (higher than 220°C), longer light bias or repeating measurements after a period of 24 hours, led to the conclusion that this kind of solar cell devices is not stable or optimal enough to be suitable for double perovskite active layers.

4.3.2. Mesoscopic Solar Cells – Results and Discussion

4.3.2.1. Thickness engineering

In the first part of the discussion of the mesoscopic solar cell results the author will discuss thickness optimization and engineering of the electron transporting layers (mesoporous TiO₂) and the active layers of the double perovskites. This idea is related to calculated and reported diffusion length in double perovskite Cs₂AgBiBr₆ solar cells of 110 nm ± 20 nm.^{81,99} The diffusion length is a measure of the average distance a charge carrier will diffuse before recombining. It can be estimated and calculated by measuring the PL decay dynamics (TRPL) of perovskite samples and perovskites in contact with HTM and ETM to obtain the effective excitation lifetime, τ_{eff} described in Chapter 1. Using a different PL quenching model (simulations) and calculations, an average photoexcitation diffusion length for electrons and holes can be estimated. For diffusion lengths above 100 nm, the double perovskites show very good carrier diffusion properties comparable to lead-based perovskites (100 nm-1 μ m).¹⁴ Solar cell performance for different thicknesses of the perovskite and mesoporous layers are investigated in order to extract more charges corresponding to diffusion length and finally improve power conversion efficiency. This process started with preparing different concentrations of electron transporting layer dispersions, (Ti-Paste dispersed in ETOH) and therefore result in different thicknesses of the layer. The following concentrations of the dispersion were prepared: 1g of TiO₂ paste in 4, 6, 8, 10, 12 mL of ETOH for 400, 280, 250, 160, 100 nm thickness of the ETL, respectively. The ETL was prepared as described in the experimental details. In Table 5 the photovoltaic parameters are shown after employing different Ti-dispersion concentrations.

Table 5 Photovoltaic performance of mesoporous solar cells using different thicknesses of m-TiO₂ layers.

Nr	Device	V _{oc} (V)	J _{sc} (mA/cm ²)	FF	PCE (%)
1	m-TiO ₂ (400 nm)/Cs ₂ AgBiBr ₆ /PTAA	0.95	1.21	68	0.79
2	m-TiO ₂ (280 nm)/Cs ₂ AgBiBr ₆ /PTAA	1.06	1.24	78	1.02
3	m-TiO ₂ (250 nm)/Cs ₂ AgBiBr ₆ /PTAA	1.01	1.12	74	0.86
4	m-TiO ₂ (160 nm)/Cs ₂ AgBiBr ₆ /PTAA	1.04	1.01	75	0.81
5	m-TiO ₂ (100 nm)/Cs ₂ AgBiBr ₆ /PTAA	1.07	0.61	55	0.36

The best performance of the solar cell was measured for 280 nm and 250 nm of mesoporous layer, showing maximal J_{sc} , FF and PCE as compared to other devices. When reducing the thickness of the mesoporous layer, a slight increase of V_{oc} can be observed, but more precisely, it remains the same within a small error bar for all devices. The reason for that could be the obvious decrease of the J_{sc} value because of less infiltration into the mesoporous layer. In addition, if the layer is too thin, there is less charge extraction. Therefore, the serial resistance increases and trap-assisted recombination becomes more possible can be concluded, that the optimal thickness of the mesoporous layer combining the 160 nm thickness of the perovskite occurs in the devices Nr 2 and Nr 3, with power conversion efficiency of 1.02% and 0.86%, respectively. In Figure 46 a less significant hysteresis for each device, and no hysteresis for the best device are observed (Figure 46 b,c). The reason for the presence of the hysteresis in these cases (Nr. 1, 4, and 5) is the different thicknesses and that the carrier generation, separation and its transport across different interfaces is not effective and recombines faster. A significant hysteresis can be seen for 400 nm of TiO₂ (Figure 46a) becoming more prominent with lower thickness of TiO₂. The J-V curve of Nr. 5 combined with different perovskite thicknesses is shown further below in Figure 50a.

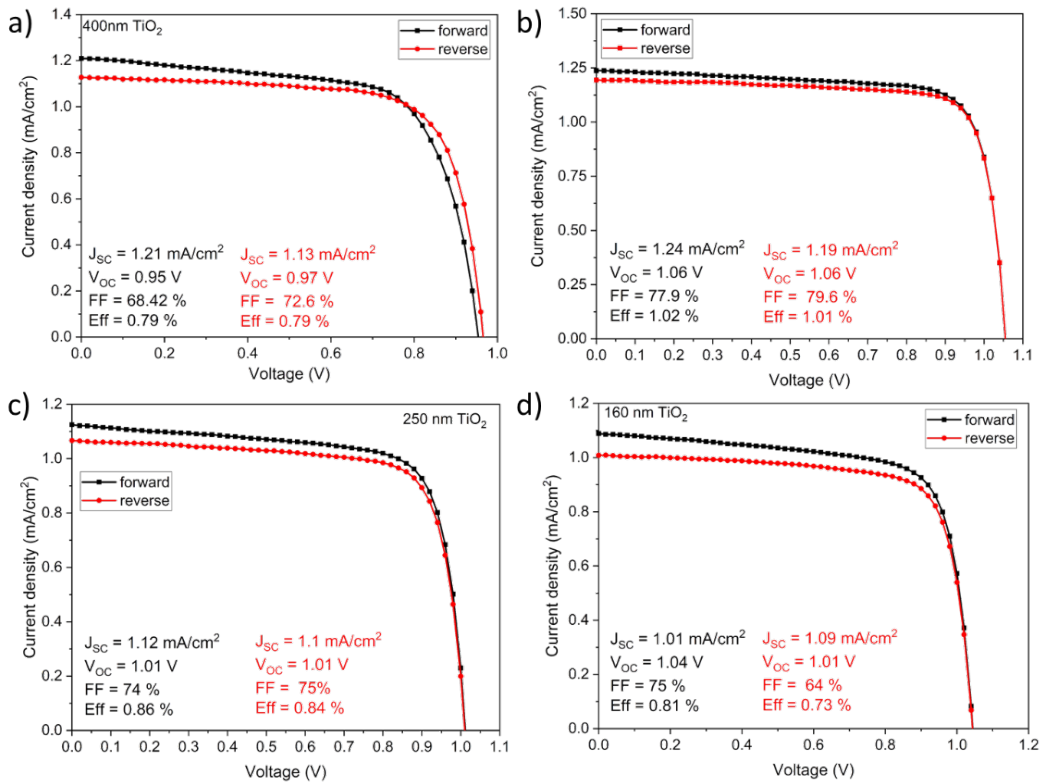


Figure 46 J-V curves of mesoporous solar cells with a) 400 nm TiO₂, b) 280 nm TiO₂, c) 250 nm TiO₂, d) 160 nm TiO₂.

Figure 47 shows the statistical distribution and all photovoltaic parameters for the 15 devices in total. The error bar, average, maximal and minimal values of each device parameter are shown.

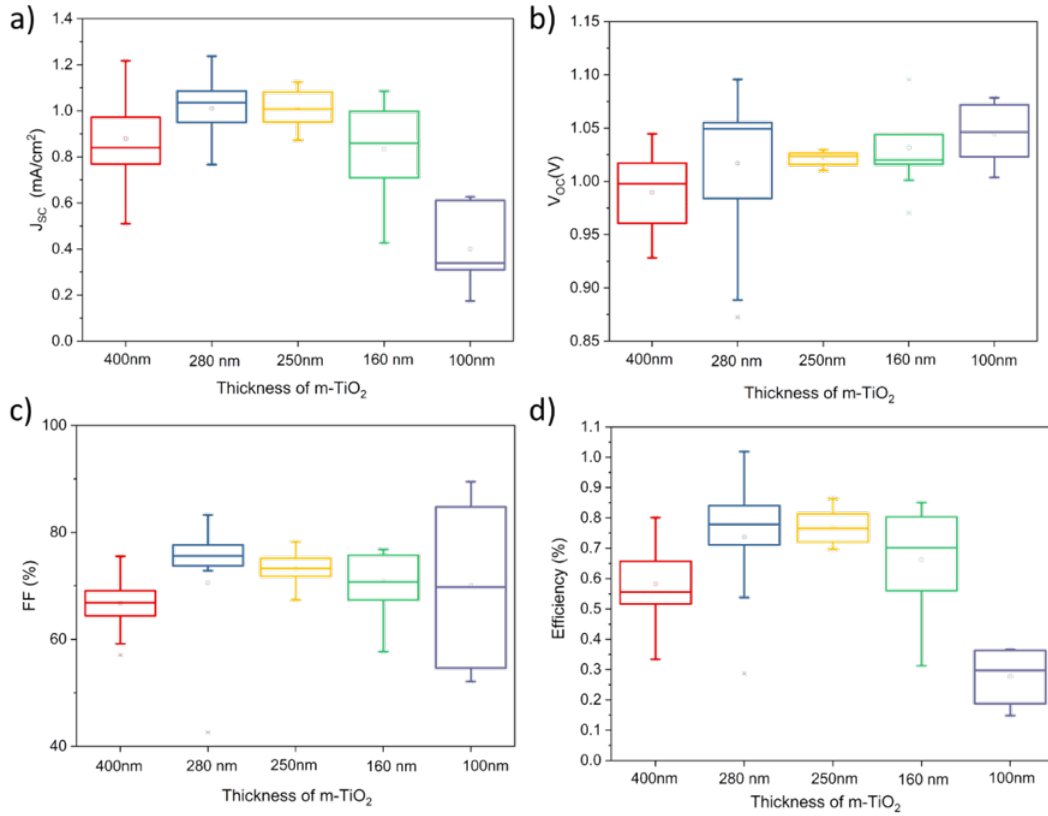


Figure 47 Statistical distribution of all prepared devices keeping the perovskite layer thickness at the same (160 nm) and changing the mesoporous layer thickness. Comparison of all photovoltaic parameters, **a)** J_{sc} , **b)** V_{oc} , **c)** FF, **d)** PCE.

After changing the thickness of the electron transporting layer, further steps have been taken using “optimal” devices with a thickness of 280 nm for ETL and a reduced thickness of the double perovskite. The double perovskite layers have been fabricated using different spin coating speeds, 4000, 5000, 6000 rpm yielding 160, 120 and 100 nm of the double perovskite layer, respectively. In Table 6 the solar cell performance for devices Nr. 6, 7, 8 is shown.

Table 6 Photovoltaic performance of mesoporous solar cells keeping the same thickness of m-TiO₂ layers (280 nm) while changing the thickness of the perovskite.

Nr	Device	V_{oc} (V)	J_{sc} (mA/cm ²)	FF	PCE(%)
6	m-TiO ₂ (280nm)/Cs ₂ AgBiBr ₆ (160 nm)/PTAA	1.01	1.20	79	1.01
7	m-TiO ₂ (280 nm)/Cs ₂ AgBiBr ₆ (120 nm)/PTAA	1.15	0.62	70	0.50
8	m-TiO ₂ (280 nm)/Cs ₂ AgBiBr ₆ (100 nm)/PTAA	1.10	0.61	70	0.46

Keeping the mesoporous layer thickness at 280 nm and reducing the perovskite layer thickness a decrease in solar cell performance can be observed. In Table 6 we see that for device Nr. 7 V_{oc} increases in the range of 1.15 V and 1.10 V with the reduction of the perovskite layer, while J_{sc} slightly decreases. The same effect is observed for device Nr 8. This may be because of poor charge extraction due to the thicker TiO₂ layer compared to a perovskite layer where the charges easily recombine in the mesoporous layer. Figure 48 shows J-V curves of devices Nr. 7 and 8. A slight decrease in hysteresis with decreasing perovskite layer thickness can be observed.

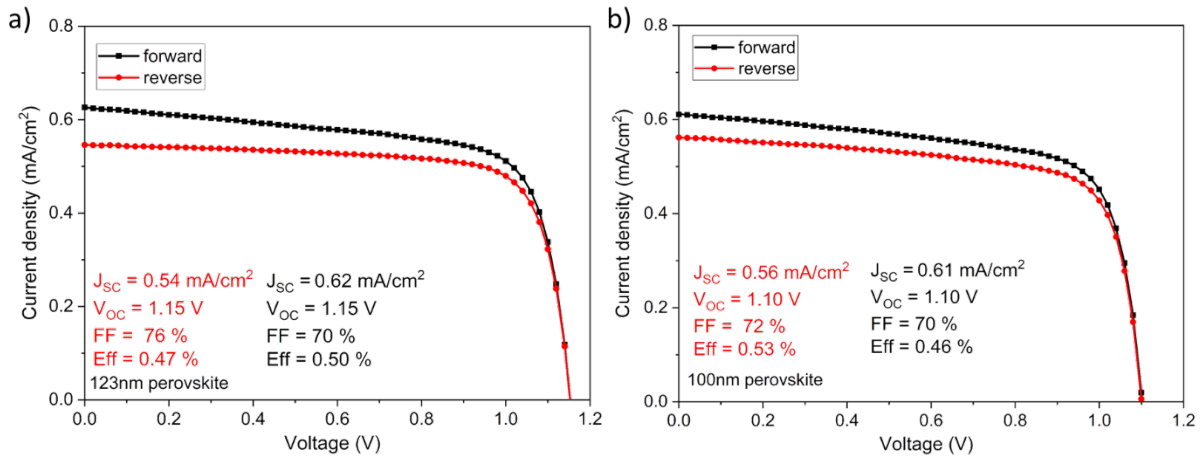


Figure 48 J-V curves of devices (7-8) with 280 nm of mesoporous layer and a) 123 nm perovskite, b) 100 nm perovskite.

A statistical distribution is provided for 9 devices and shown in Figure 49.

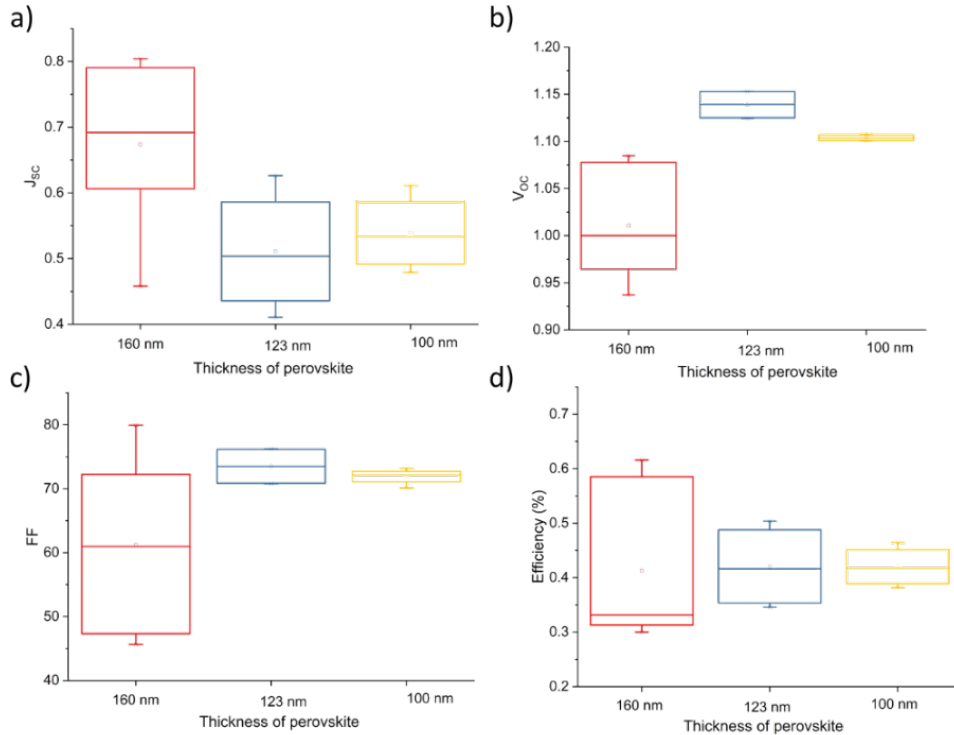


Figure 49 Statistical distribution of all prepared devices (6-8) keeping thickness of mesoporous layer at 280 nm and changing perovskite layer thickness and comparison of all photovoltaic parameters.

In the previous section we observed a decrease of the PCE keeping the ET-layer thicker than the perovskite layer. The next step in this research is to reduce ET-layer to adjust to the perovskite layer and make the devices more effective. The thickness of the ET-layer was kept at 100 nm with the lowest dispersion concentration, while the perovskite thickness has been reduced through reducing the spin coating rotation speed. As summarized in Table 7, V_{oc} hardly changes, while J_{sc} increases significantly. This means, that lowering the thicknesses of both layers yields more efficient charge extraction.

Table 7 Photovoltaic performance of mesoporous solar cells keeping the same thickness of m-TiO₂ layers, (devices 100 nm) while changing the thickness of the perovskite.

Nr	Device	V_{oc} (V)	J_{sc} (mA/cm ²)	FF	PCE (%)
9	m-TiO ₂ (100 nm)/Cs ₂ AgBiBr ₆ (160nm)/PTAA	1.07	0.61	55	0.36
10	m-TiO ₂ (100 nm)/Cs ₂ AgBiBr ₆ (120nm)/PTAA	1.12	0.83	71	0.66
11	m-TiO ₂ (100 nm)/Cs ₂ AgBiBr ₆ (100nm)/PTAA	1.10	1.00	67	0.74

The performance of the solar cells increases, showing a rise in power conversion efficiency to 0.74%. In Figure 50 the J-V curves are shown for each device are shown. In Figure 50a the hysteresis is notable. Figures 50b and 50c show a decrease of the hysteresis as the thickness gets smaller. There are several reasons concerning the different preparation parameters and mechanisms for the hysteresis being present during the J-V measurement. In this case the focus is on fabrication methods and thickness adjustments and therefore better electron collecting properties and improvement in device performance.

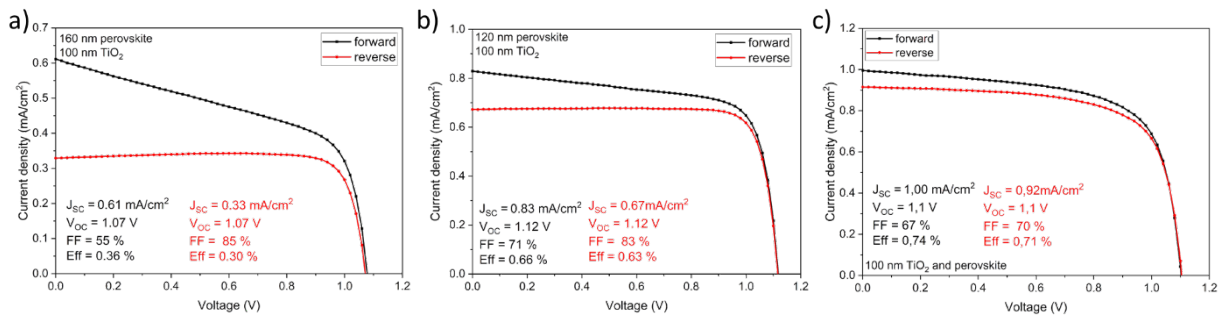


Figure 50 J-V curves of devices (9-11) with 100 nm of mesoporous layer and a) 160 nm perovskite, b) 123 nm perovskite, c) 100 nm perovskite.

Figure 50 shows a reduction of the hysteresis with reducing perovskite layer thickness while keeping the mesoporous layer at 100 nm. V_{oc} stays approximately the same, while the J_{sc} increases with lower perovskite thickness, showing effective charge separation and collection.

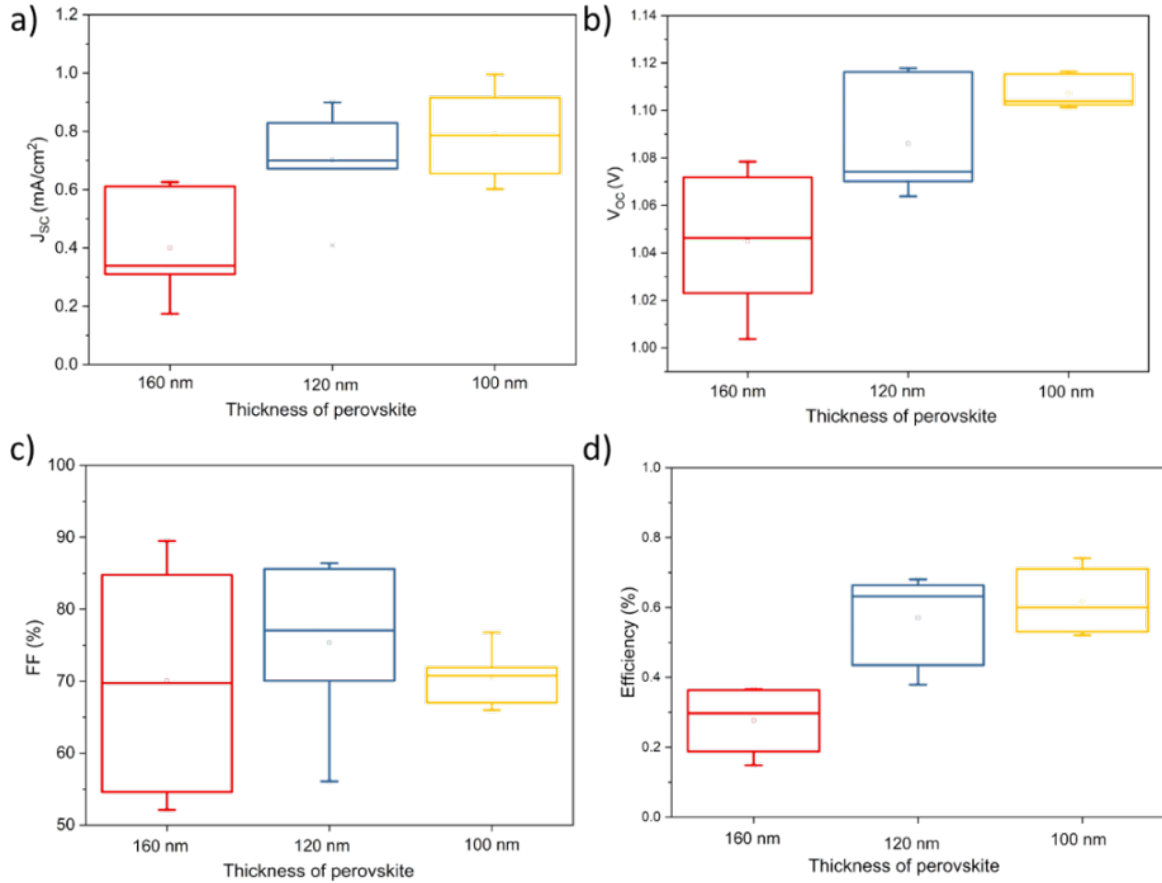


Figure 51 Statistical distribution of all devices 9-11 keeping thickness of the mesoporous layer at 100 nm and changing the perovskite layer thickness. Comparison of all photovoltaic parameters.

The statistical distribution for 9 devices shows an increase in photovoltaic parameters with decreasing layer thickness, while the fill factor remains unchanged (Figure 51).

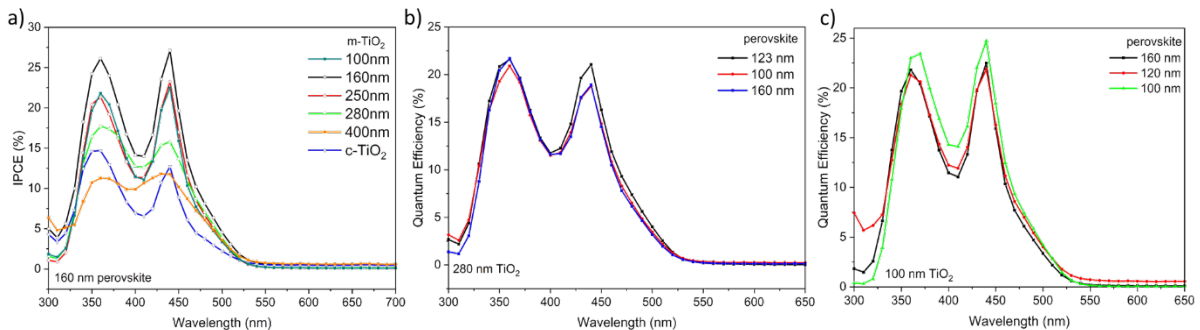


Figure 52 IPCE curves of devices **a)** (1-5) keeping 160 nm perovskite layer thickness and changing the thickness of the mesoporous TiO₂ layer, **b)** (6-8) keeping 280 nm of m-TiO₂ and changing perovskite layer, **c)** (9-11) keeping 100nm TiO₂ and changing perovskite layer.

The IPCE curves in Figure 52 show the ratio of the collected charge carriers to the number of incident photons of each specific energy illumination on the solar cell. The IPCE spectra show which spectral regions contribute to photocurrent generation: in this case the edge of the IPCE curve matches with the absorption onset at 525 nm, and in some way they follow the shape of absorption. The spectral regions of the IPCE graphs can be divided into three zones:¹³⁶ The first zone is from 320 nm to 380 nm with a peak at 355 nm and can be assign to the part of the solar cell which response to infiltrated double perovskite layer in TiO₂ electron transporting layer and shows that the photogenerated charges could be trapped near to FTO, as well explained with the maxima peak at 355 nm.

The second zone is from 380 nm to 430 nm, where the IPCE curves show an expressed dip in the middle at 410 nm. This distinct dip shows a reduction of the overall curve and can be attributed to some strong photon harvesting in the active layer or in the device itself. The very few photoelectrons in this area can be reflected, leading to weak interference in this area. It can be observed in the absorption spectra as well the same dip at this wavelength values while the strong absorption contributes to the next third zone of the spectral region. The third zone is from 430 nm to 525 nm with a peak at 450 nm. The reason for the overall generation for current with a shorter wavelengths may be due to the broad and indirect bandgap of the double perovskite. As shown in Figure 52a, the maximal value is observed for a thickness of 160 nm of m-TiO₂ (device Nr 4) while the lowest value is for 400 nm of TiO₂ and the “medium” thickness devices respond to medium EQE results. It is interesting, that the highest values of 25% correspond to the lowest thicknesses of TiO₂. This can be due to lower trapping of the charges in the ETL. Figure 52b shows different perovskite thicknesses while keeping TiO₂ constant at 280 nm. The results show no significant changes in the IPCE while there is a significant difference in the device performance, showing lower performance with thinner perovskite layer. Figure 52c shows an increase in IPCE with lower perovskite thickness which corresponds to an improvement in device performance. The highest EQE is observed for 160 nm of TiO₂ and 160 nm of perovskite reaching 28%. For the solar cells with 100 nm of TiO₂ and 100 nm of perovskite 25% EQE are reached at 450 nm.

4.3.2.2. Interface Engineering

Following the investigation and optimization of layer thickness, a detailed engineering of the mesoporous double perovskite solar cells will be shown. This has been realized by fine-tuning the material deposition parameters, thereof different temperatures for annealing, thicknesses of the mesoporous layers, ozone and TiCl₄ treatments of the mesoporous layers to improve better infiltration of double perovskite solution into the mesoporous TiO₂ and to enable the growth of a highly uniform and compact Cs₂AgBiBr₆. For this purpose, different materials have been used and investigated for engineering the device interfaces by screening different molecular and polymeric hole- and electron-transporting materials. All materials used for device engineering, as well as their energy levels, are schematically shown in Figure 53. To align and investigate the best energy levels of materials in combination with the double perovskite Cs₂AgBiBr₆, both sides of the active layer, the electron transporting and the hole transporting parts have been investigated in detail. By this kind of surface engineering and solar cell optimization more than 300 devices have been prepared in total. Finally, the optimal preparation conditions of double perovskite solar cells with champion power conversion efficiency have been found and will be discussed in the following.

In Figure 53 the structure of C70 as an electron acceptor and the structures of the hole transporting materials NiO_x, PTAA, Spiro-OMETAD, and PCPDTBT are shown.

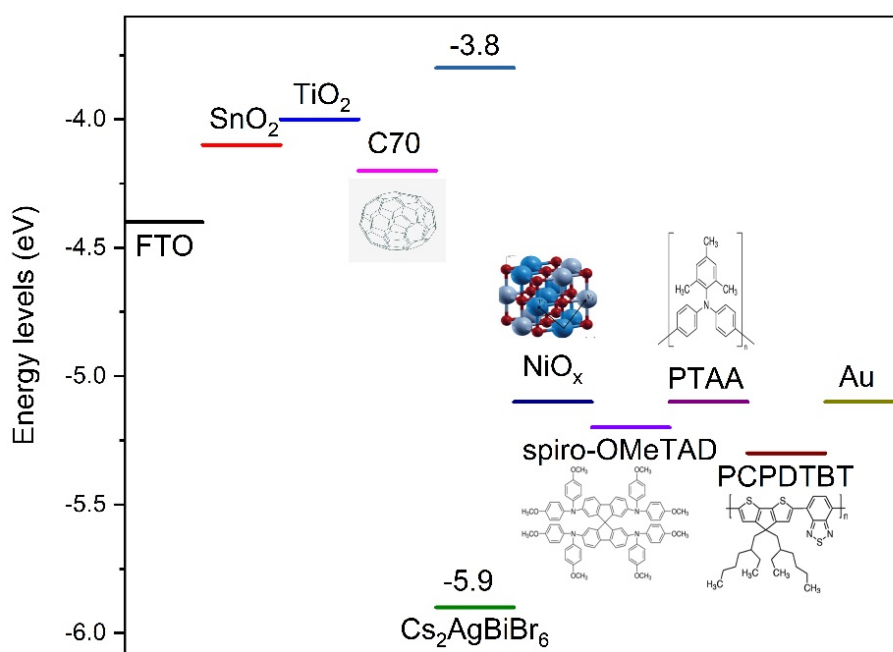


Figure 53 Energy level diagram of all materials used for device optimization and engineering.

The following part has been taken with permission from ACS Energy Letters where this research has first been published. It includes all discussion parts combined with supplementary information, is ordered in a chronological fashion, and is expanded by some general information on experiments and used materials. (e.g. PCPDTBT).

The incorporation of double perovskite Cs₂AgBiBr₆ in PSC as an active layer has so far been very limited, mainly because of the challenge in the preparation of high-quality and compact double-perovskite thin films. Although Cs₂AgBiBr₆ perovskite meso-structure solar cells with a PCE close to 2.4% have been shown by Greul et al.,⁷⁴ this value was extracted from a device characteristic severely affected by a huge hysteresis and s-shape, which casts some doubt on the real device performance. In addition, they adopted a fast crystallization process, which impedes the formation of a smooth and homogeneous Cs₂AgBiBr₆ layer. Micrometer-sized grains and a thick agglomerated morphology are formed on the capping layer, which is far from the ideal morphology for a clean interface with the HTM in the sandwiched PSC. In this work, a different strategy has been adopted for the optimization of a facile and highly reproducible deposition protocol to obtain a 200 nm thick homogeneous Cs₂AgBiBr₆ capping layer in the meso-structure solar cell architecture. Furthermore, different HTMs have been screened beyond the most used spiro-OMeTAD to optimize the perovskite/HTM interface and device parameters. As a result, a lead-free PSCs with no hysteresis in the device characteristic has been fabricated leading to a real PCE beyond 1% with high fill factor (FF) up to 0.7. It is supposed that this approach will enable surpassing the current limits in lead-free double-perovskite technology, opening the way for massive device optimization in the near future. The Cs₂AgBiBr₆ film has been deposited by using spin coating deposition of a solution of 0.5 M Cs₂AgBiBr₆ in dimethyl sulfoxide (DMSO) and annealing at high temperature. The film growth and crystal quality were monitored, while varying the annealing temperatures in the range of 250–280 °C for 5 min. Figure 54a reports on the X-ray diffraction (XRD) pattern of the double perovskite Cs₂AgBiBr₆ deposited on mesoporous TiO₂ (m-TiO₂)/FTO substrate. A main peak at 31.8° is present, representative of the (400) reflection of the double perovskite Cs₂AgBiBr₆, along with other main reflections (111, 200, 220, 311, 222, and 331). This pattern is evident for all temperature ranges used, providing solid proof for the successful formation of a phase-pure double perovskite at a temperature greater than 250 °C. (Figure 54) Notably, no additional peaks related to possible residuals of Cs₃Bi₂Br₉ or AgBr have been observed. In addition to the high temperature, we also introduced a few other control parameters to drive the material

crystallization, aiming to obtain a homogeneous film with high crystal quality.¹³⁷ In particular, we adopted a second step in the deposition, known in the standard perovskite method as an antisolvent dropping technique. In this case, we dropped chlorobenzene during the film formation before the annealing step, aiming to obtain a compact and homogeneous layer without any pinholes.

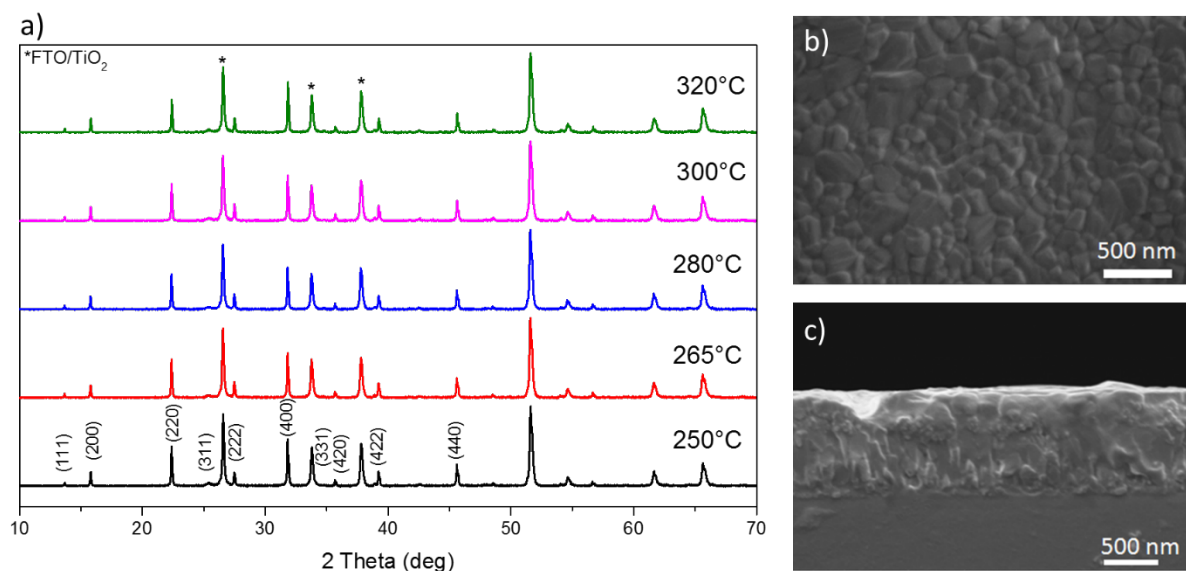


Figure 54 a) X-ray diffraction (XRD) pattern of Cs₂AgBiBr₆ thin films deposited on mesoporous TiO₂ substrate at different annealing temperatures as indicated in the legend. Scanning electron microscopy (SEM) images of, b) top view of the double-perovskite layer obtained upon spin coating at room temperature using the anti-solvent treatment with chlorobenzene and c) cross section of the FTO/c-TiO₂/m-TiO₂/ double perovskite sample, upon annealing at 280 °C.

Overall, the optimization protocols enable the realization of a 200 nm thick Cs₂AgBiBr₆ film that shows a smooth and compact double-perovskite layer with an average grain size of around 80 nm, as shown from the top surface of the scanning electron microscopy (SEM) image in Figure 54b. This achievement represents a step forward in the optimization of the double-perovskite morphology, which has highly challenged the community in the last year. This is especially relevant when compared to the state-of-the-art samples showing a dishomogenous and disconnected island-like morphology.⁷⁴ As the Cs₂AgBiBr₆ films were optimized for photovoltaics, a sufficiently thick material is mandatory for efficient harvesting of light. To optimize the optical absorption, i.e. the thickness of the film, the infiltration of the double-perovskite solution in the mesoporous oxide nanoparticle scaffold was improved by modifying the m-TiO₂ surface. The surface was pre-treated by ultraviolet (UV)-ozone for 15 min and by

an additional TiCl₄ treatment. This led to an overall change in the surface properties of m-TiO₂, further improving the material infiltration and crystallization as shown by the SEM cross-sectional image in Figure 54c. Improving the material morphology is an essential step to reduce pinholes and paths for charge recombination.¹³⁸ Overall, in our case, the optimal combination of the mentioned modifications and adjustments, such as UV-ozone and TiCl₄ treatment¹³⁹ on TiO₂, preheating solution at 75 °C before coating, antisolvent dripping technique on the spinning double-perovskite layer,¹⁴⁰ along with the annealing at high temperatures, enabled the realization of a compact film of Cs₂AgBiBr₆ for the first time. Notably, the choice of the used solvent also impacts the results obtained; indeed, the use of different concentrations of DMF and DMSO can result in a dishomogenous morphology (Figure 55 c,f). The inclusion of the preheating step turned out to also be of fundamental relevance for thin-film optimization (Figure 55).

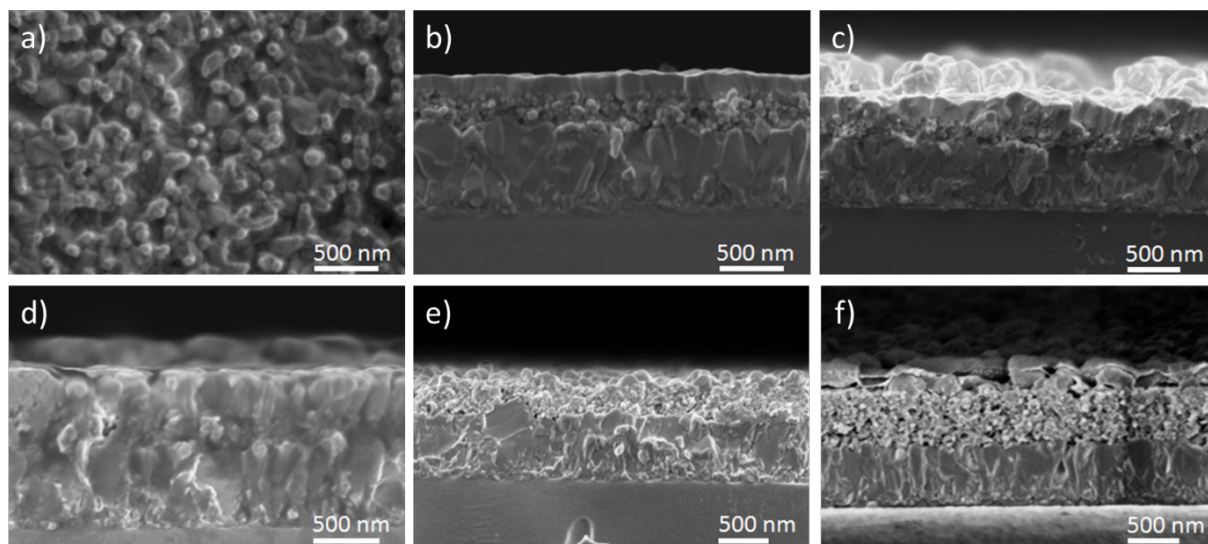


Figure 55 Double perovskite layer optimization and optimization of infiltration of double perovskite solution into mesoporous TiO₂; **a**) room temperature deposition and annealing at 220°C, **b**) cross-section of FTO/cTiO₂/mTiO₂/double perovskite, to low concentration of m-TiO₂ and no infiltration into m-TiO₂ layer, **c**) using double perovskite dissolved in DMF (0.16M) as 1st step deposition step and double perovskite dissolved in DMSO (0.5M) as 2nd step deposition step, **d**) ozone treatment on m-TiO₂ for 15min before spin coating of double perovskite, **e**) lower concentration of double perovskite dissolved in DMSO, **f**) TiCl₄ treatment.

Figure 56 reports on the optical characterization of the Cs₂AgBiBr₆ thin film in terms of optical absorption and emission properties. Absorption spectra are reported in Figure 56a. From the Tauc plot a step profile is observed, with a first onset at around 2.4 eV. In the inset, the Tauc plot considering a direct band gap transition is also shown, giving a value for band gap of 2.20 eV, similar to what was already observed for Cs₂AgBiBr₆ thin films.¹²⁰ The retrieved band gap value is consistent with that reported in literature, within a variation range due to the different

deposition approach used.¹²⁰ It is fair mentioning that, according to the Shockley–Queisser limit, a theoretical maximum PCE of 16.4% can be targeted with a material having an E_g of 2.2 eV, thus showing huge potential for working double-perovskite-based solar cells.⁷⁴ The Cs₂AgBiBr₆ emission results (emission efficiency) are weak because of the indirect band gap nature of the material. The PL spectrum peaking at 2.1 eV is shown in Figure 56b. The signal is very low in intensity due to the indirect band gap nature of the material. To assess the fate of the photogenerated carriers, we measured the time-resolved PL decay, shown in Figure 56c, monitored at the emission peak. The PL intensity shows a fast initial drop (fitted with $\tau_1 = 5$ ns), followed by a slower one ($\tau_2 = 282$ ns), which is similar to what is observed for double-perovskite thin films.¹²⁰ Notably, the fast decay is associated with trap and/or surface-state emission, which, given the weak PL signal, dominates in this case. On the other side, the longer-lifetime processes may originate from fundamental charge recombination, in agreement with the long carrier lifetime extracted in Cs₂AgBiBr₆ single crystals, which in this case is much longer than that of standard methylammonium lead iodide-based perovskites.¹²⁰

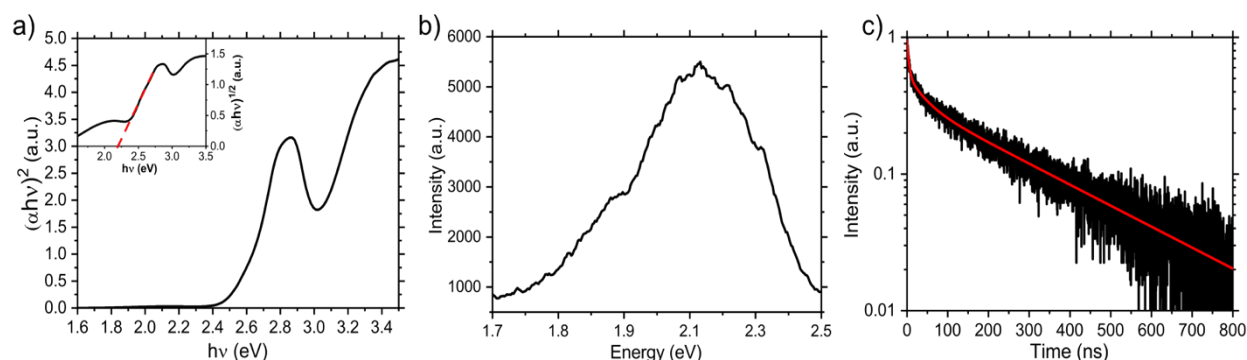


Figure 56 a) Absorption spectrum plotted in the form of Tauc plot, for an indirect bandgap, of the Cs₂AgBiBr₆ thin film deposited on glass (black). Inset: the Tauc plot for a direct bandgap with the dashed red line representing the linear fit for the band edge estimation. b) Photoluminescence (PL) spectra of the Cs₂AgBiBr₆ thin film. c) PL decay monitored at 2.1 eV. The decay is fitted using a bi-exponential function, resulting in fitted time constants of $\tau_1 = 5$ ns and $\tau_2 = 282$ ns (red).

Figure 57a shows the efficiency of solar cells prepared at different annealing temperatures for the double perovskites. The efficiency decreases for the highest annealing temperature. Thus, the optimal annealing temperature for the formation of double perovskites maintaining higher efficiency is between 265 °C and 280 °C. The solar cell performance also increases when using a higher concentration of mesoporous TiO₂ dispersed in EtOH. As is shown in Figure 57b, the optimal concentration of m-TiO₂ is 1g/4mL of EtOH. For better precipitation of the double

perovskite out of the solution into compact and smooth films, the use of anti-solvent treatment is desirable for higher solar cell performance. (Figure 57c)

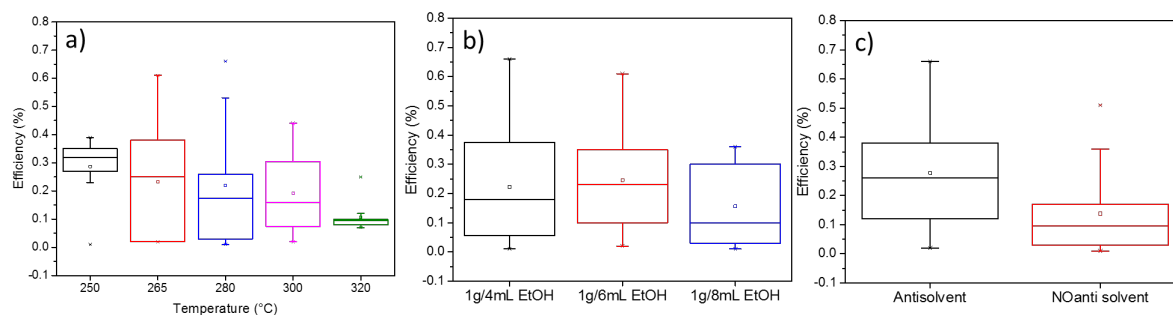


Figure 57 Device statistics on optimized layers, power conversion efficiency of solar cells; a) using different annealing temperatures (250-320°C) the Cs₂AgBiBr₆ double perovskite layer, b) using different concentrations of m-TiO₂ dispersed in EtOH, c) using antisolvent (chlorobenzene) and non-antisolvent treatment.

Using the optimized perovskite layer, the author fabricated solar devices in which the perovskite is sandwiched between the 2,2',7,7'-tetrakis(N,N-dimethoxyphenylamine)-9,9'-spirobifluorene (spiro-OMeTAD) hole-transporting material and the mesoscopic TiO₂ scaffold (m-TiO₂) electron transporter in a standard mesoporous architecture. As known from literature⁷⁴ and represented in Figure 59a, the energy level diagram shows that the conduction band (CB) of Cs₂AgBiBr₆ is well-aligned with the CB of the electron transporting mesoporous TiO₂. Aiming to improve the device performance, we explored a series of different molecular and polymeric HTMs having slightly different highest occupied molecular orbital – lowest unoccupied molecular orbital (HOMO–LUMO) values, as shown in the energy diagram in Figure 59a. In addition to spiro-OMeTAD, typically used for lead perovskite solar cells, we considered PTAA (poly[bis(4phenyl)(2,4,6-trimethylphenyl)amine]) and PCPDTBT (poly[[2,1,3-benzothiadiazole-4,7-diyl][4,4-bis(2-ethylhexyl)-4Hcyclopenta[2,1-b:3,4-b']dithiophene-2,6-diyl]]), which are used in the PSC literature as polymeric HTMs.^{141,142}

PCPDTBT is a polymer material used in hybrid solar cells, i.e. metal oxide – polymer bulk heterojunction. The reason behind choosing PCPDTBT¹³³ is its low HOMO level compared to other HTMs. Because of that it can be more compatible with the HOMO level of the Cs₂AgBiBr₆ double perovskite. Furthermore, PCPDTBT is a good material for photovoltaic application, because it possesses a lower bandgap around 1.7 eV leading to light harvesting in the near-infrared region and high hole mobility. Absorption spectrum data visualized in Figure 58a show

that the absorption of the layer-on-layer combination with double perovskites exceeds those from just regular PCPDTBT, thereby potentially improving solar cell performance. The absorption spectrum of PCPDTBT film (blue line) shows two peaks, one at 1.8 eV and another at 3.0 eV. The absorption spectra of the Cs₂AgBiBr₆ films show a peak at 2.8 eV with an absorption onset at 2.2 eV. The change in the absorption spectra is showing two peaks at 2.8 eV and 1.8 eV leading in total to broader absorption region. The same behavior can be seen in the photoluminescence spectra in Figure 58b, where the peaks shift by 0.1 eV, if a contact between DP and PCPDTBT is present. The films have been prepared using sequential deposition first of double perovskite on glass and annealing, followed by deposition of the PCPDTBT. The attempt of using the blend solution by mixing the double perovskite solution with the PCPDTBT solution resulted in agglomeration and particle segregation due to the solvents in which each material had been dissolved.

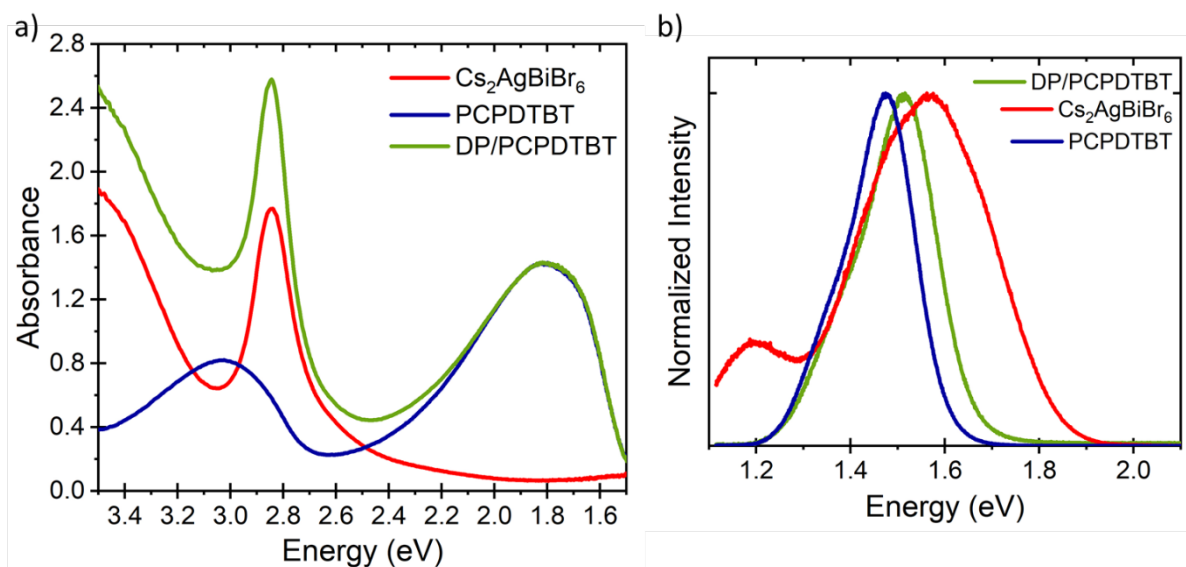


Figure 58 a) absorbance of double perovskite and PCPDTBT layer, b) photoluminescence intensity of double perovskite and PCPDTBT layer.

The current–voltage (J – V) characteristics of the solar cells under simulated air mass 1.5 global standard sunlight (AM1.5G) are reported in Figure 59b, and the device parameters are summarized in Table 8. The best solar cell performance resulted from using PTAA as HTM. A short-circuit current (J_{sc}) of 1.84 mA/cm² and an open-circuit voltage (V_{oc}) of 1.02 V were obtained (Table 8).

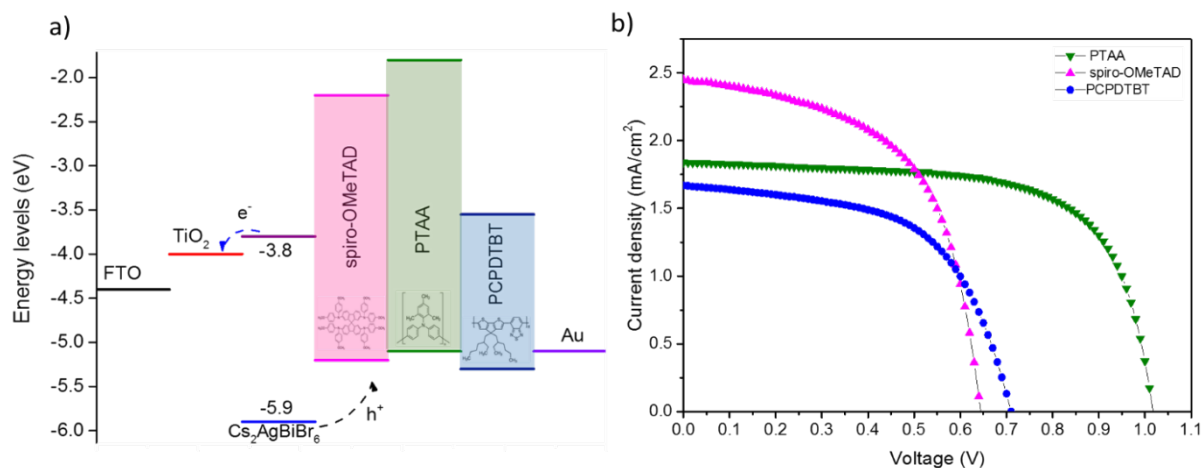


Figure 59 a) Scheme of corresponding energy level diagram with the following energy values: FTO (-4.4 eV), TiO₂ (-4.0 eV), Cs₂AgBiBr₆ (HOMO, -5.9 eV; LUMO, -3.8 eV), spiro-OMeTAD (-5.2 eV, -2.2 eV), PTAA (-5.1 eV, -1.8 eV), PCPDTBT (-5.3 eV, -3.55 eV) and Au (-5.1 eV); b) J-V curves for best-performing solar cells using different HTMs.

Table 8 Photovoltaic parameters of devices based on the different HTMs; Short-circuit current density (J_{sc}), Open-Circuit Voltage (V_{oc}), Fill Factor (FF) and Power Conversion Efficiency (PCE). Notably, device statistics has been conducted on 44 devices (spiro-OMeTAD), 27 devices (PTAA), 6 devices (PCPDTBT).

HTM	J_{sc} (mA/cm ²)	V_{oc} (V)	FF	PCE (%)
PCPDTBT	1.67	0.71	0.57	0.68
spiro-OMeTAD	2.45	0.64	0.57	0.90
PTAA	1.84	1.02	0.67	1.26

The spiro-OMeTAD-based solar cells show reasonable J_{sc} and V_{oc} values of around 0.64 V (0.8 V in the best case). It is noteworthy that the high V_{oc} value is obtained despite the similarities in the HOMO levels between spiro-OMeTAD, PCPDTBT, and PTAA, and that the value of the latter is slightly higher for the lastest.¹⁴³ Although the interface energy level alignment represents a useful rule of thumb for screening the best HTM and evaluating the device V_{oc} , a direct link between HTM energy levels and device V_{oc} cannot be derived unambiguously. This is because the device V_{oc} is affected by multiple parameters which simultaneously come into play. Interfacial energy level mismatch, any possible internal electric field established by the difference in the work functions of the interfacial layers, interface charge accumulation, and bulk charge recombination can all affect V_{oc} . Importantly, these parameters are highly sensitive to the perovskite crystal quality and film morphology.^{144,145} There are many possible parameters and processing routes affecting the V_{oc} which would extend beyond the scope of this work. The

fundamental statement derived here is that the optimization process of the perovskite film itself—modifying the perovskite crystal quality, grain boundaries, and film homogeneity—strongly influences V_{oc} (Figures 55, 57 and 60a). For instance, as shown in Figure 60a, when a device is prepared using the perovskite film without the antisolvent dropping step but keeping PTAA as HTM, a remarkable drop in the device V_{oc} is observed despite the same interfacial energy level alignment and device architecture. The incident photon to current conversion efficiency (IPCE) spectrum (Figure 60b) shows a band edge at ~ 525 nm, which is in agreement with the absorption edge in Figure 2a.

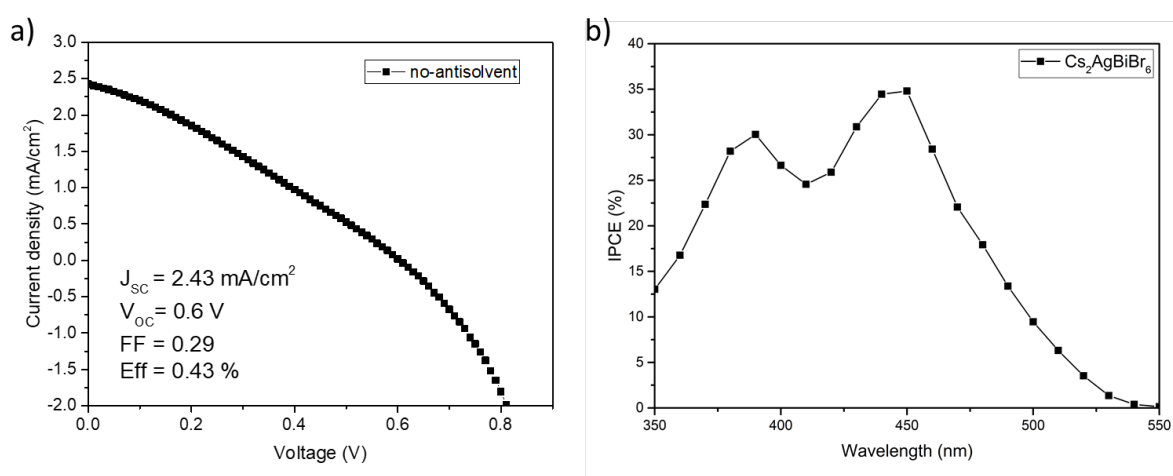


Figure 60 a) J-V curve for solar cells without antisolvent treatment and PTAA as HTM, b) IPCE spectrum of champion Cs₂AgBiBr₆ perovskite solar cells with PTAA.

On the other side, PCPDTBT-based solar cells show a reduced voltage as well as a reduced photocurrent compared to other HTM solar cells. This can result from the lower band gap of PCPDTBT and the lower LUMO level, which can decrease the charge-transfer selectivity. Overall, this suggests that not only the interface energetics but also the interface quality and photo-induced processes, such as charge recombination, are of the high importance for optimizing the device performance. Device results are confirmed based on the statistics of around 70 devices, as shown in Figure 61 a-d.

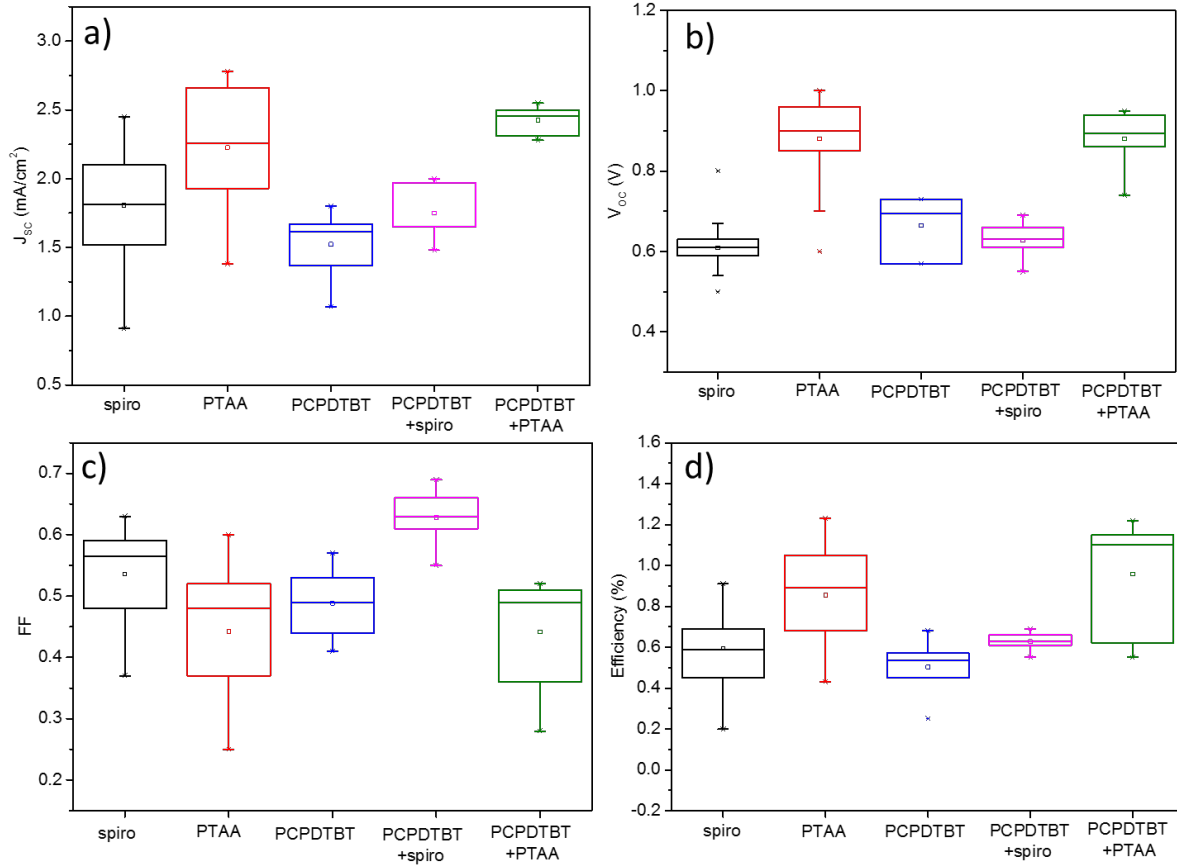


Figure 61 Statistical distribution of photovoltaic parameter for perovskite solar cells performance with different HTMs; **a)** short circuit current J_{sc} , **b)** open-circuit voltage V_{oc} , **c)** fill factor FF, **d)** power conversion efficiency.

An important characteristic that must be evaluated when measuring perovskite solar cells is the shape of the J–V curve measured at different scanning voltage directions. Indeed, for lead-based perovskites, as well as for previously reported Cs₂AgBiBr₆-based solar cells,⁷⁴ a significant difference has been observed, which is indicative of a hysteresis behaviour. Although the exact reasons behind this behaviour are subject of an ongoing debate, it is the general consensus that effects such as light-induced ion movement, “photo-instability”, or structural deformations can overall contribute to the anomalous hysteresis behavior.^{146–149} Even for Cs₂AgBiBr₆, this has been previously assigned to ion and defect movement in the device, despite the totally different material structure and composition.⁷⁴ Figure 62 shows the J–V hysteresis for devices using PTAA as HTM. Notably, a device shows a hysteresis-free behaviour, with nearly identical values for the device parameters extracted in the back and forward configurations. This contrasts to what has been shown by Greul et al., who reported a tremendous hysteresis due to migration of the halide anions and trapping–detrapping of charge carriers.⁷⁴ We observe a

different behaviour: as shown in Figure 62, no difference in carrier collection during the forward and reverse scan is observed, leading, for the first time, to the observation of a hysteresis-free device behaviour in lead-free double-perovskite solar cells. The author ascribe this to the ideal and compact film structure and morphology which have been obtained, which can reduce the material structural stability.

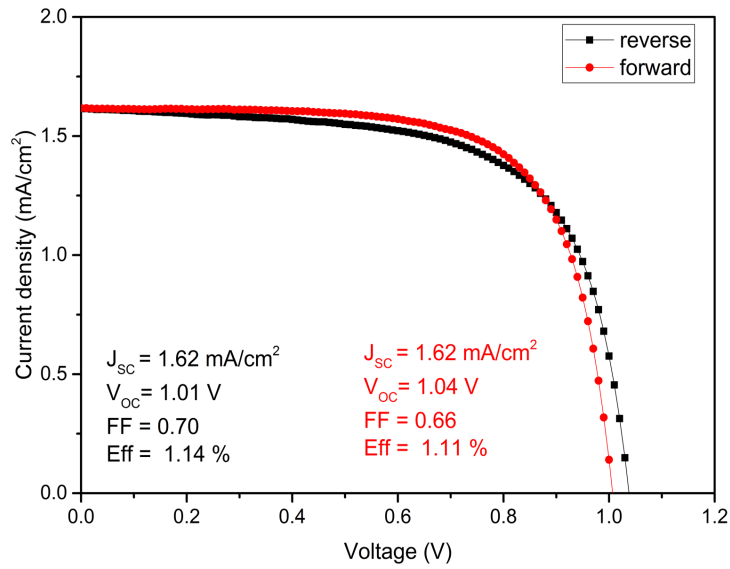


Figure 62 J-V curve of hysteresis free double perovskite solar cell..

Going beyond the usage of single polymeric HTMs, the next step was to combine PTAA and spiro-OMeTAD with PCPDTBT, by depositing PCPDTBT followed by an other HTM layer on top of the perovskites. In Figure 63a all J-V curves of these solar cells are shown next to their performance values. The best solar cells were made from the two compositions including PTAA, reaching PCE values of 1.22% and 1.26%, which also are the highest values for PCE measured during this thesis.¹

¹ End of the published article (Pantaler et al.⁸²)

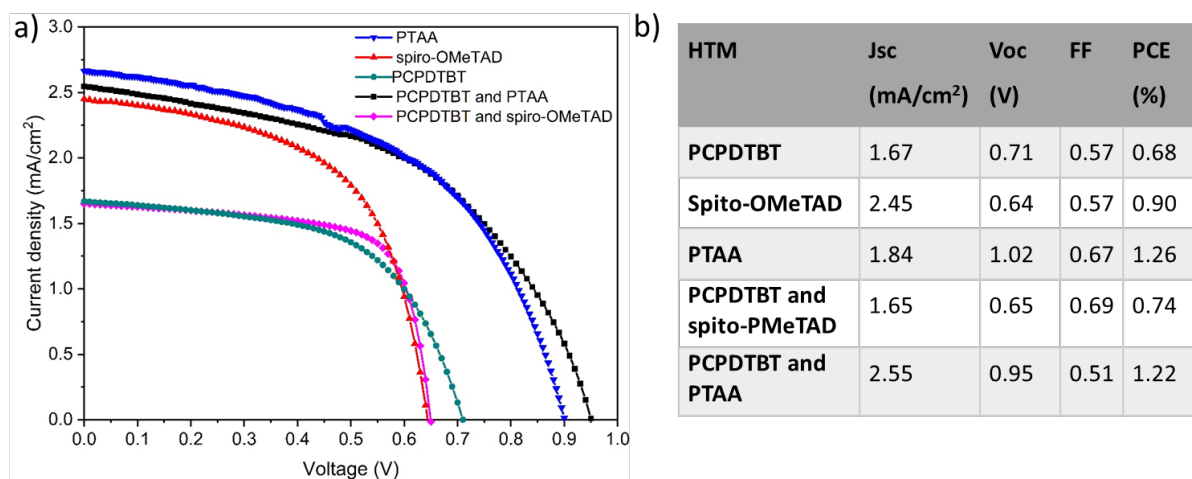


Figure 63 a) J-V curves for best performance solar cells using different HTMs, b) Photovoltaic parameters of devices based on the different HTMs related to graph: Short-circuit current density (J_{sc}), Open-Circuit Voltage (V_{oc}), Fill factor (FF) and Power Conversion Efficiency (PCE).

The images in Figure 64a show the solar cells and the cross-sectional SEM image of the most efficient device (Figure 64b).

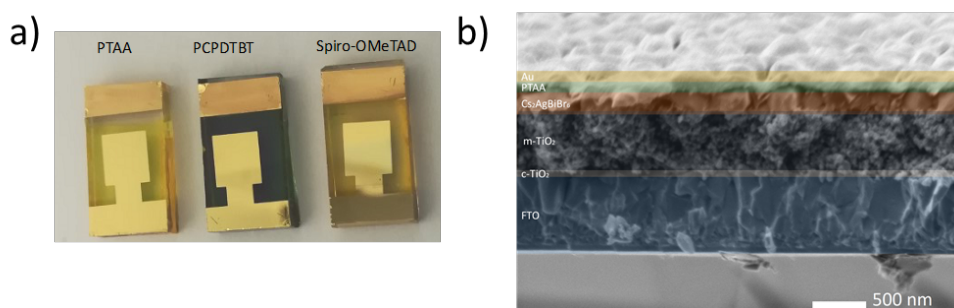


Figure 64 a) Devices of double perovskite solar cells using different HTMs b) Cross-section of optimized double perovskite solar cells using PTAA as HTM.

Apart from optimizing the HTM part of the double perovskite solar cell and modifying and optimizing the m-TiO₂ surface to improve solar cell performance, the author used C70 molecules to improve the electron transporting part of the solar cell device. Fullerenes have been used in perovskite solar cells showing several beneficial properties, e.g. reducing hysteresis, blocking ion migration, reducing the interfacial charge accumulation, reducing the trap density in the perovskite film.¹³³ The C60 is usually used in inverted planar perovskite solar cells as the electron transporting material and in the hybrid solar cells for surface functionalization as a way to photoactivate the polymer on top of the mesoporous layer in the

heterojunction. C70 has also been used in photovoltaic application. The absorbance spectra of C60 and C70 are shown in Figure 65, where the C70 absorption spectra show absorption onset at higher wavelengths. To improve electron extraction and transfer, the author modified the m-TiO₂ surface by functionalization with C70 fullerene. A C70 solution was prepared in an *o*-xylene (Sigma-Aldrich, 1,2-Dimethylbenzene) solution and stirred overnight.¹⁵⁰ The attempt of blending double perovskite Cs₂AgBiBr₆ with a small amount of C70 electron accepting molecules resulted in the agglomeration of particles due to different solvents of the starting solutions. Therefore, the layer on layer approach was used in any further experiments. The devices have been prepared by deposition of thin layers of C70 on top of the m-TiO₂ using two-step spin-coating method starting at 1000 rpm for 10 s and followed by a step at 4000 rpm for 30s. The perovskite has been deposited on top of the C70-layer. All layers were deposited by the standard method for mesoporous solar cells described in 4.1.2.

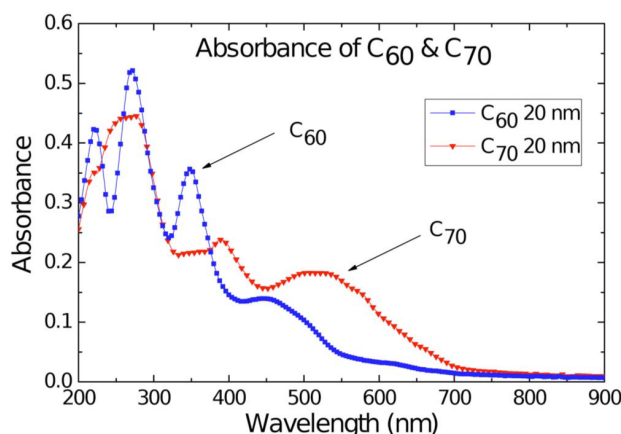


Figure 65 (Color online) Absorbance spectra of C60 (filled squares) and C70 (filled upside-down triangles) in a range of 200–900 nm. Enhanced absorption of a wide spectral range is observed for C70 compared to C60.¹⁵¹

The following solar cell fabrication has been conducted with and without different surface modifications shown in Table 9. C70 has been deposited on the m-TiO₂ for the first 4 devices without applying any mesoporous layer modifications. The solar cell performance was poor and, surprisingly, the solar cells using PCPDTBT as HTM show better solar cell performance than the devices with PTAA or spiro-OMeTAD, which showed better performance without using C70. To additionally modify the m-TiO₂ surface, the author used TiCl₄ treatment as one solution, and antisolvent treatment as another solution applied on top of the perovskite layer. A significant change can be observed, as the efficiency reaches a value of 0.89 %. The J-V curves are shown in Figure 66, where a) represents the device with antisolvent treatment and b)

represents the device using the TiCl₄ treatment. The J-V curve is broader with better cell performance. Figure 67 shows a cross section of the device using C70 and PCPDTBT.

Table 9 Photovoltaic parameters of C70 solar cells.

Device	J _{sc} (mA/cm ²)	V _{oc} (V)	FF	PCE (%)
m-TiO ₂ /C70/Cs ₂ AgBiBr ₆ /PCPDTBT/spiro-OMeTAD	1.00	0.9	0.46	0.41
m-TiO ₂ /C70/Cs ₂ AgBiBr ₆ /PCPDTBT/PTAA	2.26	0.5	0.37	0.42
m-TiO ₂ /C70/Cs ₂ AgBiBr ₆ /spiro-OMeTAD	0.80	0.7	0.48	0.28
m-TiO ₂ /C70/Cs ₂ AgBiBr ₆ /PTAA	1.00	0.7	0.37	0.29
m-TiO ₂ /TiCl ₄ /C70/Cs ₂ AgBiBr ₆ /PTAA	1.50	0.99	0.60	0.89
m-TiO ₂ /C70/Cs ₂ AgBiBr ₆ /Anti-solvent/PTAA	1.37	0.86	0.44	0.51

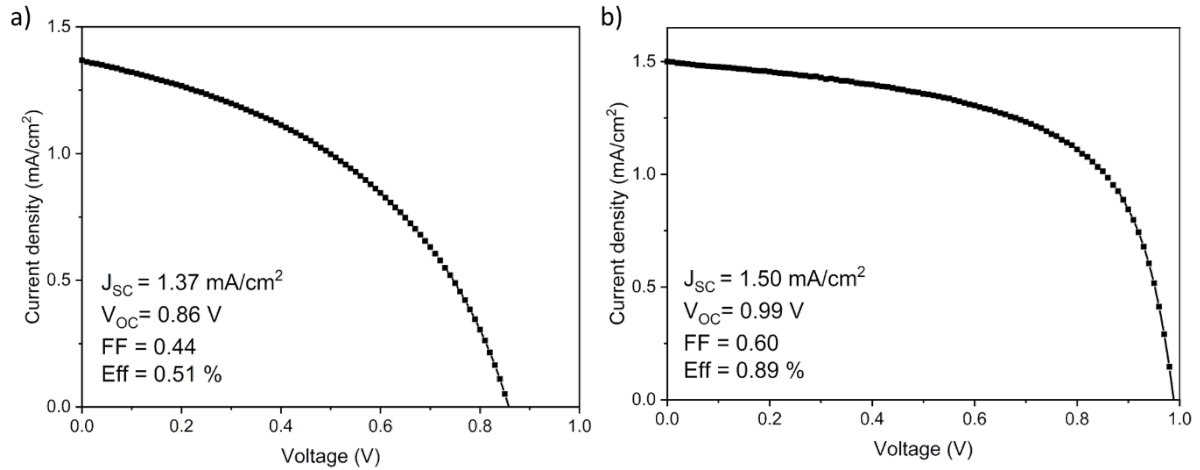


Figure 66 J-V curves of devices using C70 on top of the mesoporous layer with **a)** the anti-solvent and **b)** the TiCl₄ step and PTAA.

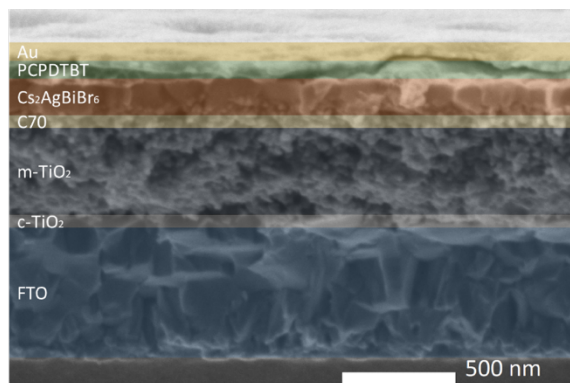


Figure 67 Cross-section of double perovskite solar cells using C70 and PCPDTBT.

A further observation made during the optimization process is that the best solar cell performance was achieved when using hole transporting materials with broader difference

between HOMO and LUMO. This can be due to the suppression of the charge carrier recombination at the interface, leading to higher open circuit voltage. Still, this is not the maximal Voc, which can be extracted from the solar cells using Cs₂AgBiBr₆ (HOMO, 5.9 eV; LUMO, 3.8 eV). Because of possible recombination when using standard HTMs, in the following part the author used new carbazole based HTMs with different polymer structure and broader bandgap to improve Voc and solar cell performance in general (Table 10).

Table 10 Energy levels of new HTMs.

HTM	HOMO, eV	LUMO, eV	E _g , eV
PTAA	5.1	1.8	3.3
PNPBC = 3-Phenyl-N-phenyl bis(carbazole)	5.6	1.6	4.0
NPBC = N-Phenyl bis(carbazole)	5.7	2.1	3.6

The hole transporting layers have been deposited using the one-step deposition method by spin coating the perovskites at 4000 rpm for 30 seconds. The whole device preparation followed the standard procedure. In Figure 68 the J-V curves are shown using new HTMs. The best performances are related to solar cells using PNPBC with a bandgap of 4.0 eV (b) while J-V curves of solar cells with NPBC show a significant hysteresis and lower performance. The LUMO level of NPBC is lower when compared to PTAA and PNPBC, and although the HOMO level matches Cs₂AgBiBr₆ better, the performance is worse. A direct comparison of the best PTAA solar cells is summarized in Table 11. The solar cells using PNPBC reach the highest J_{sc} value of 1.26 mA/cm², yet still have an efficiency value of below 1%.

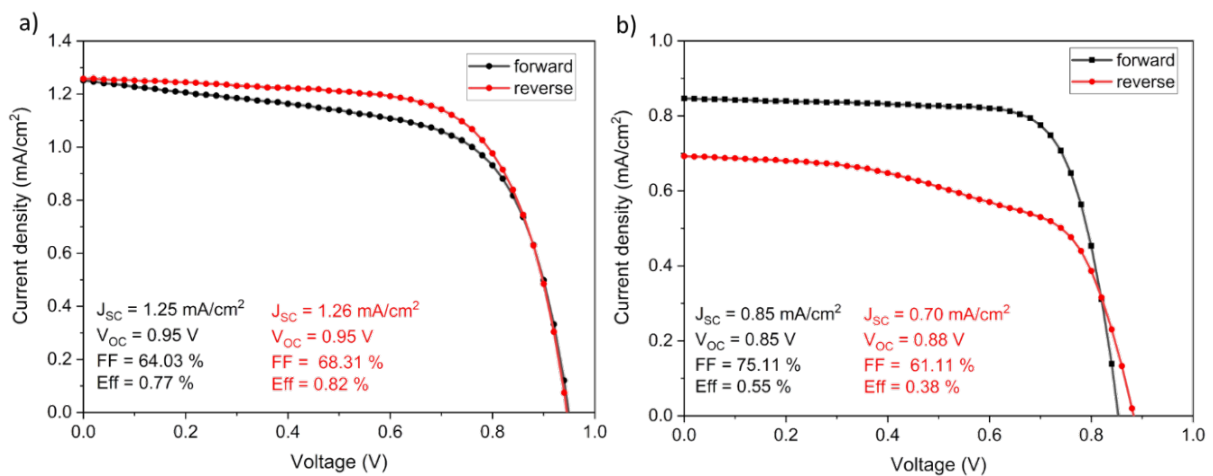


Figure 68 J-V curves of solar cell performance for a) PNPBC and b) NPBC.

Table 11 Solar cell performance for new HTMs.

Nr	Device	J _{sc} (mA/cm ²)	V _{oc} (V)	FF	PCE (%)
1	m-TiO ₂ /Cs ₂ AgBiBr ₆ /PTAA	1.24	1.06	78	1.02
2	m-TiO ₂ /Cs ₂ AgBiBr ₆ /PNPBC	1.26	0.95	66	0.82
3	m-TiO ₂ /Cs ₂ AgBiBr ₆ /NPBC	0.85	0.85	75	0.55

EQE measurements reveal the maximum quantum efficiency to be at 32% for the PNPBC solar cell at a wavelength of 450 nm (Figure 69).

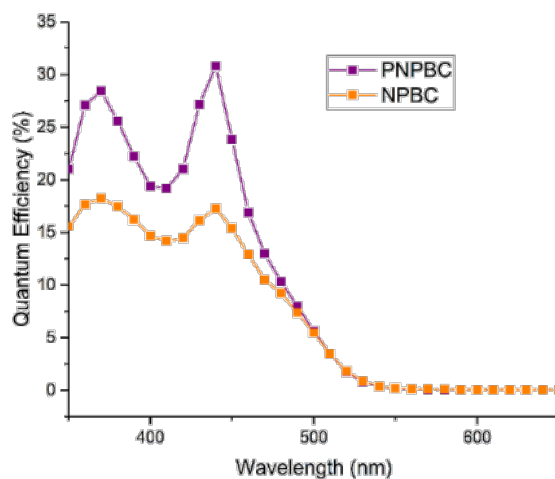


Figure 69 IPCE curves for PNPBC and NPBC mesoporous double perovskite solar cells.

To further understand the charge carrier dynamics in Cs₂AgBiBr₆ double perovskites, time resolved measurements should be conducted.^{103,131}

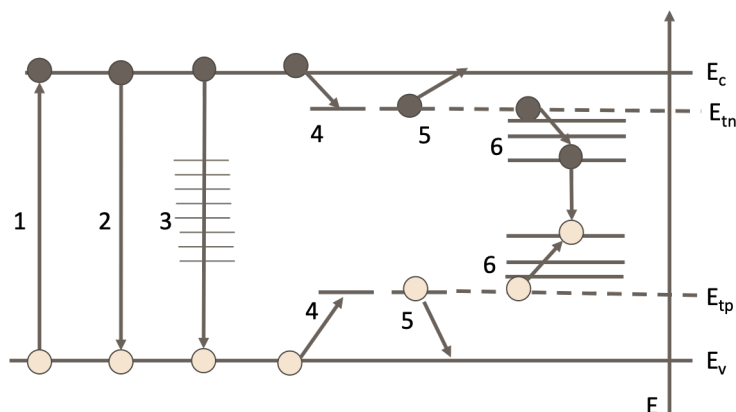


Figure 70 Schematic representation of carrier kinetic within Cs₂AgBiBr₆ according to [103, 152]. Where the (1) represents generation of free electrons and holes in the conduction (EC) and valence band (EV), respectively, (2) Band to band carrier

recombination, (3) Surface states recombination, (4) Free charges captured by trap states (shallow), (5) Trapped charges was thermally released to the band edges, (6) sub-bandgap states showing nonradiative traps and corresponding recombination.

Bartesaghy et al.¹⁰³ investigated the carrier dynamics of Cs₂AgBiBr₆ single crystals using time-resolved microwave conductance (TRMC). The results show a long-lived trace corresponding to mobile charges with microsecond lifetimes, which become dominant nearing the excitation wavelength of the bandgap. Based on the temperature- and intensity-dependent TRMC results, they found out that the shallow trap density state is around 10¹⁶ cm⁻³ in bulk. Despite the low mobility and high trap density state, they reported that the rate of trap-assisted recombination is low and that the traps are energetically shallow. Figure 70 illustrates the carrier kinetics process following the photogeneration of charge carriers close to the surface and in the bulk of Cs₂AgBiBr₆. Likewise, Yang et al.^{151,152} investigated carrier dynamics on Cs₂AgBiBr₆ nanocrystals by studying the hot-carrier relaxation dynamics in Cs₂AgBiBr₆. Previous studies have shown that the hot-hole relaxation is faster than hot-electron relaxation and that the sub-band gap states are mainly the hole-trap states in lead-based perovskite nanocrystals.^{153,154} Following these reports they suggest that the fast GSB (ground state bleaching - depletion of the ground state carriers to excited states) build-up signal (0.2 ps) is due to the relaxation of hot hole (4,5 in the Figure 70), while the fast PIA (photoinduced absorption) band decay (0.8 ps) is due to the hot electrons, and the 1.4 ps GSB decay component is assigned to holes trapping, while the 40 ps PIA decay component is related to electron trapping (6 in the Figure 70). Finally, the sub-bandgap states are commonly observed as non-radiative traps and may be one of the reasons for the low power conversion efficiency of the double perovskite solar cells. The sub-bandgap states may be the explanation for the lower solar cell performance when using HTMs with a HOMO level closer to the HOMO level of Cs₂AgBiBr₆. With the exception of the sub-band gap states in double perovskites, Gao et al.¹⁰⁰ reported on measuring the trap density using the space charge limited currents (SCLC) of Cs₂AgBiBr₆. They conducted SCLC measurement on ITO/Cu-NiO/Cs₂AgBiBr₆/Au and it seems that the Cs₂AgBiBr₆ possesses a trap density of 9.1x10¹⁶cm⁻³, which is still in the range to be comparable to Pb-based perovskites, showing promising applications in photovoltaics.

4.3.2.3. Stability

To investigate the homogeneity and the spatial distribution of the double perovskite thin films over the cross section, cross-section TEM analysis for Cs₂AgBiBr₆ deposited on TiO₂ was conducted. After the careful and demanding sample preparation, element mapping was conducted in order to determine the atom distribution across the cross section.

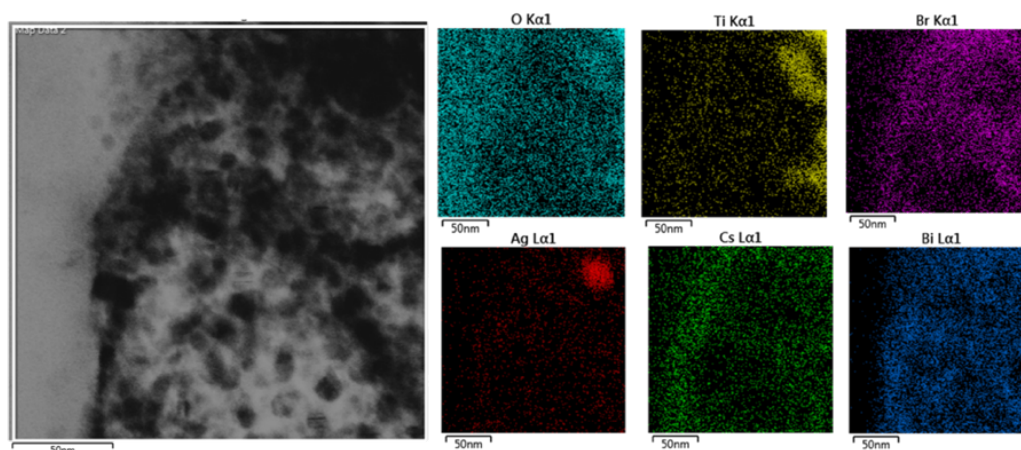


Figure 71 TEM cross section of perovskite/TiO₂, and element mapping of each element distribution across the cross section, turquoise is O, yellow Ti, violet Br, red silver, green cesium and blue bismuth.

Silver is accumulated across the cross section, which may be one of reasons for lower solar cell performance, as silver may represent a trap source and cause carrier captures or recombination. Further, SEAD (Selected area electron diffraction) patterns were obtained to investigate the crystal structure: two phases were identified, Cs₂Bi₂Br₈ and Cs₂AgBiBr₆, which explains the extra residues of silver. In any case, it is not sure if either the decomposition of Cs₂AgBiBr₆ took place because of the sample transportation, or because of the use of high energy ion beam milling during the preparation. Either way, the presence of silver increases the risk of lowering the device performance.

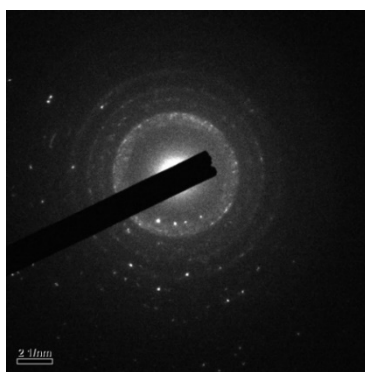
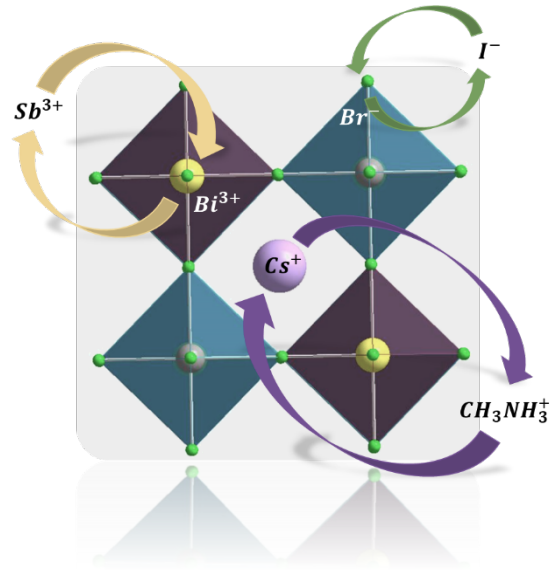


Figure 72 SAED pattern of the double perovskite cross section.



Chapter 5. Compositional Engineering of Double Perovskite Cs₂AgBiBr₆

Interest in Cs₂AgBiBr₆ and other double perovskites has been increasing in the last three years and several solar cells using different device structures have been reported. However, the efficiency of these lead-free double perovskite solar cells is merely in the range of 2%. Through the work up to now using different optimization and layer modification techniques solar cell interface engineering, the author developed the best reported solar cells with a 1.26% efficiency. To go a step further in the possible improvement of the solar cells, the author will introduce three additional elements for each double perovskite crystal structure in order to conduct compositional engineering. Thereof, MA⁺ (methyl-ammonium cation) will be introduced on the A-site to mix with a cesium cation in order to improve solubility and mobility of the active layer in the solar cells. The iodine will be introduced on the X-site of the double perovskite structure to mix with bromine in order to improve absorption and thereby the solar cell performance. Antimony will be introduced in on B'' site to mix with bismuth in order to improve absorption and charge mobility. After optimizing the preparation of these thin films, the author has carefully analyzed the effects of structure, composition, electronic structure, as well as the optical properties. Finally, the mixed system double perovskite solar cells were fabricated in a mesoscopic device architecture.

5.1. Cesium and Methyl-ammonium

Mixed systems of organic and inorganic cations in perovskite solar cells are a well-known approach.¹⁵⁵ After introducing element by element and mixing with the standard crystal structure of the perovskite in Pb-based perovskite solar cells, improvement was evident. Introducing Cs and mixing with MA or FA, the so called “triple cation” approach, improved resistance against moisture and stability at room temperature was achieved reaching efficiency values of over 21%.¹⁵⁶ In this work the focus was put on the replacing the methyl-ammonium cation with caesium. Also, the author has noticed, that the solubility of the inorganic starting materials is poor, reaching a maximal solution concentration of 0.5 M, and a thickness of the double perovskite layer in the range of 160-200 nm, while the solution concentration of lead-based perovskites is 1.2 M yielding a thickness of the perovskite layer of about 300 nm. The main motivation for this part is to improve solubility of the starting materials in DMSO, increase the solution concentration and thereby improve the thickness of double perovskite layers and film/grain quality. Except for these beneficial properties, the methyl-ammonium cations have shown a remarkable impact on the mobility of the charge carriers.¹⁵⁷ Both materials, Cs₂AgBiBr₆ and MA_xAgBiBr₆,⁷⁹ show stability in air and have a decomposition temperature higher than MAPbBr₃. Thus, cation combination may improve solar cell performance.

5.1.1. Synthesis and Thin Film Preparation

The solutions for thin film deposition have been prepared by mixing MABr (Methylammonium bromide purchased from Dyesol) with CsBr in different molar ratios, adding BiBr₃ and AgBr, (purchased from Alfa Aesar) in 1 mL DMSO. The author prepared seven perovskite solutions to form Cs_{2-x}MA_xAgBiBr₆, for x = 0.2, 0.4, 0.8, 1, 1.2, 1.6, and 2.0. All starting materials were dissolved at 50 °C and the solution concentration increased with increasing MA amount. The author used the standard one-step spin-coating deposition program using 4000 rpm for 30 seconds for thin film deposition. After deposition, the formation of each new material was investigated using several annealing temperatures. The final annealing temperatures are shown in Figure 73. The solar cell fabrication of the mixed Cs/MA system has been provided used the standard mesoporous scheme of FTO/c-TiO₂/m-TiO₂ with Cs/MA double perovskite in molar ratio 1:1 followed by PTAA and Au. The concentration of the perovskite solution was 0.8 M.

5.1.2. Results and Discussion

The results of introducing the MA⁺ into the double perovskite structure are shown in Figure 58. The XRD diffractograms are shown for all films using different Cs/MA molar ratios and the annealing temperatures, which decrease when adding MA into the system. The main reflection peaks of double perovskites are present and match the standard double perovskite structure. However, due to the additional cation, a shift is present. (Figure 73a, c) The reflection peaks (400) and (002) decreases with the increase of the MA amount, meaning that the crystal lattice expands when replacing of Cs ($r_{\text{eff}}=167$ pm) with the larger MA ($r_{\text{eff}}=217$ pm) cation.

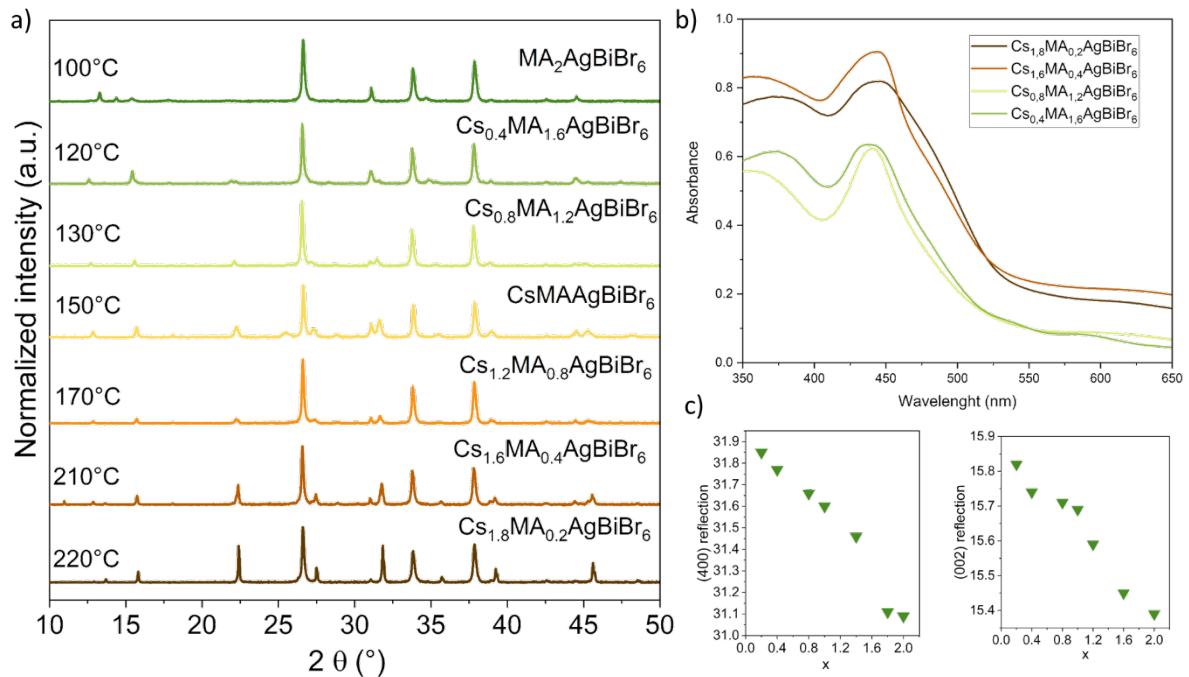


Figure 73 a) XRD diffractogram of Cs_xMAAgBiBr₆, b) Absorption spectra, c) (400) and (002) reflection.

The absorption spectra in Figure 73b show a blueshift and a lower absorption intensity after adding methylammonium. Due to the organic cation, the absorption is lower but it is still in the range of the absorption onset of the double perovskite Cs₂AgBiBr₆ thin film, 2.3-2.1 eV. Wei et al. reported on single crystals of MA₂AgBiBr₆ with a bandgap of 2.02 eV. The difference between the powder and film may be due to the thickness of the deposited films compared to powder or crystals of the same material.

5.2. Bromine and Iodine

The hybrid perovskite materials possess broad versatility and bandgap tunability. One of the solutions towards lowering the bandgap is mixing (partly replacing) a bromide ion with a larger iodide ion. The small changes in the perovskite composition can have a big influence on the material properties and device performance. Doping the MAPbBr_xI_{3-x} perovskite with bromine causes a bandgap widening and therefore improvement in device performance by increasing the open circuit voltage (V_{oc}) due to longer lifetime of the excited charge carrier. Doping the perovskite bromine materials with iodide may have an influence on the bandgap by red-shifting the absorption and improving the short circuit current (J_{sc}) and thus the device performance.¹⁵⁸ The red-shift of the bandgap going from the bromine to iodine is due to the enlargement in the covalent character of the halogen binding to the metal cation. Creutz et al¹⁵⁹ reported that applying the anion-exchange protocol on Cs₂AgBiI₆, a new nanocrystal material, using trimethylsilyl iodide with an absorption onset at 600 nm caused a significantly reduced bandgap (2 eV). In this part of the work to reduce the bandgap of Cs₂AgBiBr₆, the author applied different synthesis approaches to mix bromide and iodide to ultimately widen the absorption range.

5.2.1 Synthesis

To prepare mixed Br/I double perovskites, the author used the solution synthesis approach. Using standard precursors for double perovskite Cs₂AgBiBr₆ to dissolve in HBr (Alfa Aesar), described above in 3.1.1. An additional source of iodide was used from different starting materials, AgI (Sigma Aldrich, 99%), BiI₃ (Sigma Aldrich, 99%) and CsI (Sigma Aldrich, 99%), prepared separately. The synthesis was conducted at 130 °C to dissolve all starting materials in hydrobromic acid. Reaching the desirable temperature, after 10 minutes all compounds were dissolved leading to a reddish colour. Five different compositions of Cs₂AgBiBr_{6-x}I_x were prepared using the values $x = 0.6, 1.2, 1.8, 2.4, 3$, respectively. Because the high amounts of iodide resulted in several extra phases, mainly AgI and Cs₃Bi₂I₉, the author used $x = 0.1$ and 0.2 (Figure 59). When all precursors were dissolved the solution was kept at 130 °C for 2 hours and after that cooled down with a cooling rate of 10°C/h. Reddish powder formed, washed with ethanol and dried in a vacuum oven at room temperature overnight.

5.2.2 Results and Discussion

The mixed double perovskites show an interesting red colour indicating a possible band gap shift. For materials with $x > 0.2$ side phases were obviously present. The huge problem of preparing pure mixed double perovskite was the formation of Cs₃Bi₂Br₉ and AgI. The presence of these two side phases is hard to extract or remove by recrystallization methods (Figure 74). The formation of Cs₃Bi₂Br₉ is in this case more favorable thermodynamically.

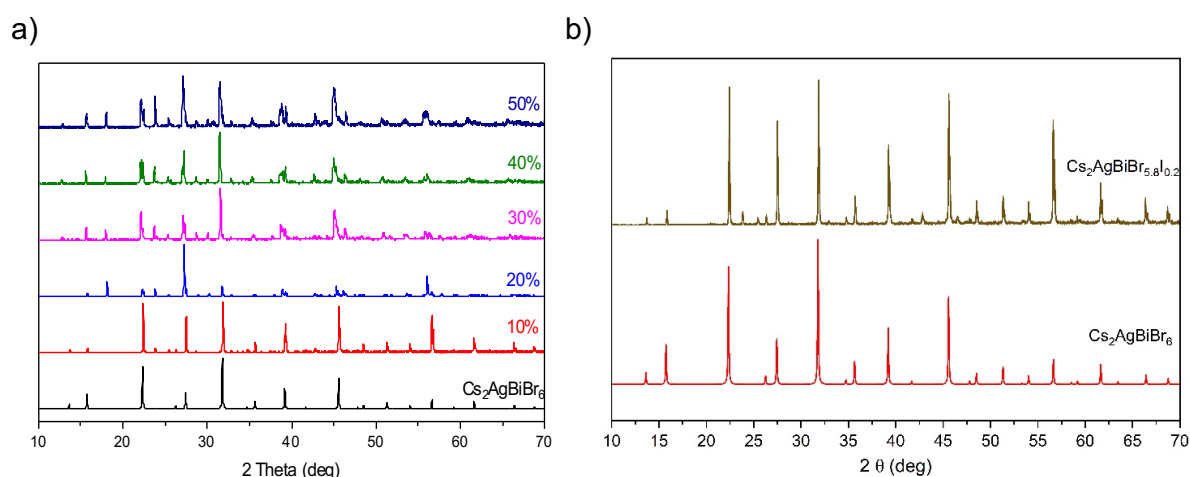


Figure 74 a) XRD diffractogram of Cs₂AgBiBr_{6-x}I_x, compared to double perovskite Cs₂AgBiBr₆ with higher amounts of iodide, b) Cs₂AgBiBr_{5.8}I_{0.2}.

In the absorption spectra (Figure 75a) the change is significant even for small amounts of iodide, leading to an absorption onset at 640 nm. Photoluminescence spectra show broad peaks from 1.6-2.3 eV and a peak at 2.0 eV which corresponds to absorption data, but without any additional peak shift (Figure 75b).

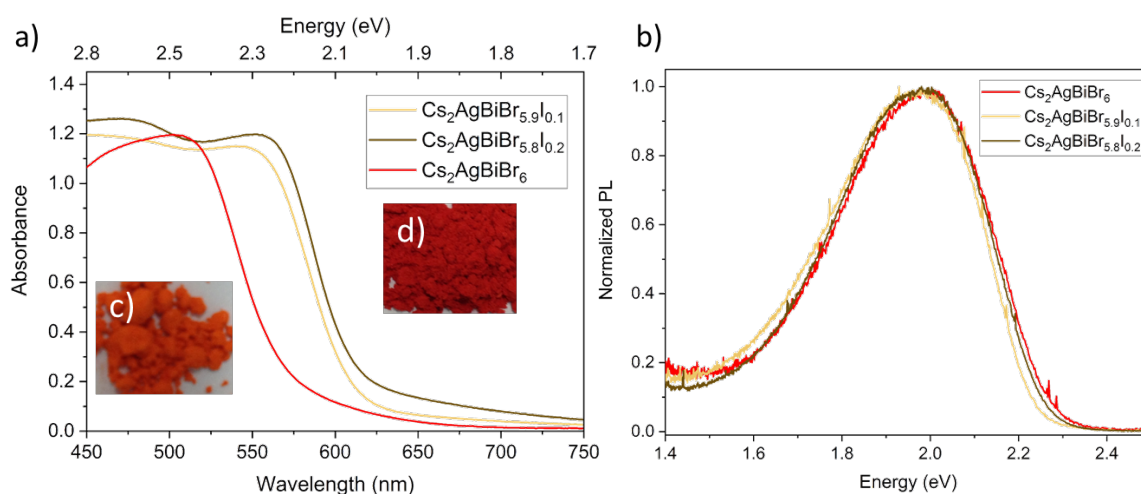


Figure 75 a) Absorbance of mixed iodine/bromine double perovskite, b) Photoluminescence of all materials, c) Cs₂AgBiBr₆ powder, d) Cs₂AgBiBr_{5.8}I_{0.2} powder.

Finally, mesoporous solar cells with CsMAAgBiBr₆ and Cs₂AgBiBr_{5.8}I_{0.2} mixed systems were fabricated.

When using MA in double perovskites, an increase in open circuit voltage (V_{oc}) can be observed. Introducing iodide into double perovskites increases the short circuit current (J_{sc}). However, the solar cell performance, due to absorption still is lower in CsMAAgBiBr₆ (Figure 76a) possibly due to the presence of side phases in Cs₂AgBiBr_{5.8}I_{0.2} (Figure 76b), reaching a maximal value around 0.3% of PCE in both cases of replacing with MA and I.

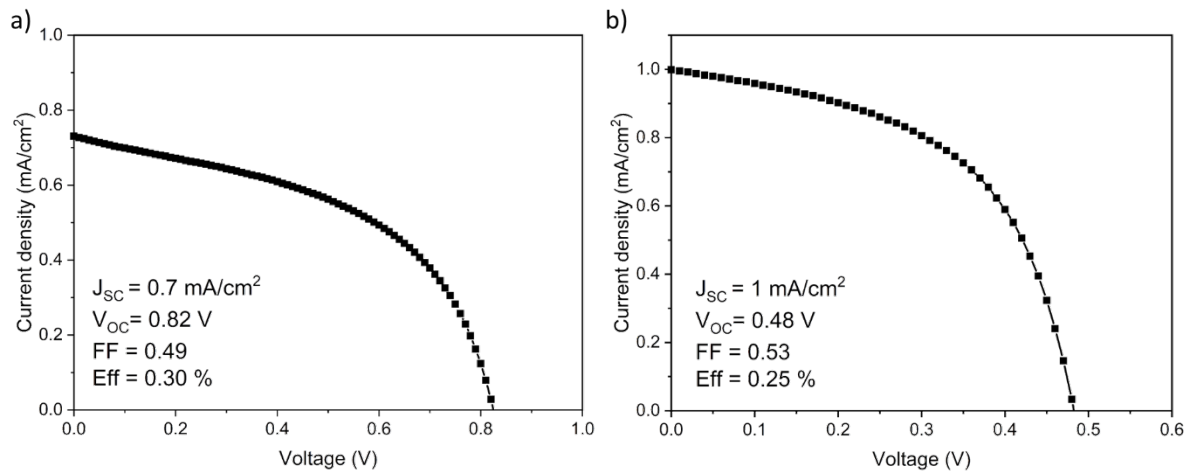


Figure 76 Solar cell performance of **a)** CsMAAgBiBr₆ double perovskite, and **b)** Cs₂AgBiBr_{5.8}I_{0.2} double perovskite.

5.3. Bismuth and Antimony

Du et al. first reported on bandgap engineering through trivalent metal alloying. They conducted bandgap engineering using In³⁺ up to 75% to increase the bandgap and Sb³⁺ up to 37.5% to decrease the bandgap replacing with bismuth on the B-site of the perovskite structure.¹⁸ Beyond decreasing the bandgap, Hutter et al. showed an increase in charge carrier mobility for decreasing temperature.¹⁶⁰ Another beneficial property of adding antimony into the perovskite systems has been shown to be the improvement of open circuit voltage reaching 1.13 V in Pb-based p-i-n heterojunction solar cells.¹⁶¹

5.3.1. Band Gap Evolution in Cs₂AgBi_{1-x}Sb_xBr₆ Systems

The calculated band gap decreases upon the addition of Sb into Cs₂AgBiBr₆.¹⁶¹ There is a minimum band gap around 75% of Sb due to the decrease of spin-orbit coupling (SOC) for pure Cs₂AgSbBr₆ (Figures 77a, b). A similar trend has been reported for MAPb_{1-x}Sn_xI₃ compounds¹⁶². The enhancement of spin-orbit coupling is observed for mixed Cs₂AgBi_{1-x}Sb_xBr₆ systems as compared to pure Cs₂AgBiBr₆, while the SOC amplitude for pure Cs₂AgSbBr₆ is close to 0, meaning that the SOC is imposed by Bi.

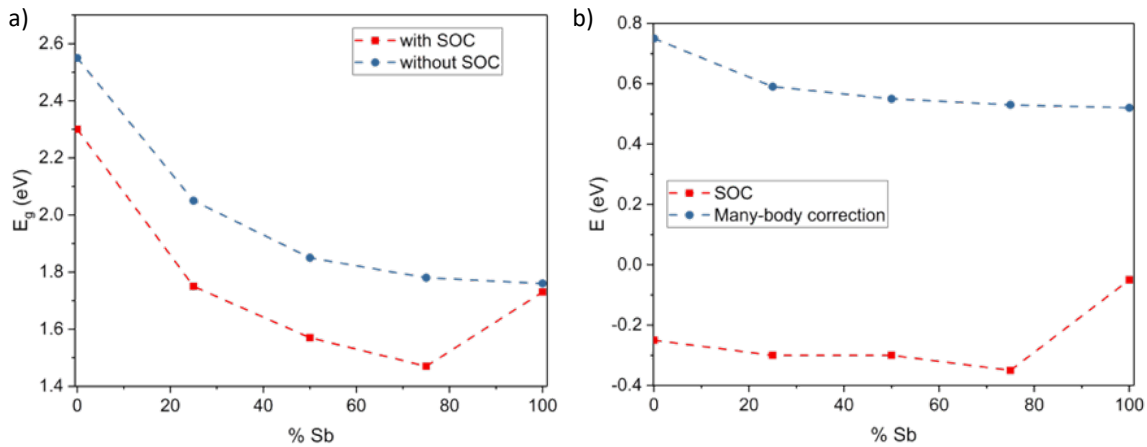


Figure 77 a) Evolution of the band gap as a function of Sb concentration, b) Contribution of many-body interactions and spin-orbit coupling into band gap, calculations conducted by Dr. Olga Syzgantseva from EPFL.

Band gaps are calculated with the GLLB-SC (Gritsenko, van Leeuwen, van Lenthe, Baerends functional, Solid, Correlation) on structures with PBE (Perdew-Burke-Ernzerhof)-optimized lattice parameters. The band gap trends are in good agreement with the experimental data reported by Mitzi and co-workers⁶⁹, the deviations are less than 0.2 eV.

5.3.2 Synthesis and Results

Solid-state synthesis has been conducted using quartz ampoules where all starting materials (described above, but here with addition of SbBr₃, Sigma-Aldrich, 99.99%) have been introduced after grinding. The ampoule has been sealed under vacuum, heated to 350°C and kept at that temperature for more than 8h and subsequently cooled down to room temperature. Figure 78 shows the XRD characterization of the prepared powders. The XRD diffractogram of mixed systems show good match with pure double perovskite, however the introduction of antimony has caused a contraction of the crystal lattice. The 2 theta value of the (002) reflection

increases with the Sb content due to the replacement of the larger Bi cation with the smaller Sb (Figure 78b). The absorption spectra shown in Figure 79 show a red shift after adding antimony. The absorption onset changes from 600 to 650 nm after adding antimony.

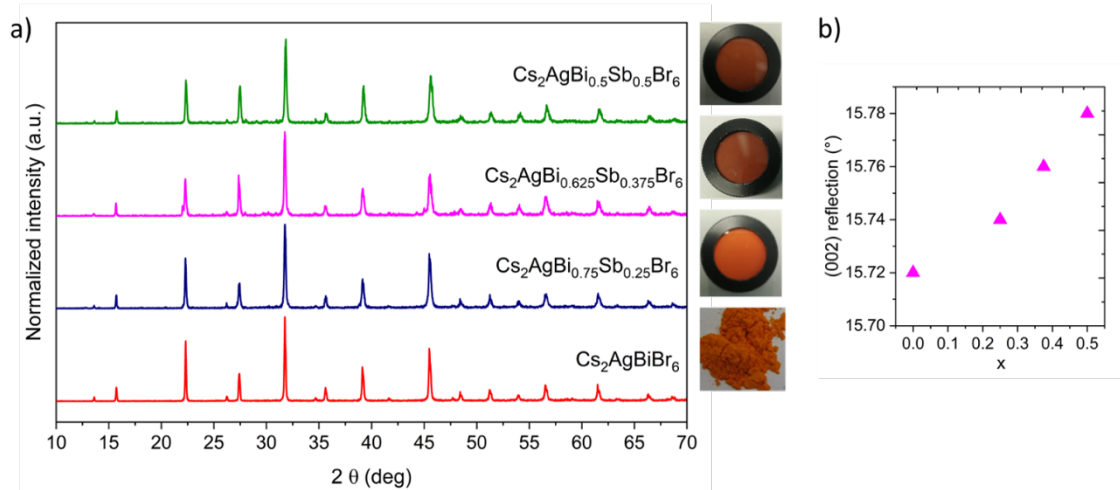


Figure 78 a) XRD diffractogram of prepared Sb-Bi mixed double perovskite using ampoule synthesis, b) (002) reflection shift.

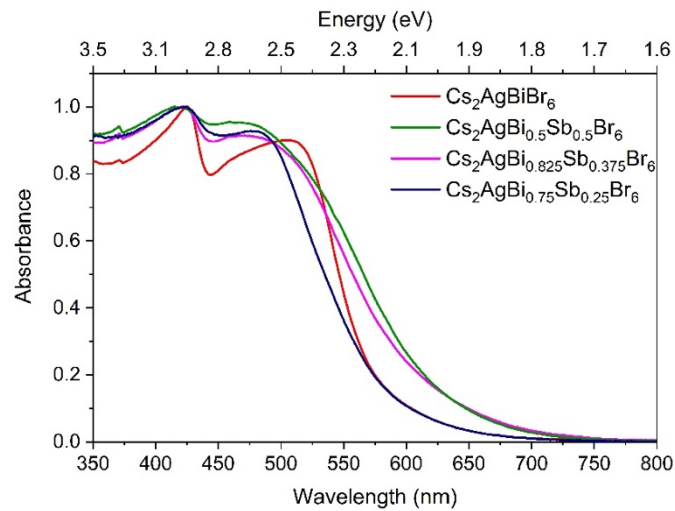


Figure 79 Absorption spectra of all mixed materials compared to standard double perovskite.

5.3.3 Bismuth-Antimony Mixed Double Perovskites $\text{Cs}_2\text{AgBi}_{1-x}\text{Sb}_x\text{Br}_6$ in Solar Cells

This part has been adopted from MRS Advances with permission (Cambridge society copywriting), where it has been accepted recently (October 2019).¹⁶³

Bismuth, as a less toxic element, could be a viable candidate for the lead-free perovskite solar cells, but due to its higher oxidation state it can only be incorporated into double perovskite structures like Cs₂AgBiBr₆. Even though much work has gone into improving preparation, film formation, and solar cell architectures for this material class, efficiency has merely reached 2.4%^{74,82}. This is mainly due to the wide bandgap and weak light absorption, the latter one brought about by the indirect bandgap. To overcome this problem, the band structure of the material has to be modified. Attempts for this include alloying or substituting bismuth with thallium⁶³ or antimony^{69,160} which decreases the bandgap, improves absorption and charge carrier mobility¹⁶⁰. In this work, the author employs different mixtures of bismuth and antimony in double perovskite Cs₂AgBi_{1-x}Sb_xBr₆ to decrease the bandgap for which the author optimize the film deposition method. The author provide extensive thin film characterization by which it can track the changes in crystal structure, composition, absorption, and electronic structure. In the end, the author test the influence of the mixing ratio on the solar cell performance using a mesoscopic device architecture.

5.3.3.1 Experimental Details

The double perovskite mixed Bi-Sb thin films were prepared using CsBr (99.9%), BiBr₃ (99.0%), AgBr (99.5%), and SbBr₃ (99.0%) purchased from Alfa Aesar. These were dissolved in DMSO (0.5 mol/L, 99.5% Sigma Aldrich) in the corresponding stoichiometric ratios. The author used one step spin coating deposition with rotation of 4000 rpm for 30 sec in inert atmosphere on ITO substrates (for XPS/UPS/IPES measurement) and on FTO substrates for solar cells fabrication. The double perovskite Cs₂AgBiBr₆ films were annealed at 260°C for 5 min, and the mixed Cs₂AgBi_{1-x}Sb_xBr₆ films were annealed at 240°C, 220°C, 200°C and 180°C for x=0.125, 0.25, 0.375, 0.50 for 5 min, respectively. Solar cells were fabricated like reported elsewhere⁸². X-ray diffraction (XRD) analysis was carried out using a Panalytical Empirian diffractometer in Bragg – Brentano configuration using Cu K α (λ = 1.54 Å) in the range of 2θ = 10° to 70°. SEM/EDX measurements were carried out on a Jeol JSM 7500F microscope. Absorption spectra were obtained using a Shimadzu UV-VIS spectrophotometer UV-2600. Photoelectron spectroscopy measurements were performed using a hemispherical electron analyser (Phoibos 100, Specs). For X-ray photoelectron spectroscopy (XPS), a Mg K α excitation source at $h\nu$ = 1252.6 eV was employed. For UV photoelectron spectroscopy a monochromatic UV microwave source (VUV 5000, VG Scienta) at $h\nu$ = 21.22 eV was used.

Inverse photoelectron spectroscopy (IPES) measurements were performed in the isochromatic mode, using a low energy electron gun (Kimball, ELG-2) and a NaCl/SrF₂ bandpass filter (Omnivac, IPES2000). J-V measurements were performed using a commercial solar simulator (Oriel, 450 W, Xenon, AAA class) for light source. The light intensity was matched to one sun (AM 1.5G) by calibrating with a Si reference cell. The cells were masked with an active area of 0.15 cm². Photoluminescence (PL) measurements were conducted using a PerkinElmer LS55 Luminescence spectrometer. The incident photon-to-electron conversion efficiency (IPCE) measurement was performed under a Xenon lamp using monochromatic equipment (Newport Cornerstone 260).

5.3.3.2. Results and Discussion

Figure 80a shows the main reflections which correspond to the face centered cubic double perovskite structure²⁰. Replacing bismuth by antimony in the double perovskite structure shifts the 002 and 222 reflections to larger 2θ values (Figure 80b, c). This is expected, since bismuth ($r_{\text{ion}}=117$ pm) is replaced by the smaller antimony cation ($r_{\text{ion}}=90$ pm)⁶⁰. The change of refraction angle between the pure Bi double perovskite and 50% Sb mixed double perovskite is approximately $\Delta 2\theta = 0.14^\circ$. Figure 81 a-d shows SEM images of these different thin films. By comparing the sizes of the crystallites in these SEM images, an increase in average grain size from 100 nm to 300 nm with increasing Sb content can be found. This could be due to doping in this case of acceptor doping and formation of vacancies⁶⁴.

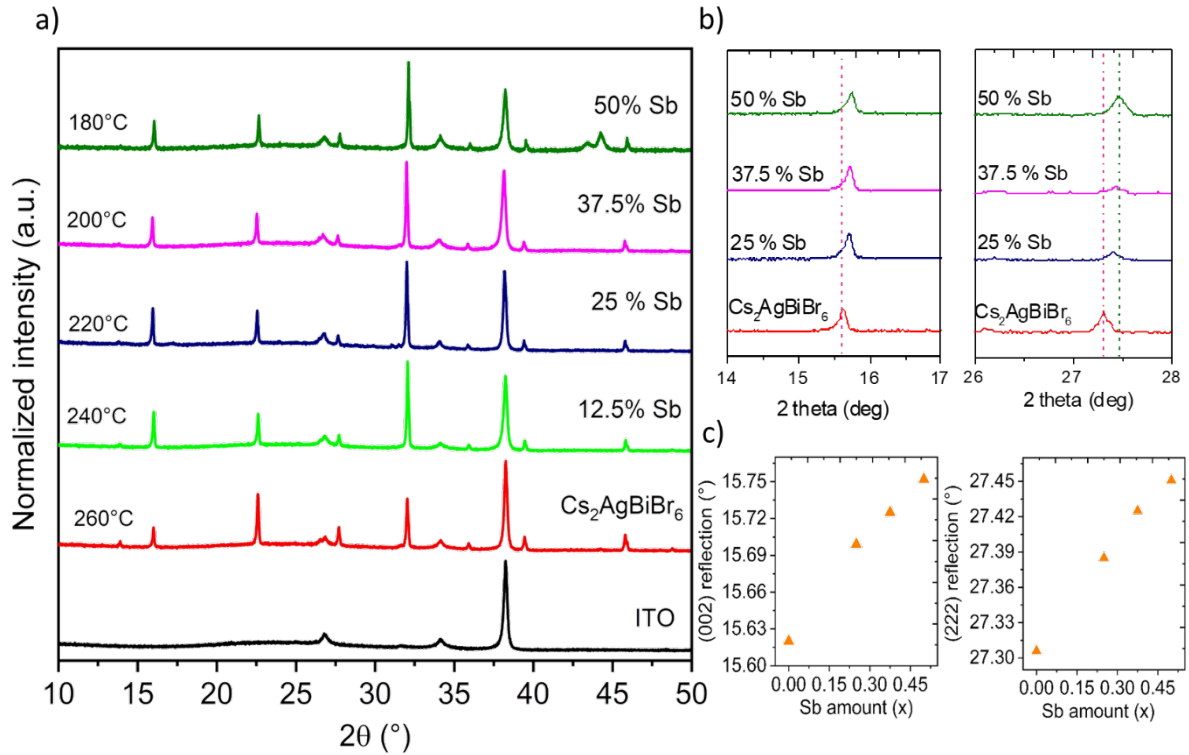


Figure 80 a) XRD diffractogram of mixed double perovskite employing different concentrations of antimony. Optimized annealing temperatures are indicated in the graph. b) Detailed view of the (002) and (222) reflections, showing the change in lattice size with Sb content. c) (002) and (222) reflection positions depending on mixing with antimony.

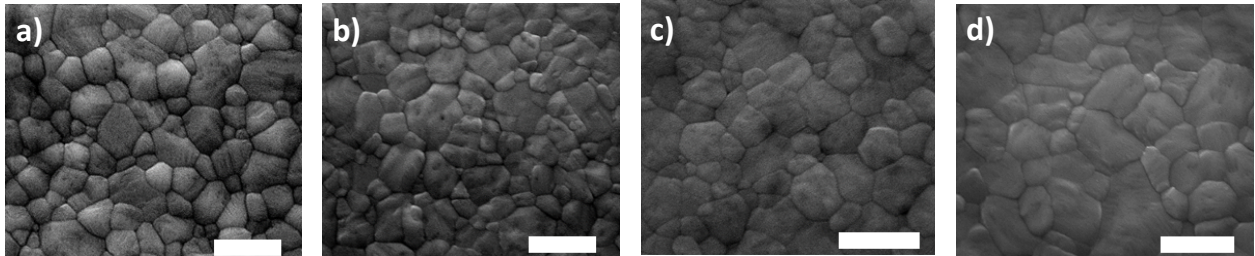


Figure 81 SEM top view image of $\text{Cs}_2\text{AgBi}_{1-x}\text{Sb}_x\text{Br}_6$ films, the white bar corresponds to 500 nm. The Sb concentrations are: a) 0%, b) 25%, c) 37.5%, and d) 50%.

For the solar cells, the optical gap is important and in order to investigate the effects of mixing ratio the author performed UV-Vis measurements. The author measured transmittance and calculated Tauc-plots for indirect bandgap materials and Figure 82a shows a slight shift in the onset values to higher wavelengths, from the energy of 2.5 eV to 2.1 eV when increasing the fraction of Sb (see Table 13).

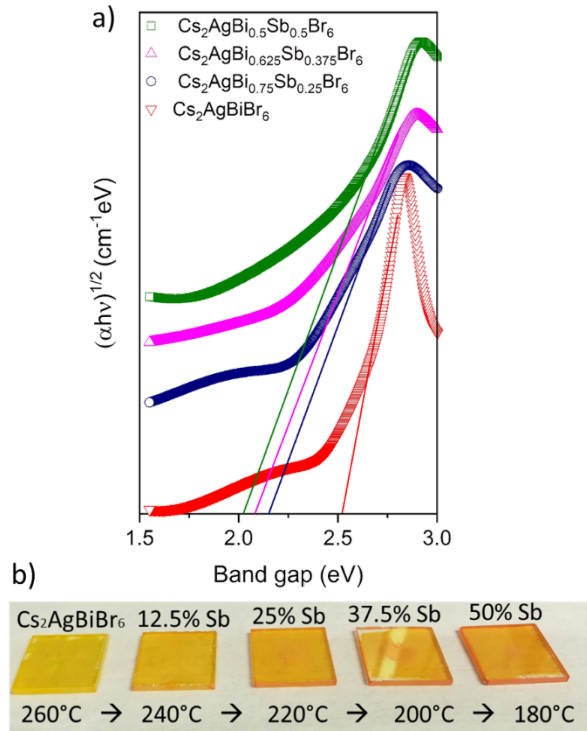


Figure 82 a) Tauc-plot of the absorbance spectra and b) corresponding photographs of the double perovskite thin films with different amount of antimony deposited on glass.

Included in this figure are photographs showing a slight change in thin film color from yellow to orange (Figure 82b). These values are somewhat different from the results presented by Du et al. who reported a decrease in bandgap from 2.12 eV to 1.86 eV when adding antimony⁶⁹. The difference likely comes from the fact that they investigated powder samples, while thin films were probed here. For thicker (i.e. powder or single crystal) layers, band tail states can play a role in absorption and narrow the apparent bandgap.

To check the chemical composition of the mixed double perovskite Cs₂AgBi_{1-x}Sb_xBr₆ films, the author performed X-ray photoemission spectroscopy (XPS) and energy dispersive X-ray spectroscopy (EDX) measurements. Due to the different depth sensitivities of these two methods (XPS several nm and EDX up to μm), phase segregation towards the surface can be probed. Figure 83a shows an XPS survey scan of the 50% Sb sample, in which all peaks have been assigned to the corresponding core levels. The detailed scans in Figure 83b show the Cs 3d_{5/2} (EB = 723.44 eV), Ag 3d_{5/2} (EB = 367.24 eV), Bi 4f_{7/2} (EB = 158.64 eV), and Sb 3d_{3/2}

(EB = 538.86 eV) and Br 3d_{5/2} (EB = 67.8 eV) features which are all present in the expected oxidation states.

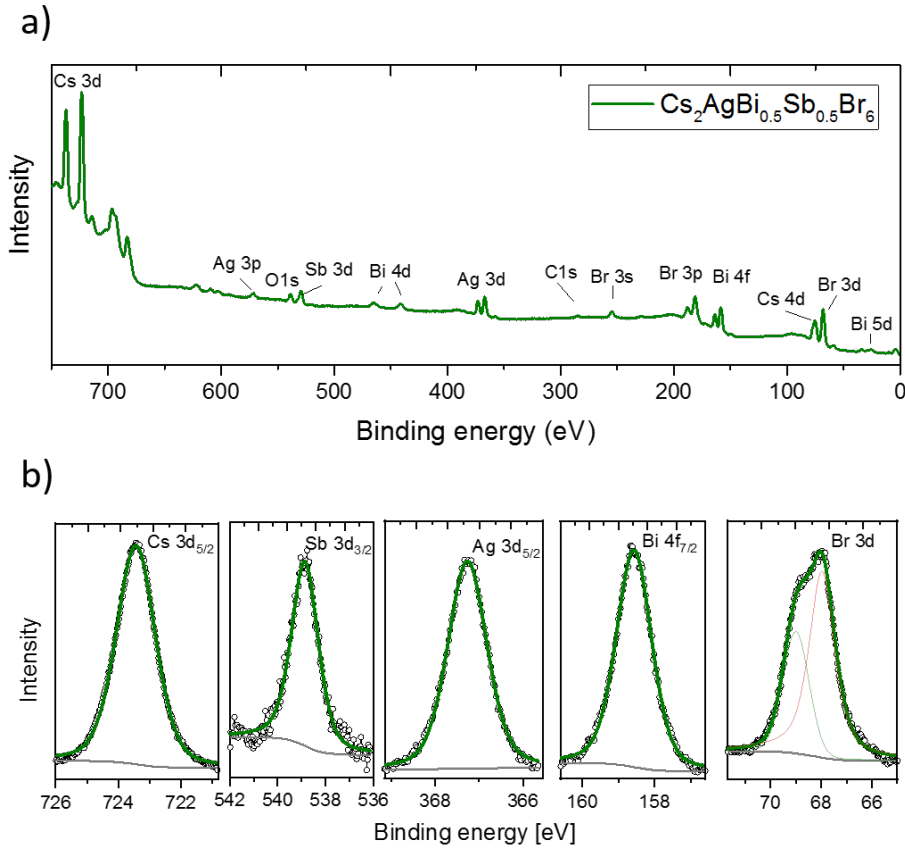


Figure 83 a) Representative XPS spectrum of one of the thin films mixed double perovskites. b) Detailed view of core level peaks of this sample, showing high resolution XPS spectra of cesium, antimony, silver, bismuth, and bromine.

From the peak areas, the film compositions can be calculated, which are listed in Table 12 along with the EDX results.

Table 12 Comparison calculated values with XPS and EDX analysis.

Intended composition	XPS (normalized to Br)	EDX (normalized to Br)
Cs ₂ AgBiBr ₆	Cs _{2.4} Ag _{1.14} Bi _{1.09} Br _{6.0}	Cs _{2.05} Ag _{0.87} Bi _{0.82} Br ₆
Cs ₂ AgBi _{0.75} Sb _{0.25} Br ₆	Cs _{2.98} Ag _{1.21} Bi _{0.92} Sb _{0.23} Br _{6.0}	Cs _{2.25} Ag _{0.87} Bi _{0.88} Sb _{0.28} Br ₆
Cs ₂ AgBi _{0.625} Sb _{0.375} Br ₆	Cs _{2.67} Ag _{1.16} Bi _{0.83} Sb _{0.40} Br _{6.0}	Cs _{1.85} Ag _{1.08} Bi _{0.57} Sb _{0.42} Br ₆
Cs ₂ AgBi _{0.5} Sb _{0.5} Br ₆	Cs _{2.34} Ag _{1.059} Bi _{0.61} Sb _{0.30} Br _{6.0}	Cs _{1.92} Ag _{0.77} Bi _{0.57} Sb _{0.38} Br ₆

Comparing the stoichiometry found with both measurement methods with the intended compositions in Table 12, the author was able to confirm that the correct amount of Sb is indeed

incorporated into the films. The higher Cs content in the XPS measurements, which has the higher surface sensitivity, indicates that the surface is likely terminated by Cs atoms. Next, also the electronic bandgap is evaluated by combined direct and inverse photoelectron spectroscopy (UPS and IPES) as shown in Figure 84. Here, the onsets of the valence band (VB) and conduction band (CB) are marked by vertical lines. The extracted values for the bandgap are listed in Table 12. Due to the limited energy resolution, especially of the IPES measurement, the error bars are larger here than for the absorption measurements. Overall, the measurements coincide, both showing some changes in bandgap. Furthermore, from the UPS and IPES measurements the values of work function (W_f), ionisation energy (IE), and electron affinity (EA) can be extracted and are also listed in Table 13.

Table 13 Calculated averaged values of work functions (Wf), ionization energies (IE) electron affinities (EA) and band gaps (Eg) of double perovskite thin films deposited on ITO substrates.

Compound	W_f/eV	IE /eV	EA /eV	E_c from UPS/IPES /eV	E_c from Tauc-Plot/eV
Cs ₂ AgBiBr ₆	5.09 ± 0.05	5.97 ± 0.05	3.72 ± 0.3	2.2 ± 0.3	2.54 ± 0.05
Cs ₂ AgBi _{0.75} Sb _{0.25} Br ₆	5.02 ± 0.05	5.95 ± 0.05	3.62 ± 0.3	2.3 ± 0.3	2.18 ± 0.05
Cs ₂ AgBi _{0.625} Sb _{0.375} Br ₆	4.96 ± 0.05	5.87 ± 0.05	3.43 ± 0.3	2.4 ± 0.3	2.15 ± 0.05
Cs ₂ AgBi _{0.5} Sb _{0.5} Br ₆	4.92 ± 0.05	5.77 ± 0.05	3.57 ± 0.3	2.2 ± 0.3	2.10 ± 0.05

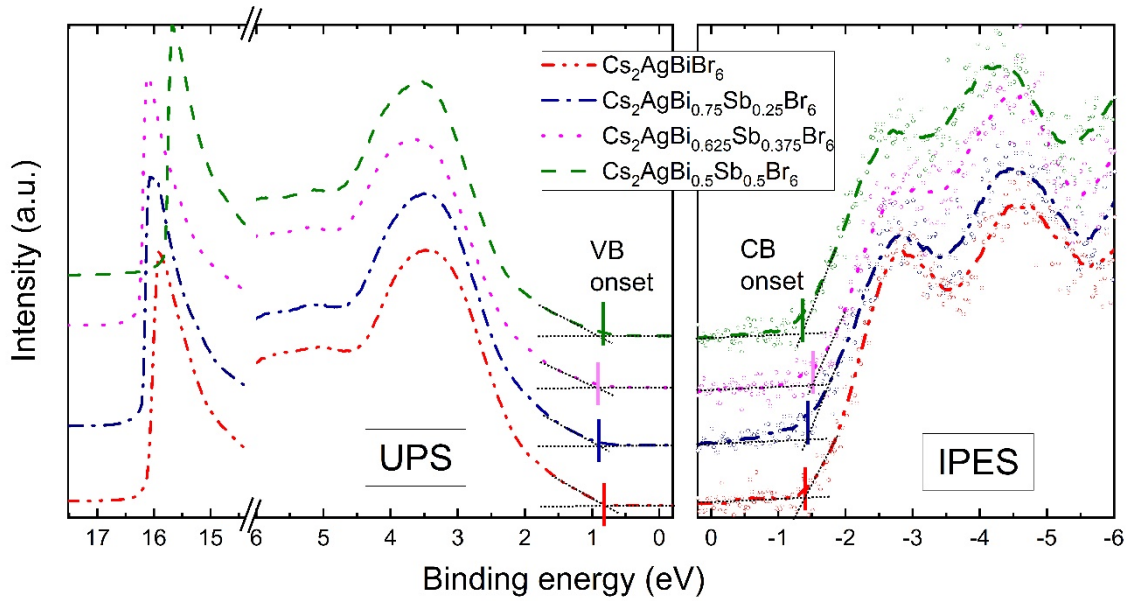


Figure 84 UPS and IPES spectrum of Cs₂AgBiBr₆ and samples with increasing amount of Sb.

Upon addition of Sb a decrease in IE is observed, meaning that the VB is shifted up by approximately 200 meV. This indicates an increase in orbital overlap, possibly induced by the smaller lattice constant. At the same time, the CB is also lifted, however the trend only holds up to a Sb content of 37.5%, after which the EA increases again. Since the metal p-states play a significant role for the CB position, there are likely opposing trends in lattice size vs. atomic orbital position¹⁶⁵. After the thin films have been optimized and their composition and electronic structure were evaluated, mesoscopic solar cells were prepared with the structure FTO/c-TiO₂/m-TiO₂/double perovskite/PTAA/Au. For two of the mixing ratios, the forward and reverse IV characteristics under 1 sun illumination are shown in Figure 85-86. Moderate hysteresis is observed (Figure 86a, b). The parameters measured in forward and backward direction are indicated in the corresponding graphs. The extracted solar cell parameters for all mixing ratios are summarized in Table 14. The author observe a decrease of the solar cell performance with increasing amount of antimony. The reason for that may be the formation of vacancies or defects with the introduction of antimony, as well as a charge trapping effect which leads to recombination centers and lower PCE.

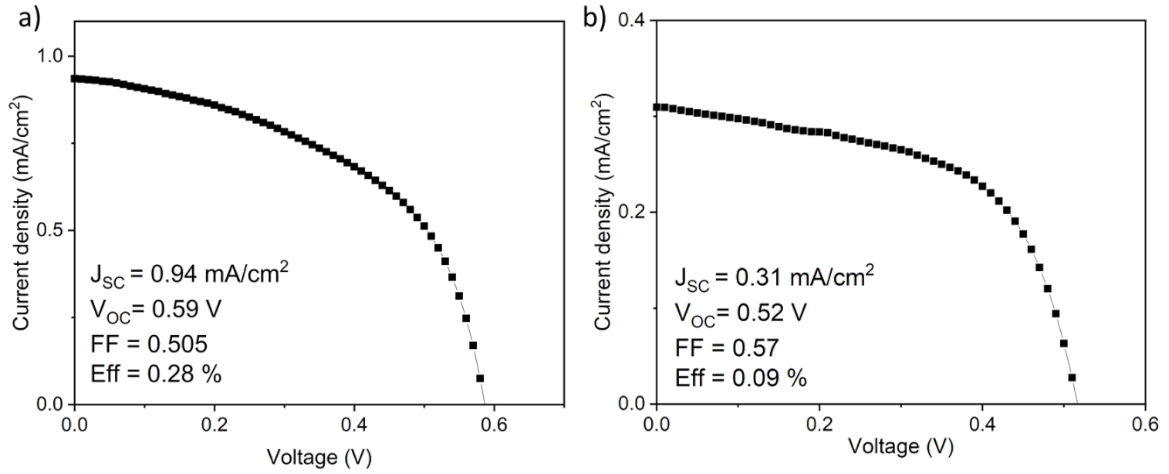


Figure 85 a) Solar cell I-V curve for 12.5% Sb doped double perovskite, b) I-V curve for 37.5% antimony doped double perovskite.

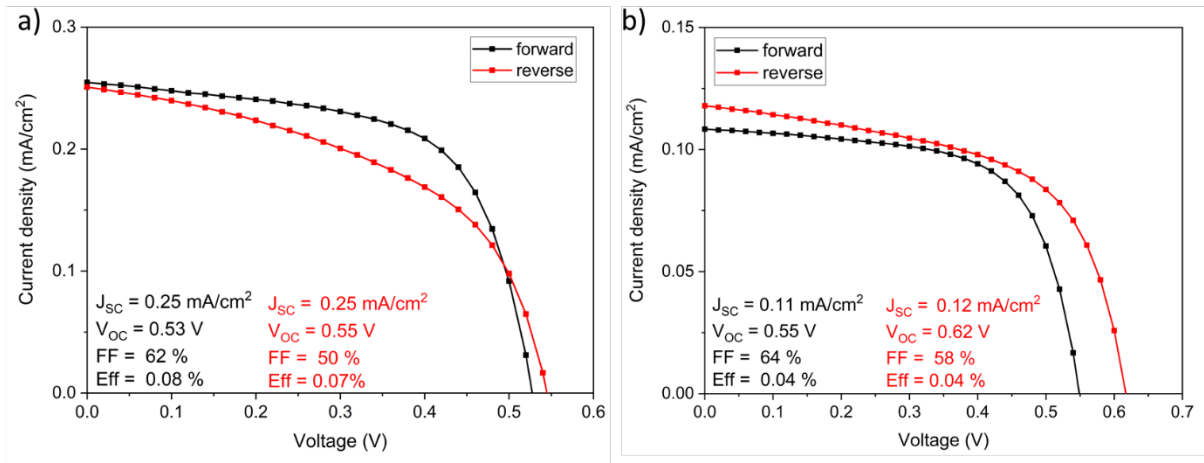


Figure 86 a) Solar cell I-V curve for 25% Sb doped double perovskite, b) I-V curve for 50% antimony doped double perovskite.

Table 14 Photovoltaic parameters of devices based on different concentrations of antimony: Short-Circuit Current Density (J_{sc}), Open-Circuit Voltage (V_{oc}), Fill Factor (FF), and Power Conversion Efficiency (PCE).

Nr	Device	V_{oc} (V)	J_{sc} (mA/cm ²)	FF	PCE (%)
1	FTO/mTiO ₂ /Cs ₂ AgBiBr ₆ /PTAA/Au	1.06	1.24	78	1.02
2	FTO/mTiO ₂ /Cs ₂ AgBi _{0.875} Sb _{0.125} Br ₆ /PTAA/Au	0.59	0.94	51	0.28
3	FTO/mTiO ₂ /Cs ₂ AgBi _{0.8} Sb _{0.2} Br ₆ /PTAA/Au	0.78	0.48	44	0.16
4	FTO/mTiO ₂ /Cs ₂ AgBi _{0.75} Sb _{0.25} Br ₆ /PTAA/Au	0.55	0.25	50	0.08
5	FTO/mTiO ₂ /Cs ₂ AgBi _{0.625} Sb _{0.375} Br ₆ /PTAA/Au	0.52	0.31	57	0.09
6	FTO/mTiO ₂ /Cs ₂ AgBi _{0.5} Sb _{0.5} Br ₆ /PTAA/Au	0.62	0.12	58	0.04

To study the underlying reason The author inspected the photoluminescence in Figure 87a. Here clearly an increase in quenching is observed. This is due to the formation of recombination centers or defects, and is likely the reason why solar cells perform worse connecting with IPCE data shown in Figure 87b.

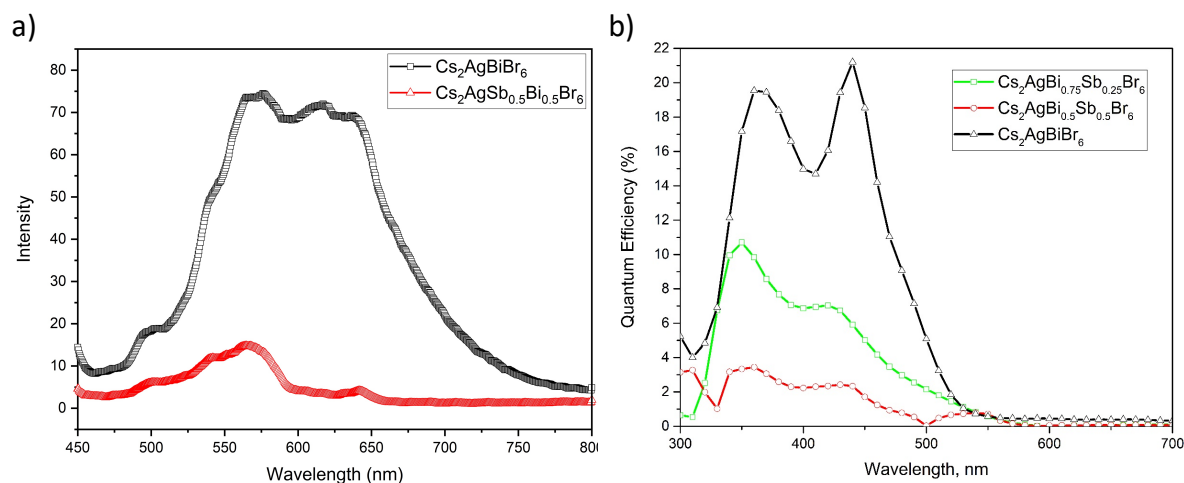
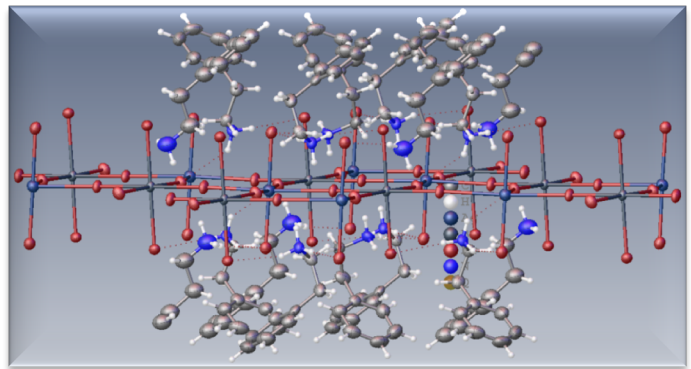


Figure 87 a) Photoluminescence of Cs₂AgBiBr₆ and Cs₂AgBi_{0.5}Sb_{0.5}Br₆. b) IPCE of double perovskite solar cells, Cs₂AgBiBr₆, Cs₂AgBi_{0.75}Sb_{0.25}Br₆, and Cs₂AgBi_{0.5}Sb_{0.5}Br₆.

A detailed investigation of optimized lead-free bismuth-antimony mixed double perovskite Cs₂AgBi_{1-x}Sb_xBr₆ thin films has been presented. XPS and EDX measurements prove the successful integration of the Sb atoms into the double perovskite structure while XRD analysis shows a decrease in lattice constant upon insertion of this smaller Sb cation. Absorption measurements reveal the desired reduction in bandgap when adding antimony while photoelectron spectroscopy shows that the ionization energy and electron affinity both decrease with rising Sb content. Importantly, the author did not find the expected increase in short circuit current by bandgap modification. Rather, these studies suggest that the presence of Sb leads to the formation of trap states, which act as recombination centres. These quench the photoluminescence and decrease the overall solar cell performance. Therefore, this double perovskite is no viable candidate unless further strategies to mitigate the newly created trap states are developed.²

Recently, Yang et al.¹⁶⁶ reported on charge carrier dynamics of Cs₂AgSb_{1-y}Bi_yX₆ and thereof the two fast trapping process, self-trapping and surface-defect trapping, which may also be an additional reason of lower device performance.

² End of the published article (Pantaler et al.¹⁶³)



Chapter 6. Dimensional engineering of double perovskite Cs₂AgBiBr₆

Lowering the dimensionality of hybrid perovskites is an attractive strategy for a the improvement of solar cell stability and for discovering new physical properties behind low dimensional systems. In this chapter the author develops Cs₂AgBiBr₆ lead-free double perovskites with reduced dimensionality by partially replacing Cs with large Phenethylammonium (PEA) and Benzylamine (BeA) cations leading to the formation of the n=1 compound (PEA)₂AgBiBr₆, the n=2 compounds (PEA)₂CsAgBiBr₆ and (BeA)₂CsAgBiBr₆, and the 0D compounds (BeA)₃BiBr₆, (BeA)₃BiI₆ and (PeA)₃BiI₆, so far unexplored. Single Crystals and thin films are studied by a combination of structural and optical characterization and advanced ab-initio calculations.

6.1 Introduction to low dimensional perovskites

The electronic configuration of the semiconductor materials is influenced by the chemical composition and dimensionality.^{70,71} Controlling the ordering parameter at the mixed sub-lattice, the band structure of Cs₂AgBiBr₆ changes continuously from an indirect bandgap to a narrowed pseudo-direct bandgap. This is because of the band hybridization and increased disorder of crystallization. For further controlling the ordering parameter, the octahedra are shifted and different steric sizes can be introduced to the A-site by doping or atomic substitution, such as methylammonium (MA) or formamidinium (FA), to further alternate the electronic configuration.⁷² The use of the organic cations is theoretically investigated for a few double perovskites. Some double perovskites with Ag⁺ and Bi³⁺ have been synthesized showing the potential for replacing Pb²⁺ in double perovskites when coupled with organic species.^{77,78,79} Elemental substitution is an effective method for tuning the optoelectronic properties. Thus, several attempts have been made to modify the electronic structure of double perovskites.⁶³ To the other extreme, reducing the perovskite dimensionality is an interesting way to fine tune the material band gap and vary the physical properties. To date, only a few compounds have been investigated, which are fully lead-free. Tin based low dimensional lead-free perovskites show excellent optoelectronic properties such as high hole mobility¹⁶⁷, bright orange electroluminescence¹⁶⁸ and stable, highly oriented perovskite films³⁵. Except of potential use in LEDs, the tin based low dimensional perovskites have shown stable and so far best tin based performance lead free solar cells. Solar cells using tin (Sn) perovskites with lower dimensionality by incorporating 5-ammoniumvaleric acid (5-AVA)¹⁶⁹ organic cations and employing quasi 2D iodide perovskite and second the mixed organic cations n-butylamine (BA) and phenylethylamine (PEA) in 2D Ruddlesden-Popper Sn perovskite reached in both cases power conversion efficiencies up to 9%.³⁵ Recently, the new class of low dimensional lead free double perovskite materials has been introduced.^{170,171} First low dimensional double perovskite material have been reported by Connor et al. They investigated the dimensional confinement of double perovskites introducing butylamine cation into the double perovskite structure resulting in layered perovskites for n=1 (BA)_nAgBiBr₆ and n=2 (BA)₂CsAgBiBr₆, where *n* is the number of octahedra layers. Furthermore, Jana et al. reported on 2D silver-bismuth iodide double perovskites by introducing the spacer molecule 5,5'-diylbis(aminoethyl)-[2,2'-bithiophene] (named AE2T) resulting in the lead-free 2D double perovskite [AE2T]₂AgBiI₆. In both cases the alteration from the indirect to direct bandgap by lowering the dimensionality was observed.

6.1.1 Low Dimensional Lead Free Perovskites: PeABr1 and PeABr2

In this section the author introduced the phenylethylamine (PEA⁺ cation) into the double perovskite matrix to lower the material dimensionality and investigate the resulting structural, optical properties of such newly designed materials.^{170,171} The low dimensional lead-free is designed perovskite by introducing the PEA⁺ cation in the inorganic matrix of double perovskites. This defines low dimensional double perovskites in the form of n=1 and n=2 where n is the number of the inorganic octahedra layers separating by organic cation layer. The resulting materials with n=1 is (PEA)_nAgBiBr₆, the material with n=2 is (PEA)_nCsAgBiBr₆. A combined theoretical and experimental study is presented showing the massively different optoelectronic properties and energetic structure when going from n=1 to n=2. The band gap goes back from direct to indirect for n=2, promoting the existence of a long living emissive species in the mid gap region. Owing to the peculiar electronic structure, the n=2 perovskite shows a broad emission ranging from 525 nm to 725 nm.

6.1.1.1 Experimental results

In order to determine the structural properties of such low dimensional class of double perovskites, both single crystals and thin films have been prepared.

(PEA)_nAgBiBr₆ (short *PeABr1*) and (PEA)_nCsAgBiBr₆ (short *PeABr2*) in the form of single crystals have been prepared following a slow crystallization method. To obtain PeABr1 single crystals, phenylethylamine bromide (PeABr, 2 mmol), bismuth bromide (BiBr₃, 0.5 mmol), and silver bromide (AgBr, 0.5 mmol) were dissolved in 4mL hydrobromic acid (HBr) at 100°C. For PeABr2, phenylethylamine bromide (PeABr, 1 mmol), bismuth bromide (BiBr₃, 0.5 mmol), and silver bromide (AgBr, 0.5 mmol) and caesium bromide (CsBr, 0.4 mmol) were dissolved in 4 mL hydrobromic acid (HBr) at 100°C. The solution was saturated and kept at 100°C for 1h until all compounds were dissolved. The single crystals were prepared growing from the saturated aq. HBr solution by cooling the solution down with a cooling rate of 3°C/h. The yellow crystals were filtered. After filtration, the crystals were washed with a diethyl ether and dried in a vacuum oven at room temperature overnight. The materials yielded into yellow plate-like crystals with crystal size of around 3x3x0.2 mm³ as shown in the inset of Figure 88c.

The single crystals were characterized by single crystal X-ray diffraction (XRD). The results are shown in Figure 88c and the crystallographic data are reported in Table 15 compared to

cubic Cs₂AgBiBr₆ ($n=\infty$) double perovskite as a reference. Figure 88a shows the layered structure of the PeABr1 \rightarrow (PEA)₄AgBiBr₈ single crystal structure. It crystallizes in the triclinic (P-1 space group) structure with lattice parameters $a=11.5184 \text{ \AA}$, $b=11.6000 \text{ \AA}$ and $c=17.3678 \text{ \AA}$ and $\alpha=106.624$, $\beta=100.528$ and $\gamma=90.203^\circ$ with (100) orientation. The inorganic layer is composed of corner-sharing AgBr₆ and BiBr₆ octahedra spaced by the large phenylethylamine (PEA⁺) cations. Figure 88b shows the layered structure of the PeABr2 \rightarrow (PEA)₂CsAgBiBr₇ single crystal which also exhibits a triclinic structure (P-1 space group) with lattice parameters $a=7.9591 \text{ \AA}$, $b=8.0394 \text{ \AA}$ and $c=22.6161 \text{ \AA}$ and $\alpha=97.634$, $\beta=93.818$ and $\gamma=90.2700^\circ$. A marked (100) orientation is observed also in this case. Here, the inorganic sheets are thicker, constituted by two layers of AgBr₆ and BiBr₆ octahedra held together by the caesium (Cs⁺) cation, separated by the layer of the organic cation PEA⁺. Notable, the inorganic sheets in both compounds are highly distorted at the Ag site. For (PEA)₄AgBiBr₈ the Ag-Br octahedra show a tetragonal distortion due to a shortening of the bond lengths between the Ag and the axial boundary bromides ($\text{Ag-Br}_{\text{ax}} = 2.66 \text{ \AA}$) and an elongation of the bond length between the Ag and the bridging equatorial bromides ($\text{Ag-Br}_{\text{eq}} = 3.05 \text{ \AA}$). For (PEA)₂CsAgBiBr₇ the Ag atoms lie out of plane on either side of the inorganic sheets. The reason can be associated to the *pseudo-Jahn-Teller effect* as observed in other low dimensional perovskites where the empty *d* orbitals of the monovalent Ag are mixed with filled high energy *p* orbitals (bromine) to stabilize a distorted structure observed as well by Connor et al.¹⁷⁰

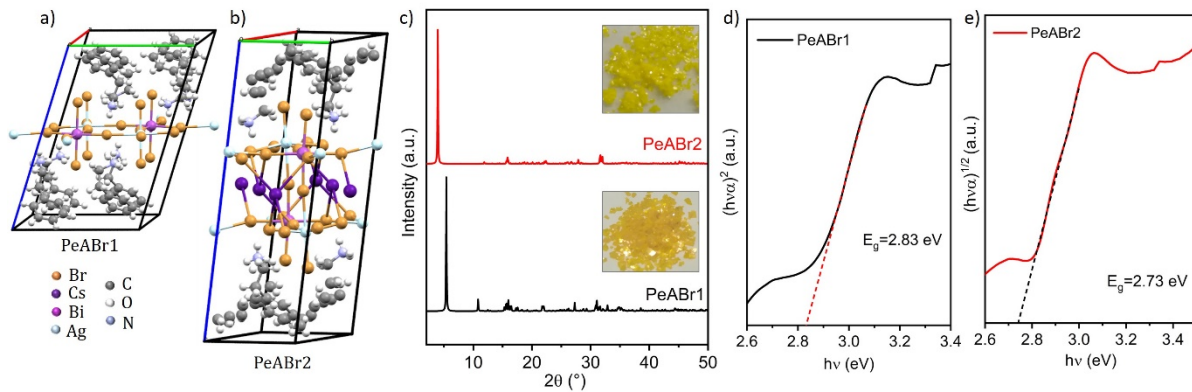


Figure 88 **a)** Crystal structure of (PEA)₄AgBiBr₈ (named PeABr1), **b)** crystal structure of (PEA)₂CsAgBiBr₇ (named PeABr2) **c)** XRD diffraction of single crystals PeABr1 and PeABr2, (the inset shows the single crystals) **d)** Tauc plot of the PeABr1 and **e)** PeABr2 derived from reflectance measurements.

Figure 88c shows the XRD patterns of the single crystals of (PEA)₄AgBiBr₈ and (PEA)₂CsAgBiBr₇. The main reflections display the (100) orientation. One can see a peak shift

from 5.397° to 3.945° going from material with n=1 (PeABr1) to higher dimensionality of material with n=2 (PEABr2), in agreement to what is expected for perovskites upon reducing dimensionality.¹⁷²

Table 15 Derived crystallographic data of the (PEA)_nAgBiBr₆ and (PEA)_nCsAgBiBr₆ single crystals compared to the reference Cs₂AgBiBr₆.

Perovskites	PeABr1 → (PEA) ₁ AgBiBr ₆		PeABr2 → (PEA) ₂ CsAgBiBr ₆		Cs ₂ AgBiBr ₆	
Space group	Triclinic (P -1)		Triclinic (P -1)		cubic	
Lattice parameters	a = 11.518 Å	α = 106.624°	a = 7.9591 Å	α = 97.634°	a = 11.2499 Å	α = 90 °
	b = 11.600 Å	β = 100.528°	b = 8.0394 Å	β = 93.818°	b = 11.2499 Å	β = 90°
	c = 17.368 Å	γ = 90.203°	c = 22.616 Å	γ = 90.2700°	c = 11.2499 Å	γ = 90°

6.1.1.2 Theoretical calculations for the lead – free layered perovskites

(Theoretical calculations have been conducted by prof. David Beljonne group from Universite de Mons)

Theoretical calculations were performed at the Density Functional Theory (DFT) level¹⁷³ with Periodic Boundary Conditions (PBC) in order to study the impact of the dimensionality reduction in the electronic structure of these materials. All calculations have been conducted by the group of Prof. David Beljonne within Quantum Espresso work package.¹⁷⁴ Figure 89b shows the band structures for the studied double perovskites Cs₂AgBiBr₆, PeABr2 and PeABr1 were the relativistic effects were included (SOC) or avoided (no SOC). The spin orbit coupling (SOC) is mainly affecting the *p* states of the Bi atoms, which are mainly localized at the conductance band (CB) edges. As a result, the bandgap values are substantially lowered respect the non-relativistic calculations. This effect is especially remarkable in Cs₂AgBiBr₆ (Figure 89a), which reveals the importance of including relativistic effects for a proper description of the electronic structure in this type of perovskites, as it has been already pointed out for both bulk⁵⁸ and layered^{170,171} systems. The most important consequences of the quantum confinement is the change in the nature of the bandgap and the bands dispersion. While Cs₂AgBiBr₆ and PeABr2 systems presents indirect bandgaps corresponding to the X→L and A→B transitions respectively; PeABr1 displays a direct bandgap in Γ point. The same behaviour was reported

with BA spacers employed as organic layer,[Connor et al.] which confirms that the modification in the nature of the bandgap is a consequence of the dimensionality reduction independently of the organic layer employed, at least for Type I inorganic quantum wells (QWs). Regarding the band dispersion, the bands become flatter when reducing the dimensionality of the perovskites. In order to quantify this effect, we have estimated the hole/electron effective masses by means of parabolic fitting around the VB/CB edges along the in-plane (100), (010), (110) and out-of-plane (001) directions. The magnitude of these effective masses is presented in Table 16. Both hole and electron masses become heavier due to the quantum confinement effects, being this outcome notably considerable for the hole transport in PEABr₂ and the electron transport in PEABr₁. This finding has been detected in standard metal-organic lead halide perovskites as well, but in this case the magnitude of the effective masses is much lower (3-6 times) respect the systems studied in this work.^{175,176}

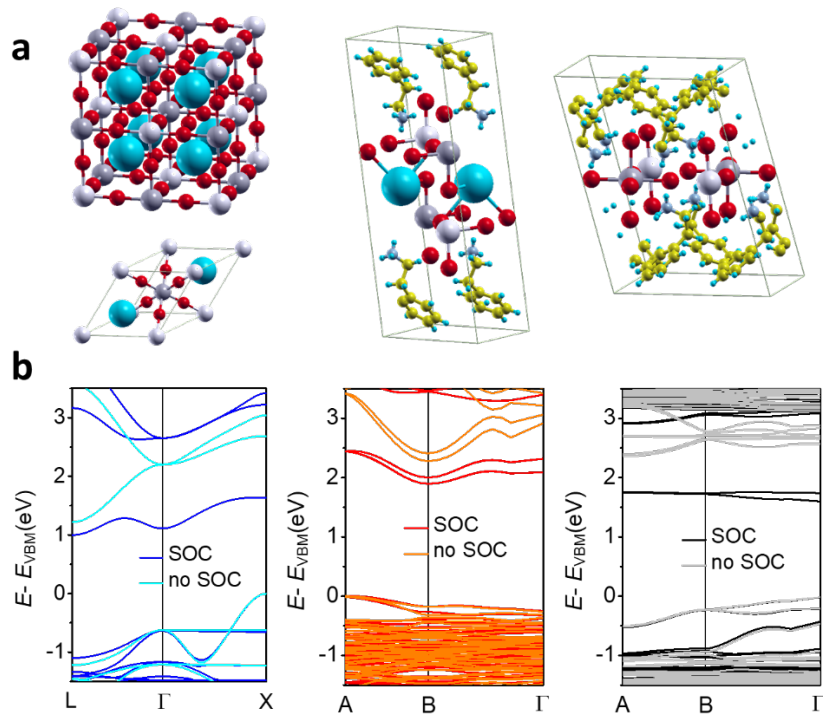


Figure 89 a) Perspective view of the unit cells employed in the modelling and b) band structures for Cs₂AgBiBr₆, PeABr₂ and PeABr₁ systems (from left to right). Note that for the band structures the energy of the VB edge has been selected as energy reference; and the A and B points in the layered systems are the equivalent to X and L points of the bulk in the reciprocal space. Color legend is: Cs (light blue, bigger atoms), Bi (dark grey, bigger atoms), Br (red), C (yellow), H (blue, smaller atoms) and N (grey, smaller atoms).

Table 16 Calculated effective masses by parabolic fitting.

	Cs ₂ AgBiBr ₆			PEABr2			PEABr1		
	h^{\dagger}	e^{\dagger}	μ	h^{\dagger}	e^{\dagger}	μ	h^{\dagger}	e^{\dagger}	μ
	<i>in-plane</i>								
G → 100	0.32	0.63	0.21	1.02	0.90	0.48	1.00	1.87	0.65
G → 010	0.32	0.63	0.21	1.80	0.37	0.30	1.21	1.86	0.73
G → 110	0.26	0.37	0.15	0.99	0.26	0.21	0.55	0.96	0.35
	<i>out-of-plane</i>								
G → 001	0.32	0.63	0.21	∞	∞	∞	∞	∞	∞

According to the composition of the band edges, as it is expected due to the relatively large gap of the organic layers, both VB and CB edges are localized on the inorganic perovskite part, thus displaying the characteristics from a Type I inorganic QW where the organic part is not directly participating in the opto-electronic properties of the system. Moreover, the energetic barrier in the VB between organic and inorganic parts is increasing when reducing the dimensionality of the perovskite layer (Figure 90ab). The CB edge composition is very similar for the three perovskites with a 50:50 composition of Bi 6*p*- Br 4*p* states. In the case of Cs₂AgBiBr₆, there is some contribution from the Ag 5*s*. Regarding the VB edge, both Cs₂AgBiBr₆ and PeABr2 compositions are identical, being dominated by the Br 4*p* orbitals, due to their similar gap behaviour. However, PeABr1 VB edge possesses an important mix between Ag *d*- Br 4*p*, which results in an Ag→Bi charge transfer (CT) character at the band edges centred at Γ . This CT behaviour may explain the weak absorption in the VIS region presented by this compound (see Figure 94a).

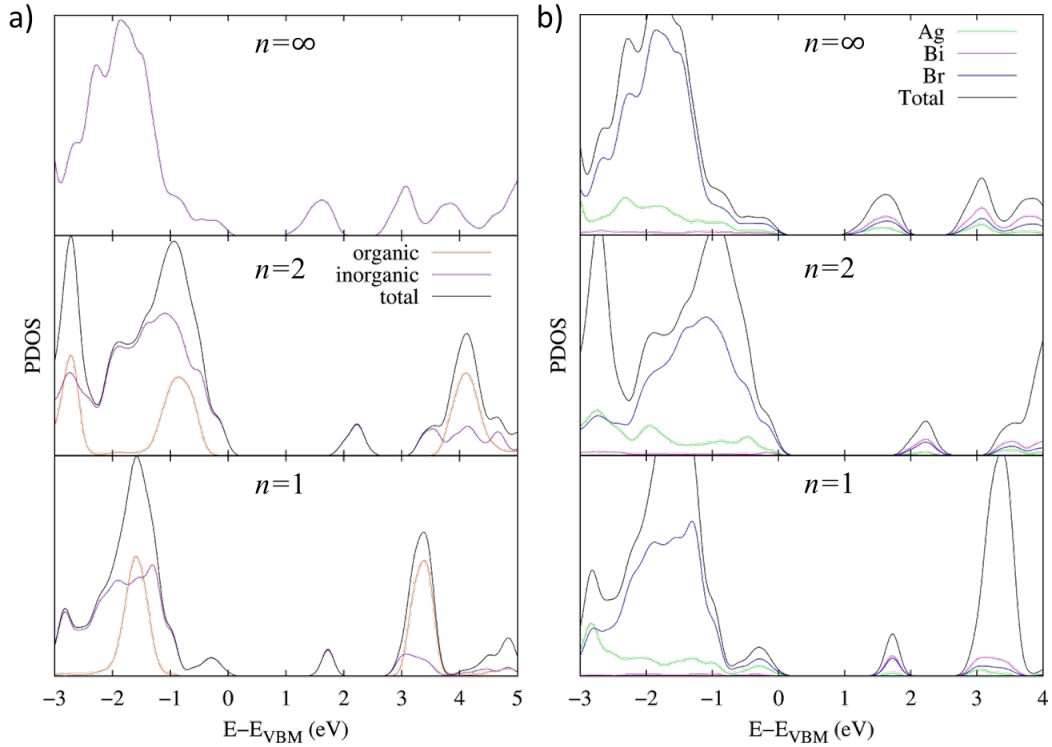


Figure 90 Projected Density of States (PDOS) over **a)** organic (orange) and inorganic (purple) parts; and **b)** Ag (green), Bi (purple), and Br (blue) atoms. The energy of the VB edge has been taken as reference.

By looking at the absolute value of the calculated gaps, one realizes that the magnitudes of the estimated gaps are about 1 eV lower respect the experiments. As it has been pointed out in the literature, the correct estimation of the energy gaps implies the description of many body and relativistic effects.^{177,178} In this purpose, we employed hybrid functionals where a percentage of Hartree-Fock exchange-correlation (25%) is added to the previous DFT calculations in order to correct the values of the gap. Since the magnitudes of the gaps are highly biased by the distortion of the octahedra structure⁷⁹, we have compared the results of the bandgaps calculated when using the experimental cell (fixed unit cell) or optimizing the cell parameters during the optimization. The values of the calculated gaps are collected in Table 17. As one may expect, the relaxation of the cell parameters allows the structures to go under a larger orbital overlap, which implies smaller values for the gap. This result is remarkably larger for PeABr₂. The calculated values are close to those obtained by Tauc plot analysis (Figure 88d) especially for the variable cell relaxation, showing both methods an increase in the gap magnitude of 0.8 eV when moving from the bulk to the layered systems, as a result of the quantum confinement.

Table 17 Bandgap values in eV estimated by DFT calculations (theo) with fixed (left) and variable (right) unit cell parameters; and by Tauc plot (exp).

Unit cell eV	fixed unit cell			variable unit cell		
	$n=\infty$	$n=2$	$n=1$	$n=\infty$	$n=2$	$n=1$
$E_{g\text{ theo}}$	2.30	3.20	3.02	2.15	2.94	2.96
$E_{g\text{ exp}}$	2.2	2.8	2.8	2.2	2.8	2.8

Finally, we have analysed the indirect influence of the organic layers in the calculated gaps. In order to do so, we have compared the values of the gaps calculated at standard DFT level of theory with those obtained from the layered perovskites of the work of Connor et al, where BA was used as organic spacer. In addition, in order to rationalize these quantities, we have plotted the values of the gaps as a function of the in-plane and out-of-plane octahedra tilted angles. This graph is showed in Figure 91. The gaps of PeABr₂ are slightly higher respect the ones of PeABr₁, mainly motivated by the broad out-of-plane tilting of the octahedra centred at the Ag atoms present in PeABr₂ structures. As it was pointed in the previous paragraph, this energy gap difference is reduced when relaxing the cell parameters of the unit cells (Table 17). By comparing the values of the gaps obtained with both PeA and BA spacers, one note that for both layered systems the former case possesses larger gaps. The reason behind that is the bigger rigidity of the PeA vs BA spacers, which hinder the relaxation of the structures and enhances the distortion, as it can be verified by checking the values of both tilted angles (Figure 91).

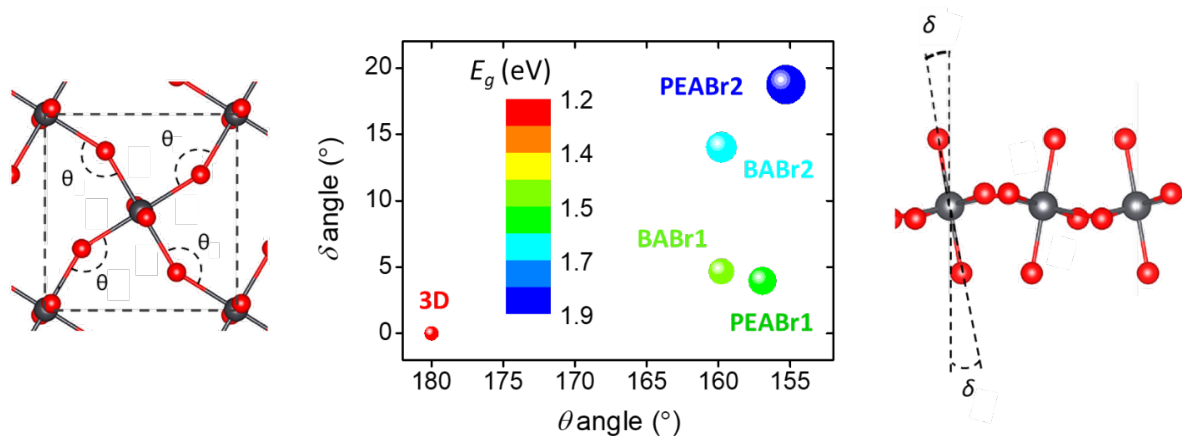


Figure 91 Band gap values (colour scale inset) as function of the in-plane (θ as represented on the left onset) and out-of-plane (δ , on the right onset) tilted angles for Cs₂AgBiBr₆, PeABr₂, PeABr₁, BABr₂ and BABr₁ compounds.

6.1.1.3 Optical and Structural Characterization

The theoretical results are in fair agreement with the experimental data (Figure 88). Figures 88d,e show the calculated Tauc-plot from reflectance measurements (Figure 92). For PeABr1 (Figure 88d) an estimated value of 2.83 eV for the band gap is obtained considering a direct transition while for PeABr2 (Figure 88e) a bandgap of 2.73 eV has been retrieved using the indirect transition formula. According to the electronic landscape $\text{Cs}_2\text{AgBiBr}_6$ shows an indirect band gap where the valence band has contribution of Ag d , Bi s , and Br p orbitals at \mathbf{X} , whereas the conduction band contains contribution of Ag s , Bi p , and Br p orbitals at \mathbf{L} . In the calculations, the band structure of PeABr2 is very similar to $\text{Cs}_2\text{AgBiBr}_6$. A further electronic consequence of dimensionality reduction in the PeABr1 case, is that we observe a direct band gap at $\mathbf{\Gamma}$ where the valence band is almost entirely composed of Ag d and Br p orbitals while to conduction band contributes to the Bi and Br p orbitals.

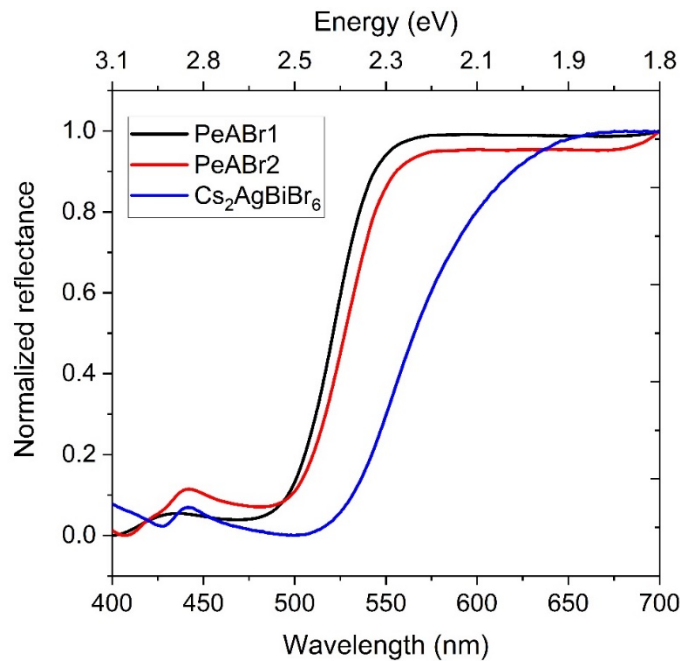


Figure 92 Reflectance for the powder samples PeABr1, PeABr2 and $\text{Cs}_2\text{AgBiBr}_6$.

The solutions for the thin films were prepared by dissolving the starting materials BiBr_3 , AgBr and PeABr in DMF for $n=1$ (PeABr1) and in DMSO for $n=2$ (PeABr2) with addition of CsBr at final concentration of 0.5 mol/L. Thin films were prepared by spin-coating deposition, using a two step program, first at 500 rpm for 30 sec and second, at 5000 rpm for 60 sec. All films were then annealed at 80°C for PeABr1 and at 100°C for PeABr2 for 4 minutes. Images of the

resulting film are shown in the inset of Figure 93c for PeABr1 and 93b for PeABr2 with the SEM images where the particles of the new materials have a needle shape. The XRD diffractogram is presented in Figure 93a showing the main reflectance (001), (002), and (003) at lower angles matching with the single crystal XRD data reported in Figure 88b. In agreement, a peak shift arises to lower diffraction angle going from $n=1$ to $n=2$.

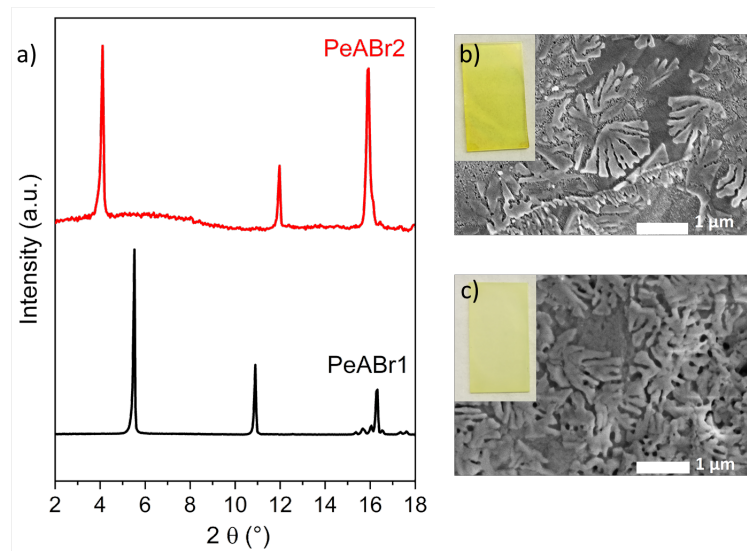


Figure 93 a) XRD diffraction of thin films for PeABr2 and PeABr1 b) SEM image of PeABr2 and c) SEM image of PeABr1.

To further investigate the properties of these thin films the absorption and photoluminescence (PL) spectra are measured as a function of temperature from 300 K to 80 K (Figure 94 and 95). Figure 96a shows the UV-VIS absorption spectra for PeABr1 and PeABr2 at 300K. In agreement with previous works, the normalized absorbance spectra were measured using thin films. They show a broad excitonic peak at 382 nm with absorbance onset at 463 nm for PeABr1, while PeABr2 shows an absorption onset at 475 nm and a narrow excitonic peak at 435 nm.

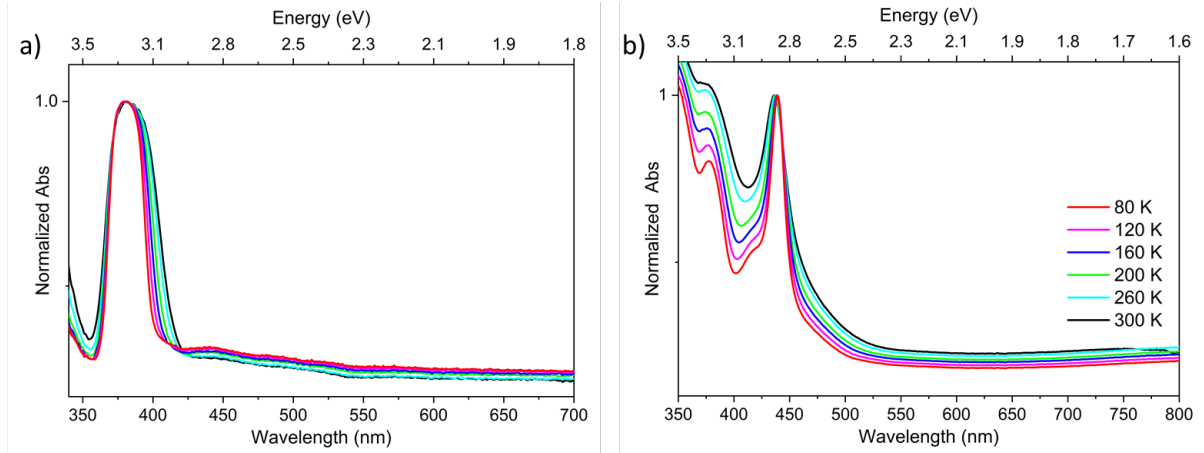


Figure 94 Low temperature absorbance for a) PeABr1 and b) PeABr2.

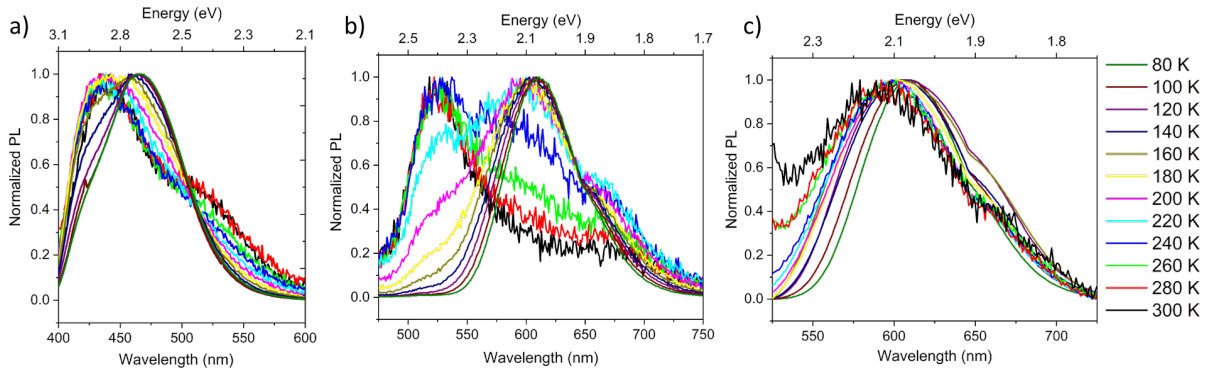


Figure 95 Low temperature PL shows a slight redshift for a) PeABr1, b) PeABr2, c) Cs₂AgBiBr₆.

Notably, for $n=1$ the broad peak at the band edge has no T dependence (Figure 94a), ruling out an excitonic character. The broad band can be assigned to a transition involving localized energy levels with a high density of states that gives strong optical absorption over a narrow energy window, consistent with the fairly flat VB and CB¹⁷⁰. In contrast to literature, in this case a remarkable peak is observed at room temperature which gets sharper at lower temperature, indicative of an excitonic transition peaking at 2.9 eV. On top of Figure 94b, at higher energies around 3.2 eV an onset is overlapping with the absorption edge for $n=1$ suggesting that they arise from a related transition and they might possess Ag-Bi charge transfer (CT) character. In $n=1$ this CT transition occurs at the band gap, while in $n=2$ it is far from the band extrema at higher energy transitions (in agreement with Connor et al.¹⁷⁰). A striking difference is here observed related to a clear exciton like feature in the absorption spectra for $n=2$.

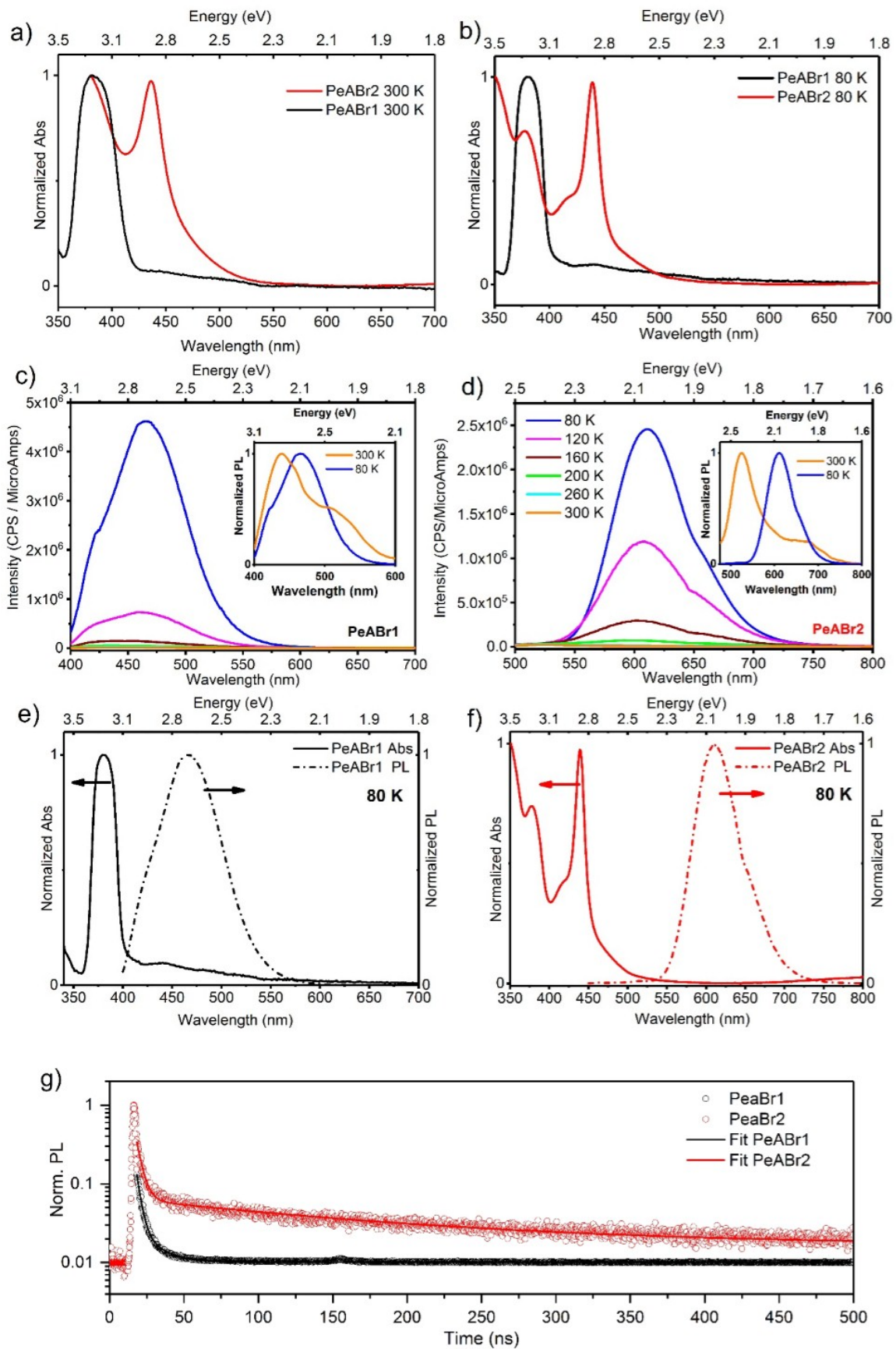


Figure 96 a) Absorption of PeABr1 and PeABr2 at 300K and b) at 80K, c) The low temperature PL of PeABr1 with inset of extreme normalized values (comparison between 80 K and 300 K), d) the low temperature PL of PeABr2 with inset of extreme

normalized values comparison, e) comparison of normalized photoluminescence and absorption of PeABr1 at 80K, f) comparison of normalized photoluminescence and absorption of PeABr2 at 80K, g) The PL decay fitted with a biexponential function for PeABr1 at 450 nm and PeABr2 at 600 nm, at their relative peak position.

For PeABr2 and Cs₂AgBiBr₆ materials it is an indirect transition contributed by the Bi *s-p* transition while in PeABr1 the transition nature may be direct and contributed by the Ag-Bi CT character. Note that upon reducing temperature, the author does not observe any additional phase change or rigid shift indicative of no structural changes in the temperature range investigated (Figure 94).

All absorption and photoluminescence data of samples measured at room and low temperature are summarized in Table 18.

Table 18 Absorption and photoluminescence data of thin films of 2D double perovskites.

Material		Exitonic peak	PL	Bandgap
n=1	(PEA) _n AgBiBr ₆	3.25 eV (300K) 3.27 eV (80K) No exitonic?	2.86 eV (300 K) 2.66 eV (80K)	Direct 2.83 eV
n=2	(PEA) ₂ CsAgBiBr ₆	2.85 eV (300 K) 2.82 eV (80K) Excitonic	2.33 eV (300K) 2.03 eV (80 K)	Indirect 2.73 eV

Figure 96b, c show the PL spectra upon reducing T. For n=1 a weak but clear emission is observed. In contrast to previous literature it gains intensity with reducing temperature. On the other side, the PL for n=2 is completely different. Lowering the temperature, it experience a severe red shift and it increases in intensity, showing a broad below gap emission. In the inset of Figure 96c a red shift of 2.86 eV to 2.66 eV can be observed when decreasing temperature. Such band can be assigned to mid gap states as a result of possible self-trapping.

Figure 96g shows the TRPL signal collected at room temperature at the PL peak position. From n=2 the lifetime increases from 50 ns to more than the investigated time window of 500 ns, which can be related to long living self-trapped excitons in the system, delivering a broad white emission.

The PL decays are displayed in Figure 96g and Table 19. The decay can be fitted with a biexponential function giving a first fast time constant of $\tau_1=3.7$ ns for PeABr1 and $\tau_1=2.8$ ns for PeABr2 followed by a slower drop of $\tau_2=12.7$ ns and $\tau_2=159.7$ ns, respectively. The fast decay can be associated to excitonic surface recombination, while the longer lifetime can be related to trap-assisted recombination.

Table 19 PL decay parameters for PeABr1 and PeABr2.

Equation	ExpDecay2	
	$y = y_0 + A_1 * \exp(-(x-x_0)/t_1) + A_2 * \exp(-(x-x_0)/t_2)$	
Compound	PeaBr2	PeaBr1
y0	0.01661 ± 1.0297E-4	0.01013 ± 7.10028E-6
x0	18 ± 0	18 ± 0
A1	0.30382 ± 0.00192	0.11714 ± 5.47447E-4
τ_1 (ns)	3.67916 ± 0.0341	2.77475 ± 0.02166
A2	0.04598 ± 3.0729E-4	0.01782 ± 6.08278E-4
τ_2 (ns)	159.68899 ± 2.01854	12.65886 ± 0.28589
Reduced Chi-Sqr	1.20185E-05	1.87635E-07
Adj. R-Square	0.969584786	0.993830997

6.1.2. BeABr1 and BeABr2

6.1.2.1 Experimental Results: Material Preparation

In order to determine the structural properties of the low dimensional class of double perovskites, the benzylamine cation (BeA) has also been considered. Both single crystals and thin films have been prepared.

(BeA)₃BiBr₆ (shorted *BeABr1*) and (BEA)₂CsAgBiBr₆ (shorted *BeABr2*) in the form of single crystals were prepared following a slow crystallization method. To obtain BeABr1 single crystals, benzylamine bromide (BeABr, Sigma Aldrich, 2 mmol), bismuth bromide (BiBr₃, Sigma Aldrich, 0.5mmol), and silver bromide (AgBr, Sigma Aldrich, 0.5mmol) have been dissolved in 4mL hydrobromic acid (HBr) at 100°C. For BeABr2, benzylamine bromide (BeABr, Sigma Aldrich, 1 mmol), bismuth bromide (BiBr₃, Sigma Aldrich, 0.5mmol), silver bromide (AgBr, Sigma Aldrich, 0.5mmol), and caesium bromide (CsBr, 0.5 mmol) have been dissolved in 4mL hydrobromic acid (HBr) at 100°C. The solution was saturated and kept at 100°C for 1h until all compounds dissolved. The single crystals were prepared growing from the saturated aq. HBr solution by cooling down the solution with a cooling rate of 3°C/h. The as-obtained yellow crystals were filtered. After filtration, the crystals were washed with diethyl ether and dried in a vacuum oven at room temperature overnight. The fabricated single crystals were characterized by single crystal X-ray diffraction (XRD). The results are shown in Figure 97 for n=1 (calculated) and Figure 98 for n=2. Crystallographic data are reported in Table 20. Figure 97 shows the molecular 0D structure of the BeABr1 → (BEA)₃BiBr₆ single crystal. It crystallizes in a monoclinic (P21/c space group) crystal structure with lattice parameters a=15.2973 Å, b= 8.0840 Å and c= 24.3024 Å and α=90°, β=99.738° and γ =90° with dominant diffraction at 5.86° and (100) orientation (Figure 97b). The inorganic part of the compound is composed by corner-sharing BiBr₆ octahedra spaced of the benzylamine (BEA⁺) cations. There is no layered structure formed. The layered structure in the case of BeABr1 is not achieved due to the crystallization process and the silver. Ag is not incorporated into the double perovskite structure (Figure 97a). In literature similar materials have been reported (i.e. BeABiI₃) showing humidity stability for optoelectronic applications with more than 330 days, which is the longest humidity stability reported to date for lead-free perovskite materials showing a possibility in LEDs applications.¹⁸⁰ For BeABr1 there are no reported data in literature yet.

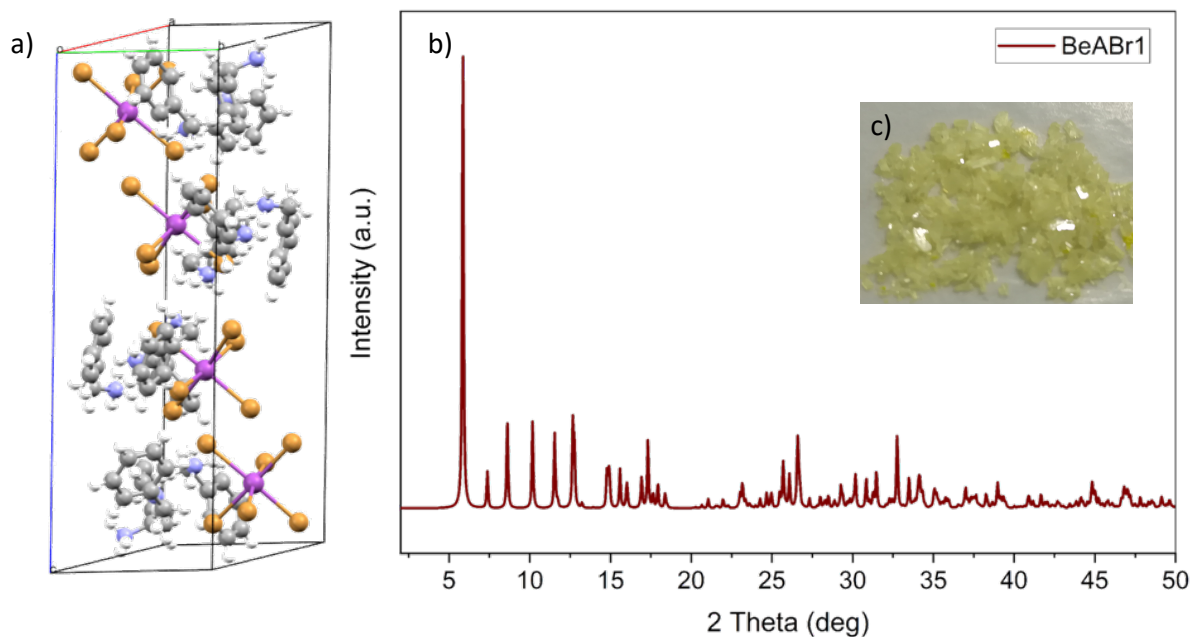


Figure 97 a) Crystal structure of (BEA)₂BiBr₆ (named BeABr1), where the atoms are Br-orange, Bi-violet, C-grey, N-blue, H-white b) XRD diffraction of single crystals BeABr1, c) in the inset the single crystals picture.

Figure 98a shows the layered structure of the BeABr₂ → (BEA)₂CsAgBiBr₇ single crystals which crystallize in the triclinic structure (P-1 space group) with lattice parameters $a=11.2826$ Å, $b=11.333$ Å and $c=22.6028$ Å and $\alpha=87.255$, $\beta=81.929$ and $\gamma=89.529^\circ$ with (100) orientation at 3.95° . The inorganic sheets are layered, constituted by two layers of AgBr₆ and BiBr₆ octahedra held together by caesium (Cs⁺) cation, separated by the organic cation BEA⁺ layer. The inorganic sheets in this compound are also highly distorted compared to PeABr1 and PeABr2 at the Ag site. The (BEA)₂CsAgBiBr₇, the Ag atoms are out of plane from either side of the inorganic sheets also associated to the *pseudo-Jahn-Teller effect* as observed in other low dimensional perovskites.¹⁷⁰ The materials are yellow plate-like crystals with a crystal size of around $3 \times 3 \times 0.2$ mm³ as shown in Figure 97c and 98c.

Related to previous theoretical calculations for the new compounds with PeA cation, the author assumes that in the case of the BeA low dimensional double perovskites, the bandgap alter from indirect to pseudo-direct for quasi 2D.

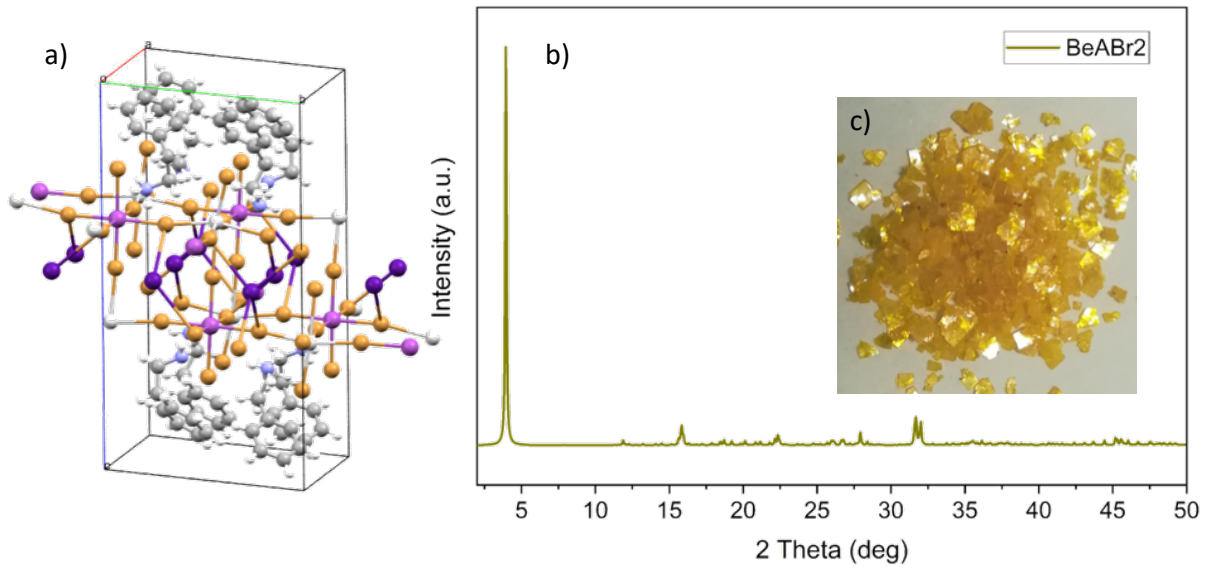


Figure 98 a) crystal structure of (BEA)₂CsAgBiBr₆ (named BeABr₂) where the atoms are Br-orange, Bi-violet, C-grey, N-blue, H-white, Ag- light grey and Cs- dark violet b) XRD diffraction of single crystals BeABr₂, c) image of single crystals.

Table 20 Crystallographic data of the (BEA)₂BiBr₆ and (BEA)₂CsAgBiBr₆ single crystals.

Perovskites	BeABr1		BeABr2	
Space group	P2 1/c - monoclinic		P-1 triclinic	
Lattice parameters	a = 15.2973 Å	$\alpha = 90^\circ$	a = 11.2826 Å	$\alpha = 87.255^\circ$
	b = 8.0840 Å	$\beta = 99.738^\circ$	b = 11.3333 Å	$\beta = 81.929^\circ$
	c = 24.3024 Å	$\gamma = 90^\circ$	c = 22.6028 Å	$\gamma = 89.529^\circ$

6.1.2.2. Optical and Structural Characterization

Optical measurements were conducted on thin films. The films were prepared using the same fabrication method described above. The solutions for the thin films were prepared by dissolving the starting materials BiBr₃, AgBr and BeABr in DMF for n=1 (BeABr1) and in DMSO for n=2 (BeABr2) with addition of CsBr of 0.5 mol/L. Thin films were prepared by spin-coating deposition using a two step program, first at 500 rpm for 30 sec and second, at 5000 rpm for 60 sec. All films were then annealed at 100° for BeABr1 and at 135°C for BeABr2 for 4 and 7 minute, respectively, resulting in yellow color and needle-like particles shown in

Figure 100bc. The figure 99 and Table 21 shows the UV-VIS absorption spectra and PL for the BeABr1 and BeABr2 at 300K.

For BeABr1 (Figure 99a) a bandgap of 2.7 eV is found, and for BeABr2 (Figure 99b) a bandgap of 2.73 eV using the absorption onset. Additional calculation for these two compounds have to be provided to simulate the band diagrams and provide the nature of the transition mechanism. The author assume that the band structure of the BeABr2 may be very similar to double perovskite Cs₂AgBiBr₆ and PeABr2 resulting in an indirect bandgap and broad PL emission. The normalized absorption spectra for n=1 (BeABr1) has a broad excitonic peak at 2.96 eV, likely no exciton, and an emissive PL peak at 2.7 eV shown in Figure 99a. The normalized absorption for n=2 is narrow and more intensive than for n=1. The PL spectra in Figure 99b show broad emission with a PL peak at 2.1 eV indicating the Ag-Bi CT transition or self-trapping recombination.

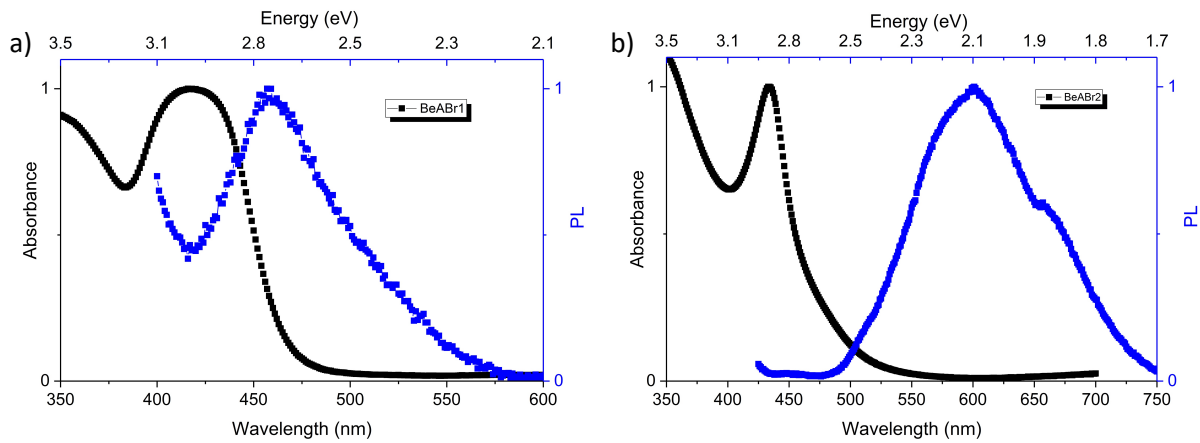


Figure 99 Normalized absorbance and photoluminescence measured at room temperature for a) BeABr1 and b) BeABr2.

Table 21 Absorption and photoluminescence data of thin films of new BeABr1 and BeABr2.

Compound	Exciton peak	PL	Band gap
(BEA) ₂ BiBr ₆	2.96 eV (300K) No excitonic	2.71 eV	Direct 2.6 eV
(BEA) ₂ CsAgBiBr ₆	2.91 eV (300 K) Excitonic	2.07 eV	Indirect 2.4 eV

Figure 100 shows the TRPL signal collected at room temperature at the PL peak position. The PL decay is similar to the previous one for PeABr1 and PeABr2 materials. For BeABr2 the

lifetime increases which can be related to long living self-trapped exciton in the system, delivering a broad white emission, similar to the PeABr₂ case.

The decays are fitted with a biexponential function (Table 22) giving a first fast time constant of $\tau_1 = 3.95$ ns for the BeABr₁ and $\tau_1 = 3.3$ ns for BeABr₂ followed by slower drop of $\tau_2 = 108.75$ ns and $\tau_2 = 118.86$ ns, respectively. The fast decay can be associated with excitonic surface recombination, while the longer lifetime can be related to trap-assisted recombination which is similar to the PeA case.

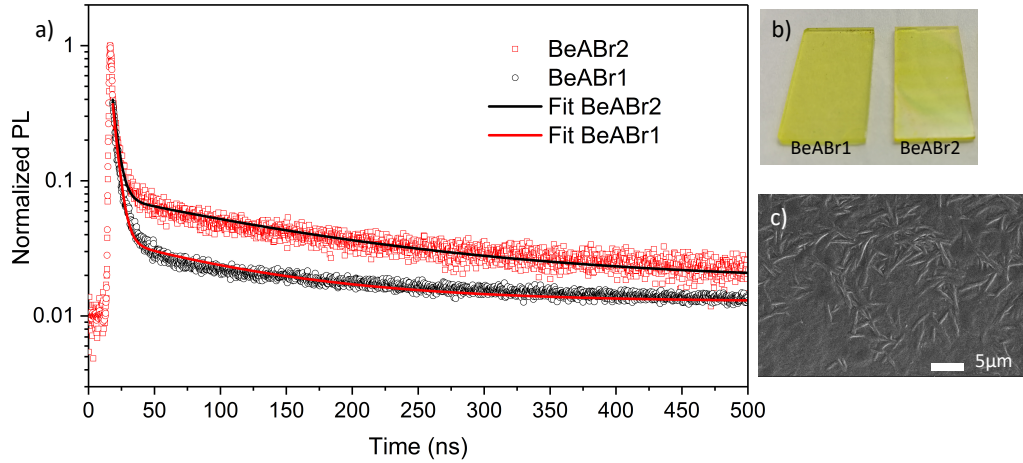


Figure 100 a) The PL decay fitted with a biexponential function for BeABr₁ at 450 nm and BeABr₂ at 600 nm, at their relative peak positions, b) images of thin films, c) SEM of BeABr₂.

Table 22 PL decay parameters for BeABr₁ and BeABr₂.

Equation	ExpDecay2	
	$y = y_0 + A1 \cdot \exp(-(x-x_0)/t_1) + A2 \cdot \exp(-(x-x_0)/t_2)$	
Compound	BeaBr2	BeaBr1
y ₀	$0.01512 \pm 7.14043E-5$	$0.01278 \pm 4.78246E-5$
x ₀	18 ± 0	18 ± 0
A ₁	0.35856 ± 0.00177	0.36453 ± 0.00111
τ_1 (ns)	3.33613 ± 0.02428	3.94902 ± 0.0186
A ₂	$0.03715 \pm 3.20151E-4$	$0.0234 \pm 2.50903E-4$
τ_2 (ns)	118.86175 ± 1.63593	108.74781 ± 1.74495
Reduced Chi-Sqr	$8.93082E-6$	$4.38121E-6$
Adj. R-Square	0.97592	0.98777

6.1.3. PeAI1 and BeAI1

6.1.3.1. Experimental results

The author used iodine to engineer the bandgap of the low dimensional double perovskites. The following materials were synthesised. (PEA)₂BiI₆ (shorted *PeAI1*) and (BEA)₂BiI₆ (shorted *BeAI2*) in the form of single crystals and thin films. The single crystals were synthesized by the slow crystallization method. To obtain PeAI1 single crystals, phenylethylamine iodine (PeAI, 2 mmol), bismuth iodide (BiI₃, 0.5 mmol), and silver iodine (AgI, 0.5 mmol) were dissolved in 4mL hydroiodic acid (HI) at 100°C. The solution was saturated and kept at 100°C for 1h until all compounds dissolved. The single crystals were prepared growing from the saturated aq. HI solution by cooling down the solution of a cooling rate of 3°C/h. The as-obtained red crystals were filtered. After filtration the crystals were washed with a diethyl ether and dried in a vacuum oven at room temperature overnight. Red plate-like crystals resulted with crystal sizes of around 3x3x0.2 mm³ as shown in the inset of Figures 101c, 102c.

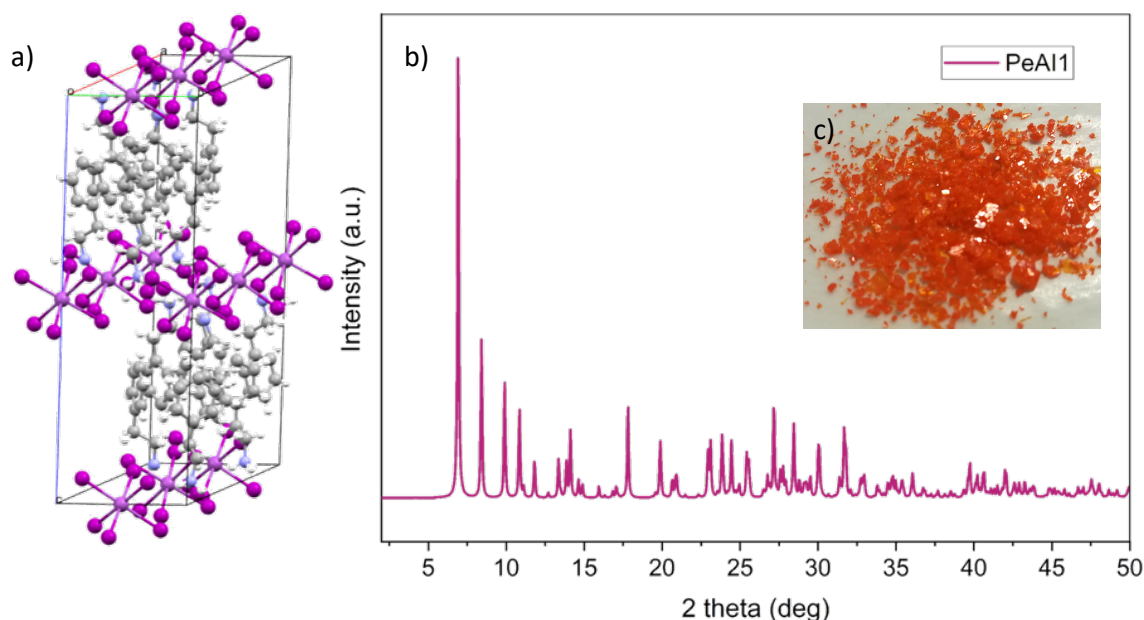


Figure 101 **a)** Crystal structure of (PEA)₂BiI₆ (named PeAI1), **b)** XRD diffraction of single crystals PeAI1, **c)** in the inset the single crystals pictures.

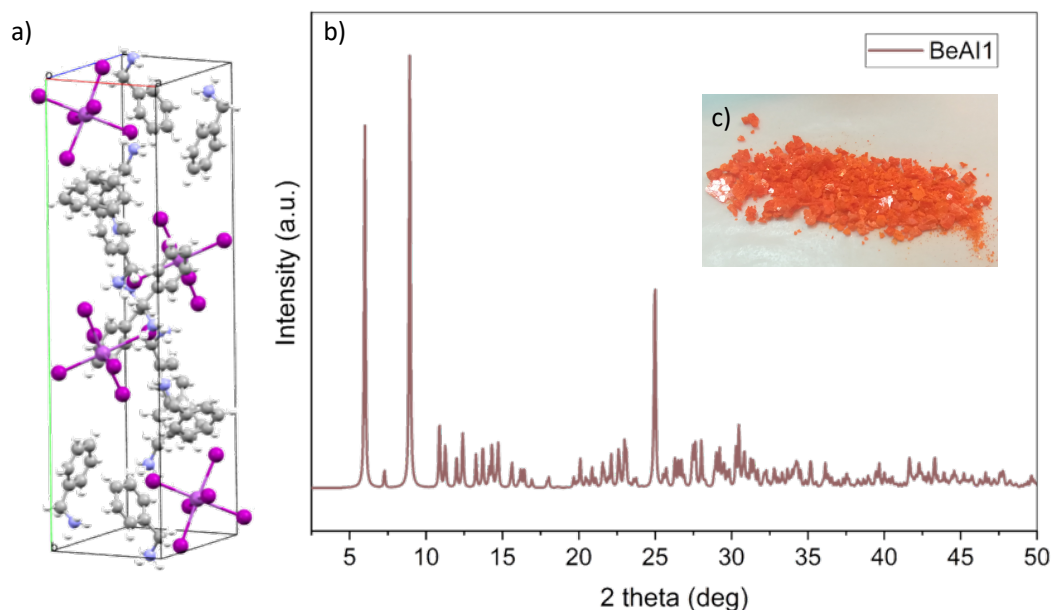


Figure 102 a) Crystal structure of (BEA)₂BiI₄ (named BeAl1), b) XRD diffraction of single crystals BeAl1, c) in the inset the single crystals pictures.

The single crystals were characterized by X-ray diffraction (XRD) at 260K. The results are shown in Figure 101ab and crystallographic data are reported in Table 23. Figure 101a shows the partially layered structure of PeAl1 \rightarrow (PEA)₂BiI₄ single crystals. It crystallizes in a monoclinic structure (P21/c space group) with lattice parameters $a=21.341 \text{ \AA}$, $b=8.5988 \text{ \AA}$ and $c=25.946 \text{ \AA}$ and $\alpha=90^\circ$, $\beta=100.253^\circ$ and $\gamma=90^\circ$ with a dominant reflection at 7.06° with (020) orientation. The inorganic layer is composed of partial corner-sharing BiI₄ octahedra spaced by the large phenylethylamine (PEA⁺) cations. Figure 102 shows the molecular 0D structure of the BeAl1 \rightarrow (BEA)₂BiI₄ single crystals which are also monoclinic (P21/n space group) with lattice parameters $a=8.5497 \text{ \AA}$, $b=29.480 \text{ \AA}$ and $c=13.9718 \text{ \AA}$ and $\alpha=90^\circ$, $\beta=107.422^\circ$ and $\gamma=90^\circ$ with two dominant reflection at 6.1° and 9.1° for the (020) and (030) orientation, respectively.

Table 23 Derived crystallographic data of the (PEA)₂(Ag)BiI₄ and (BEA)₂(Ag)BiI₄ single crystals.

Perovskites	PeAl1		BeAl1	
Space group	P2 1/c		P2 1/n	
Lattice parameters	$a = 21.341 \text{ \AA}$	$\alpha = 90^\circ$	$a = 8.5497 \text{ \AA}$	$\alpha = 90^\circ$
	$b = 8.5988 \text{ \AA}$	$\beta = 100.253^\circ$	$b = 29.480 \text{ \AA}$	$\beta = 107.422^\circ$
	$c = 25.946 \text{ \AA}$	$\gamma = 90^\circ$	$c = 13.9718 \text{ \AA}$	$\gamma = 90^\circ$

Similar materials have been reported with different halides observing an interesting behaviour by using different halides which can affect the connectivity of the inorganic octahedral clusters, leading to varied crystal stoichiometries and 3D crystal structure resulting in an indirect bandgap. The (PEA)₃Bi₂Br₉, (PEA)₄Bi₂Cl₁₀, and (PEA)₃Bi₂I₉ are reported to have improved resistance to humidity and temperature compared to MA₃Bi₂I₉. Compared to the MA cation they presented that the bulky PEA cation (hydrophobic character) significantly promotes the coverage and low surface roughness of the bismuth organohalide thin-films. Due to reported advantages this materials are interesting for further investigations.¹⁸¹

6.1.3.2. Optical and Structural Characterization

The solutions for the thin films were prepared by dissolving starting materials BiI₃, AgI and PeAI in DMSO for PeAI1 and BeAI, BiI₃, AgI for BeAI1 with concentration of 0.5 mol/L. Thin films were prepared by spin-coating deposition, using a two step program, first at 500 rpm for 30 sec and second, at 5000 rpm for 60 sec. All films have been then annealed at 80° C for PeAI1 and at 60°C for BeAI1 for 4 minutes. Images of the resulting film are shown in inset of Figure 103ab. To further investigate the properties of these thin films the author measured the absorption and photoluminescence (PL) spectra at room temperature. For PeABr1 (Figure 103a) an estimated value of 2.25 eV for the band gap is obtained from the absorption onset. For BeAI1 (Figure 103b) a bandgap of 2.36 eV is estimated using the absorption onset (Table 24).

Table 24 Absorption and photoluminescence data of thin films of PeAI1 and BeAI1.

Compound	Exciton peak	PL	Band gap
(PEA) ₃ BiI ₉	2.6 eV	2.35 eV	~2.25 eV
(BEA) ₃ BiI ₉	2.6 eV	2.37 eV	~2.36 eV

Compare to bromine compounds, here the red-shift is observed. The low dimensional materials n=0 or n=1 possess the similar Abs/PL effect comparing with the n=2 or 3D double perovskite where the PL is broader. That may indicate the presence of some defects states in the materials with higher dimensionalities.

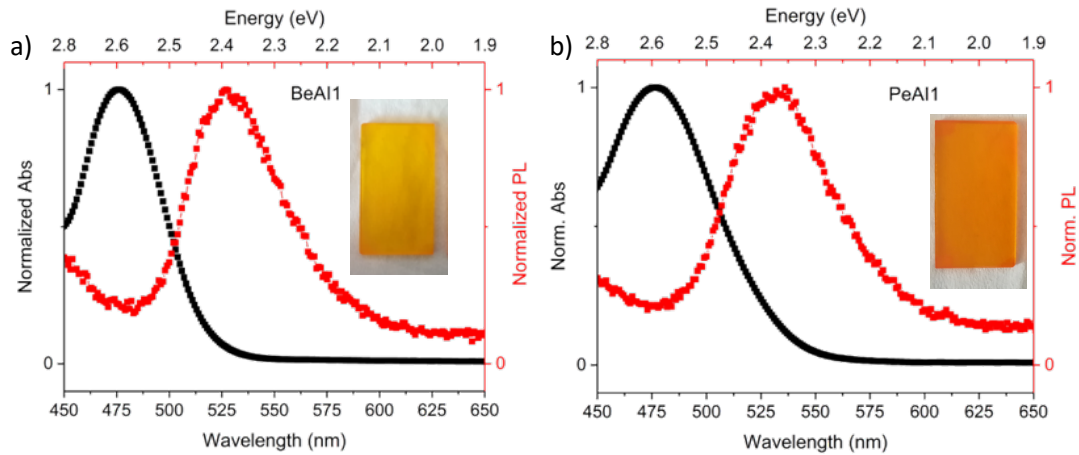


Figure 103 Normalized absorbance and photoluminescence for a) BeAlI and b) PeAlI.

The last investigation of this chapter has opened up new perspectives for exploring new materials, single crystals and films. Some parts of the results are good subject for immediate publication. Further research and characterization of the new material is beyond the scope of this thesis and is the basis for a new dissertation where the properties of these materials will be explored in detail.

7. Conclusions and Future Perspectives

7.1. Summary

7.1.1. Chapter 2 – “State of the art” $\text{Cs}_2\text{AgBiBr}_6$

Chapter 2 presents the overview of theoretical calculations of the optoelectronic properties for lead-free $\text{Cs}_2\text{AgBiBr}_6$ double perovskite showing the properties and potential for future applications in photovoltaics and beyond together with experimental findings in the literature nowadays.

The structural formability is very important to obtain a stable perovskite structure with a stable cubic lattice and shows numerous possible combinations of new lead-free double perovskites. The use of the tolerance factor along with the octahedral factor for lead-free double perovskite can help for an effective evaluation and material property prediction. Using the different combinations of B' and B'' narrows down the range of searching for lead-free perovskite alternatives. Bi-based double perovskites have the $6s^0 6p^0$ electronic configuration and the different electronic configurations between Ag and Bi result in an indirect bandgap of the prototypical $\text{Cs}_2\text{AgBiBr}_6$. The indirect bandgap is formed due to the existence of lone-pair electrons from V groups, and may lead to a large trap density, exciton effect, and the electron–phonon coupling which hinders its application in solar cells. Elemental substitution and doping $\text{Cs}_2\text{AgBiBr}_6$ with Sb, In, Sn, Rb or Tl has shown to be an effective method for bandgap engineering improving the photovoltaic performance with tunable bandgap and optoelectronic properties.

The different synthesis routes for $\text{Cs}_2\text{AgBiBr}_6$ result in different stoichiometric ratios and the nucleation and crystal growth kinetics can be well controlled to create high-quality thin films. A standard perovskite solar cell is usually composed of a perovskite active layer deposited between two selective layers to extract the charge carriers. Experimental details of double perovskites including the deposition methodology, post-treatment, chemical composition, nanostructure, and doping effects show the best solar cell performance of 2.5% power conversion efficiency reported until now.

The double perovskites have shown an improved thermal and ambient stability compared to Pb-based perovskite solar cells but a humble photovoltaics performance. Optoelectronic applications including photocatalytics, thermochromism, LEDs, photodetectors, and X-ray detectors have delivered promising results due to the unique properties of double perovskites.

7.1.2. Chapter 3 – Cs₂AgBiBr₆ double perovskite thin film characterization

Chapter 3 shows numerous synthesis routes for Cs₂AgBiBr₆ double perovskite powder, single crystals, and thin films. For characterization and application of these material, some thin film deposition routes were considered, described and discussed. From synthesis and optimization of deposition, the author showed and described all characterization methods relevant for photovoltaic applications.

The author showed the application of physical vapor deposition with different deposition routes to obtain Cs₂AgBiBr₆ thin films. It turned out that so far, the vapor deposition of Cs₂AgBiBr₆ itself and a two-step sequential deposition process of Cs₂Bi₂Br₈ and AgBr can be promising approaches. Alternatively, solution processing of Cs₂AgBiBr₆ dissolved in DMSO is possible under inert atmosphere and allows for the preparation of smooth and homogenous planar thin films.

The author provided a proof-of-principle for a substrate dependent work function of the double perovskite which points out the low defect density in the obtained thin films. Using the absorption and photoluminescence measurements, a predominant bimolecular recombination was observed in the material.

7.1.3. Chapter 4 – Cs₂AgBiBr₆ solar cells and interface engineering

In Chapter 4, four main conclusions are to be pointed out:

1. p-i-n device architecture of lead free double perovskite solar cells.

The author provided a solution based, low temperature processed, double perovskite based, planar, inverted solar cell achieving power conversion efficiencies of up to 0.42 %. In contrast to other reported cell designs, this one exhibits no hysteresis. To increase the PCE of planar inverted double perovskite based solar cells towards the expected maximum efficiency of 7.9 %, the hole and electron transporting materials have to be adjusted and film thickness must be increased. Also the device architecture must be adjusted.

2. Thickness engineering.

Thickness engineering has been conducted for the double perovskite layer and mesoporous TiO₂ in the n-i-p solar cells. After several possibilities where the author varied and combined by using different concentrations and deposition techniques of both thicknesses, the optimal layer thicknesses were found. The best solar cell performance was achieved for 160 nm of double perovskite and 280 nm of mesoporous TiO₂. The charges separated at the interfaces between TiO₂/Cs₂AgBiBr₆ are slightly advantageous for carrier transport. (Nr. 1-5) This means that once the carriers are injected into TiO₂, they have better chances to be collected. However, if the thickness is too thick (over 400 nm), they may suffer from pore-filling (not completed fill into the mesoporous TiO₂) or transport issues and when the TiO₂ layers are too thin normally they do not work effectively. This also implies that the carrier transport in perovskite itself is not very efficient so that high interfaces are required. Therefore, the proper TiO₂ thickness (~280 nm), the thick junction and the overlaid perovskite worked better. Since the diffusion length is not long in Cs₂AgBiBr₆, the performance did not improve when the thin TiO₂ with thicker Cs₂AgBiBr₆ (Nr. 7, 8, 9) were fabricated. This also suggested that perovskite layer far from mesoscopic junction do not contribute much to the photovoltaic action.

3. Fabrication of n-i-p solar cell.

The author investigated the interface of Cs₂AgBiBr₆ using a new deposition approach following a multistep optimization protocol. This enabled the realization of a compact thin film of

$\text{Cs}_3\text{AgBiBr}_6$ double perovskite with optimal infiltration into the m- TiO_2 oxide scaffold. When embodied in solar cells, different contact polymers have been considered as hole transporting materials. PTAA has here been adopted reaching a maximal power conversion efficiency of 1.26% and showing no device hysteresis. A robust and easy optimization approach of double-perovskite thin films is described, which is paramount for hysteresis-free lead-free solar cells. While measuring solar cells with different HTM with broader bandgaps it has been noticed that, after all possible optimization, the power conversion efficiency does not increase. A reason for that may lie in the sub-gap states in the bandgap of the double perovskite, which can indicate faster recombination and self-trapping of charges. Further work is ongoing to clarify this point to gain a deeper understanding of the ion movement and interface charge accumulation dynamics.

4. Stability of double perovskite layer.

Using the TEM technique for cross-sections of the double perovskite attached to mesoporous TiO_2 , some traces of silver were found and two phases are formed, $\text{Cs}_3\text{Bi}_2\text{Br}_6$ and $\text{Cs}_3\text{AgBiBr}_6$, indicating the decomposition of the pure phase under high power conditions. However, the thin film prepared for the optical measurements has showed the stability over two years.

7.1.4. Chapter 5 – Compositional Engineering of Double Perovskites $\text{Cs}_2\text{AgBiBr}_6$

In Chapter 5, the author showed compositional engineering to improve the photovoltaic properties of double perovskite solar cells. For better stability and mobility, methylammonium was used in combination with cesium at the A-site. Incorporation of the organic cation resulted in the reflection shift and absorption shift to lower wavelengths. Maximal replacement of cations reached a 1:1 ratio. The solar cells prepared using CsMAAgBiBr_6 reached 0.3% power conversion efficiency.

Further on, iodine was used for bandgap tuning in order to improve the absorbance as well as the solar cell performance. Iodine was used at the X-site mixing with bromine. The maximal replacement of bromine with iodine was up to 2%. For higher amounts of iodine the extra phase of $\text{Cs}_3\text{Bi}_2\text{I}_9$ was easily formed. Solar cells using $\text{Cs}_2\text{AgBiBr}_{5.9}\text{I}_{0.1}$ achieved 0.3% power conversion efficiency despite the bandgap shift.

The third option considered in this work for improving the solar cell performance by compositional engineering was replacing bismuth with antimony at the B-site. The author presented a detailed investigation of optimized lead-free bismuth-antimony mixed double perovskite $\text{Cs}_2\text{AgBi}_{1-x}\text{Sb}_x\text{Br}_6$ thin films. XPS and EDX measurements prove the successful integration of the Sb atoms into the double perovskite structure. XRD analysis shows a decrease in lattice constant upon insertion of this smaller Sb cation. Absorption measurements reveal the desired reduction in bandgap when adding antimony. Photoelectron spectroscopy shows that the ionization energy and electron affinity both decrease with rising Sb content. Importantly, the expected increase in short circuit current by the bandgap modification has not been found in this case. Rather, this study suggests that the presence of Sb leads to the formation of trap states, which act as recombination centers. These quench the photoluminescence and decrease the overall solar cell performance. Therefore, this double perovskite is no viable candidate unless further strategies to mitigate the newly created trap states are developed.

7.1.5 Chapter 6 – Dimensional engineering of double perovskite $\text{Cs}_2\text{AgBiBr}_6$

In chapter 6 the author showed new double perovskite materials using the organic cations phenylethylamine and benzylamine with lower dimensionality. This process was provided by a slow crystallization method by cooling down the solution with precursors in HBr acid in stoichiometric ratio. The synthesis resulted with yellow crystals, which were characterized and described. Except the single crystal and powder, the thin film optimization was shown.

In this chapter the author showed the formation of new materials using the phenylethylamine cation to form $(\text{PEA})_n\text{AgBiBr}_6$ and $(\text{PeA})_n\text{CsAgBiBr}_7$. These materials showed interesting optical behaviour leading from non-excitonic to excitonic nature. Also using theoretical calculations it is assumed that the bandgap alters from indirect to direct by lowering the dimensionality. In addition, $(\text{PEA})_2\text{CsAgBiBr}_7$ shows a broad below-gap emission which gains intensity when lowering the temperature (while a weak emission at the band edge is observed for the $(\text{PEA})_n\text{AgBiBr}_6$). Interestingly, for $n=2$, this low energy emission has a very long recombination lifetime, extending to hundreds of nanoseconds possibly related to exciton self-trapping.

This kind of behaviour can be observed also in new double perovskites materials using the benzylamine cation; $(\text{BeA})_n\text{BiBr}_6$ and $(\text{BeA})_n\text{CsAgBiBr}_7$, forming a molecular and layered crystal structure, respectively. The photoluminescence in this case shows a broad emission for $n=2$ compare to $n=1$ indicating emission from defect states. This may open the path for exploring specifically designed low dimensional double perovskites for their possible use as non-toxic white light emitting materials.

Furthermore, the author considered the same organic cation in the double perovskite framework but with iodine. An interesting structure was formed leading to molecular 0D $(\text{BeA})_n\text{BiI}_6$ and partial layered structure $(\text{PeA})_n\text{BiI}_7$, which may be due to the particular crystallization process. The resulting bandgaps were red-shifted for ~ 0.5 eV compared to bromine materials. Future calculations may help to understand the band structure of these materials.

7.2. Future perspectives

The 3D double perovskite $\text{Cs}_2\text{AgBiBr}_6$ reached the best use as a promising material in the literature together with the low dimensional double perovskite $(\text{PeA})_2\text{AgBiBr}_6$ as an X-ray detector. Aside of the many optimization steps and hard work on the device for solar cell application, interface and compositional engineering, there is still space to work and investigate this interesting material class. One solution is to passivate the surface in order to suppress the recombination process and improve charge separation. In the combination with 2D materials, it may improve the stability and charge separation as well. To investigate the density of traps in these 3D and 2D lead free double perovskite materials the transient space charge limited current (SCLC) measurement may be used. The indirect bandgap of the double perovskite $\text{Cs}_2\text{AgBiBr}_6$ is a bottleneck of this stable and interesting material. Therefore, further attempts on compositional engineering should be considered. For further solar cell applications, double perovskites with indirect bandgap of $\sim 2\text{eV}$ are promising candidates for application in tandem solar cells as it was already shown for methylammonium lead bromide, $(\text{CH}_3\text{NH}_3\text{PbBr}_3)$ which features a slightly larger E_g of 2.3 eV. There are already some findings and attempts to go in that direction.

Nowadays, the absorbing materials as single crystal demand a detailed electronic and dielectric measurements to understand the physics of these materials behind. This counts for 3D and 2D, but as well for 0D materials. It could be interesting to investigate different orientations of thin film materials and their surface defect dynamics to improve charges separation and to investigate the physics behind, especially potential ferroelectricity with semiconducting behaviour¹⁸² for layered perovskites and the transport mechanisms at the surface depend on crystal direction.^{117,183}

List of Figures

Figure 1 Annual solar radiation compared to stock of fossil fuels and nuclear fuels and the annual consumption of energy in the world. ⁴	2
Figure 2 Best-research-cell chart showing the evolution of different PV technologies adopted from NREL online sources with update on 1st of November 2019. ³	4
Figure 3 Promotion of an electron from the valence band to the conduction band. a) Photons with energy $E < E_g$ cannot promote an electron to the excited state. b) The incident photon with $E = E_g$ can promote an electron to the conduction band. For this reason it is the incident photon flux of sufficient energetic photons ($h\nu > E_g$) and not the photon energy density which determines photogeneration. Once excited, the electrons remain in the excited state for a relatively long time. c) Photons with $E \geq E_g$ can raise the electron but any excess energy is quickly lost when heat as the carriers relax to the band edges via thermalization and finally recombination. ⁶	6
Figure 4 Direct and indirect bandgaps for electronic states. ⁷	7
Figure 5 Mechanism of radiative, band-to-band recombination, non-radiative via trap state presenting electron trapping and detrapping, electron-hole recombination and hole trapping and detrapping, and finally Auger recombination. ⁶	8
Figure 6 Equivalent circuit of an ideal solar cell adopted from “The physics of solar cells” by Jenny Nelson. ⁶	9
Figure 7 Example IV curve for a solar cell with an illustration of the square summing up the maximum power spanned by the V_{Pmax} and I_{Pmax} crosses and the open circuit voltage and short circuit current points.	10
Figure 8 Schematic band diagrams of intrinsic and doped semiconductors a) intrinsic semiconductor, b) n-type semiconductor, c) p-type semiconductor. ⁷	12
Figure 9 Scheme of the simplified perovskite structure for different section where the A is the cation centered and B cation is centered (X is the largest anion, A is intermediate and B is the smallest).	13
Figure 10 The green arrow represents improvement in the device architecture of perovskite solar cells. The graph shows progress in perovskite solar cells (PrSCEs) of mesoscopic perovskite solar cells and n-i-p (where n-type layer is represented by the TiO_2 electron transporting layer, i-type as perovskite layer and p-type material as hole transporting layer) and p-i-n perovskite solar cells (representing the hole transporting layer and electron transporting layer vice versa to n-i-p), where the PHJ stands for planar heterojunction. Adopted with permission. ¹⁹	15

Figure 11 Schematic representation of the structures of simple and double perovskites showing the difference in the elemental composition on the B-site. The A^+ , B^{2+} , B^+ , B^{3+} , and X ions are denoted by the cyan, grey, yellow, pink, and purple, respectively. Adopted with permission.⁶⁴ 24

Figure 12 a) Electronic band structures of $Cs_2AgBiBr_6$ resulting from the DFT calculations. Reproduced with permission.⁵⁸ **b)** Molecular orbital diagrams in double perovskite $Cs_2AgBiBr_6$.
⁶⁰ Copyright © 2016, American Chemical Society 26

Figure 13 The plane-averaged charge difference and CDC of a) $Ag_2Bi_2Br_8/TiO_2$, b) Cs_4Br_4/TiO_2 , c) $Ag_2Bi_2Cl_8/TiO_2$, and d) Cs_4Cl_4/TiO_2 heterojunctions in Cs_2AgBiX_6 ($X = \frac{1}{4} Br$ and Cl)/ TiO_2 . The upper and lower scale bars represent the plane-averaged charge difference and the CDC, respectively. Reproduced with permission. Copyright 2017, American Chemical Society. ⁸⁶. 30

Figure 14 a) PBE calculated band structure provided an indication of the weak transition parameter in $Cs_2AgInCl_6$. **b)** PBE calculated band structures provided an indication of the strong transition parameter in $Cs_2InBiCl_6$. **c)** A table of probable combinations for $A_2B'B''X_6$ along with their parity dependent transitions. Reproduced with permission.⁹¹ Copyright © 2017 American Chemical Society. 31

Figure 15 Schematic diagram showing the bonding and antibonding bands of $Cs_2AgSb_xIn_{1-x}Cl_6$. The lower shaded boxes represent the valence (occupied) bands while the top blank boxes represent the conduction (unoccupied) bands. The band gaps decrease with the transition from direct to indirect character * permission from Royal Society of Chemistry. 34

Figure 16 Solution synthesis experiment. 44

Figure 17 a) All starting materials grounded and inserted into a quartz ampoule before solid-state synthesis at 500°C, **b)** alumina crucible for solid state synthesis of double perovskite at 210 °C. 45

Figure 18 Hydrothermal synthesis setup. 46

Figure 19 Summary of all synthesis routes. **a)** Solid state synthesis, **b)** hydrothermal synthesis, **c)** solution synthesis, **d)** single crystal synthesis, **e)** XRD of all materials compared to theoretical, **f)** UV-Vis reflectance of $Cs_2AgBiBr_6$ powder samples. 46

Figure 20 a) Spectros 150 system, Kurt J. Lesker - High vacuum deposition apparatus, **b)** working scheme of the thermal evaporation system. 48

Figure 21 Vacuum display screen - Operation control program. 48

Figure 22 Spin coater and glovebox system. 50

Figure 23 a) Scheme of the Bragg Brentano geometry of diffraction on the picture of the XRD instrument, b) Bragg's law shows the interplanar spacing d determined by measuring the angle 2θ between the incident and diffracted directions of the radiation with wavelength λ in a material respect to a normal line (s), where the (hkl) correspond to particular set of planes, in fact to a particular point in the reciprocal space.¹²⁶ 52

Figure 24 Photoelectron emission process, a) XPS, b) UPS, c) IPES.¹²⁶ 56

Figure 25 Schematic representation of the sequential vapor deposition processes, images, deposition parameters and AFM images of the resulting films; a) single source $\text{Cs}_2\text{AgBiBr}_6$, b) triple source BiBr_3 - AgBr - CsBr , and c) dual source $\text{Cs}_2\text{Bi}_2\text{Br}_9$ and AgBr 58

Figure 26 XRD pattern of the films using the full evaporation scheme a) $\text{Cs}_2\text{AgBiBr}_6$, b) BiBr_3 - AgBr - CsBr , and c) $\text{Cs}_2\text{Bi}_2\text{Br}_9$ and AgBr .(+ AgBr , * BiOBr) 60

Figure 27 UV-Vis spectra for the three deposition approaches. 61

Figure 28 deposition process by spin coating and SEM images of $\text{Cs}_2\text{AgBiBr}_6$ thin film surfaces after annealing at 120°C and 220°C (scale bars: 200nm)..... 62

Figure 29 XRD of $\text{Cs}_2\text{AgBiBr}_6$ deposited on different sublayers. 64

Figure 30 Tauc-plots of $\text{Cs}_2\text{AgBiBr}_6$ thin film and powder..... 64

Figure 31 a) XPS survey spectrum of $\text{Cs}_2\text{AgBiBr}_6$ spin coated on glass/PEDOT:PSS and b) corresponding high resolution XPS-spectra of cesium, silver, bismuth, and bromine peaks. . 65

Figure 32 Combines He I UPS and IPES spectrum of $\text{Cs}_2\text{AgBiBr}_6$ on mesoporous TiO_2 (lower curve, blue) and PEDOT:PSS upper curve, red)..... 66

Figure 33 a) Absorption spectrum of a $\text{Cs}_2\text{AgBiBr}_6$ thin film sample on glass (main panel). Normalized PL spectrum of the sample and Tauc-plot of the low energy tail of the absorption spectrum assuming an indirect allowed transition (inset). Excitation fluence dependent photoluminescence. b) Normalized PL spectra of a $\text{Cs}_2\text{AgBiBr}_6$ thin film sample on glass for different excitation fluences (blue/red) and Gaussian fits (black). The peaks centers are indicated by the dotted lines, corresponding energy values are denoted. c) Dependence of the PL intensity of each emission feature on the excitation fluence extracted by cumulative fitting of the spectra shown in b) with Gaussian profiles. 67

Figure 34 Time resolved photoluminescence traces of a $\text{Cs}_2\text{AgBiBr}_6$ thin film on glass measured at different emission energies (main panel) and triple exponential fits (black lines). Inset: Corresponding PL spectrum (black) and cumulative fit with four Gaussian functions (red). The spectral regions examined via TRPL are shadowed according to the colors in the main panel. 68

Figure 35 Glass substrate cleaning process **a)** measuring resistivity, **b)** cleaning in different solvents using ultrasonic, **c)** ozone cleaning. 71

Figure 36 a) Inverted planar solar cell device, cross-sectional scheme, **b)** schematic illustration of the device architecture with ITO as transparent conductive anode and silver (Ag) as the metal cathode with 7 contact points, **c)** picture of prepared double perovskite solar cell. 72

Figure 37 a) Etching approach on FTO substrates, **b)** scheme of mesoporous solar cells with layers used in this approach, **c)** final solar cell with an active area ready for measurement.... 73

Figure 38 a) setup for measurements of current density – voltage curves under simulated solar light, and a voltage setup function is applied to the device while measuring the current response **b)** schematic of solar cell measurement holder where the device is illuminated through shadow mask and defined the active area (Scheme was remade from the book “Organic and hybrid solar cells”.)..... 74

Figure 39 Experimental setup for external quantum efficiency measurements (Scheme was remade from the book “Organic and hybrid solar cells”.) 75

Figure 40 a) J-V curve of a planar solar cell using SnO₂ as electron transporting layer, **b)** J-V curve and hysteresis of the planar solar cell using c-TiO₂ as ETL..... 77

Figure 41 Energy level diagram of the inverted cell structure. 78

Figure 42 a) J-V curve for best performing device and **b)** 2 scan directions of J-V curve showing no hysteresis SEM image cross section of double perovskite solar cell..... 78

Figure 43 a) Boxplot of efficiencies of solar cells built on 2 different days, **b)** stabilized power output. 79

Figure 44 Dependence of different electrical parameters on the efficiency of the solar cells: **a)** short circuit current J_{sc} , **b)** open circuit voltage V_{oc} , **c)** serial resistance R_s and **d)** shunt resistance R_{sh} 79

Figure 45 a) J-V characteristics of solar cells with a perovskite layer annealed at 210°C and 285°C, **b)** The J_{sc} doesn't change, but the FF and V_{oc} decrease meaning that there is more recombination with a time. 80

Figure 46 J-V curves of mesoporous solar cells with a) 400 nm TiO₂, b) 280 nm TiO₂, c) 250 nm TiO₂, d) 160 nm TiO₂..... 83

Figure 47 Statistical distribution of all prepared devices keeping the perovskite layer thickness at the same (160 nm) and changing the mesoporous layer thickness. Comparison of all photovoltaic parameters, **a)** J_{sc} , **b)** V_{oc} , **c)** FF, **d)** PCE..... 84

Figure 48 J-V curves of devices (7-8) with 280 nm of mesoporous layer and **a)** 123 nm perovskite, **b)** 100 nm perovskite..... 85

Figure 49 Statistical distribution of all prepared devices (6-8) keeping thickness of mesoporous layer at 280 nm and changing perovskite layer thickness and comparison of all photovoltaic parameters..... 85

Figure 50 J-V curves of devices (9-11) with 100 nm of mesoporous layer and **a)** 160 nm perovskite, **b)** 123 nm perovskite, **c)** 100 nm perovskite..... 86

Figure 51 Statistical distribution of all devices 9-11 keeping thickness of the mesoporous layer at 100 nm and changing the perovskite layer thickness. Comparison of all photovoltaic parameters..... 87

Figure 52 IPCE curves of devices **a)** (1-5) keeping 160 nm perovskite layer thickness and changing the thickness of the mesoporous TiO₂ layer, **b)** (6-8) keeping 280 nm of m-TiO₂ and changing perovskite layer, **c)** (9-11) keeping 100nm TiO₂ and changing perovskite layer..... 87

Figure 53 Energy level diagram of all materials used for device optimization and engineering. 89

Figure 54 a) X-ray diffraction (XRD) pattern of Cs₂AgBiBr₆ thin films deposited on mesoporous TiO₂ substrate at different annealing temperatures as indicated in the legend. Scanning electron microscopy (SEM) images of, **b)** top view of the double-perovskite layer obtained upon spin coating at room temperature using the anti-solvent treatment with chlorobenzene and **c)** cross section of the FTO/c-TiO₂/m-TiO₂/ double perovskite sample, upon annealing at 280 °C..... 91

Figure 55 Double perovskite layer optimization and optimization of infiltration of double perovskite solution into mesoporous TiO₂; **a)** room temperature deposition and annealing at 220°C, **b)** cross-section of FTO/cTiO₂/mTiO₂/double perovskite, to low concentration of m-TiO₂ and no infiltration into m-TiO₂ layer, **c)** using double perovskite dissolved in DMF (0.16M) as 1st step deposition step and double perovskite dissolved in DMSO (0.5M) as 2nd step deposition step, **d)** ozone treatment on m-TiO₂ for 15min before spin coating of double perovskite, **e)** lower concentration of double perovskite dissolved in DMSO, **f)** TiCl₄ treatment. 92

Figure 56 a) Absorption spectrum plotted in the form of Tauc plot, for an indirect bandgap, of the Cs₂AgBiBr₆ thin film deposited on glass (black). Inset: the Tauc plot for a direct bandgap with the dashed red line representing the linear fit for the band edge estimation. **b)** Photoluminescence (PL) spectra of the Cs₂AgBiBr₆ thin film. **c)** PL decay monitored at 2.1 eV.

The decay is fitted using a bi-exponential function, resulting in fitted time constants of $\tau_1 = 5\text{ns}$ and $\tau_2 = 282\text{ns}$ (red)..... 93

Figure 57 Device statistics on optimized layers, power conversion efficiency of solar cells; **a)** using different annealing temperatures (250-320°C) the Cs₂AgBiBr₆ double perovskite layer, **b)** using different concentrations of m-TiO₂ dispersed in EtOH, **c)** using antisolvent (chlorobenzene) and non-antisolvent treatment. 94

Figure 58 a) absorbance of double perovskite and PCPDTBT layer, **b)** photoluminescence intensity of double perovskite and PCPDTBT layer..... 95

Figure 59 a) Scheme of corresponding energy level diagram with the following energy values: FTO (-4.4 eV), TiO₂(-4.0 eV), Cs₂AgBiBr₆ (HOMO, -5.9 eV; LUMO, -3.8 eV), spiro-OMeTAD (-5.2 eV, -2.2 eV), PTAA (-5.1 eV, -1.8 eV), PCPDTBT (-5.3 eV, -3.55 eV) and Au (-5.1 eV); **b)** J-V curves for best-performing solar cells using different HTMs..... 96

Figure 60 a) J-V curve for solar cells without antisolvent treatment and PTAA as HTM, **b)** IPCE spectrum of champion Cs₂AgBiBr₆ perovskite solar cells with PTAA. 97

Figure 61 Statistical distribution of photovoltaic parameter for perovskite solar cells performance with different HTMs; **a)** short circuit current J_{sc} , **b)** open-circuit voltage V_{oc} , **c)** fill factor FF, **d)** power conversion efficiency. 98

Figure 62 J-V curve of hysteresis free double perovskite solar cell.. 99

Figure 63 a) J-V curves for best performance solar cells using different HTMs, **b)** Photovoltaic parameters of devices based on the different HTMs related to graph: Short -circuit current density (J_{sc}), Open-Circuit Voltage (V_{oc}), Fill factor (FF) and Power Conversion Efficiency (PCE)..... 100

Figure 64 a) Devices of double perovskite solar cells using different HTMs **b)** Cross-section of optimized double perovskite solar cells using PTAA as HTM..... 100

Figure 65 (Color online) Absorbance spectra of C60 (filled squares) and C70 (filled upside-down triangles) in a range of 200–900 nm. Enhanced absorption of a wide spectral range is observed for C70 compared to C60.¹⁵¹ 101

Figure 66 J-V curves of devices using C70 on top of the mesoporous layer with **a)** the antisolvent and **b)** the TiCl₄ step and PTAA..... 102

Figure 67 Cross-section of double perovskite solar cells using C70 and PCPDTBT 102

Figure 68 J-V curves of solar cell performance for **a)** PNPBC and **b)** NPBC..... 103

Figure 69 IPCE curves for PNPBC and NPBC mesoporous double perovskite solar cells. .104

Figure 70 Schematic representation of carrier kinetic within $\text{Cs}_2\text{AgBiBr}_6$ according to [103, 152]. Where the (1) represents generation of free electrons and holes in the conduction (EC) and valence band (EV), respectively, (2) Band to band carrier recombination, (3) Surface states recombination, (4) Free charges captured by trap states (shallow), (5) Trapped charges was thermally released to the band edges, (6) sub-bandgap states showing nonradiative traps and corresponding recombination. 104

Figure 71 TEM cross section of perovskite/ TiO_2 , and element mapping of each element distribution across the cross section, turquoise is O, yellow Ti, violet Br, red silver, green cesium and blue bismuth..... 106

Figure 72 SAED pattern of the double perovskite cross section..... 106

Figure 73 a) XRD diffractogram of $\text{Cs}_{2-x}\text{MA}_x\text{AgBiBr}_6$, **b)** Absorption spectra, **c)** (400) and (002) reflection. 109

Figure 74 a) XRD diffractogram of $\text{Cs}_2\text{AgBiBr}_{6-x}\text{I}_x$ compared to double perovskite $\text{Cs}_2\text{AgBiBr}_6$ with higher amounts of iodide, **b)** $\text{Cs}_2\text{AgBiBr}_{5.8}\text{I}_{0.2}$ 111

Figure 75 a) Absorbance of mixed iodine/bromine double perovskite, **b)** Photoluminescence of all materials, **c)** $\text{Cs}_2\text{AgBiBr}_6$ powder, **d)** $\text{Cs}_2\text{AgBiBr}_{5.8}\text{I}_{0.2}$ powder..... 111

Figure 76 Solar cell performance of **a)** CsMAAgBiBr_6 double perovskite, and **b)** $\text{Cs}_2\text{AgBiBr}_{5.8}\text{I}_{0.2}$ double perovskite. 112

Figure 77 a) Evolution of the band gap as a function of Sb concentration, **b)** Contribution of many-body interactions and spin-orbit coupling into band gap, calculations conducted by Dr. Olga Syzgantseva from EPFL. 113

Figure 78 a) XRD diffractogram of prepared Sb-Bi mixed double perovskite using ampoule synthesis, **b)** (002) reflection shift..... 114

Figure 79 Absorption spectra of all mixed materials compared to standard double perovskite. 114

Figure 80 a) XRD diffractogram of mixed double perovskite employing different concentrations of antimony. Optimized annealing temperatures are indicated in the graph. **b)** Detailed view of the (002) and (222) reflections, showing the change in lattice size with Sb content. **c)** (002) and (222) reflection positions depending on mixing with antimony..... 117

Figure 81 SEM top view image of $\text{Cs}_2\text{AgBi}_{1-x}\text{Sb}_x\text{Br}_6$ films, the white bar corresponds to 500 nm. The Sb concentrations are: **a)** 0%, **b)** 25%, **c)** 37.5%, and **d)** 50%. 117

Figure 82 a) Tauc-plot of the absorbance spectra and **b)** corresponding photographs of the double perovskite thin films with different amount of antimony deposited on glass. 118

Figure 83 a) Representative XPS spectrum of one of the thin films mixed double perovskites.	
b) Detailed view of core level peaks of this sample, showing high resolution XPS spectra of cesium, antimony, silver, bismuth, and bromine.....	119
Figure 84 UPS and IPES spectrum of $\text{Cs}_2\text{AgBiBr}_6$ and samples with increasing amount of Sb.	
.....	121
Figure 85 a) Solar cell I-V curve for 12.5% Sb doped double perovskite, b) I-V curve for 37.5% antimony doped double perovskite.	122
Figure 86 a) Solar cell I-V curve for 25% Sb doped double perovskite, b) I-V curve for 50% antimony doped double perovskite.	122
Figure 87 a) Photoluminescence of $\text{Cs}_2\text{AgBiBr}_6$ and $\text{Cs}_2\text{AgBi}_{0.5}\text{Sb}_{0.5}\text{Br}_6$ b) IPCE of double perovskite solar cells, $\text{Cs}_2\text{AgBiBr}_6$, $\text{Cs}_2\text{AgBi}_{0.75}\text{Sb}_{0.25}\text{Br}_6$, and $\text{Cs}_2\text{AgBi}_{0.5}\text{Sb}_{0.5}\text{Br}_6$	123
Figure 88 a) Crystal structure of $(\text{PEA})_x\text{AgBiBr}_8$ (named PeABr1), b) crystal structure of $(\text{PEA})_x\text{CsAgBiBr}_8$ (named PeABr2) c) XRD diffraction of single crystals PeABr1 and PeABr2, (the inset shows the single crystals) d) Tauc plot of the PeABr1 and e) PeABr2 derived from reflectance measurements.	128
Figure 89 a) Perspective view of the unit cells employed in the modelling and b) band structures for $\text{Cs}_2\text{AgBiBr}_6$, PeABr2 and PeABr1 systems (from left to right). Note that for the band structures the energy of the VB edge has been selected as energy reference; and the A and B points in the layered systems are the equivalent to X and L points of the bulk in the reciprocal space. Color legend is: Cs (light blue, bigger atoms), Bi (dark grey, bigger atoms), Br (red), C (yellow), H (blue, smaller atoms) and N (grey, smaller atoms).	130
Figure 90 Projected Density of States (PDOS) over a) organic (orange) and inorganic (purple) parts; and b) Ag (green), Bi (purple), and Br (blue) atoms. The energy of the VB edge has been taken as reference.	132
Figure 91 Band gap values (colour scale inset) as function of the in-plane (θ as represented on the left onset) and out-of-plane (δ , on the right onset) tilted angles for $\text{Cs}_2\text{AgBiBr}_6$, PeABr2, PeABr1, BABr2 and BABr1 compounds.	133
Figure 92 Reflectance for the powder samples PeABr1, PeABr2 and $\text{Cs}_2\text{AgBiBr}_6$	134
Figure 93 a) XRD diffraction of thin films for PeABr2 and PeABr1 b) SEM image of PeABr2 and c) SEM image of PeABr1.	135
Figure 94 Low temperature absorbance for a) PeABr1 and b) PeABr2.....	136
Figure 95 Low temperature PI shows a slight redshift for a) PeABr1, b) PeABr2, c) $\text{Cs}_2\text{AgBiBr}_6$	136

Figure 96 a) Absorption of PeABr1 and PeABr2 at 300K and b) at 80K, c) The low temperature PL of PeABr1 with inset of extreme normalized values (comparison between 80 K and 300 K), d) the low temperature PL of PeABr2 with inset of extreme normalized values comparison, e) comparison of normalized photoluminescence and absorption of PeABr1 at 80K, f) comparison of normalized photoluminescence and absorption of PeABr2 at 80K, g) The PL decay fitted with a biexponential function for PeABr1 at 450 nm and PeABr2 at 600 nm, at their relative peak position..... 137

Figure 97 Crystal structure of $(\text{BEA})_3\text{BiBr}_6$ (named BeABr1), where the atoms are Br-orange, Bi-violet, C-grey, N-blue, H-white b) XRD diffraction of single crystals BeABr1, c) in the inset the single crystals picture..... 141

Figure 98 a) crystal structure of $(\text{BEA})_2\text{CsAgBiBr}_7$ (named BeABr2) where the atoms are Br-orange, Bi-violet, C-grey, N-blue H-white, Ag- light grey and Cs- dark violet b) XRD diffraction of single crystals BeABr2, c) image of single crystals..... 142

Figure 99 Normalized absorbance and photoluminescence measured at room temperature for a) BeABr1 and b) BeABr2..... 143

Figure 100 The PL decay fitted with a biexponential function for BeABr1 at 450 nm and BeABr2 at 600 nm, at their relative peak positions. b) images of thin films, c) SEM of BeABr2. 144

Figure 101 Crystal structure of $(\text{PEA})_4\text{BiI}_7$ (named PeAI1), b) XRD diffraction of single crystals PeAI1, c) in the inset the single crystals pictures..... 145

Figure 102 Crystal structure of $(\text{BEA})_3\text{BiI}_6$ (named BeAI1), b) XRD diffraction of single crystals BeAI1, c) in the inset the single crystals pictures. 146

Figure 103 Normalized absorbance and photoluminescence for a) BeAI1 and b) PeAI1..... 148

List of Tables

Table 1 Device architecture and photovoltaic parameters of double perovskite-based solar cells. ⁴⁹	36
Table 2 Solvent engineering.	50
Table 3 Calculated average values of work functions (W_i), ionization energies (IE), electron affinities (EA) and band gaps (E_g) of double perovskite thin films deposited on mesoporous TiO_2 and PEDOT:PSS.	67
Table 4 Photovoltaic performance of planar solar cells using SnO_2 and c- TiO_2 as electron transporting layer and PTAA as hole transporting layer	77
Table 5 Photovoltaic performance of mesoporous solar cells using different thicknesses of TiO_2 layers.....	82
Table 6 Photovoltaic performance of mesoporous solar cells keeping the same thickness of TiO_2 layers (280 nm) while changing the thickness of the perovskite.....	84
Table 7 Photovoltaic performance of mesoporous solar cells keeping the same thickness of TiO_2 layers, (devices 100 nm) while changing the thickness of the perovskite.	86
Table 8 Photovoltaic parameters of devices based on the different HTMs; Short –circuit current density (J_{sc}), Open-Circuit Voltage (V_{oc}), Fill Factor (FF) and Power Conversion Efficiency (PCE). Notably, device statistics has been conducted on 44 devices (spiro-OMeTAD), 27 devices (PTAA), 6 devices (PCPDTBT).....	96
Table 9 Photovoltaic parameters of C70 solar cells.	102
Table 10 Energy levels of new HTMs.	103
Table 11 Solar cell performance for new HTMs.....	104
Table 12 Comparison calculated values with XPS and EDX analysis.	119
Table 13 Calculated averaged values of work functions (Wf), ionization energies (IE) electron affinities (EA) and band gaps (E_g) of double perovskite thin films deposited on ITO substrates.	120
Table 14 Photovoltaic parameters of devices based on different concentrations of antimony: Short-Circuit Current Density (J_{sc}), Open-Circuit Voltage (V_{oc}), Fill Factor (FF), and Power Conversion Efficiency (PCE).....	122
Table 15 Derived crystallographic data of the $(PEA)_4AgBiBr_8$ and $(PEA)_2CsAgBiBr_7$ single crystals compared to the reference $Cs_2AgBiBr_6$	129
Table 16 Calculated effective masses by parabolic fitting.	131

Table 17 Bandgap values in eV estimated by DFT calculations (theo) with fixed (left) and variable (right) unit cell parameters; and by Tauc plot (exp)..... 133

Table 18 Absorption and photoluminescence data of thin films of 2D double perovskites..138

Table 19 PL decay parameters for PeABr1 and PeABr2..... 139

Table 20 Crystallographic data of the $(\text{BEA})_2\text{BiBr}_6$ and $(\text{BEA})_2\text{CsAgBiBr}_7$ single crystals... 142

Table 21 Absorption and photoluminescence data of thin films of new BeABr1 and BeABr2.
..... 143

Table 22 PL decay parameters for BeABr1 and BeABr2..... 144

Table 23 Derived crystallographic data of the $(\text{PEA})_2(\text{Ag})\text{BiI}_8$ and $(\text{BEA})_2(\text{Ag})\text{BiI}_7$ single crystals. 146

Table 24 Absorption and photoluminescence data of thin films of PeAI1 and BeAI1..... 147

References

- (1) Tang, H.; He, S.; Peng, C. A Short Progress Report on High-Efficiency Perovskite Solar Cells, *Nanoscale Res. Lett.*, **2017**, *12*, 410.
- (2) Kojima, A.; Teshima, K.; Shirai, Y.; Miyasaka, T. Organometal halide perovskites as visible-light sensitizers for photovoltaic cells, *J. Am. Chem. Soc.*, **2009**, *131*, 6050–6051.
- (3) http://www.nrel.gov/ncpv/images/efficiency_chart.jpg. efficiency-chart Rev. 28.01. **2020**.
- (4) <https://www.dgs.de/aktuell/> Deutsche Gesellschaft für Sonnenenergie e.V. **2020**
- (5) Kim, H.-S.; Lee, J.-W.; Yantara, N.; Boix, P. P.; Kulkarni, S. A.; Mhaisalkar, S.; Grätzel, M.; Park, N.-G. High efficiency solid-state sensitized solar cell-based on submicrometer rutile TiO₂ nanorod and CH₃NH₃PbI₃ perovskite sensitizer, *Nano Lett.*, **2013**, *13*, 2412–2417.
- (6) Nelson J., *The physics of solar cells*; Imperial College Press, World Scientific Publishing Co. Pte. Ltd, London, **2003**.
- (7) Schmidt-Mende L., W. eickert J., *Organic and Hybrid Solar Cells*; Deutsche Nationalbibliografie, Berlin, **2016**.
- (8) Tauc, J., Grigorovici, R. and Vancu, A. Optical Properties and Electronic Structure of Amorphous Germanium, *phys. stat. sol. (b)*, **1966**, *15*, 627–637.
- (9) Davis, E. A.; Mott, N. F. Conduction in non-crystalline systems V. Conductivity, optical absorption and photoconductivity in amorphous semiconductors, *Philosophical Magazine*, **1970**, *22*, 903–922.
- (10) Khazaei M., Materials for Halide-Based Thin Film Solar Cells, *Dissertation*, University Duisburg-Essen **2019**, DOI:10.17185/dupublico/70076).
- (11) Green M. A., Ho-Baillie A., Snaith H. J. The emergence of perovskite solar cells, *Nature Photon* **2014**, *8*, 506–514

- (12) Brenner, T. M.; Egger, D. A.; Kronik, L.; Hodes, G. Cahen, D. Hybrid organic—
inorganic perovskites, *Nat. Rev. Mater.*, **2016**, 16011.
- (13) Noh, J. H.; Im, S. H.; Heo, J. H.; Mandal, T. N. Seok, S. I. Chemical management for
colorful, efficient, and stable inorganic-organic hybrid nanostructured solar cells, *Nano
Lett*, **2013**, *13*, 1764–1769.
- (14) S. D. Stranks, G. E. Eperon, G. Grancini, C. Menelaou, M. J. P. Alcocer, T. Leijtens, L.
M. Herz, A. Petrozza, H. J. Snaith. Electron-Hole Diffusion Lengths Exceeding 1
Micrometer in an Organometal Trihalide Perovskite Absorber, *Science*, **2013**, *342*, 341–
344.
- (15) Brandt, R. E.; Stevanović, V.; Ginley, D. S. Buonassisi, T. Identifying defect-tolerant
semiconductors with high minority-carrier lifetimes, *Materials Research Society*, **2015**,
5, 265–275.
- (16) Wehrenfennig, C.; Eperon, G. E.; Johnston, M. B.; Snaith, H. J. Herz, L. M. High Charge
Carrier Mobilities and Lifetimes in Organolead Trihalide Perovskites, *Adv. Mater.*, **2014**,
26, 1584–1589.
- (17) Aristidou, N.; Sanchez-Molina, I.; Chotchuangchutchaval, T.; Brown, M.; Martinez, L.;
Rath, T. Haque, S. A. The Role of Oxygen in the Degradation of Methylammonium Lead
Trihalide Perovskite Photoactive Layers, *Angew. Chem. Int. Ed. Engl.*, **2015**, *54*, 8208–
8212.
- (18) Babayigit, A.; Ethirajan, A.; Muller, M. Conings, B. Toxicity of organometal halide
perovskite solar cells, *Nat. Mater.*, **2016**, *15*, 247–251.
- (19) Kim, H.; Lim, K.-G. Lee, T.-W. Planar heterojunction organometal halide perovskite
solar cells, *Energy Environ. Sci.*, **2016**, *9*, 12–30.
- (20) Giustino, F., Snaith, H. J. Toward Lead-Free Perovskite Solar Cells, *ACS Energy Lett.*,
2016, *1*, 1233–1240.

- (21) Beal, R. E.; Slotcavage, D. J.; Leijtens, T.; Bowring, A. R.; Belisle, R. A.; Nguyen, W. H.; Burkhard, G. F.; Hoke, E. T. McGehee, M. D. Cesium Lead Halide Perovskites with Improved Stability for Tandem Solar Cells, *J. Phys. Chem. Lett.*, **2016**, *7*, 746–751.
- (22) Smith, I. C.; Hoke, E. T.; Solis-Ibarra, D.; McGehee, M. D. Karunadasa, H. I. A layered hybrid perovskite solar-cell absorber with enhanced moisture stability, *Angew. Chem. Int. Ed. Engl.*, **2014**, *53*, 11232–11235.
- (23) Hao, F.; Stoumpos, C. C.; Cao, D. H.; Chang, R. P. H. Kanatzidis, M. G. Lead-free solid-state organic–inorganic halide perovskite solar cells, *Nature Photon*, **2014**, *8*, 489–494.
- (24) Noel, N. K.; Stranks, S. D.; Abate, A.; Wehrenfennig, C.; Guarnera, S.; Haghighirad, A.-A.; Sadhanala, A.; Eperon, G. E.; Pathak, S. K.; Johnston, M. B.; Petrozza, A.; Herz, L. M. Snaith, H. J. Lead-free organic–inorganic tin halide perovskites for photovoltaic applications, *Energy Environ. Sci.*, **2014**, *7*, 3061.
- (25) Stoumpos, C. C.; Frazer, L.; Clark, D. J.; Kim, Y. S.; Rhim, S. H.; Freeman, A. J.; Ketterson, J. B.; Jang, J. I. Kanatzidis, M. G. Hybrid germanium iodide perovskite semiconductors: active lone pairs, structural distortions, direct and indirect energy gaps, and strong nonlinear optical properties, *J. Am. Chem. Soc.*, **2015**, *137*, 6804–6819.
- (26) Li, L.; Zhang, F.; Hao, Y.; Sun, Q.; Li, Z.; Wang, H.; Cui, Y. Zhu, F. High efficiency planar Sn–Pb binary perovskite solar cells, *J. Mater. Chem. C*, **2017**, *5*, 2360–2367.
- (27) Liu, J.; Ozaki, M.; Yakumar, S.; Handa, T.; Nishikubo, R.; Kanemitsu, Y.; Saeki, A.; Murata, Y.; Murdey, R. Wakamiya, A. Lead-Free Solar Cells based on Tin Halide Perovskite Films with High Coverage and Improved Aggregation, *Angew. Chem. Int. Ed. Engl.*, **2018**, *57*, 13221–13225.
- (28) Zhao, Z.; Gu, F.; Li, Y.; Sun, W.; Ye, S.; Rao, H.; Liu, Z.; Bian, Z. Huang, C. Mixed-Organic-Cation Tin Iodide for Lead-Free Perovskite Solar Cells with an Efficiency of 8.12, *Adv. Sci. (Weinh)*, **2017**, *4*, 1700204.

- (29) Ito, N.; Kamarudin, M. A.; Hirotsu, D.; Zhang, Y.; Shen, Q.; Ogomi, Y.; Iikubo, S.; Minemoto, T.; Yoshino, K.; Hayase, S. Mixed Sn-Ge Perovskite for Enhanced Perovskite Solar Cell Performance in Air, *J. Phys. Chem. Lett.*, **2018**, *9*, 1682–1688.
- (30) Krishnamoorthy, T.; Ding, H.; Yan, C.; Leong, W. L.; Baikie, T.; Zhang, Z.; Sherburne, M.; Li, S.; Asta, M.; Mathews, N.; Mhaisalkar, S. G. Lead-free germanium iodide perovskite materials for photovoltaic applications, *J. Mater. Chem. A*, **2015**, *3*, 23829–23832.
- (31) Jiang, Y.; Zhang, H.; Qiu, X.; Cao, B. The air and thermal stabilities of lead-free perovskite variant Cs₂SnI₆ powder, *Materials Letters*, **2017**, *199*, 50–52.
- (32) Qiu, X.; Cao, B.; Yuan, S.; Chen, X.; Qiu, Z.; Jiang, Y.; Ye, Q.; Wang, H.; Zeng, H.; Liu, J.; Kanatzidis, M. G. From unstable Cs₂SnI₆ to air-stable Cs₂SnI₆, *Solar Energy Materials and Solar Cells*, **2017**, *159*, 227–234.
- (33) Angelis, F. de; Kamat, P. V. Riding the New Wave of Perovskites, *ACS Energy Lett.*, **2017**, *2*, 922–923.
- (34) Angelis, F. de. Modeling materials and processes in hybrid/organic photovoltaics, *Acc. Chem. Res.*, **2014**, *47*, 3349–3360.
- (35) Liao, Y.; Liu, H.; Zhou, W.; Yang, D.; Shang, Y.; Shi, Z.; Li, B.; Jiang, X.; Zhang, L.; Quan, L. N.; Quintero-Bermudez, R.; Sutherland, B. R.; Mi, Q.; Sargent, E. H.; Ning, Z. Highly Oriented Low-Dimensional Tin Halide Perovskites with Enhanced Stability and Photovoltaic Performance, *J. Am. Chem. Soc.*, **2017**, *139*, 6693–6699.
- (36) Cao, D. H.; Stoumpos, C. C.; Yokoyama, T.; Logsdon, J. L.; Song, T.-B.; Farha, O. K.; Wasielewski, M. R.; Hupp, J. T.; Kanatzidis, M. G. Thin Films and Solar Cells Based on Semiconducting Two-Dimensional Ruddlesden–Popper (CH₃(CH₂)₃NH₃)₂(CH₃NH₃)_{n-1}SnI_{n-3n+1} Perovskites, *ACS Energy Lett.*, **2017**, *2*, 982–990.

- (37) Babayigit, A.; Duy Thanh, D.; Ethirajan, A.; Manca, J.; Muller, M.; Boyen, H.-G. Conings, B. Assessing the toxicity of Pb- and Sn-based perovskite solar cells in model organism *Danio rerio*, *Sci. Rep.*, **2016**, *6*, 18721.
- (38) Boopathi, K. M.; Karuppuswamy, P.; Singh, A.; Hanmandlu, C.; Lin, L.; Abbas, S. A.; Chang, C. C.; Wang, P. C.; Li, G. Chu, C. W. Solution-processable antimony-based light-absorbing materials beyond lead halide perovskites, *J. Mater. Chem. A*, **2017**, *5*, 20843–20850.
- (39) Zhang, Z.; Li, X.; Xia, X.; Wang, Z.; Huang, Z.; Lei, B. Gao, Y. High-Quality $(\text{CH}_3\text{NH}_3)_2\text{Bi}_2\text{I}_8$ Film-Based Solar Cells, *J. Phys. Chem. Lett.*, **2017**, *8*, 4300–4307.
- (40) Saparov, B.; Hong, F.; Sun, J.-P.; Duan, H.-S.; Meng, W.; Cameron, S.; Hill, I. G.; Yan, Y. Mitzi, D. B. Thin-Film Preparation and Characterization of $\text{Cs}_3\text{Sb}_2\text{I}_9$, *Chem. Mater.*, **2015**, *27*, 5622–5632.
- (41) Park, B.-W.; Philippe, B.; Zhang, X.; Rensmo, H.; Boschloo, G. Johansson, E. M. J. Bismuth Based Hybrid Perovskites $\text{A}_3\text{Bi}_2\text{I}_8$ (A: Methylammonium or Cesium) for Solar Cell Application, *Adv. Mater.*, **2015**, *27*, 6806–6813.
- (42) Lester R. Morss; M. Siegal; L. Stengerand Norman Edelstein. Preparation of cubic chloro complex compounds of trivalent metals: $\text{Cs}_2\text{NaMCl}_6$, *Inorg. Chem.*, **1970**, *9*, 1771–1775.
- (43) Smit, W. M. A.; Dirksen, G. J. Stufkens, D. J. Infrared And Raman Spectra Of The Elpasolites $\text{Cs}_2\text{NaSbCl}_6$, And $\text{Cs}_2\text{NaBiCl}_6$, Evidence For A Pseudo Jahn-Teller Distorted Ground State, *J. Phys. Chem. Solids*, **1990**, *51*, 189–196.
- (44) Urland, W. The Assessment Of The Crystal Field Parameters For fⁿ-Electron Systems By The Angular Overlap Model. Rare-Earth Ions M^{3+} In $\text{Cs}_2\text{NaMCl}_6$, *Chem. Phys. Lett.*, **1981**, *83* (1), 116–119.
- (45) Barbier, P.; Drache, M.; Mairesse, G. Ravez. Phase Transitions in a $\text{Cs}_{2-x}\text{K}_{1+x}\text{BiCl}_6$ Solid Solutions, *Journal of Solid State Chemistry*, **1982**, *42*, 130–135.

- (46) Benachenhou, F.; Mairesse, G.; Nowogrocki, G. Thomas, D. Structural Studies of Cs-K-Bi Mixed Chlorides Relation to the Crystal Structures of A_2BMX_6 , A_3MX_6 , and A_2MX_6 , *Journal of Solid State Chemistry*, **1986**, *65*, 13–26.
- (47) Flora, G.; Gupta, D. Tiwari, A. Toxicity of lead: A review with recent updates, *Interdiscip. Toxicol.*, **2012**, *5*, 47–58.
- (48) Savory, C. N.; Walsh, A. Scanlon, D. O. Can Pb-Free Halide Double Perovskites Support High-Efficiency Solar Cells?, *ACS Energy Lett.*, **2016**, *1*, 949–955.
- (49) Kung, P.-K.; Li, M.-H.; Lin, P.-Y.; Jhang, J.-Y.; Pantaler, M.; Lupascu, D. C.; Grancini, G. Chen, P. Lead-Free Double Perovskites for Perovskite Solar Cells, *Sol. RRL*, **2019**, *131*, 1900306.
- (50) Fronel, C. New data on elpasolite and hagemanite, *American Mineralogist*, **1948**, *33*, 84–87.
- (51) Knox K., Mitchell D. W. The preparation and structure of K_2NaCrF_6 , K_2NaFeF_6 and K_2NaGaF_6 , *Journal of Onorganic and Nuclear Chemistry*, **1961**, *21*, 253–258.
- (52) Yi, X.; Li, R.; Zhu, H.; Gao, J.; You, W.; Gong, Z.; Guo, W. Chen, X. K_2NaAlF_6 : Mn^{2+} red phosphor: room-temperature synthesis and electronic/vibronic structures, *J. Mater. Chem. C*, **2018**, *6*, 2069–2076.
- (53) Morris, L. R. Robinson, W. R. Crystal structure of $Cs_2NaBiCl_6$, *Acta Cryst.*, **1972**, *B28*, 653.
- (54) Van der Steen, A. C., Dirksen, G. J. Luminescence and crystal growth of Cs_2NaYCl_6 , *Chem. Phys. Lett.*, **1978**, *59*, 110–112.
- (55) Samulon E. C., Gundiah B., Gascón M., Khodyuk I. V., Derenzo S. E., Bizarri G. A., Bourret-Courchesne E. D., Luminescence and scintillation properties of Ce^{3+} -activated $Cs_2NaGdCl_6$, Cs_2GdCl_6 , $Cs_2NaGdBr_6$ and Cs_2GdBr_6 , *Journal of Luminescence*, **2014**, *153*, 64–72.

- (56) Vasala, S., Karppinen, M. A. B'B''O₆ perovskites, *Progress in Solid State Chemistry*, **2015**, *43*, 1–36.
- (57) Slavney, A. H.; Hu, T.; Lindenberg, A. M. Karunadasa, H. I. A Bismuth-Halide Double Perovskite with Long Carrier Recombination Lifetime for Photovoltaic Applications, *J. Am. Chem. Soc.*, **2016**, *138*, 2138–2141.
- (58) McClure, E. T.; Ball, M. R.; Windl, W. Woodward, P. M. Cs₂AgBiX₆ (X = Br, Cl), *Chem. Mater.*, **2016**, *28*, 1348–1354.
- (59) Volonakis, G.; Filip, M. R.; Haghighirad, A. A.; Sakai, N.; Wenger, B.; Snaith, H. J. Giustino, F. Lead-Free Halide Double Perovskites via Heterovalent Substitution of Noble Metals, *J. Phys. Chem. Lett.*, **2016**, *7*, 1254–1259.
- (60) Filip, M. R.; Hillman, S.; Haghighirad, A. A.; Snaith, H. J. Giustino, F. Band Gaps of the Lead-Free Halide Double Perovskites Cs₂BiAgCl₆ and Cs₂BiAgBr₆ from Theory and Experiment, *J. Phys. Chem. Lett.*, **2016**, *7*, 2579–2585.
- (61) Zhao, X.-G.; Yang, J.-H.; Fu, Y.; Yang, D.; Xu, Q.; Yu, L.; Wei, S.-H. Zhang, L. Design of Lead-Free Inorganic Halide Perovskites for Solar Cells via Cation-Transmutation, *J. Am. Chem. Soc.*, **2017**, *139*, 2630–2638.
- (62) Zhao, X.-G.; Yang, D.; Sun, Y.; Li, T.; Zhang, L.; Yu, L. Zunger, A. Cu-In Halide Perovskite Solar Absorbers, *J. Am. Chem. Soc.*, **2017**, *139*, 6718–6725.
- (63) Slavney, A. H.; Leppert, L.; Bartesaghi, D.; Gold-Parker, A.; Toney, M. F.; Savenije, T. J.; Neaton, J. B. Karunadasa, H. I. Defect-Induced Band-Edge Reconstruction of a Bismuth-Halide Double Perovskite for Visible-Light Absorption, *J. Am. Chem. Soc.* **2017**, *139*, *14*, 5015–5018.
- (64) Zhang, P.; Yang, J. Wei, S.-H. Manipulation of cation combinations and configurations of halide double perovskites for solar cell absorbers, *J. Mater. Chem. A*, **2018**, *6*, 1809–1815.

- (65) Umebayashi, T.; Asai, K.; Kondo, T.; Nakao, A. Electronic structures of lead iodide based low-dimensional crystals, *Phys. Rev. B*, **2003**, *67*, 1.
- (66) Bekenstein, Y.; Dahl, J. C.; Huang, J.; Osowiecki, W. T.; Swabeck, J. K.; Chan, E. M.; Yang, P.; Alivisatos, A. P. The Making and Breaking of Lead-Free Double Perovskite Nanocrystals of Cesium Silver-Bismuth Halide Compositions, *Nano. Lett.*, **2018**, *18*, 6, 3502–3508
- (67) Li, Q.; Wang, Y.; Pan, W.; Yang, W.; Zou, B.; Tang, J.; Quan, Z. High-Pressure Band-Gap Engineering in Lead-Free Cs₂AgBiBr₆ Double Perovskite, *Angew. Chem. Int. Ed. Engl.*, **2017**, *56*, 15969–15973.
- (68) Hoye, R. L. Z.; Schulz, P.; Schelhas, L. T.; Holder, A. M.; Stone, K. H.; Perkins, J. D.; Vigil-Fowler, D.; Siol, S.; Scanlon, D. O.; Zakutayev, A.; Walsh, A.; Smith, I. C.; Melot, B. C.; Kurchin, R. C.; Wang, Y.; Shi, J.; Marques, F. C.; Berry, J. J.; Tumas, W.; Lany, S.; Stevanović, V.; Toney, M. F.; Buonassisi, T. Perovskite-Inspired Photovoltaic Materials, *Chem. Mater.*, **2017**, *29*, 1964–1988.
- (69) Du, K.-Z.; Meng, W.; Wang, X.; Yan, Y.; Mitzi, D. B. Bandgap Engineering of Lead-Free Double Perovskite Cs₂AgBiBr₆ through Trivalent Metal Alloying, *Angew. Chem. Int. Ed. Engl.*, **2017**, *56*, 8158–8162.
- (70) Wilson, J. N.; Idriss, H. Structure sensitivity and photocatalytic reactions of semiconductors. Effect of the last layer atomic arrangement, *J. Am. Chem. Soc.*, **2002**, *124*, 11284–11285.
- (71) Bellaiche L., Zunger A. Effects of atomic short-range order on the electronic and optical properties of GaAsN, GaInN, and GaInAs alloys, *Phys. Rev. B*, **1998**, *57*, 4425.
- (72) Filip, M. R.; Eperon, G. E.; Snaith, H. J.; Giustino, F. Steric engineering of metal-halide perovskites with tunable optical band gaps, *Nat. Commun.*, **2014**, *5*, 5757.

- (73) Li, T.; Zhao, X.; Yang, D.; Du, M.-H.; Zhang, L. Intrinsic Defect Properties in Halide Double Perovskites for Optoelectronic Applications, *Phys. Rev. Applied*, **2018**, *10*.
- (74) Greul, E.; Petrus, M. L.; Binek, A.; Docampo, P.; Bein, T. Highly stable, phase pure Cs₂AgBiBr₆ double perovskite thin films for optoelectronic applications, *J. Mater. Chem. A*, **2017**, *5*, 19972–19981.
- (75) Xiao, Z.; Yan, Y.; Hosono, H.; Kamiya, T. Roles of Pseudo-Closed s² Orbitals for Different Intrinsic Hole Generation between Tl-Bi and In-Bi Bromide Double Perovskites, *J. Phys. Chem. Lett.*, **2018**, *9*, 258–262.
- (76) Xiao, Z.; Meng, W.; Wang, J.; Yan, Y. Thermodynamic Stability and Defect Chemistry of Bismuth-Based Lead-Free Double Perovskites, *Chem. Sus. Chem.*, **2016**, *9*, 2628–2633.
- (77) Cheng, P.; Wu, T.; Li, Y.; Jiang, L.; Deng, W.; Han, K. Combining theory and experiment in the design of a lead-free ((CH₃NH₃)₂AgBiI₆) double perovskite, *New. J. Chem.*, **2017**, *41*, 9598–9601.
- (78) Li, Y.-J.; Wu, T.; Sun, L.; Yang, R.-X.; Jiang, L.; Cheng, P.-F.; Hao, Q.-Q.; Wang, T.-J.; Lu, R.-F.; Deng, W.-Q. Lead-free and stable antimony–silver-halide double perovskite (CH₃NH₃)₂AgSbI₆, *RSC Adv*, **2017**, *7*, 35175–35180.
- (79) Wei, F.; Deng, Z.; Sun, S.; Zhang, F.; Evans, D. M.; Kieslich, G.; Tominaka, S.; Carpenter, M. A.; Zhang, J.; Bristowe, P. D.; Cheetham, A. K. Synthesis and Properties of a Lead-Free Hybrid Double Perovskite, *Chem. Mater.*, **2017**, *29*, 1089–1094.
- (80) Wu, C.; Zhang, Q.; Liu, Y.; Luo, W.; Guo, X.; Huang, Z.; Ting, H.; Sun, W.; Zhong, X.; Wei, S.; Wang, S.; Chen, Z.; Xiao, L. The Dawn of Lead-Free Perovskite Solar Cell, *Adv. Sci. (Weinh)*, **2018**, *5*, 1700759.
- (81) Ning, W.; Wang, F.; Wu, B.; Lu, J.; Yan, Z.; Liu, X.; Tao, Y.; Liu, J.-M.; Huang, W.; Fahlman, M.; Hultman, L.; Sum, T. C.; Gao, F. Long Electron-Hole Diffusion Length in High-Quality Lead-Free Double Perovskite Films, *Adv Mater*, **2018**, *30*, e1706246.

- (82) Pantaler, M.; Cho, K. T.; Queloz, V. I. E.; García Benito, I.; Fetterhauer, C.; Anusca, I.; Nazeeruddin, M. K.; Lupascu, D. C., Grancini, G. Hysteresis-Free Lead-Free Double-Perovskite Solar Cells by Interface Engineering, *ACS Energy Lett.*, **2018**, *3*, 1781–1786.
- (83) Wang, M.; Zeng, P.; Bai, S.; Gu, J.; Li, F.; Yang, Z. Liu, M. High-Quality Sequential-Vapor-Deposited Cs₂AgBiBr₆ Thin Films for Lead-Free Perovskite Solar Cells, *Sol. RRL*, **2018**, *2*, 1800217.
- (84) Zhang, C.; Gao, L.; Teo, S.; Guo, Z.; Xu, Z.; Zhao, S. Ma, T. Design of a novel and highly stable lead-free Cs₂NaBiI₆ double perovskite for photovoltaic application, *Sustainable Energy Fuels*, **2018**, *2*, 2419–2428.
- (85) Chen, M.; Ju, M.-G.; Carl, A. D.; Zong, Y.; Grimm, R. L.; Gu, J.; Zeng, X. C.; Zhou, Y. Padture, N. P. Cesium Titanium(IV) Bromide Thin Films Based Stable Lead-free Perovskite Solar Cells, *Joule*, **2018**, *2*, 558–570.
- (86) Feng, H.-J.; Deng, W.; Yang, K.; Huang, J. Zeng, X. C. Double Perovskite Cs₂BBiX₆ (B = Ag, Cu; X = Br, Cl)/TiO₂ Heterojunction, *J. Phys. Chem. C*, **2017**, *121*, 4471–4480.
- (87) Volonakis, G.; Haghghirad, A. A.; Milot, R. L.; Sio, W. H.; Filip, M. R.; Wenger, B.; Johnston, M. B.; Herz, L. M.; Snaith, H. J. Giustino, F. Cs₂InAgCl₆: A New Lead-Free Halide Double Perovskite with Direct Band Gap, *J. Phys. Chem. Lett.*, **2017**, *8*, 772–778.
- (88) Filip, M. R.; Liu, X.; Miglio, A.; Hautier, G. Giustino, F. Phase Diagrams and Stability of Lead-Free Halide Double Perovskites Cs₂BB'X₆. B = Sb and Bi, B' = Cu, Ag, and Au, and X = Cl, Br, and I, *J. Phys. Chem. C*, **2018**, *122*, 158–170.
- (89) Xiao, Z.; Du, K.-Z.; Meng, W.; Mitzi, D. B. Yan, Y. Chemical Origin of the Stability Difference between Copper(I)- and Silver(I)-Based Halide Double Perovskites, *Angew. Chem. Int. Ed. Engl.*, **2017**, *56*, 12107–12111.

- (90) Zhou, J.; Xia, Z.; Molokeev, M. S.; Zhang, X.; Peng, D.; Liu, Q. Composition design, optical gap and stability investigations of lead-free halide double perovskite Cs₂AgInCl₆, *J. Mater. Chem. A*, **2017**, *5*, 15031–15037.
- (91) Meng, W.; Wang, X.; Xiao, Z.; Wang, J.; Mitzi, D. B.; Yan, Y. Parity-Forbidden Transitions and Their Impact on the Optical Absorption Properties of Lead-Free Metal Halide Perovskites and Double Perovskites, *J. Phys. Chem. Lett.*, **2017**, *8*, 2999–3007.
- (92) Xu, J.; Liu, J.-B.; Liu, B.-X.; Huang, B. Intrinsic Defect Physics in Indium-based Lead-free Halide Double Perovskites, *J. Phys. Chem. Lett.*, **2017**, *8*, 4391–4396.
- (93) Xu, J.; Liu, J.-B.; Liu, B.-X.; Wang, J.; Huang, B. Defect Engineering of Grain Boundaries in Lead-Free Halide Double Perovskites for Better Optoelectronic Performance, *Adv. Funct. Mater.*, **2019**, *29*, 1805870.
- (94) Ball, J. M., Petrozza A., Defects in perovskite-halides and their effects in solar cells, *Nat. Energy*, **2016**, *1*.
- (95) Lan, C.; Zhao, S.; Luo, J.; Fan, P. First-principles study of anion diffusion in lead-free halide double perovskites, *Phys. Chem. Chem. Phys.*, **2018**, *20*, 24339–24344.
- (96) Pan, W.; Wu, H.; Luo, J.; Deng, Z.; Ge, C.; Chen, C.; Jiang, X.; Yin, W.-J.; Niu, G.; Zhu, L.; Yin, L.; Zhou, Y.; Xie, Q.; Ke, X.; Sui, M.; Tang, J. Cs₂AgBiBr₆ single-crystal X-ray detectors with a low detection limit, *Nature Photon.*, **2017**, *11*, 726–732.
- (97) Lindquist, K. P.; Mack, S. A.; Slavney, A. H.; Leppert, L.; Gold-Parker, A.; Stebbins, J. F.; Salleo, A.; Toney, M. F.; Neaton, J. B.; Karunadasa, H. I. Tuning the bandgap of Cs₂AgBiBr₆ through dilute tin alloying, *Chem. Sci.*, **2019**, *10*, 10620–10628.
- (98) Tran, T. T.; Panella, J. R.; Chamorro, J. R.; Morey, J. R.; McQueen, T. M. Designing indirect–direct bandgap transitions in double perovskites, *Mater. Horiz.*, **2017**, *4*, 688–693.

- (99) Igbari, F.; Wang, R.; Wang, Z.-K.; Ma, X.-J.; Wang, Q.; Wang, K.-L.; Zhang, Y.; Liao, L.-S.; Yang, Y. Composition Stoichiometry of Cs₂AgBiBr₆ Films for Highly Efficient Lead-Free Perovskite Solar Cells, *Nano. Lett.*, **2019**, *19*, 2066–2073.
- (100) Gao, W.; Ran, C.; Xi, J.; Jiao, B.; Zhang, W.; Wu, M.; Hou, X.; Wu, Z. High-Quality Cs₂AgBiBr₆ Double Perovskite Film for Lead-Free Inverted Planar Heterojunction Solar Cells with 2.2 % Efficiency, *Chem. Phys. Chem.*, **2018**, *19*, 1696.
- (101) Dong, L.; Sun, S.; Deng, Z.; Li, W.; Wei, F.; Qi, Y.; Li, Y.; Li, X.; Lu, P.; Ramamurty, U. Elastic properties and thermal expansion of lead-free halide double perovskite Cs₂AgBiBr₆, *Computational Materials Science*, **2018**, *141*, 49–58.
- (102) Haque, E.; Hossain, M. A. Origin of ultra-low lattice thermal conductivity in Cs₂BiAgX₆ (X = Cl, Br) and its impact on thermoelectric performance, *Journal of Alloys and Compounds*, **2018**, *748*, 63–72.
- (103) Bartesaghi, D.; Slavney, A. H.; Gélvez-Rueda, M. C.; Connor, B. A.; Grozema, F. C.; Karunadasa, H. I.; Savenije, T. J. Charge Carrier Dynamics in Cs₂AgBiBr₆ Double Perovskite, *J. Phys. Chem. C, Nanomater Interfaces*, **2018**, *122*, 4809–4816.
- (104) Kentsch, R.; Scholz, M.; Horn, J.; Schlettwein, D.; Oum, K.; Lenzer, T. Exciton Dynamics and Electron–Phonon Coupling Affect the Photovoltaic Performance of the Cs₂AgBiBr₆ Double Perovskite, *J. Phys. Chem. C*, **2018**, *122*, 25940–25947.
- (105) Brian F. Aull and Hans P. Jenssen. Impact of ion-host interactions on the 5d-to-4f spectra of lanthanide rare-earth-metal ions. II. The Ce-doped elpasolites *Phys. Rev. B* **1986**, *34*, 6647.
- (106) da Fonesca, R.J.M., Sosman, L.P., Tavares, A.D., Jr., Bordallo, H.N. Vibrational Analysis of the Elpasolites Cs₂NaAlF₆ and Cs₂NaGaF₆ Doped with Cr³⁺ Ions by Fluorescence Spectroscopy, *Journal of Fluorescence*, **2000**, *10*, 375–381.

- (107) Zhou, L.; Xu, Y.-F.; Chen, B.-X.; Kuang, D.-B.; Su, C.-Y. Synthesis and Photocatalytic Application of Stable Lead-Free Cs₂AgBiBr₆ Perovskite Nanocrystals, *Small*, **2018**, *14*, e1703762.
- (108) Ning, W.; Zhao, X.-G.; Klarbring, J.; Bai, S.; Ji, F.; Wang, F.; Simak, S. I.; Tao, Y.; Ren, X.-M.; Zhang, L.; Huang, W.; Abrikosov, I. A.; Gao, F. Thermochromic Lead-Free Halide Double Perovskites, *Adv. Funct. Mater.*, **2019**, *29*, 1807375.
- (109) Yang, B.; Mao, X.; Hong, F.; Meng, W.; Tang, Y.; Xia, X.; Yang, S.; Deng, W.; Han, K. Lead-Free Direct Band Gap Double-Perovskite Nanocrystals with Bright Dual-Color Emission, *J. Am. Chem. Soc.*, **2018**, *140*, 17001–17006.
- (110) Locardi, F.; Cirignano, M.; Baranov, D.; Dang, Z.; Prato, M.; Drago, F.; Ferretti, M.; Pinchetti, V.; Fanciulli, M.; Brovelli, S.; Trizio, L.; deManna, L. Colloidal Synthesis of Double Perovskite Cs₂AgInCl₆ and Mn-Doped Cs₂AgInCl₆ Nanocrystals, *J. Am. Chem. Soc.*, **2018**, *140*, 12989–12995.
- (111) Luo, J.; Wang, X.; Li, S.; Liu, J.; Guo, Y.; Niu, G.; Yao, L.; Fu, Y.; Gao, L.; Dong, Q.; Zhao, C.; Leng, M.; Ma, F.; Liang, W.; Wang, L.; Jin, S.; Han, J.; Zhang, L.; Etheridge, J.; Wang, J.; Yan, Y.; Sargent, E. H.; Tang, J. Efficient and stable emission of warm-white light from lead-free halide double perovskites, *Nature*, **2018**, *563*, 541–545.
- (112) Luo, J.; Li, S.; Wu, H.; Zhou, Y.; Li, Y.; Liu, J.; Li, J.; Li, K.; Yi, F.; Niu, G.; Tang, J. Cs₂AgInCl₆ Double Perovskite Single Crystals: Parity Forbidden Transitions and Their Application For Sensitive and Fast UV Photodetectors, *ACS Photonics*, **2018**, *5*, 398–405.
- (113) Lei, L.-Z.; Shi, Z.-F.; Li, Y.; Ma, Z.-Z.; Zhang, F.; Xu, T.-T.; Tian, Y.-T.; Di Wu; Li, X.-J.; Du, G.-T. High-efficiency and air-stable photodetectors based on lead-free double perovskite Cs₂AgBiBr₆ thin films, *J. Mater. Chem. C*, **2018**, *6*, 7982–7988.

- (114) Wu, C.; Du, B.; Luo, W.; Liu, Y.; Li, T.; Wang, D.; Guo, X.; Ting, H.; Fang, Z.; Wang, S.; Chen, Z.; Chen, Y. Xiao, L. Highly Efficient and Stable Self-Powered Ultraviolet and Deep-Blue Photodetector Based on Cs₂AgBiBr₆/SnO₂ Heterojunction, *Advanced Optical Materials*, **2018**, *6*, 1800811.
- (115) Li, Y.; Shi, Z.; Lei, L.; Li, S.; Yang, D.; Di Wu; Xu, T.; Tian, Y.; Lu, Y.; Wang, Y.; Zhang, L.; Li, X.; Zhang, Y.; Du, G. Shan, C. Ultrastable Lead-Free Double Perovskite Photodetectors with Imaging Capability, *Adv. Mater. Interfaces*, **2019**, *6*, 1900188.
- (116) Li, H.; Shan, X.; Neu, J. N.; Geske, T.; Davis, M.; Mao, P.; Xiao, K.; Siegrist, T. Yu, Z. Lead-free halide double perovskite-polymer composites for flexible X-ray imaging, *J. Mater. Chem. C*, **2018**, *6*, 11961–11967.
- (117) Yuan, W.; Niu, G.; Xian, Y.; Wu, H.; Wang, H.; Yin, H.; Liu, P.; Li, W. Fan, J. In Situ Regulating the Order–Disorder Phase Transition in Cs₂AgBiBr₆ Single Crystal toward the Application in an X-Ray Detector, *Adv. Funct. Mater.*, **2019**, *29*, 1900234.
- (118) Hu, Q.; Deng, Z.; Hu, M.; Zhao, A.; Zhang, Y.; Tan, Z.; Niu, G.; Wu, H. Tang, J. X-ray scintillation in lead-free double perovskite crystals, *Sci. China Chem.*, **2018**, *61*, 1581–1586.
- (119) Pantaler, M.; Fettkenhauer, C.; Nguyen, H. L.; Anusca, I. Lupascu, D. C. Deposition routes of Cs₂AgBiBr₆ double perovskites for photovoltaic applications, *MRS Adv.*, **2018**, *3*, 1819–1823.
- (120) Slavney, A. H.; Hu, T.; Lindenberg, A. M. Karunadasa, H. I. A Bismuth-Halide Double Perovskite with Long Carrier Recombination Lifetime for Photovoltaic Applications, *J. Am. Chem. Soc.*, **2016**, *138*, 2138–2141.
- (121) Karlin K. D. *Progress in inorganic chemistry: Volume 48*; Wiley: New York, **1999**.

- (122) Edri, E.; Kirmayer, S.; Cahen, D. Hodes, G. High Open-Circuit Voltage Solar Cells Based on Organic-Inorganic Lead Bromide Perovskite, *J. Phys. Chem. Lett.*, **2013**, *4*, 897–902.
- (123) Fan, P.; Di Gu; Liang, G.-X.; Luo, J.-T.; Chen, J.-L.; Zheng, Z.-H. Zhang, D.-P. High-performance perovskite $\text{CH}_3\text{NH}_3\text{PbI}_3$ thin films for solar cells prepared by single-source physical vapour deposition, *Sci. Rep.*, **2016**, *6*, 29910.
- (124) Ono, L. K.; Leyden, M. R.; Wang, S. Qi, Y. Organometal halide perovskite thin films and solar cells by vapor deposition, *J. Mater. Chem. A*, **2016**, *4*, 6693–6713.
- (125) Cai, B.; Zhang, W.-H. Qiu, J. Solvent engineering of spin-coating solutions for planar-structured high-efficiency perovskite solar cells, *Chinese Journal of Catalysis*, **2015**, *36*, 1183–1190.
- (126) Sardela M., *Practical Materials Characterization*; Springer: London, **2014**.
- (127) Smallwood I. M., *Handbook of organic solvent properties*; Arnold: London, **1996**.
- (128) Emara, J.; Schnier, T.; Pourdavoud, N.; Riedl, T.; Meerholz, K. Olthof, S. Impact of Film Stoichiometry on the Ionization Energy and Electronic Structure of $\text{CH}_3\text{NH}_3\text{PbI}_3$ Perovskites, *Adv. Mater.*, **2016**, *28*, 553–559.
- (129) Schulz, P.; Whittaker-Brooks, L. L.; MacLeod, B. A.; Olson, D. C.; Loo, Y.-L. Kahn, A. Electronic Level Alignment in Inverted Organometal Perovskite Solar Cells, *Adv. Mater. Interfaces*, **2015**, *2*, 1400532.
- (130) Bass, K. K.; Estergreen, L.; Savory, C. N.; Buckeridge, J.; Scanlon, D. O.; Djurovich, P. I.; Bradforth, S. E.; Thompson, M. E. Melot, B. C. Vibronic Structure in Room Temperature Photoluminescence of the Halide Perovskite $\text{Cs}_2\text{Bi}_2\text{Br}_8$, *Inorg Chem*, **2017**, *56*, 42–45.

- (131) Yang, B.; Chen, J.; Hong, F.; Mao, X.; Zheng, K.; Yang, S.; Li, Y.; Pullerits, T.; Deng, W.; Han, K. Lead-Free, Air-Stable All-Inorganic Cesium Bismuth Halide Perovskite Nanocrystals, *Angew. Chem. Int. Ed. Engl.*, **2017**, *56*, 12471–12475.
- (132) Abou-Ras D., Kirchartz T., Rau U. *Advanced characterization techniques for thin film solar cells*; Wiley-VCH Verlag: Weinheim, Germany, 2016.
- (133) Grancini, G.; Santosh Kumar, R. S.; Abrusci, A.; Yip, H.-L.; Li, C.-Z.; Jen, A.-K. Y.; Lanzani, G.; Snaith, H. J. Boosting Infrared Light Harvesting by Molecular Functionalization of Metal Oxide/Polymer Interfaces in Efficient Hybrid Solar Cells, *Adv. Funct. Mater.*, **2012**, *22*, 2160–2166.
- (134) Mali, S. S.; Shim, C. S.; Hong, C. K. Highly stable and efficient solid-state solar cells based on methylammonium lead bromide ($\text{CH}_3\text{NH}_3\text{PbBr}_3$) perovskite quantum dots, *NPG Asia Mater*, **2015**, *7*, e208–e208.
- (135) Meng, L.; You, J.; Guo, T.-F.; Yang, Y. Recent Advances in the Inverted Planar Structure of Perovskite Solar Cells, *Acc. Chem. Res.*, **2016**, *49*, 155–165.
- (136) Li, L.; Zhang, F.; Wang, W.; Fang, Y.; Huang, J. Revealing the working mechanism of polymer photodetectors with ultra-high external quantum efficiency, *Phys. Chem. Chem. Phys.*, **2015**, *17*, 30712–30720.
- (137) Cho, K. T.; Grancini, G.; Lee, Y.; Oveisi, E.; Ryu, J.; Almora, O.; Tschumi, M.; Schouwink, P. A.; Seo, G.; Heo, S.; Park, J.; Jang, J.; Paek, S.; Garcia-Belmonte, G.; Nazeeruddin, M. K. Selective growth of layered perovskites for stable and efficient photovoltaics, *Energy Environ. Sci.*, **2018**, *11*, 952–959.
- (138) Ostapchenko, V. Effect of TiCl_4 Treatment on Different TiO_2 Blocking Layer Deposition Methods, *Int. J. Electrochem. Sci.*, **2017**, 2262–2271.

- (139) Singh, T., Miyasaka, T. Stabilizing the Efficiency Beyond 20% with a Mixed Cation Perovskite Solar Cell Fabricated in Ambient Air under Controlled Humidity, *Adv. Energy Mater.*, **2018**, 8, 1700677.
- (140) Konstantakou, M.; Perganti, D.; Falaras, P. Stergiopoulos, T. Anti-Solvent Crystallization Strategies for Highly Efficient Perovskite Solar Cells, *Crystals*, **2017**, 7, 291.
- (141) Heo, J. H.; Im, S. H.; Noh, J. H.; Mandal, T. N.; Lim, C.-S.; Chang, J. A.; Lee, Y. H.; Kim, H.-j.; Sarkar, A.; Nazeeruddin, M. K.; Grätzel, M. Seok, S. I. Efficient inorganic–organic hybrid heterojunction solar cells containing perovskite compound and polymeric hole conductors, *Nature Photon*, **2013**, 7, 486–491.
- (142) Calió, L.; Kazim, S.; Grätzel, M. Ahmad, S. Hole-Transport Materials for Perovskite Solar Cells, *Angew. Chem. Int. Ed. Engl.*, **2016**, 55, 14522–14545.
- (143) Jiménez-López, J.; Cambarau, W.; Cabau, L. Palomares, E. Charge Injection, Carriers Recombination and HOMO Energy Level Relationship in Perovskite Solar Cells, *Sci. Rep.*, **2017**, 7, 6101.
- (144) Tang, Z.; Wang, J.; Melianas, A.; Wu, Y.; Kroon, R.; Li, W.; Ma, W.; Andersson, M. R.; Ma, Z.; Cai, W.; Tress, W. Inganäs, O. Relating open-circuit voltage losses to the active layer morphology and contact selectivity in organic solar cells, *J. Mater. Chem. A*, **2018**, 270, 1789.
- (145) Ravishankar, S.; Gharibzadeh, S.; Roldán-Carmona, C.; Grancini, G.; Lee, Y.; Ralaiarisoa, M.; Asiri, A. M.; Koch, N.; Bisquert, J. Nazeeruddin, M. K. Influence of Charge Transport Layers on Open-Circuit Voltage and Hysteresis in Perovskite Solar Cells, *Joule*, **2018**, 2, 788–798.
- (146) Frost, J. M. Walsh, A. What Is Moving in Hybrid Halide Perovskite Solar Cells?, *Acc. Chem. Res.*, **2016**, 49, 528–535.

- (147) Bi, E.; Chen, H.; Xie, F.; Wu, Y.; Chen, W.; Su, Y.; Islam, A.; Grätzel, M.; Yang, X.Han, L. Diffusion engineering of ions and charge carriers for stable efficient perovskite solar cells, *Nat. Commun.*, **2017**, *8*, 15330.
- (148) Kim, H.-S.; Jang, I.-H.; Ahn, N.; Choi, M.; Guerrero, A.; Bisquert, J.Park, N.-G. Control of I-V hysteresis in $\text{CH}_3\text{NH}_3\text{PbI}_3$ perovskite solar cell, *J. Phys. Chem. Lett.*, **2015**, *6*, 4633–4639.
- (149) Bastiani, M. de; Dell'Erba, G.; Gandini, M.; D'Innocenzo, V.; Neutzner, S.; Kandada, A. R. S.; Grancini, G.; Binda, M.; Prato, M.; Ball, J. M.; Caironi, M.Petrozza, A. Ion Migration and the Role of Preconditioning Cycles in the Stabilization of the J - V Characteristics of Inverted Hybrid Perovskite Solar Cells, *Adv. Energy Mater.*, **2016**, *6*, 1501453.
- (150) Gharibzadeh, S.; Valduga de Almeida Camargo, F.; Roldán-Carmona, C.; Gschwend, G. C.; Pascual, J.; Tena-Zaera, R.; Cerullo, G.; Grancini, G.Nazeeruddin, M. K. Picosecond Capture of Photoexcited Electrons Improves Photovoltaic Conversion in $\text{MAPbI}_3\text{:C70}$ -Doped Planar and Mesoporous Solar Cells, *Adv. Mater.*, **2018**, e1801496.
- (151) Pfuetzner S., Meiss J., Petrich A., Riede, M., Leo K., Improved bulk heterojunction organic solar cells employing C70 fullerenes. *Appl. Phys. Lett.* **2009**, *94*, 223307.
- (152) Yang, B.; Chen, J.; Yang, S.; Hong, F.; Sun, L.; Han, P.; Pullerits, T.; Deng, W.Han, K. Lead-Free Silver-Bismuth Halide Double Perovskite Nanocrystals, *Angew. Chem. Int. Ed. Engl.*, **2018**, *57*, 5359–5363.
- (153) Zheng, K.; Žídek, K.; Abdellah, M.; Chen, J.; Chábera, P.; Zhang, W.; Al-Marri, M. J.Pullerits, T. High Excitation Intensity Opens a New Trapping Channel in Organic–Inorganic Hybrid Perovskite Nanoparticles, *ACS Energy Lett.*, **2016**, *1*, 1154–1161.
- (154) Zheng, K.; Zhu, Q.; Abdellah, M.; Messing, M. E.; Zhang, W.; Generalov, A.; Niu, Y.; Ribaud, L.; Canton, S. E.Pullerits, T. Exciton Binding Energy and the Nature of

- Emissive States in Organometal Halide Perovskites, *J. Phys. Chem. Lett.*, **2015**, *6*, 2969–2975.
- (155) Correa-Baena, J.-P.; Abate, A.; Saliba, M.; Tress, W.; Jesper Jacobsson, T.; Grätzel, M. Hagfeldt, A. The rapid evolution of highly efficient perovskite solar cells, *Energy Environ. Sci.*, **2017**, *10*, 710–727.
- (156) Saliba, M.; Matsui, T.; Seo, J.-Y.; Domanski, K.; Correa-Baena, J.-P.; Nazeeruddin, M. K.; Zakeeruddin, S. M.; Tress, W.; Abate, A.; Hagfeldt, A. Grätzel, M. Cesium-containing triple cation perovskite solar cells: improved stability, reproducibility and high efficiency, *Energy Environ. Sci.*, **2016**, *9*, 1989–1997.
- (157) Anusca, I.; Balčiūnas, S.; Gemeiner, P.; Svirskas, Š.; Sanlialp, M.; Lackner, G.; Fettkenhauer, C.; Belovickis, J.; Samulionis, V.; Ivanov, M.; Dkhil, B.; Banys, J.; Shvartsman, V. V., Lupascu, D. C. Dielectric Response: Answer to Many Questions in the Methylammonium Lead Halide Solar Cell Absorbers, *Adv. Energy Mater.*, **2017**, *7*, 1700600.
- (158) Yan, W.; Rao, H.; Wei, C.; Liu, Z.; Bian, Z.; Xin, H. Huang, W. Highly efficient and stable inverted planar solar cells from $(\text{FAI})_{1-x}(\text{MABr})_x\text{PbI}_3$ perovskites, *Nano Energy*, **2017**, *35*, 62–70.
- (159) Creutz, S. E.; Crites, E. N.; Siena, M. C. deGamelin, D. R. Colloidal Nanocrystals of Lead-Free Double-Perovskite (Elpasolite) Semiconductors: Synthesis and Anion Exchange To Access New Materials, *Nano Lett*, **2018**, *18*, 1118–1123.
- (160) Hutter, E. M.; Gélvez-Rueda, M. C.; Bartesaghi, D.; Grozema, F. C. Savenije, T. J. Band-Like Charge Transport in $\text{Cs}_2\text{AgBiBr}_6$ and Mixed Antimony-Bismuth $\text{Cs}_2\text{AgBi}_{1-x}\text{Sb}_x\text{Br}_6$ Halide Double Perovskites, *ACS Omega*, **2018**, *3*, 11655–11662.

- (161) Chatterjee, S.; Dasgupta, U., Pal, A. J. Sequentially Deposited Antimony-Doped $\text{CH}_3\text{NH}_3\text{PbI}_3$ Films in Inverted Planar Heterojunction Solar Cells with a High Open-Circuit Voltage, *J. Phys. Chem. C*, **2017**, *121*, 20177–20187.
- (162) Im, J.; Stoumpos, C. C.; Jin, H.; Freeman, A. J. Kanatzidis, M. G. Antagonism between Spin-Orbit Coupling and Steric Effects Causes Anomalous Band Gap Evolution in the Perovskite Photovoltaic Materials $\text{CH}_3\text{NH}_3\text{Sn}_{1-x}\text{Pb}_x\text{I}_3$, *J. Phys. Chem. Lett.*, **2015**, *6*, 3503–3509.
- (163) Pantaler, M.; Olthof, S.; Meerholz, K. Lupascu, D. C. Bismuth-Antimony mixed double perovskites $\text{Cs}_2\text{AgBi}_{1-x}\text{Sb}_x\text{Br}_6$ in solar cells, *MRS Adv.*, **2019**, 1–8.
- (164) Slouka, C.; Kainz, T.; Navickas, E.; Walch, G.; Hutter, H.; Reichmann, K. Fleig, J. The Effect of Acceptor and Donor Doping on Oxygen Vacancy Concentrations in Lead Zirconate Titanate (PZT), *Materials (Basel)*, **2016**, *9*.
- (165) Tao, S.; Schmidt, I.; Brocks, G.; Jiang, J.; Tranca, I.; Meerholz, K. Olthof, S. Absolute energy level positions in tin- and lead-based halide perovskites, *Nat. Commun.*, **2019**, *10*, 2560.
- (166) Yang, B.; Hong, F.; Chen, J.; Tang, Y.; Yang, L.; Sang, Y.; Xia, X.; Guo, J.; He, H.; Yang, S.; Deng, W. Han, K. Colloidal Synthesis and Charge-Carrier Dynamics of $\text{Cs}_2\text{AgSb}_{1-y}\text{Bi}_y\text{X}_6$ (X: Br, Cl; $0 \leq y \leq 1$) Double Perovskite Nanocrystals, *Angew. Chem. Int. Ed. Engl.*, **2019**, *58*, 2278–2283.
- (167) Shen, H.; Li, J.; Wang, H.; Ma, J.; Wang, J.; Luo, H. Li, D. Two-Dimensional Lead-Free Perovskite $(\text{C}_6\text{H}_5\text{C}_2\text{H}_4\text{NH}_3)_2\text{CsSn}_2\text{I}_7$ with High Hole Mobility, *J. Phys. Chem. Lett.*, **2019**, *10*, 7–12.
- (168) Zhang, X.; Wang, C.; Zhang, Y.; Zhang, X.; Wang, S.; Lu, M.; Cui, H.; Kershaw, S. V.; Yu, W. W. Rogach, A. L. Bright Orange Electroluminescence from Lead-Free Two-Dimensional Perovskites, *ACS Energy Lett.*, **2019**, *4*, 242–248.

- (169) Xu, H.; Jiang, Y.; He, T.; Li, S.; Wang, H.; Chen, Y.; Yuan, M.; Chen, J. Orientation Regulation of Tin-Based Reduced-Dimensional Perovskites for Highly Efficient and Stable Photovoltaics, *Adv. Funct. Mater.*, **2019**, *29*, 1807696.
- (170) Connor, B. A.; Leppert, L.; Smith, M. D.; Neaton, J. B.; Karunadasa, H. I. Layered Halide Double Perovskites, *J. Am. Chem. Soc.*, **2018**, *140*, 5235–5240.
- (171) Jana, M. K.; Janke, S. M.; Dirkes, D. J.; Dovletgeldi, S.; Liu, C.; Qin, X.; Gundogdu, K.; You, W.; Blum, V.; Mitzi, D. B. Direct-Bandgap 2D Silver-Bismuth Iodide Double Perovskite: The Structure-Directing Influence of an Oligothiophene Spacer Cation, *J. Am. Chem. Soc.*, **2019**, *141*, 7955–7964.
- (172) Cao, D. H.; Stoumpos, C. C.; Farha, O. K.; Hupp, J. T.; Kanatzidis, M. G. 2D Homologous Perovskites as Light-Absorbing Materials for Solar Cell Applications, *J. Am. Chem. Soc.*, **2015**, *137*, 7843–7850.
- (173) Kohn, W., Nobel Lecture: Electronic structure of matter—wave functions and density functionals, *Rev. Mod. Phys.*, **1999**, *71*, 1253–1266.
- (174) Giannozzi, P.; Baroni, S.; Bonini, N.; Calandra, M.; Car, R.; Cavazzoni, C.; Ceresoli, D.; Chiarotti, G. L.; Cococcioni, M.; Dabo, I.; Dal Corso, A.; Gironcoli, S. de; Fabris, S.; Fratesi, G.; Gebauer, R.; Gerstmann, U.; Gougoussis, C.; Kokalj, A.; Lazzeri, M.; Martin-Samos, L.; Marzari, N.; Mauri, F.; Mazzarello, R.; Paolini, S.; Pasquarello, A.; Paulatto, L.; Sbraccia, C.; Scandolo, S.; Sclauzero, G.; Seitsonen, A. P.; Smogunov, A.; Umari, P.; Wentzcovitch, R. M. QUANTUM ESPRESSO: a modular and open-source software project for quantum simulations of materials, *J. Phys. Condens. Matter.*, **2009**, *21*, 395502.
- (175) Quarti, C.; Marchal, N.; Beljonne, D. Tuning the Optoelectronic Properties of Two-Dimensional Hybrid Perovskite Semiconductors with Alkyl Chain Spacers, *J. Phys. Chem. Lett.*, **2018**, *9*, 3416–3424.

- (176) Giorgi, G.; Yamashita, K.; Palummo, M. Nature of the Electronic and Optical Excitations of Ruddlesden-Popper Hybrid Organic-Inorganic Perovskites: The Role of the Many-Body Interactions, *J. Phys. Chem. Lett.*, **2018**, *9*, 5891–5896.
- (177) Even, J.; Pedesseau, L.; Jancu, J.-M.; Katan, C. Importance of Spin–Orbit Coupling in Hybrid Organic/Inorganic Perovskites for Photovoltaic Applications, *J. Phys. Chem. Lett.*, **2013**, *4*, 2999–3005.
- (178) Even, J.; Pedesseau, L.; Katan, C. Comment on "Density functional theory analysis of structural and electronic properties of orthorhombic perovskite $\text{CH}_3\text{NH}_3\text{PbI}_3$ ", *Phys. Chem. Chem. Phys.*, **2014**, *16*, 8697–8698.
- (179) Traore, B.; Pedesseau, L.; Assam, L.; Che, X.; Blancon, J.-C.; Tsai, H.; Nie, W.; Stoumpos, C. C.; Kanatzidis, M. G.; Tretiak, S.; Mohite, A. D.; Even, J.; Kepenekian, M.; Katan, C. Composite Nature of Layered Hybrid Perovskites: Assessment on Quantum and Dielectric Confinements and Band Alignment, *ACS Nano*, **2018**, *12*, 3321–3332.
- (180) Li, X.-L.; Gao, L.-L.; Ding, B.; Chu, Q.-Q.; Li, Z.; Yang, G.-J. $(\text{C}_6\text{H}_5\text{NH}_3)\text{BiI}_4$, a lead-free perovskite with >330 days humidity stability for optoelectronic applications, *J. Mater. Chem. A*, **2019**, *7*, 15722–15730.
- (181) Ghasemi, M.; Lyu, M.; Roknuzzaman, M.; Yun, J.-H.; Hao, M.; He, D.; Bai, Y.; Chen, P.; Bernhardt, P. V.; Ostrikov, K.; Wang, L. Phenethylammonium bismuth halides: from single crystals to bulky-organic cation promoted thin-film deposition for potential optoelectronic applications, *J. Mater. Chem. A*, **2019**, *7*, 20733–20741.
- (182) Liao, W.-Q.; Zhang, Y.; Hu, C.-L.; Mao, J.-G.; Ye, H.-Y.; Li, P.-F.; Huang, S.; Xiong, R.-G. A lead-halide perovskite molecular ferroelectric semiconductor, *Nat. Commun.*, **2015**, *6*, 7338.

- (183) Stecker, C.; Liu, K.; Hieulle, J.; Ohmann, R.; Liu, Z.; Ono, L. K.; Wang, G. Q.; Qi, Y. Surface Defect Dynamics in Organic-Inorganic Hybrid Perovskites: From Mechanism to Interfacial Properties, *ACS Nano*, **2019**, *13*, 12127–12136.